

**DOCKETED**

<b>Docket Number:</b>	21-BSTD-02
<b>Project Title:</b>	2022 Energy Code Update CEQA Documentation
<b>TN #:</b>	238765
<b>Document Title:</b>	Holland & Knight LLP Comments - Holland & Knight References (6 of 11)
<b>Description:</b>	N/A
<b>Filer:</b>	System
<b>Organization:</b>	Holland & Knight LLP
<b>Submitter Role:</b>	Public
<b>Submission Date:</b>	7/8/2021 4:56:31 PM
<b>Docketed Date:</b>	7/8/2021

*Comment Received From: Holland & Knight LLP  
Submitted On: 7/8/2021  
Docket Number: 21-BSTD-02*

## **Holland & Knight References (6 of 11)**

The attached document is the sixth of 11 separate uploads that contain the references cited in Holland & Knight's DEIR Comment Letter.

*Additional submitted attachment is included below.*

Sources: Al Jazeera, Anthropocene Magazine, BBC, Business Insider, Climate Home News, The CT Mirror, Earth Journal Network, Los Angeles Times, National Geographic, Nature.com, The New York Times, PBS News Hour, Scientific American, The Third Pole, United Nations Economic and Social Commission for Asia and the Pacific, U.S. Department of Energy, U.S. Environmental Protection Agency, World Bank, World Resources Institute, Yale Environment 360, Yale School of Forestry and Environmental Studies, Zero Mass Water

Photo Credits: The 73-megawatt Lopburi solar power plant in central Thailand is the largest solar photovoltaic project in the world. May 2011, courtesy of the Asian Development Bank.

**Topics:** [backdraft](#), [community-based](#), [democracy and governance](#), [development](#), [energy](#), [environment](#), [featured](#), [food security](#), [Infrastructure](#), [land](#), [livelihoods](#), [natural resources](#), [solar](#), [water](#)

#### ALSO ON NEW SECURITY BEAT

<p><b>Why Feminism Is Good for Your Health</b></p> <p>10 months ago • 1 comment</p> <p>As a world still dominated by patriarchy struggles with a deadly pandemic, the ...</p>	<p><b>Valerie M. Hudson on How Sex ...</b></p> <p>6 months ago • 1 comment</p> <p>“The very first political order in any society is the sexual political order ...</p>	<p><b>Leverage COVID-19 Data Collection ...</b></p> <p>5 months ago • 4 comments</p> <p>Environmental peacebuilding could benefit from COVID-era data ...</p>	<p><b>A</b></p> <p><b>D</b></p> <p>8</p> <p>“V</p> <p>in</p> <p>re</p>
---	--	---	--



## 25 **1. Introduction**

26 Increasing interest in sustainable infrastructure encourages the design of cost-effective low-energy residential  
27 buildings, and efforts to reach net-zero (ready) energy performance. The chosen definition of net-zero (e.g., site energy  
28 versus source energy) and location of the building being constructed (e.g., climate) impact the feasibility of net zero  
29 building design. However, there is limited research on the impact of heating fuel type selection on sustainability  
30 performance when evaluating low-energy buildings. Space and water heating accounts for a significant fraction of  
31 home energy consumption, and consumers often have an option between natural gas and electric heating systems. The  
32 residential sector accounts for ~21% of total U.S. energy consumption, with residential space and water heating  
33 contributing to ~40% of sector energy use (EIA 2017a).

34 The most important factors determining heating equipment selection include: (1) cost by fuel type and equipment, (2)  
35 climate/region, and (3) home age. Other factors, such as maintenance costs, safety issues, and personal preference,  
36 may also impact heating equipment choice. Natural gas is the most widely used fuel type and class of heating  
37 technology in the U.S. (EIA 2017b), with projections of significant increases in natural gas for heating relative to  
38 electricity (EIA 2017a). However, regional differences exist, with the Hot-Humid and Mixed-Humid climate regions  
39 being predominantly electric and equal shares electric and natural gas respectively (DOE 2015).

40 There are tradeoffs in using natural gas for heating. Currently, the cost of natural gas is lower than that of electricity  
41 per unit of energy and tends to have lower source emissions rates. However, natural gas systems require connecting  
42 to the local distribution system, have lower site efficiency than electric heating systems, and increase exposure risks  
43 to leaking gas and exhaust. Gas heating has been recommended for colder climates with more extreme heating loads,  
44 while electric heating is recommended in warmer climates.

45 Although many homeowners have the option between electric and gas-fired heating systems, there has yet to be a  
46 significant amount of research investigating some of the underlying tradeoffs of such a decision. For example, use of  
47 natural gas presently leads to fewer GHG emissions (given current electricity fuel mixes) – however, it could lead to  
48 increases in other environmental inputs. There also has been minimal research exploring how the interactions between  
49 a building's gas heating systems and its other systems differ from interactions between all-electric systems.  
50 Researchers at the National Institute of Standards and Technology (NIST) have developed a database available in an  
51 online software tool capable of addressing some of these gaps in research. The Building Industry Reporting and Design

52 for Sustainability (BIRDS) tool evaluates the performance of U.S. buildings using whole-building sustainability  
53 metrics for energy use, life-cycle costs, and life-cycle environmental performance.

54 Numerous sustainability studies (Kneifel et al. 2018, Kneifel, O'Rear, and Webb 2016a, Kneifel and O'Rear 2015)  
55 have already been completed based on residential building data compiled in previous versions of BIRDS assuming  
56 electric heating equipment. Recent BIRDS updates have included natural gas heating options, allowing for much  
57 broader analyses. Using data from the BIRDS v4.0 Incremental Energy Efficiency for Residential Buildings Database  
58 in conjunction with whole-building sustainability metrics, this study evaluates alternative options for space and water  
59 heating, observing differences in the impacts alternative energy sources for heating can have on a building's overall  
60 sustainability. Although there has been some work comparing electric-driven and gas-driven heating equipment  
61 (Brenn, Soltic, and Bach 2010, Sanaye, Meybodi, and Chahartaghi 2010), there has been minimal work done making  
62 such comparisons within the context of a validated whole-building energy model of a single-family dwelling, none of  
63 which for the United States. Additionally, there is an absence of work investigating the full interaction of other  
64 building energy efficiency measures (EEMs) with changes in the heating equipment type and energy source. The  
65 findings of this paper will help to fill some of these gaps in the literature.

## 66 **2. Literature Review**

67 Three types of space and water heating equipment are considered in this study: gas furnace, electric resistance furnace,  
68 and electric heat pump for space heating, and gas fired water heater, electric resistance water heater, and heat pump  
69 water heater for water heating. The literature related to space and water heating in residential buildings will be  
70 discussed in each subsection below. Any of the heating methods considered in this study can be supplemented with a  
71 solar thermal heating element. It is rare for a water heater to rely solely on solar heating in the U.S. due to the need  
72 for faster heating during peak demand times and the impact of cloudy days on the ability to collect thermal energy  
73 (U.S. Department of Energy 2017). A discussion on why solar thermal was removed from the current analysis is  
74 presented as well.

### 75 *2.1. Gas vs. electric space heating comparisons*

76 The literature on direct comparisons of the economic and environmental efficiency of gas and electric heating is  
77 limited in part because fuel price per unit of energy is highly dependent on fuel mix and the time of consumption,  
78 efficiency of the heating system, and the climate region (EIA 2017c). Fuel mix for electricity generation varies across  
79 the U.S. and has a significant impact on environmental performance. These differences mean that studies are not

80 necessarily transferrable, as cost and fuel efficiency will inevitably vary across geographical regions. If the electricity  
81 in a comparison is generated at a coal plant, the results may be very different environmentally and economically than  
82 if production is from a mixture of renewable energy sources and traditional fossil fuels. As such, all results relating to  
83 electricity that follow are implicitly based on the fuel mix of the region in each study.

84 Belsie (2012) found that, when comparing costs of heating fuel types in the EIA's Northeast region, natural gas was  
85 the cheapest, 28% lower than electricity. A similar analysis finds that the U.S. average winter expenditure (per  
86 household) for natural gas used for heating (\$578) is \$352 less than for electricity (\$930) (EIA 2015). This is supported  
87 by Jeong, Kim, and Lee (2011) which found that natural gas has a higher utility (function of equipment price, energy  
88 price, and energy consumption given a budget constraint) when compared with electricity generation in South Korea.

89 Gustavsson and Karlsson (2002) found that electrical heating systems could be either the most energy-efficient option  
90 or the least, depending on whether a high efficiency heat pump or an electric boiler with a resistance heater were used.

91 Several studies focused on the U.K. and the European Union have generally found that air-source heat pumps are  
92 better than gas heating in terms of direct greenhouse gas emissions (Cabrol and Rowley 2012, Kelly and Cockroft  
93 2011, Dorer and Weber 2009), but more costly to operate than gas heating (Kelly and Cockroft 2011). Dorer and  
94 Weber (2009) focused on micro-cogeneration, which is different than the focus of this paper, while Kelly and Cockroft  
95 (2011) and Cabrol and Rowley (2012) looked at gas condensing boilers, which are typically more efficient than forced  
96 air (non-condensing) furnaces. This result is also found by Yang, Zmeureanu, and Rivard (2008) in comparing electric  
97 and gas fired hot water systems and forced air furnaces for space heating in Quebec.

98 The situation in the U.S. is more complicated due to differences in fuel mix for generating electricity. Shah, Debella,  
99 and Ries (2008) found that heat pumps have higher environmental impacts in places where there is a high percentage  
100 of fuel generation from fossil fuels. From 15% to 40% of fossil fuel generation would need to be converted to  
101 renewable sources to minimize the heat pump's impact. Brenn, Soltic, and Bach (2010) performed a comparison of  
102 electric and natural gas driven heat pumps that found, in general, natural gas heat pumps were roughly equivalent to  
103 electric heat pumps powered from highly efficient natural gas combined power plants. Alternatively, if the electrical  
104 grid utilized low-CO<sub>2</sub> fuel sources, an electric heat pump is a better choice. Pitt et al. (2012) looked at retrofits for air-  
105 source heat pumps and gas furnaces in Blackburn, VA and found that gas heating had less CO<sub>2</sub> emissions. This  
106 difference in findings is due to Europe using far more nuclear (25%) and renewables (30%) than the U.S. (18% nuclear  
107 and 21% renewables), with the U.S. relying substantially more on coal in 2016 (IEA 2017). Europe sees similar

108 variation in optimal technology by country (Martinopoulos, Papakostas, and Papadopoulos 2018) and within country  
109 (Martinopoulos, Papakostas, and Papadopoulos 2016, Abusoglu and Sedeeq 2013).

## 110 *2.2. Water heating comparison*

111 There is little direct comparison of water heating technology in the literature for the U.S., however there have been  
112 multiple studies on energy and environmental performance done in Europe. Tsilingiridis, Martinopoulos, and Kyriakis  
113 (2004) compared the lifetime environmental impact of a gas, electric, passive solar, and two types of hybrid passive  
114 solar water heaters (one using electricity and one using natural gas). Using life-cycle assessment (LCA) and a variety  
115 of system sizes, the authors found that there is a net gain in environmental performance for the hybrid system using  
116 electricity over a purely electric water heater, and a smaller net gain (reduction by a factor of 4) when natural gas is  
117 used in the hybrid system compared to an electric water heater. Tsilingiridis, Martinopoulos, and Kyriakis (2004) also  
118 found that the purely natural gas water heater outperformed the hybrid system using electricity, though only due to  
119 the electrical portion of the hybrid system being less efficient. Hong and Howarth (2016) found that natural gas had a  
120 larger negative impact on direct greenhouse gas emissions than high efficiency electric heat pumps when used for  
121 domestic water heating across both coal and natural gas produced electricity. Their findings suggest that natural gas  
122 technologies can result in higher emissions than using coal.

123 A study of environmental impacts beyond emissions focused on solar thermal water heating versus heat pumps and  
124 gas boilers found tradeoffs across environmental impacts. The results from Greening and Azapagic (2014) indicated  
125 that solar thermal systems are not necessarily the “cleanest” option in terms of overall environmental impact. While  
126 solar thermal outperformed electric resistance water heaters in eight of the eleven environmental categories  
127 considered, they underperformed the gas boiler in six out of the eleven. Solar water heating outperformed electric heat  
128 pump water heaters in seven of the eleven categories. Greening and Azapagic (2014) estimated that for 5 million  
129 installations of solar thermal water heating systems in the U.K., there would be a 9% reduction in global warming  
130 potential and fossil fuel usage from water heating. When looking only at direct emissions, the decrease in greenhouse  
131 gas emissions is only 1% for the domestic sector and 0.28% of all U.K. emissions while increasing the depletion of  
132 abiotic elements and toxicity-related impacts due to the manufacturing of the solar thermal collectors by 25%.

133 Economic comparisons between technologies are also lacking in the literature, however trade groups have done their  
134 own comparisons. Gas water heaters tend to cost less to operate and last slightly longer on average than an electric  
135 water heater and are generally less efficient on a site energy basis due to energy loss through venting of flue gases.

136 Although solar thermal water heaters can help reduce greenhouse gas emissions as noted previously, the bulk of  
137 literature suggests that it is not economical for the United States. A report by Clark (2012) found that solar thermal  
138 had a payback period for installation costs of roughly 30 years. This analysis is backed by findings from Croxford and  
139 Scott (2006) that suggest a short carbon payback time (no longer than 20 % of system lifetime), but a simple payback  
140 time of 100's of years for solar thermal, and 30 years for a building-integrated photovoltaic roof system if grants are  
141 included. National Renewable Energy Laboratory (NREL) found that break-even costs were not unobtainable based  
142 on available solar resources and electricity prices in some locations, however are precluded in areas with low  
143 electricity and natural gas prices (Cassard, Denholm, and Ong 2011). Solar thermal was also found to be more likely  
144 to replace some conventional electric systems as opposed to natural gas systems. This is further supported by a separate  
145 NREL report for the GSA that suggests proper siting and careful consideration can make solar thermal economically  
146 efficient in certain locations in the United States (Rockenbaugh et al. 2016). If conventional heating sources are used  
147 to supplement solar thermal, then a hybrid system can outperform traditional water heaters even in suboptimal climates  
148 (Hang, Qu, and Zhao 2012).

149 While solar thermal is not cost effective for most of the United States, studies in the European Union have shown that  
150 in the appropriate climate and with sufficient solar resources solar thermal can be cost competitive and provide  
151 enhanced environmental performance (Martinopoulos 2014, Martinopoulos and Tsalikis 2014, Martinopoulos 2018).  
152 An LCA by Simons and Firth (2011) found that 100% solar thermal for apartment buildings in Europe had superior  
153 performance to all other heating sources in terms of primary energy purchased and reductions in emissions, however  
154 the manufacturing processes involved can be as high as 38 times that for natural gas. Other potential environmental  
155 impacts were marginally worse for heat pumps and fossil fuel systems as a result. Solar thermal systems were found  
156 to be better overall for human health than fossil fuel systems and similar to heat pump systems. A study on  
157 performance, economic and environmental life cycle by Kalogirou (2009) found that a solar thermal system coupled  
158 with a gas or electric backup proved viable in terms of reducing greenhouse gas emissions and a realistic payback  
159 period while achieving desired performance. A cost-benefit analysis of solar thermal water heating in Greece  
160 concluded that, given Greece's solar radiation levels, solar water heating had a benefit-cost ratio (BCR) greater than  
161 one when compared to electric water heaters, however natural gas was superior in terms of BCR over solar water  
162 heating (Diakoulaki et al. 2001). Subsequent work by Martinopoulos, Papakostas, and Papadopoulos (2018) has shown  
163 that advancements in solar thermal have led it to be more cost-effective in Greece.

164 The data used in this paper, further discussed in Section 3, uses a fuel mix and technologies (appropriate for the  
165 selected location) that lead to inclusion of a solar thermal system being non-optimal in all cases based on the energy  
166 and economic efficiency metrics being used, and is therefore, excluded from the discussion of the current analysis.  
167 Changes in fuel mix of electricity in Maryland since the data have been generated or future developments in the  
168 installed costs of solar thermal systems may change its relative applicability.

### 169 **3. Measuring Building Sustainability using BIRDS**

170 BIRDS was developed to assist in evaluating the performance of U.S. buildings using whole-building sustainability  
171 metrics to assess the performance of the materials and energy used by a building spanning its construction, operation,  
172 and disposal. These metrics are based on applications of: (1) whole-building energy simulation modeling, (2) life-  
173 cycle costing, and (3) life-cycle impact assessment (LCIA) methods. Life-cycle costing – which serves as a metric of  
174 economic performance – is integrated with 12 environmental performance metrics to produce science-based measures  
175 of the business case for investment options in high-performance green buildings (Lippiatt et al. 2013). BIRDS metrics  
176 for whole-building environmental performance are based on a hybridized LCA approach which considers an inventory  
177 of inputs and outputs covering all phases of a building’s service life. Also captured is the energy use associated with  
178 the operation of the building and any energy produced on site via renewable energy generation systems (Lippiatt et  
179 al. 2013). Environmental LCIA quantifies the potential contribution of these LCA inventory items to a range of  
180 environmental impacts categories, which are based on EPA’s TRACI 2 impact categories (Bare 2011) plus two  
181 additional impact categories for land and water use.

182 The latest version of BIRDS, v4.0, is scheduled to be released in 2018 and includes several updates. The commercial  
183 and residential databases are condensed into a single database called “Building Energy Standards/Codes Database,”  
184 while the existing low-energy residential database – now called the “Incremental Energy Efficiency for Residential  
185 Buildings Database” – has been expanded to include additional equipment/fuel type system options for household  
186 space and domestic water heating, as well as a larger PV array option (12.1 kW). The analysis conducted in this study  
187 is based on data contained in the new Incremental Energy Efficiency for Residential Buildings Database (referred to  
188 as the BIRDS Database hereafter), which allows for detailed analyses of incremental EEMs for Gaithersburg, MD.

189 Users have an opportunity to consider the impacts of alternative underlying assumptions: (1) study period length, (2)  
190 discount rate, (3) construction quality, (4) financing type, (5) exterior wall finish, and (6) heating fuel type. Users can  
191 select a study period length ranging from 1 year to 30 years. Two options are available for both the discount rate (3%

192 and 8%) and the construction quality (average and luxury). BIRDS users can factor quality into their LCC estimates  
193 by choosing either of the two options for construction quality: average and luxury. Two options are available for  
194 financing type: (1) an upfront, full cash purchase, and (2) a mortgage financing loan which assumes a 20% down  
195 payment with the remainder of the initial investment financed at 4.375%. Two options are available for exterior wall  
196 finish: brick veneer and wood siding. Like construction quality, exterior wall finish type has minimal to no impact on  
197 the changes in LCC. The final options for heating (electricity vs. natural gas) will be discussed later in this section.  
198 Table A1 through Table A3 in the Appendix list alternative EEM options available for building envelope (i.e., wall,  
199 roof/ceiling, foundation, windows, doors) constructions. The exterior wall, basement wall and floor, and roof/ceiling  
200 constructions (Table A1) are listed in order of increasing thermal efficiency. The five window construction options  
201 (Table A2) are also increasing in energy efficiency and vary according to U-Factor and Solar Heat Gain Coefficient  
202 (SHGC). The air leakage rates (Table A3) are based on requirements of 2009 International Energy Conservation Code  
203 (IECC),<sup>3</sup> while Option 2 and Option 3 are based on 2015 IECC and the measured air leakage of the NZERTF,  
204 respectively.<sup>4</sup> Rates are expressed in terms of air changes per hour at 50 Pa ( $ACH_{50}$ ) using a blower door test.  
205 Listed in Table A-4 through Table A-7 are the updated EEM options for building systems. Lighting wattage options  
206 (Table A-4) are expressed as a fraction of total fixed lighting fixtures that use high-efficiency bulbs. These fractions  
207 are based on a “typical/baseline” lighting mix from Hendron and Engebrecht (2010), requirements defined in editions  
208 of IECC, and the NZERTF.<sup>5</sup> The four heating and cooling equipment options (Table A-5) cover both electric- and  
209 gas-powered space heating options as constrained by the heating fuel type selection in the analysis assumptions.  
210 Option 1 reflects a “standard efficiency” system that satisfies minimum federal efficiency and IECC requirements.  
211 There is mechanical dedicated outdoor air (OA) ventilation that meets ventilation requirements defined by ASHRAE  
212 62.2-2010 (ASHRAE 2010a). The second option is a higher efficiency air-to-air heat pump system. Mechanical  
213 ventilation is provided using a separate, dedicated OA system with a heat recovery ventilator (HRV) to meet ASHRAE  
214 62.2-2010. Both options include an electric heating element (0.98 efficiency) to supplement the heat pump when the  
215 primary system cannot meet the thermal loads. Option 3 is a standard efficiency split system that uses electric-based

---

<sup>3</sup> The 2003 and 2006 IECC set no maximum limit on air leakage. The 2009 IECC limit is assumed for those editions in this study.

<sup>4</sup> Required conversion from air changes per hour to effective leakage area (ELA) done using formula in Chapter 16 of ASHRAE (2012). The ELA is split between the two conditioned floors based on fractional volume.

<sup>5</sup> Additional details on all EEM alternatives can be found in Kneifel, Lavappa et al. (2016).

216 cooling and natural gas for heating. Like Option 1, it provides mechanical dedicated OA ventilation. Option 4 is the  
217 higher efficiency gas-electric split system that uses a separate HRV system.

218 Eight DHW system options are available (Table A-6). Option 1 is an installed “standard” efficiency (Energy Factor  
219 (EF) = 0.95) electric water heater (50 gal) serving as the primary system. Option 2 is an air-to-water heat pump water  
220 heater (HPWH) with a Coefficient of Performance (COP) of 2.36 serving as the primary system. Option 3 and Option  
221 4 are like Option 1 and Option 2, respectively, except that they both include an auxiliary two-panel, 4.6 m<sup>2</sup> (50 ft<sup>2</sup>)  
222 solar thermal system. Option 5 and Option 6 swap out the electric water heaters for 50-gallon gas water heaters at EFs  
223 of 0.78 and 0.90, respectively. Option 7 and Option 8 add the auxiliary solar thermal systems to the primary gas  
224 systems in Option 5 and Option 6. The six roof-mounted solar photovoltaic (PV) system options (Table A-7) are based  
225 on the NIST NZERTF roof-mounted system (Option 5). The first four options depict the incremental removal of one-  
226 quarter capacity of the 10.2 kW system, while Option 6 depicts the addition of one-quarter capacity to 12.7 kW.

#### 227 **4. Research Methodology**

228 This study explores tradeoffs in sustainability performance between residential building designs that use electric  
229 equipment to satisfy its space and domestic water heating demands, and those that rely on natural gas-powered  
230 systems. Three aspects of sustainability performance – energy, environmental, and economic performance are  
231 evaluated under a set of analysis assumptions.

##### 232 *4.1 Energy performance*

233 Operating energy is based on an estimate of total net source energy use by a building’s occupants during the  
234 operational phase. The JEPlus parametric simulation tool is used to run the EnergyPlus (E+) v8.3 whole-building  
235 simulation model to compute annual household site energy use and solar PV production (DOE 2015a, Zhang and  
236 Korolija 2015).<sup>6,7</sup> Total net site energy use is then calculated by taking the difference, capturing any offsetting of  
237 household energy use by on-site renewable energy production. Total net source energy use is derived using a  
238 conversion multiplier to scale net site operating energy use.<sup>8</sup>

---

<sup>6</sup> Site energy refers to the amount of energy shown on a utility bill. It is the final form of energy consumed by the homeowner.

<sup>7</sup> The weather file used for the simulations is the Typical Meteorological Year 3 (TMY3) for Gaithersburg, MD (KGAI weather station) obtained from Weather Analytics (Weather Analytics 2014).

<sup>8</sup> Source energy refers to the total amount of raw fuel used to power a building and maintain its daily operations. It considers all energy use, including production, transmission, and delivery losses.

239 Annual operating energy use is assumed constant from year-to-year with proper maintenance to simplify the analysis.  
240 This assumption does not hold true in the case of on-site solar PV production as previous research studies have  
241 observed consistent degradation of solar panels. It is assumed that there is an annual production degradation of 0.5%  
242 over the lifetime of the solar PV system (Kneifel, Webb, and O’Rear 2016). The estimates for net operating energy  
243 use over a selected study period are also used to derive net operating CO<sub>2</sub> emissions over the same study period.

#### 244 *4.2 Environmental performance*

245 The evaluation of whole-building environmental performance in BIRDS uses LCA inventory data in conjunction with  
246 life-cycle impact assessment (LCIA) methods to quantify and link environmental impact contributions to twelve  
247 impact categories.<sup>9</sup> To address the complexities of a whole building, BIRDS takes a multi-layered approach to  
248 inventory analysis using a hybrid LCIA framework developed by Suh and Lippiatt (2012) that integrates top-down  
249 (Input-Output-based) and bottom-up (process-based) data in the inventory analysis LCA step (Bagley and Crawford  
250 2015, Crawford et al. 2016, Stephan and Crawford 2016, Stephan, Jensen, and Crawford 2017, Crawford and Stephan  
251 2013). For additional details on the LCA inventory data included in BIRDS, refer to Lippiatt et al. (2013). The  
252 environmental flows associated with a building’s life-cycle stages fit into two categories: embodied (those associated  
253 with initial construction, maintenance, repair, and replacement (MRR), and disposal of building components and  
254 systems) and operating flows (those resulting from any energy consumed and produced during the building’s use  
255 phase). See Kneifel et al. (2018) for descriptions on the approaches used to calculate embodied and operating  
256 environmental flows.<sup>10,11</sup>

257 Forming overall conclusions about the environmental performance of an individual building design based on LCIA  
258 can be difficult because each of the LCIA are measured in different units. BIRDS addresses this through a metric that  
259 combines the performance of all twelve categories into a single numeric environmental impact score (EIS) (Lippiatt  
260 et al. 2013). EISs are calculated using fixed scale normalization references based on annual contributions of U.S.  
261 economic activity to the LCIA categories (Table A8). For more information on EISs, refer to Lippiatt et al. (2013).

---

<sup>9</sup> The twelve categories can be found in Table A8. More information on the impact categories, refer to Lippiatt et al. (2013).

<sup>10</sup> Building operation includes the energy consumed by the building and associated environmental flows over the study period. The energy use emissions are derived using LCA data based on the emissions rates for electricity and natural gas generation in Maryland, which treats all consumption and production (electricity only) the same temporally.

<sup>11</sup> Natural gas environmental flows are calculated by multiplying the source flow per unit of natural gas by the total net number of units of natural gas consumed each year in the study period and summing across all years. The sum of the flows for electricity and natural gas gives the total operational energy-related flows.

262 *4.3 Economic performance*

263 BIRDS uses a life-cycle cost (LCC) methodology to evaluate the cost-effectiveness of buildings (Fuller and Petersen  
264 1996, ASTM 2012b). Life-cycle costing accounts for the discounted present value of all costs related to the  
265 construction, operating, maintenance, repairs, replacements, and disposing or resale (i.e. residual value) of a building  
266 for a given study period. In the case of comparing a baseline building design to a series of alternative designs, such as  
267 in BIRDS, the design alternative with the lowest LCC is the most cost-effective (Kneifel et al. 2018). The difference  
268 in LCCs (i.e., Net Savings) between a specified baseline design and an alternative that may install different building  
269 technologies (e.g., alternative heating system) reveals the additional costs (or savings) incurred by the homeowner. A  
270 positive net savings (NS) implies that the design alternative is more cost-effective than the baseline for the given study  
271 period. The general formula for calculating the LCCs of a building is:

272 
$$LCC = C + O + MRR - RV$$

273 The LCC estimates use data from a combination of sources. Initial construction costs (C) include all costs of  
274 constructing the building, which is estimated using RS Means (2017) to estimate the typical construction costs for a  
275 simple family dwelling of the building plus the additional incremental costs of upgrading the design with each  
276 implemented EEM from Faithful and Gould (2012), Kneifel and O'Rear (2016b), and local contractor quotes  
277 (depending on the EEM). Maintenance, repair, and replacement rates and costs (MRR) are obtained from Census  
278 (2011), Faithful and Gould (2012), National Association of Home Builders (NAHB) Research Center (2007), and  
279 ENERGY STAR (2011). Maintenance, repair, and replacement costs and associated residual values (RV) are  
280 calculated separately for each building component that is replaced at different rates than the building structure (e.g.  
281 windows and equipment). Operational costs (O) include the energy costs and are the estimated combination of  
282 electricity and natural gas costs over the assumed study period. Operational energy costs are based on the standard  
283 residential rate schedule for electricity in Montgomery County, MD (PEPCO 2018) and annual average residential  
284 cost data for Maryland (EIA 2017d). Energy price escalation rates are based on Lavappa, Kneifel, and O'Rear (2017).  
285 All residual values are calculated using a linear depreciation method as defined in ASTM (2012a). More information  
286 on the above cost data and life-cycle cost approach can be found in Kneifel, O'Rear et al. (2018).

287 *4.4 Building Component Options and Analysis Assumptions*

288 This analysis compares the performance of a designated baseline building design constructed according to 2015 IECC  
289 (Maryland code-compliant or MCC design), to alternative building design options included in the BIRDS Database.

290 Each alternative has its own EEM combination, which may be more (or less) efficient than the baseline. Table 4-1  
 291 lists the building envelope and system specifications (excluding HVAC and DHW systems) for the baseline design.

292 **Table 4-1 Maryland Code-Compliant Home Design Specifications**

Category	Specifications	MCC
<b>Windows</b>	U-Factor and SHGC	1.99 W/m <sup>2</sup> -K and 0.40
<b>Framing and Insulation</b>	Framing	5.1 cm x 10.2 cm – 40.6 cm OC
	Exterior Wall ( <i>finish: wood siding</i> )	R <sub>SI</sub> -3.5 or R <sub>SI</sub> -2.3+0.9†
	Basement Wall and Floor	R <sub>SI</sub> -1.8† and R <sub>SI</sub> -0†
	Roof/Ceiling Assembly	Ceiling: R <sub>SI</sub> -8.6
<b>Air Change Rate</b>	Air Change Rate – Blower Door Test	3.00 ACH <sub>50</sub>
	Effective Leakage Area (1 <sup>st</sup> Floor; 2 <sup>nd</sup> Floor)	403.6 cm <sup>2</sup> ; 368.1 cm <sup>2</sup>
<b>Lighting</b>	Efficient Lighting (%)	75% efficient built-in fixtures
† Interior Wall Cavity + Exterior Continuous Insulation		

293 Given that the BIRDS Database includes designs that have either electric- or natural-gas powered space heating and  
 294 DHW heating systems, two types of baseline MCC designs are considered: (1) all-electric MCC design (**MCC-E**) and  
 295 (2) MCC design with natural gas-powered space heating and DHW systems (**MCC-NG**). Table 4-2 lists HVAC and  
 296 DHW specifications for **MCC-E** and **MCC-NG**.

297 **Table 4-2 HVAC and DHW Specifications for Alternative Baseline Designs**

Category	Specifications	MCC-E	MCC-NG
<b>HVAC</b>	Heating/Cooling*	Air-to-air heat pump (SEER 13.0/HSPF 7.7)	Gas-electric split A/C system (SEER 13.0/80% AFUE)
<b>DHW</b>	Water Heater	189 L electric (EF = 0.95)	189 L gas (EF = 0.78)
* Minimum outdoor air requirements are based on ASHRAE 62.2-2010 (0.04 m <sup>3</sup> /s) SEER = seasonal energy efficiency ratio; HSPF = heating seasonal performance factor; AFUE = annual fuel utilization efficiency			

298  
 299 The alternative low and net-zero energy designs for comparison are selected based on their relative energy and  
 300 economic performance under the assumptions of a 3% discount rate, 80% mortgage loan financing (20% down  
 301 payment), average construction quality, 30-year study period, and wood siding exterior wall finish. Currently, the  
 302 BIRDS Database does not account for financial incentives, but for this analysis the Federal Solar Investment Tax  
 303 Credit (Congress 2015) is included because it's a significant factor in the economics of solar PV systems.

304 **5. Results/Discussion**

305 This study compares two Maryland code-compliant designs – electric-heated and gas-heated – using the sustainability  
 306 performance metrics (energy, economic, and environmental performance) mentioned earlier. Analysis is extended to  
 307 consider additional designs, many of which are low-energy or net-zero energy, to evaluate impacts of increasing  
 308 energy efficiency in residential building codes in Maryland or other locations in the Mixed-Humid Climate Zone.

309 *5.1 Electric vs. Natural Gas Heating*

310 Sustainability performance results for the MCC-E and MCC-NG building designs are compared to identify co-benefits  
 311 and tradeoffs in energy, economic, and environmental performance between fuel types. The results in Table 5-1  
 312 indicate that electric space and DHW equipment leads to higher construction costs (+\$1,200), energy costs (+\$7,940),  
 313 and total LCC (+\$9,715). Differences in construction costs are driven by the inclusion of a higher cost air-to-air heat  
 314 pump, while the higher energy costs are driven by the comparatively higher cost per unit of energy for electricity. The  
 315 MCC-NG design results in higher net site energy consumption (1,555,028 kWh) as the use of natural gas more than  
 316 offsets reduced electricity consumption relative to the MCC-E design. Even with greater site energy use, the cost  
 317 difference of natural gas versus electricity (\$0.115/kWh-eq) leads to LCC savings for MCC-NG relative to MCC-E.<sup>12</sup>

318 **Table 5-1 Sustainability Performance Results for the MCC-E and MCC-NG Building Designs**

	Units	MCC-E	MCC-NG
<b>Construction Costs</b>	U.S.\$ (2017)	364,292	363,092
<b>Energy Costs</b>	U.S.\$ (2017)	80,570	72,630
<b>Total LCC</b>	U.S.\$ (2017)	358,806	349,091
<b>Total Electricity Consumption</b>	kWh	706,646	301,226
<b>Total Natural Gas Consumption</b>	kWh	0	1,253,802
<b>EIS (BEES and EPA Advisory Board)</b>	n/a	15.30 and 13.86	9.92 and 9.19

319  
 320 To assess differences in how the two systems meet thermal comfort requirements, this analysis utilizes a thermal  
 321 comfort metric based on ASHRAE Standard 55 that estimates the number of hours for which indoor conditions do not  
 322 meet thermal comfort requirements of a building’s occupants (ASHRAE 2010b), labeled “total hours  
 323 uncomfortable.”<sup>13</sup> For additional information on thermal comfort in BIRDS, refer to Kneifel et al. (2017). With 622  
 324 total hours uncomfortable annually, and roughly four times greater than that of the MCC-NG design (152 hours  
 325 annually), the MCC-E design is “less comfortable,” which is driven by the sizing of the heating equipment. E+ sizes  
 326 an HVAC system by calculating capacities to meet the load for each HVAC system’s heating and cooling components.  
 327 The heating equipment in the MCC-E design is sized to 9933 W with a 5000 W electric resistance back-up element  
 328 while the split AC system in the MCC-NG design includes a 29 667 W gas furnace. As the capacity of the gas furnace  
 329 is about twice the size of the combination of the heat pump and electric back-up element, the MCC-NG can stabilize  
 330 indoor temperatures more consistently than the all-electric alternative, leading to fewer total hours uncomfortable.

<sup>12</sup> Assumed electricity price is ~\$0.154/kWh. Assumed natural gas cost is ~\$0.41/m<sup>3</sup> or \$0.04/kWh (conversion factor of 10 350 kWh/m<sup>3</sup>).

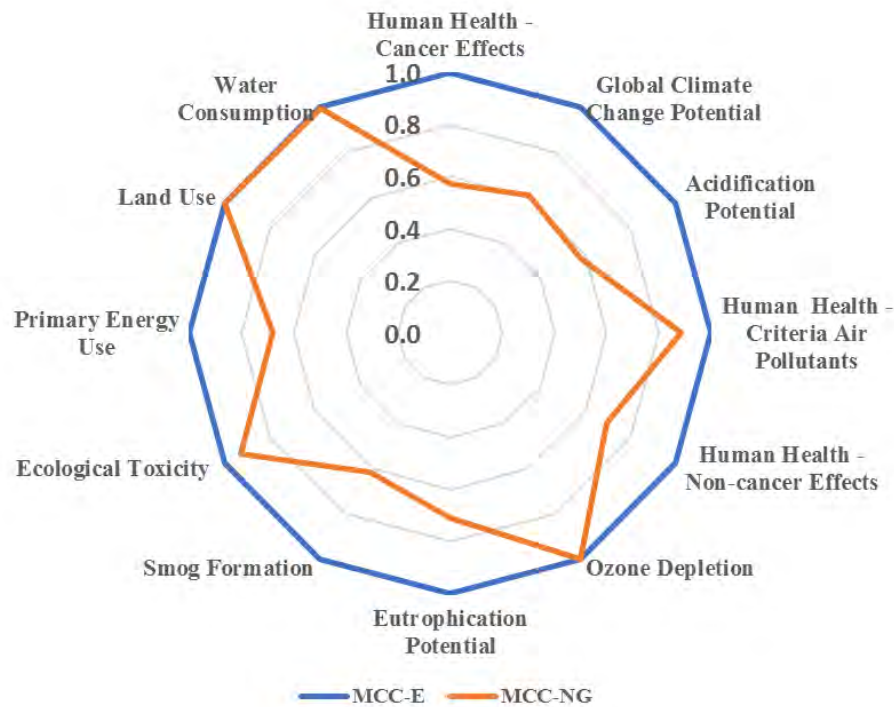
<sup>13</sup> Total hours uncomfortable computed by the E+ Building Energy Simulation Software refers to the total number of hours in a year that indoor building temperatures are outside pre-defined setpoint temperature levels

331 The BEES and SAB EISs suggest that the MCC-NG is more environmentally-friendly than the MCC-E design with  
332 EIS values of 9.92 and 9.19 versus 15.3 and 13.9, respectively. Figure 5-1 compares the MCC-NG design results for  
333 each of the environmental impact categories relative to the MCC-E design as a baseline (normalize each impact  
334 category value to 1.0). Using natural gas-fired heating systems reduces all but three impact categories (i.e., land use,  
335 water consumption, and ozone depletion). Despite greater energy use over the 30 years, improvements in the  
336 environmental performance by the MCC-NG design – in particular, in the categories of Primary Energy Use, Global  
337 Climate Change Potential, and Smog Formation – are largely driven by differences in: (1) site energy consumption  
338 and (2) emissions rates for the two fuels. Although total on-site energy consumption is ~2.2 times greater for the  
339 MCC-NG design, the assumed source CO<sub>2</sub> eq./kWh emissions rate for electricity in Maryland (0.65 kg CO<sub>2</sub> eq./kWh)  
340 is ~2.7 times higher than that of the assumed source emissions rate for natural gas (~0.24 kg CO<sub>2</sub> eq./kWh). This  
341 result is driven by the significant share of coal used for electricity generation in Maryland (> 50 %) in combination  
342 with transmission/distribution losses.<sup>14</sup> Lower overall source energy flows for the MCC-NG design, combined with  
343 the considerable difference in emissions rates for electricity and natural gas, bring about improvements in the  
344 environmental impact categories.<sup>15</sup>

---

<sup>14</sup> U.S. Environmental Protection Agency (2008)

<sup>15</sup> The 2016 release of eGRID shows a shift away from coal towards more natural gas and nuclear generation in Maryland, which would lead to a reduction in source emissions rates for electricity in the analysis. Future research should evaluate how the shift impacts the results of this study.



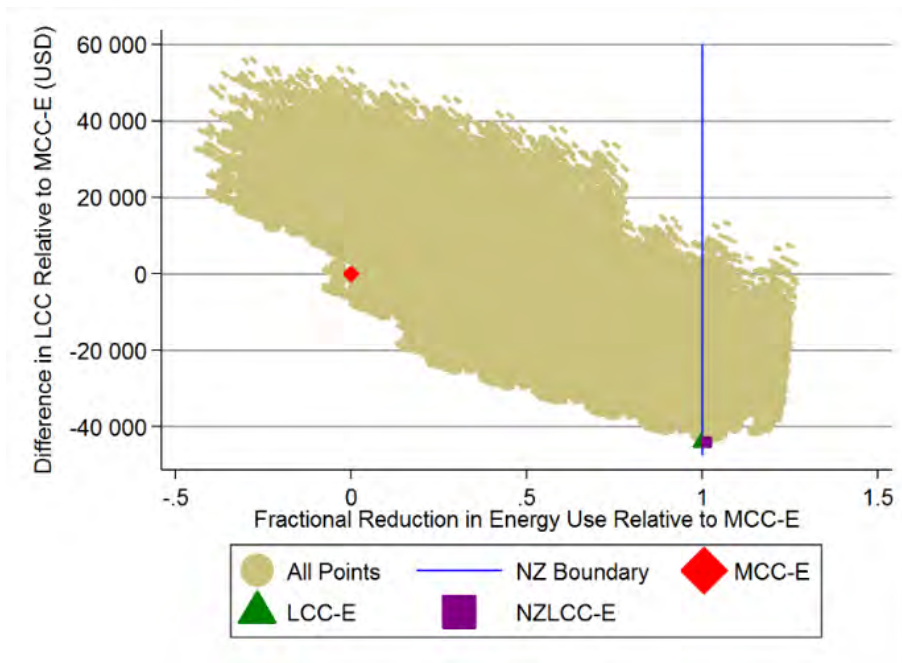
345  
346 **Figure 5-1 MCC-E vs. MCC-NG Designs (fractional performance relative to MCC-E)**

347  
348 *5.2 All-electric designs in the BIRDS Database*

349 The results discussed in this section are based on an analysis of all the building designs in the BIRDS Database  
 350 adopting fully-electric space and water heating equipment (including the **MCC-E** design). Figure 5-2 displays energy  
 351 and economic results based on the assumptions in Section 4.4 for 240 000 designs, each with a unique combination  
 352 of EEMs with an assumed location of Gaithersburg, MD and identical usage patterns. Each data point includes either  
 353 Option 1 or Option 2 for space heating (Table A5), as well as one of the first four options for domestic water heating  
 354 (Table A6). The horizontal axis is the fractional reduction in total energy use relative to the code-compliant design  
 355 (MCC-E), while the vertical axis is the change in LCC relative to the MCC-E design. All data points located on or to  
 356 the right of the NZ-boundary line (blue) are building designs that perform at net-zero (site production equals or exceeds  
 357 site consumption) or better over the 30-year study period.

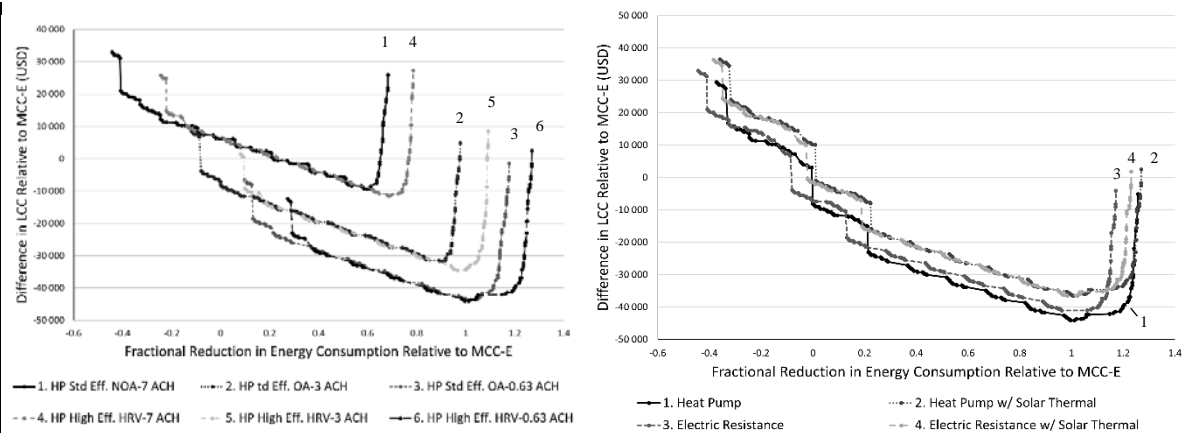
358 Two main points can be drawn from the results: (1) fractional reductions in net energy consumption and changes in  
 359 LCC are negatively correlated up to net-zero energy performance and (2) fractional reductions in net energy  
 360 consumption and changes in LCC are positively correlated for designs that are net producers of electricity. The pivot  
 361 at net-zero performance is driven by a discontinuity within the net metering structure in Maryland. Homeowners are

362 reimbursed the retail price of electricity including all charges, fees, and taxes (15.4¢/kWh) for any electricity  
 363 generation that offsets their consumption while excess generation is reimbursed only the generation charge  
 364 (6.7¢/kWh). Consequently, additional reductions in net electricity consumption are uneconomical. We identify a group  
 365 of designs that satisfy optimality conditions that will be elaborated on later: (1) electric-heated code-compliant design  
 366 (MCC-E), (2) lowest cost design (LCC-E), and (3) design performing at net-zero or better at least cost (NZLCC-E).  
 367



368  
 369 **Figure 5-2 All-Electric Designs**

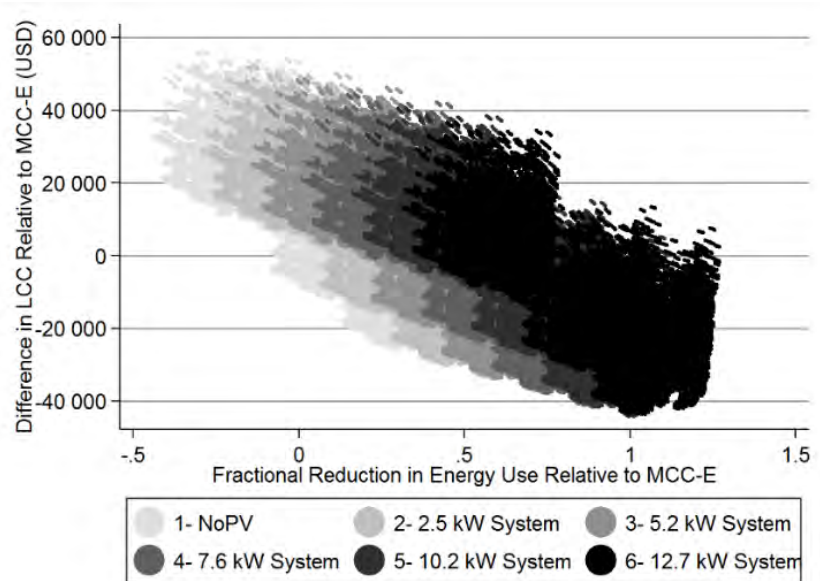
370 Figure 5-3 illustrates the LCC optimization curves for each level of net site energy reduction for alternative  
 371 configurations of the household HVAC and DHW systems. Figure 5-3(a) is based on six different configurations for  
 372 the HVAC system, ventilation method, and air leakage rates. The first three configurations (Setup 1 through Setup 3)  
 373 include a standard efficiency (SEER 13/HSPF 7.7) air-to-air heat pump, while the remaining three configurations  
 374 (Setup 4 through Setup 6) include a high efficiency (SEER 15.8/HSPF 9.05) heat pump with separate HRV system.  
 375 Findings suggest that designs performing at net-zero or better at least cost must be constructed for minimal air leakage  
 376 (0.63 ACH). Although heat pump efficiency contributes to net energy use reductions, lower air leakage rates prove to  
 377 be a bigger driver behind the declines in energy use.



378  
379 **Figure 5-3 Optimization Curves for All-Electric Designs based on (a) HVAC System and (b) DHW System**

380 Net-zero energy performance is achievable with all DHW system configurations (Figure 5-3(b)). The least costly  
 381 reductions in energy use are achieved with the use of a HPWH (Setup 1), while designs pairing the HPWH with an  
 382 auxiliary two-panel solar thermal system (Setup 2) achieve similar cutbacks in energy use but at a much greater cost  
 383 to the homeowner given the additional cost of the solar thermal system. A similar dynamic is observed with designs  
 384 using a typical electric resistance water heater with and without the additional solar thermal system.

385 Figure 5-4 displays the variation in solar PV system capacities across all building designs. Two major inferences can  
 386 be drawn: (1) rooftop solar PV is a necessary EEM for low-energy or net-zero (or better) energy performance, and (2)  
 387 system capacities must be at least 10.2 kW to reach net-zero. For medium to large capacities, the rooftop PV system  
 388 will be the most expensive EEM in upfront costs for any given combination of EEMs. However, significant offsets in  
 389 annual energy costs lead to declining LCCs, with the change in LCCs falling as the system capacities increase.



390  
391 **Figure 5-4 All-Electric Designs based on Solar PV System Capacities**

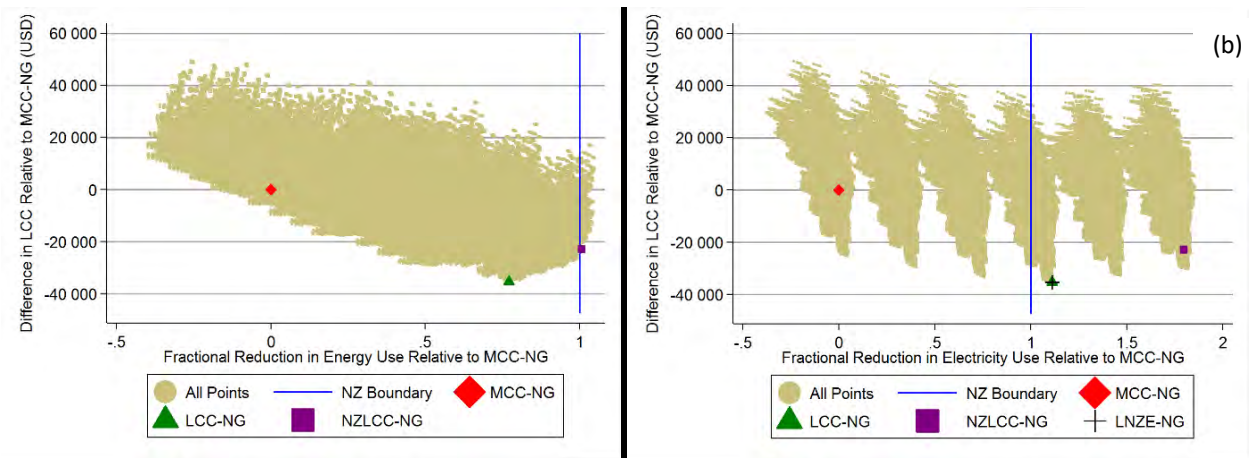
392

393 *5.3 Natural gas designs in the BIRDS Database*

394 The results discussed in this section are based on an analysis of building designs using gas-fired HVAC and DHW  
395 equipment. Four key building designs are identified and will be discussed later: (1) gas-heated, code-compliant design  
396 (**MCC-NG**), (2) lowest cost design (**LCC-NG**), (3) net-zero energy design at least cost (**NZLCC-NG**) and (4) net-  
397 zero site electricity design at least cost (**LNZE-NG**).

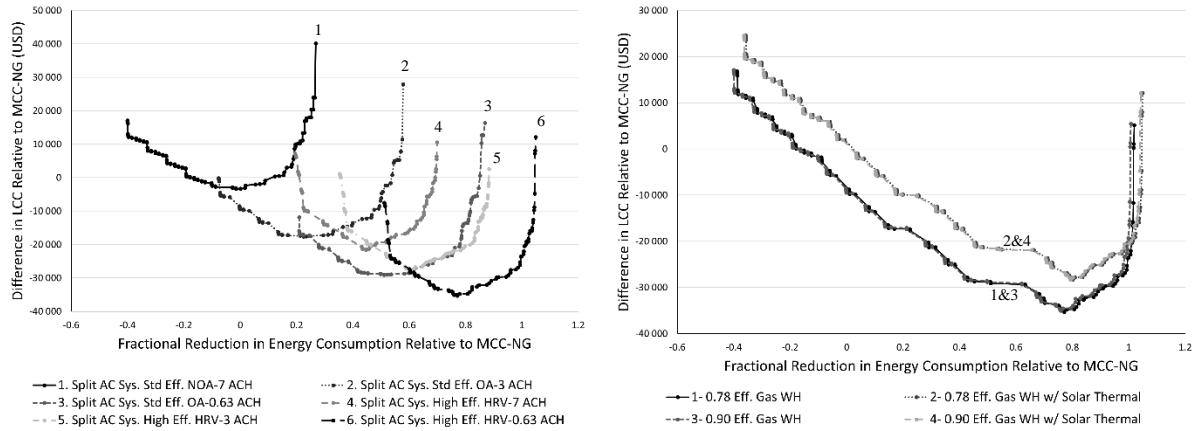
398 Figure 5-5(a) displays the relative performance of each building design with the fractional reduction in total source  
399 energy use relative to the MCC-NG the horizontal axis and the difference in LCC relative to the MCC-NG design on  
400 the vertical axis. Both the LCC-NG and LNZE-NG designs are the same. When compared to Figure 5-2, the  
401 distribution is similar, but with the cost-optimal design occurring at ~77% reduction in site energy consumption instead  
402 of ~101% with fewer net-zero building designs. In fact, only the NZLCC-NG design is located beyond the NZ-  
403 Boundary (blue). This is a result of three factors: (1) higher initial total site energy use by the MCC-NG design, (2)  
404 smaller potential savings from heating equipment, and (3) net metering structure. Fewer designs can reach net-zero  
405 energy performance because greater reductions in energy use are required while the efficiency improvements in  
406 heating equipment are smaller for natural-gas fired equipment relative to electric equipment. For example, the EF of  
407 the gas water heater increases from 0.78 to 0.90 versus the increase in efficiency/COP from 0.95 for the electric water

408 heater to 2.33 for the HPWH. Figure 5-5(b) shows the change in LCC relative to net electricity consumption. The  
 409 LCC-optimal design (LCC-NG) is located just beyond net-zero electricity consumption.



410  
 411 **Figure 5-5 Gas-heated Designs based on Fractional Reduction in (a) Total Energy Use and (b) Electricity Use**

412 Figure 5-6(a) illustrates the LCC optimization curves for each level of net site energy reduction for six alternative  
 413 configurations for the HVAC system, varying based on the efficiency of the split ac system, method of outdoor  
 414 ventilation, and air leakage rate. The first three setups include the standard efficiency gas-electric split AC system  
 415 (SEER 13/80% AFUE), while the remaining three include the higher efficiency split system (SEER 16/96% AFUE).  
 416 Like the analysis of the design cases, low air leakage rates (0.63 ACH) when paired with a high-efficiency split AC  
 417 and HRV system (Setup 6), are the primary drivers behind the reductions in net energy use for all designs performing  
 418 at net-zero energy or better. Large reductions in net energy use are attainable with a high efficiency split system (Setup  
 419 4 and Setup 5) – however, similar, less costly reductions can be attained when the standard efficiency system is paired  
 420 with a leakage rate of 0.63 ACH (Setup 3). Figure 5-6(b) shows that only two of the four possible configurations for  
 421 the DHW system lead to this design being a net-zero energy building: Setup 3 and Setup 4. Both configurations include  
 422 a high efficiency gas-fired water heater. The addition of the solar thermal system produces marginally greater  
 423 reductions in net energy use at a greater cost to the homeowner due to additional equipment costs.



424  
425 **Figure 5-6 Optimization Curves for Gas-heated Designs based on (a) HVAC System and (b) DHW System**

426 Inclusion of rooftop solar PV (not pictured) is also a necessary feature to reach net-zero energy performance when  
427 gas-fired heating equipment is installed. Only building designs with a 12.7 kW rooftop PV system can achieve net-  
428 zero energy performance because of the higher initial energy consumption of the MCC-NG design.

429 *5.4 Cross-comparisons of selected building designs*

430 This section discusses differences between key electric and heating system options based on combinations of EEMs,  
431 energy, and economic performance. Again, all key designs were chosen under assumptions of a 3 % discount rate,  
432 average construction quality, financed mortgage, and 30-year study period.

433 Table A-9 describes the design characteristics of the four key building designs. The energy and economic performance  
434 of these designs are shown in total values and relative to two baselines (MCC-E and MCC-NG). Note that it was  
435 previously reported that the MCC-E design has lower total site energy consumption but higher LCC relative to the  
436 MCC-NG design. To allow for comparability purposes to previous results, the analysis will focus on results relative  
437 to the MCC-E design regardless of heating fuel source. There are some consistent EEM selections regardless of heating  
438 fuel source. Energy savings realized by all four designs suggest use of higher efficiency lighting and HVAC and DHW  
439 equipment and lower building envelope air leakage can lower annual energy use. Across these designs, the solar PV  
440 system is sized to meet electricity consumption regardless of the heating fuel source selected.

441 Relative to results found in Kneifel, O'Rear et al. (2018), the optimal all-electric building designs implement different  
442 EEMs. Both LCC-optimal design (LCC-E) and lowest cost net-zero design (NZLCC-E) use less efficient windows  
443 and lower R-value wall assemblies while installing a more efficient HVAC system. These differences have been driven  
444 by the use of newer construction cost data, showing how the optimal design options can change over time as

445 location-specific costs change. Additionally, there are likely building designs implementing different EEMs that are  
446 near optimal that would be reasonable design options.

447 The LCC-E design realizes greater energy savings (99.7% versus 50%), but less LCC savings (\$44,103 versus  
448 \$45,040) relative to the LCC-NG design. These results are driven by two factors. First, the value of a larger solar PV  
449 system is driven by the marginal value of electricity. Gas-fired heating equipment decreases electricity consumption,  
450 leading to a smaller installed solar PV system (7.6 kW) needed to reach net-zero electricity consumption but offsetting  
451 minimal amounts of energy use from natural gas consumption. Since LCC-E uses only electricity, the marginal value  
452 of reducing energy remains the same up to the point of reaching net-zero energy performance, resulting in a larger  
453 (10.2 kW) system selection. Second, the LCC-NG design leads to lower costs than the LCC-E design because the  
454 marginal cost of a unit of energy from natural gas consumption is lower than a unit of energy from electricity. The  
455 combination of lower energy costs with lower costs of construction (smaller solar PV system) lead to lower LCC for  
456 the homeowner. Given these results, there is a financial incentive to use natural gas for heating instead of electricity  
457 while natural gas prices will remain significantly cheaper than electricity on a per unit of energy basis in Maryland.

458 From the perspective of reaching net-zero site energy performance, electric heating equipment is preferable to natural  
459 gas heating equipment. The NZLCC-E design is the same as the LCC-E design, which nearly reaches net-zero at  
460 99.6% energy reductions, except for the selection of a higher thermal performance roof assembly to exceed net-zero  
461 (~101%). As a result, the LCC savings are nearly identical. The NZLCC-NG design is more expensive to construct  
462 and has higher LCC by \$11,489. To reach net-zero using gas-fired heating equipment requires additional EEMs,  
463 including higher thermal performance windows and wall assemblies. Even with the improved thermal performance of  
464 the building envelope, the NZLCC-NG design consumes an additional 104,575 kWh-eq. than the NZLCC-E design.  
465 Therefore, a larger solar PV system (12.7 kWh) is required to reach total net site energy consumption comparable to  
466 that of the NZLCC-E design.

467 The difference in total hours uncomfortable across the two LCC designs is negligible, suggesting that the LCC-E  
468 design is equally as comfortable as the LCC-NG design. Total hours uncomfortable measures for the NZLCC-E and  
469 NZLCC-NG designs are consistent with estimates for the MCC-E and MCC-NG designs, where the gas-heated  
470 building design proves to be the more comfortable of the two (difference of 117 hours/year). This difference is driven  
471 by additional insulation installed in the exterior wall cavity, lower U-factor windows, and larger sized space heating  
472 unit of the NZLCC-NG design.

473 With BEES- and SAB-weighted EISs of 6.19 and 5.96, respectively, the LCC-NG design appears to have lower  
474 environmental impacts than the LCC-E design, which has a BEES-weighted EIS of 7.14 and a SAB-weighted EIS of  
475 6.84. A more in-depth comparison across the 12 impact categories reveals that the LCC-NG designs lower the  
476 environmental impact in 9 impact categories and equal impacts in 3 categories (Land, Water, and Ozone Depletion)  
477 relative to the LCC-E design. Reduced impacts are largely driven by the difference in energy use between the two  
478 designs, as well as differences in the types and/or capacities of the building equipment. For example, use of a smaller  
479 7.6 kW PV system in the LCC-NG design has less of an environmental impact than the 10.2 kW system adopted by  
480 the LCC-E design. Similarly, the NZLCC-NG design is the more environmentally-friendly of the two net-zero designs  
481 with BEES- and SAB-weighted scores of 7.00 and 6.72, respectively – outperforming the NZLCC-E design in 7 out  
482 of 12 impact categories (i.e., Cancer Effects, Global Climate Change Potential, Acidification Potential, Criteria Air  
483 Pollutants, Non-cancer Effects, Smog Formation, and Primary Energy Use).<sup>16</sup> Again, these differences are largely  
484 driven by the differences in the types and/or capacities of the building equipment (e.g. solar PV system).

## 485 **6. Conclusion, Implications, and Future Research**

486 This paper uses data from the BIRDS Database with whole-building sustainability metrics to conduct a case study  
487 examining the impacts of alternative electric and gas-fired heating systems on the sustainability performance of a  
488 single-family dwelling located in Maryland under an assumed usage by a four-person family. Results suggest that low  
489 natural gas prices provide incentives to install natural-gas fired equipment when minimizing life-cycle costs is the  
490 primary goal. Meanwhile, electric heating equipment is likely to perform better economically in reaching net-zero  
491 energy performance, but with higher environmental impacts due to (currently) higher source emissions rates of  
492 electricity relative to natural gas.

493 In comparing two Maryland state code-compliant homes (2015 IECC), one all-electric and one with gas-fired space  
494 and water heating equipment, the natural gas-heated (MCC-NG) design is more economical (lower LCC) and  
495 environmentally-friendly (lower environmental impacts across numerous impact categories). Due to larger system  
496 capacities and faster heating responses, gas-fired equipment enjoys advantages with respect to indoor comfort.

497 Regardless of the optimization goal (energy and/or costs) relative to current state building codes, there are some  
498 consistent EEM selections across heating fuel source options: (1) higher efficiency lighting, (2) higher efficiency  
499 HVAC and DHW equipment, (3) lower building envelope air leakage, and (4) solar PV system sized to meet total

---

<sup>16</sup> The NZLCC-E design has a BEES-weighted score of 4.66 and a SAB-weighted score of 4.62.

500 electricity load. EEMs precluded from the optimal building designs on cost-effectiveness grounds are additional rigid  
501 insulation in the roof assembly and the solar thermal system. Relative to results found in a previous study of the  
502 NZERTF, the optimal all-electric building designs implement different EEMs, using less efficient windows and lower  
503 R-value wall assemblies while installing a more efficient HVAC system, driven by the newer construction cost data  
504 used for the analysis. These results show how the variability in construction costs should be considered when  
505 interpreting the results of this study. Additionally, there are building designs implementing different EEMs that are  
506 near optimal that would be reasonable design choices.

507 The relative cost of electricity and natural gas combined with the marginal value of electricity discontinuity at net-  
508 zero electricity consumption (first unit of excess electricity production) created by the net metering structure in  
509 Maryland leads to varying optimal selections of heating equipment. The cost-optimal design uses natural-gas heating  
510 equipment (LCC-NG design), saving an additional \$937 in LCC over the study period. Although the LCC-NG design  
511 saves half the site energy that the lowest cost all-electric (LCC-E) design does, it leads to lower overall environmental  
512 impacts because of the (currently) lower emissions rate for natural gas relative to electricity in Maryland.

513 The electricity value discontinuity is also the reason the lowest cost net-zero energy design uses electric heating  
514 equipment (NZLCC-E design), which increases LCC by \$956 relative to the cost-optimal (LCC-NG) design. The  
515 lowest cost design that reaches net-zero energy performance using gas-fired electricity (NZLCC-NG) increases LCC  
516 by additional \$11,489 relative to the NZLCC-E design due to additional construction costs and the lower marginal  
517 value of excess generation. These results could change if the relative cost of natural gas and electricity were to change  
518 or the net metering regulation were altered. The relative environmental performance remains (marginally) in favor of  
519 natural gas-fired heating equipment due to the assumed fuel mix of electricity.

520 Impacts of alternative HVAC and DHW systems on total hours uncomfortable appear to decrease as energy efficiency  
521 increases. There is a difference in maintaining indoor conditions for state code-compliant designs, with the natural  
522 gas-fired HVAC system having 152 “uncomfortable hours” relative to the comparable all-electric design at 622 “hours  
523 uncomfortable,” which is driven primarily by the difference in heating equipment capacity. However, differences in  
524 occupant comfort between electric and gas-fired heating equipment decrease with greater energy efficiency. Hours  
525 uncomfortable are nearly identical for the two cost-optimal designs (307 for LCC-E and 309 for LCC-NG) and both  
526 net-zero designs perform better than the cost-optimal designs (262 for NZLCC-E and 145 for NZLCC-NG).  
527 Regardless of heating fuel, these net-zero building designs perform as well or better than code-compliant designs.

528 This study focused on the use of electric- versus natural gas-fired systems for household space heating and domestic  
529 water heating requirements for new, average-sized, single-family home constructed in Gaithersburg, MD. However,  
530 the study is limited in scope in terms of equipment, occupant loads, and location considered. The research could be  
531 expanded in the future to include alternative equipment such as ground source heat exchangers, multi-split, mini-split,  
532 and small-duct high velocity HVAC systems and be expanded to other locations to account for differences in climate  
533 and costs. Also, the sensitivity of the results to alternative occupant loads should be considered because building  
534 operation varies widely from occupant to occupant. Additionally, several underlying assumptions in the current  
535 analysis change over time, potentially leading to changes in the relative sustainability performance of alternative  
536 building designs. Building construction costs and materials environmental impacts, energy costs and fuel mixes, and  
537 the cost and efficiency of solar PV all are changing. Future research must account for these dynamics to remain  
538 current and accurate over time.

## 539 7. References

- 540 Abusoglu, A., and M.S. Sedeeq. 2013. "Comparative exergoenvironmental analysis and assessment of various  
541 residential heating systems." *Energy and Buildings* 62:268-277.
- 542 ASHRAE. 2010a. "American Society of Heating, Refrigerating and Air-Conditioning Engineers Standard 62.2-2010."  
543 [www.ashrae.org](http://www.ashrae.org).
- 544 ASHRAE. 2010b. Thermal Environmental Conditions for Human Occupancy, ASHRAE Standard 55-2010. Atlanta,  
545 GA: American Society of Heating, Refrigerating and Air-Conditioning Engineers.
- 546 ASHRAE. 2012. *2012 ASHRAE Handbook: Fundamentals*. Atlanta, GA: American Society of Heating, Refrigerating,  
547 and Air-Conditioning Engineers.
- 548 ASTM. 2012a. *ASTM Standards on Building Economics: 7th Edition*. West Conshohocken, PA: ASTM International.
- 549 ASTM. 2012b. Standard Guide for Selecting Economic Methods for Evaluating Investments in Buildings and Building  
550 Systems, ASTM Designation E1185-12. West Conshohocken, PA.
- 551 Bagley, Sheena, and Robert H Crawford. 2015. "Using life cycle assessment to reduce the energy use and global  
552 warming impacts of a detached house in Melbourne, Australia." *Living and Learning: Research for a Better  
553 Built Environment: Proceeding of the 49th International Conference of the Architectural Science  
554 Association*.
- 555 Bare, Jane. 2011. "TRACI 2.0: the tool for the reduction and assessment of chemical and other environmental impacts  
556 2.0." *Clean Technologies and Environmental Policy* 13 (5):687-696.
- 557 Belsie, Laurent. 2012. "Cheapest way to heat your home? Four fuels compared."  
558 [https://www.csmonitor.com/Environment/2012/1207/Cheapest-way-to-heat-your-home-Four-fuels-  
559 compared/Heating-oil-2-526](https://www.csmonitor.com/Environment/2012/1207/Cheapest-way-to-heat-your-home-Four-fuels-compared/Heating-oil-2-526).
- 560 Brenn, J, P Soltic, and Ch Bach. 2010. "Comparison of natural gas driven heat pumps and electrically driven heat  
561 pumps with conventional systems for building heating purposes." *Energy and Buildings* 42 (6):904-908.
- 562 Cabrol, Loïc, and Paul Rowley. 2012. "Towards low carbon homes—A simulation analysis of building-integrated air-  
563 source heat pump systems." *Energy and Buildings* 48:127-136.
- 564 Cassard, Hannah, Paul Denholm, and Sean Ong. 2011. Break-even cost for residential solar water heating in the United  
565 States: key drivers and sensitivities. National Renewable Energy Laboratory (NREL), Golden, CO.
- 566 Census. 2011. "American Housing Survey (AHS) for the United States, Series H-150, Complete Set of Tables and  
567 Standard Errors." Department of Commerce, U.S. Census Bureau. [http://www.census.gov/programs-  
568 surveys/ahs/](http://www.census.gov/programs-surveys/ahs/).
- 569 Clark, Duncan. 2012. "Householders unlikely to recover solar heating installation costs for 30 years."  
570 <https://www.theguardian.com/environment/2012/sep/21/householders-green-heating-costs>.
- 571 U.S. Congress,. 2015. *H.R. 2029 - Consolidated Appropriations Act, 2016*.

572 Crawford, Robert , Erika Bartak, André Stephan, and Christopher Jensen. 2016. "Evaluating the life cycle energy  
573 benefits of energy efficiency regulations for buildings." *Renewable and Sustainable Energy Reviews* 63:435-  
574 451.

575 Crawford, Robert H, and André Stephan. 2013. "The significance of embodied energy in certified passive houses."  
576 Proceedings of World Academy of Science, Engineering and Technology.

577 Croxford, Ben, and Kat Scott. 2006. "Can PV or solar thermal systems be cost effective ways of reducing CO 2  
578 emissions for residential buildings?"

579 Diakoulaki, D, A Zervos, J Sarafidis, and S Mirasgedis. 2001. "Cost benefit analysis for solar water heating systems."  
580 *Energy Conversion and Management* 42 (14):1727-1739.

581 DOE. 2015. "Building America Climate Region Map." U.S. Department of Energy (DOE),, accessed April 4.  
582 <http://energy.gov/eere/buildings/building-america-climate-specific-guidance>.

583 EnergyPlus Simulation Software Version 8.3.0. U.S. Department of Energy, Building Technologies Program (BTP).

584 Dorer, Viktor, and Andreas Weber. 2009. "Energy and CO2 emissions performance assessment of residential micro-  
585 cogeneration systems with dynamic whole-building simulation programs." *Energy Conversion and*  
586 *Management* 50 (3):648-657.

587 EIA. 2015. "Household heating costs are expected to be lower than previous two winters." U.S. Energy Information  
588 Administration,. [https://www.eia.gov/todayinenergy/detail.php?id=23232#tabs\\_3](https://www.eia.gov/todayinenergy/detail.php?id=23232#tabs_3).

589 EIA. 2017a. Annual Energy Outlook, with Projections to 2050. Washington, DC: U.S. Energy Information  
590 Administration.

591 EIA. 2017b. "U.S. households' heating equipment choices are diverse and vary by climate region." U.S. Energy  
592 Information Administration,. <https://www.eia.gov/todayinenergy/detail.php?id=30672>.

593 EIA. 2017c. "FREQUENTLY ASKED QUESTIONS: How do I compare the cost of heating fuels?". U.S. Energy  
594 Information Administration,. <https://www.eia.gov/tools/faqs/faq.php?id=987&t=7>.

595 EIA. 2017d. "Natural Gas Prices." U.S. Energy Information Administration (EIA),,  
596 [https://www.eia.gov/dnav/ng/ng\\_pri\\_sum\\_a\\_EPG0\\_PRS\\_DMcf\\_a.htm](https://www.eia.gov/dnav/ng/ng_pri_sum_a_EPG0_PRS_DMcf_a.htm).

597 ENERGY STAR. 2011. "Certified Products - Lighting." [https://www.energystar.gov/products/lighting\\_fans](https://www.energystar.gov/products/lighting_fans).

598 Faithful and Gould. 2012. Residential Energy Efficiency Measures: Prototype Estimate and Cost Data Revision 6.0.  
599 National Renewable Energy Laboratory.

600 Fuller, S, and S Petersen. 1996. "Life-Cycle Costing Manual for the Federal Energy Management Program, 1995  
601 Edition." *NIST handbook* 135.

602 Greening, Benjamin, and Adisa Azapagic. 2014. "Domestic solar thermal water heating: A sustainable option for the  
603 UK?" *Renewable Energy* 63:23-36.

604 Gustavsson, Leif, and Åsa Karlsson. 2002. "A system perspective on the heating of detached houses." *Energy policy*  
605 30 (7):553-574.

606 Hang, Y., M. Qu, and F. Zhao. 2012. "Economic and environmental life cycle analysis of solar hot water systems in  
607 the United States." *Energy and Buildings* 45:181-188.

608 Hendron, R, and C Engebrecht. 2010. Building America House Simulation Protocols. edited by Energy Efficiency  
609 and Renewable Energy: National Renewable Energy Laboratory.

610 Hong, Bongghi, and Robert W Howarth. 2016. "Greenhouse gas emissions from domestic hot water: heat pumps  
611 compared to most commonly used systems." *Energy Science & Engineering* 4 (2):123-133.

612 IEA. 2017. Statistics: Key electricity trends 2016. Paris, France: International Energy Agency (IEA).

613 Jeong, Jaehoon, Chang Seob Kim, and Jongsu Lee. 2011. "Household electricity and gas consumption for heating  
614 homes." *Energy Policy* 39 (5):2679-2687.

615 Kalogirou, S. 2009. "Thermal performance, economic and environmental life cycle analysis of thermosiphon solar  
616 water heaters." *Solar Energy* 83 (1):39-48.

617 Kelly, NJ, and J Cockroft. 2011. "Analysis of retrofit air source heat pump performance: Results from detailed  
618 simulations and comparison to field trial data." *Energy and Buildings* 43 (1):239-245.

619 Kneifel, J, and E O'Rear. 2015. "Benefits and Costs of Energy Standard Adoption for New Residential Buildings:  
620 National Summary." *NIST Special Publication* 1194.

621 Kneifel, J, E O'Rear, and D Webb. 2016a. "Evaluating the Sustainability Performance of Alternative Residential  
622 Building Designs using the BIRDS Low-Energy Residential Database." *NIST Special Publication* 1205.

623 Kneifel, J, D Webb, and E O'Rear. 2016. "Energy and Economic Implications of Solar Photovoltaic Performance  
624 Degradation." *Special Publication (NIST SP)-1203*.

625 Kneifel, Joshua, Priya Lavappa, E O'Rear, Anne Landfield Greig, and Sangwon Suh. 2017. "BIRDS v3.1 Low-Energy  
626 Residential Database Technical Manual." *NIST Technical Note* 1956.

627 Kneifel, Joshua, and Eric O'Rear. 2016b. "Net-Zero Energy Residential Building Component Cost Estimates and  
628 Comparisons." *NIST Special Publication* 1207.

629 Kneifel, Joshua, Eric O'Rear, David Webb, and Cheyney O'Fallon. 2018. "An exploration of the relationship between  
630 improvements in energy efficiency and life-cycle energy and carbon emissions using the BIRDS low-energy  
631 residential database." *Energy and Buildings* 160 (Supplement C):19-33. doi:  
632 <https://doi.org/10.1016/j.enbuild.2017.11.030>.

633 Lavappa, P, J Kneifel, and E O'Rear. 2017. Energy Price Indices and Discount Factors for Life-Cycle Cost Analysis -  
634 2017, Annual Supplement to NIST Handbook 135. edited by National Institute of Standards and Technology.

635 Lippiatt, B, J Kneifel, P Lavappa, S Suh, and A Greig. 2013. "Building Industry Reporting and Design for  
636 Sustainability (BIRDS) Technical Manual and User Guide." *NIST Technical Note* 1814.

637 Martinopoulos, G. 2014. "Solar Heating Systems as a Viable Solution Towards Nearly Zero Energy Buildings."  
638 ASME 2014 8th International Conference on Energy Sustainability collocated with the ASME 2014 12th  
639 International Conference on Fuel Cell Science, Engineering and Technology June 2014.

640 Martinopoulos, G. 2018. "Life Cycle Assessment of solar energy conversion systems in energetic retrofitted  
641 buildings." *Journal of Building Engineering* 20:256-263.

642 Martinopoulos, G., K.T. Papakostas, and A.M. Papadopoulos. 2016. "Comparative analysis of various heating systems  
643 for residential buildings in Mediterranean climate." *Energy and Buildings* 124:79-87.

644 Martinopoulos, G., K.T. Papakostas, and A.M. Papadopoulos. 2018. "A comparative review of heating systems in EU  
645 countries, based on efficiency and fuel cost." *Renewable and Sustainable Energy Reviews* 90:687-699.

646 Martinopoulos, G., and G. Tsalikis. 2014. "Active solar heating systems for energy efficient buildings in Greece: A  
647 technical economic and environmental evaluation." *Energy and Buildings* 68:130-137.

648 National Association of Home Builders (NAHB) Research Center. 2007. Study of Life Expectancy of Home  
649 Components. National Association of Home Builders.

650 PEPCO. 2018. "Maryland Residential Service Scheduler R."  
651 <http://www.pepco.com/MyAccount/MyBillUsage/Documents/Updated%20010418-%20R.pdf>.

652 Pitt, Damian, John Randolph, David St Jean, and Mark Chang. 2012. "Estimating potential community-wide energy  
653 and greenhouse gas emissions savings from residential energy retrofits." *Energy and Environment Research*  
654 2 (1):44.

655 Rockenbaugh, Caleb, Jesse Dean, David Lovullo, Lars Lisell, Greg Barker, Ed Hanckock, and Paul Norton. 2016.  
656 High Performance Flat Plate Solar Thermal Collector Evaluation. National Renewable Energy Lab.(NREL),  
657 Golden, CO (United States).

658 RS Means. 2017. <https://www.rsmeans.com>.

659 Sanaye, Sepehr, Mehdi Aghaei Meybodi, and Mahmood Chahartaghi. 2010. "Modeling and economic analysis of gas  
660 engine heat pumps for residential and commercial buildings in various climate regions of Iran." *Energy and*  
661 *Buildings* 42 (7):1129-1138.

662 Shah, Viral P, David Col Debella, and Robert J Ries. 2008. "Life cycle assessment of residential heating and cooling  
663 systems in four regions in the United States." *Energy and buildings* 40 (4):503-513.

664 Simons, A., and S.K. Firth. 2011. "Life-cycle assessment of a 100% solar fraction thermal supply to a European  
665 apartment building using water-based sensible heat storage." *Energy and Buildings* 43 (6):1231-1240.

666 Stephan, André, and Robert H Crawford. 2016. "The relationship between house size and life cycle energy demand:  
667 Implications for energy efficiency regulations for buildings." *Energy* 116:1158-1171.

668 Stephan, André, Christopher A Jensen, and Robert H Crawford. 2017. "Improving the life cycle energy performance  
669 of apartment units through façade design."

670 Suh, Sangwon, and Barbara C Lippiatt. 2012. "Framework for hybrid life cycle inventory databases: a case study on  
671 the Building for Environmental and Economic Sustainability (BEES) database." *The International Journal*  
672 *of Life Cycle Assessment* 17 (5):604-612.

673 Tsilingiridis, GMNKG, G Martinopoulos, and N Kyriakis. 2004. "Life cycle environmental impact of a  
674 thermosyphonic domestic solar hot water system in comparison with electrical and gas water heating."  
675 *Renewable Energy* 29 (8):1277-1288.

676 U.S. Department of Energy. 2017. "Solar Water Heaters." [https://www.energy.gov/energysaver/water-heating/solar-](https://www.energy.gov/energysaver/water-heating/solar-water-heaters)  
677 [water-heaters](https://www.energy.gov/energysaver/water-heating/solar-water-heaters).

678 Weather Analytics. 2014. TMY Meteorological Year 3 (TMY) Formatted Weather Data File. edited by Atlas - Global  
679 Weather Database. <https://www.athenium.com/>: Athenium Analytics (formerly Weather Analytics).

680 Yang, Lijun, Radu Zmeureanu, and Hugues Rivard. 2008. "Comparison of environmental impacts of two residential  
681 heating systems." *Building and Environment* 43 (6):1072-1081.

682 jEPlus v1.5.1 Version 8.0.0. Building Technologies Program.

683 8. Appendix  
684

Wall Constructions <sup>17</sup>		Option 1	Option 2	Option 3	Option 4	Option 5•
Exterior Wall	Framing	Typical†	Typical	Advanced††	Advanced	Advanced
	Insulation	R <sub>SI</sub> -2.3	R <sub>SI</sub> -2.3+0.9*	R <sub>SI</sub> -3.5	R <sub>SI</sub> -3.5+2.1*	R <sub>SI</sub> -3.5+4.2*
Foundation Constructions		Option 1	Option 2	Option 3	Option 4•	
Basement	Wall; Slab	R <sub>SI</sub> -1.41; R <sub>SI</sub> -0	R <sub>SI</sub> -1.76; R <sub>SI</sub> -0	R <sub>SI</sub> -3.9; R <sub>SI</sub> -0	R <sub>SI</sub> -3.9; R <sub>SI</sub> -1.8	
Roof/Ceiling Constructions		Option 1	Option 2	Option 3	Option 4	Option 5•
Roof/Ceiling	Roof**	R <sub>SI</sub> -0	R <sub>SI</sub> -0	R <sub>SI</sub> -7.92+0.7	R <sub>SI</sub> -7.92+2.64	R <sub>SI</sub> -7.92+5.28
	Ceiling***	R <sub>SI</sub> -6.69	R <sub>SI</sub> -8.63	R <sub>SI</sub> -0	R <sub>SI</sub> -0	R <sub>SI</sub> -0

† 5.1 cm x 10.2 cm – 40.6 cm OC; †† 5.1 cm x 15.2 cm – 61.0 cm OC; \*Interior Wall Cavity + Exterior; \*\*Insulation in Rafters + Exterior Roof; \*\*\* Insulation blown into ceiling joists; • NZERTF Design

685 Table A1 Constructions – Roof, Ceiling, Wall and Foundation  
686

Parameter <sup>18</sup>	Units	Option 1	Option 2	Option 3	Option 4	Option 5
U-Factor; SHGC	W/m <sup>2</sup> -K; Fraction	2.57; 0.60	2.28; 0.60	2.00; 0.60	2.00; 0.40	1.14; 0.25

687 Table A2 Window Design Options  
688

Design Option	Assumed Effective Leakage Area (cm <sup>2</sup> )		
	ACH <sub>50</sub> <sup>19</sup>	1 <sup>st</sup> Floor	2 <sup>nd</sup> Floor
Option 1 (2003 & 2006 / 2009 IECC)	No Maximum / 7.00	1473.3	1343.3
Option 2 (2012/2015 IECC)	3.00	403.6	368.1
Option 3 (NZERTF)	0.63	132.6	120.9

689 Table A3 Design Options for Alternative Air Leakage Rates  
690

	Option 1 (2003/2006)	Option 2 (2009)	Option 3 (2012/2015)	Option 4 (NZERTF)
Fraction	34 %	50 %	75 %	100 %

691 Table A4 Fraction of High Efficiency Fixtures by Requirement  
692

Design Option	System Components <sup>20</sup>
Option 1	Air-to-air heat pump (SEER 13/HSPF 7.7); Min. Outdoor Air (0.04 m <sup>3</sup> /s)
Option 2 (NZERTF)	Air-to-air heat pump (SEER 15.8/HSPF 9.05); Separate HRV system (0.04 m <sup>3</sup> /s)
Option 3	Gas-electric split A/C system (SEER 13/80 % AFUE); Min. Outdoor Air (0.04 m <sup>3</sup> /s)
Option 4	Gas-electric split A/C system (SEER 16/96 % AFUE); Separate HRV system (0.04 m <sup>3</sup> /s)

693 Table A5 Heating and Cooling Equipment Design Options  
694

<sup>17</sup> The R-values (R) in Table A1 refers to the capacity of an insulating material to resist heat flow. A higher R-value implies a greater insulating power. The R<sub>SI</sub> values are the derived SI units.

<sup>18</sup> U-factor refers to the heat loss of a window assembly. A lower U-factor implies a greater resistance by the window to heat flow. The solar heat gain coefficient (SHGC), a fractional number between 0 and 1, refers to the fractional amount of incident solar radiation admitted through a window.

<sup>19</sup> ACH<sub>50</sub> – Air Changes per Hour at 50 Pascals

<sup>20</sup> SEER is the rated cooling efficiency. HSPF is a measure of heating efficiency for air-source heat pumps. Annual fuel utilization efficiency (AFUE) factor indicates how efficiently a furnace utilizes it fuel.

Design Option	System Components <sup>21</sup>
Option 1	189 L electric water heater (EF = 0.95); No Auxiliary
Option 2	189 L HPWH (COP 2.36); No Auxiliary
Option 3	189 L electric water heater (EF = 0.95); 2 panel, 302.8 L solar thermal storage tank
Option 4 (NZERTF)	189 L HPWH (COP 2.36); 2 panel, 302.8 L solar thermal storage tank
Option 5	189 L gas water heater (EF = 0.78); No Auxiliary
Option 6	189 L gas water heater (EF = 0.90); No Auxiliary
Option 7	189 L gas water heater (EF = 0.78); 2 panel, 302.8 L solar thermal storage tank
Option 8	189 L gas water heater (EF = 0.90); 2 panel, 302.8 L solar thermal storage tank

**Table A6 Domestic Hot Water System Design Options**

Design Option	Option 1	Option 2	Option 3	Option 4	Option 5	Option 6
System Size (kW)	0.0	2.5	5.1	7.6	10.2	12.7

**Table A7 Solar PV System Options**

Impact Category	Normalization reference	Units	EPA Science Advisory Board	BEES Stakeholder Panel
Global Warming	7.16E+12	kg CO <sub>2</sub> eq.	18	29.9
Primary Energy Consumption	3.52E+13	kWh	7	10.3
HH – Criteria Air	2.24E+10	kg PM10 eq.	7	9.3
HH – Cancer (Carcinogenic)	1.05E+04	CTUh	8	8.2
Water Consumption	1.69E+14	L	3	8.2
Ecological Toxicity	3.82E+13	CTUe	12	7.2
Eutrophication	1.01E+10	kg N eq.	5	6.2
Land Use	7.32E+08	hectare	18	6.2
HH – Non-cancer (Non-Carcinogenic)	5.03E+05	CTUh	5	5.2
Smog Formation	4.64E+11	kg O <sub>3</sub> eq.	7	4.1
Acidification	1.66E+12	mol H+ eq.	5	3.1
Ozone Depletion	5.10E+07	kg CFC-11-eq.	5	2.1

**Table A8 Normalization References (Annual U.S. Contributions) and EIS Weights**

<sup>21</sup> Energy efficiency of a water heater is indicated by EF based on the amount of hot water produced per unit of fuel consumed over a typical day. COP is the ratio of useful heating/cooling to work required, characterizing heat pump/AC unit performance.

Design Category	LCC-E	LCC-NG	NZLCC-E	NZLCC-NG
<b>Windows (U; SHGC)</b>	2.56 W/m <sup>2</sup> -K; 0.60	2.56 W/m <sup>2</sup> -K; 0.60	2.56 W/m <sup>2</sup> -K; 0.60	1.99 W/m <sup>2</sup> -K; 0.60
<b>Heating &amp; Cooling</b>	SEER 16.5/ HSPF 9.1	SEER 16.0/ AFUE 96%	SEER 16.5/ HSPF 9.1	SEER 16.0/ AFUE 96%
<b>Ventilation</b>	Separate HRV	Separate HRV	Separate HRV	Separate HRV
<b>Air Leakage</b>	0.63 ACH <sub>50</sub>	0.63 ACH <sub>50</sub>	0.63 ACH <sub>50</sub>	0.63 ACH <sub>50</sub>
<b>Lighting</b>	100% efficient fixtures	100% efficient fixtures	100% efficient fixtures	100% efficient fixtures
<b>Solar PV</b>	10.2 kW	7.6 kW	10.2 kW	12.7 kW
<b>DHW</b>	Heat Pump	Gas – 90%	Heat Pump	Gas – 90%
<b>Roof</b>	Ceiling: R <sub>SI</sub> -6.7	Roof: R <sub>SI</sub> -7.92 + 0.9	Roof: R <sub>SI</sub> -7.92 + 0.9	Roof: R <sub>SI</sub> -7.92 + 0.9
<b>Wall</b>	Typical Frame R <sub>SI</sub> -2.3	Typical Frame R <sub>SI</sub> -2.3	Typical Frame R <sub>SI</sub> -2.3	Advanced Frame R <sub>SI</sub> -3.5+4.2
<b>Found. Wall</b>	R <sub>SI</sub> -1.41	R <sub>SI</sub> -1.41	R <sub>SI</sub> -1.41	R <sub>SI</sub> -1.41
<b>Found. Floor</b>	R <sub>SI</sub> -0	R <sub>SI</sub> -0	R <sub>SI</sub> -0	R <sub>SI</sub> -0
<b>Site Energy (kWh)</b>	~2,435	~355,880	~7,908	~9,628
<b>Total LCC</b>	\$324,760	\$321,259	\$324,779	\$338,733
<b>Energy Savings vs MCC-NG*</b>	-	~77%	-	~101%
<b>Δ LCC vs MCC-NG*</b>	-	-\$35,325	-	-\$22,880
<b>Energy Savings vs MCC-E</b>	99.7%	50%	~101%	~101%
<b>Δ LCC vs MCC-E*</b>	-\$44,103	-\$45,040	-\$44,084	-\$32,595
<b>Hrs Uncomfort./Yr</b>	~307	~309	~262	~145
*30-yr study period				

701

Table A9 Design Features for All-Electric and Gas-heated EE and LCC Building Designs

# California Greenhouse Gas Emissions for 2000 to 2018

## Trends of Emissions and Other Indicators

### Executive Summary

The annual statewide greenhouse gas (GHG) emission inventory is an important tool in tracking progress towards meeting statewide GHG goals. This document summarizes the trends in emissions and indicators in the California GHG Emission Inventory (“the GHG Inventory”). The 2020 edition of the inventory includes GHG emissions released during 2000-2018 calendar years. In 2018, emissions from GHG emitting activities statewide were 425 million metric tons of carbon dioxide equivalent (MMT $\text{CO}_2\text{e}$ ), 0.8 MMT $\text{CO}_2\text{e}$  higher than 2017 levels and 6 MMT $\text{CO}_2\text{e}$  below the 2020 GHG Limit of 431 MMT $\text{CO}_2\text{e}$ . The most notable highlights in the 2020 edition inventory include:

- California statewide GHG emissions dropped below the 2020 GHG Limit in 2016 and have remained below the 2020 GHG Limit since then.
- Transportation emissions decreased in 2018 compared to the previous year, which is the first year over year decrease since 2013.
- Since 2008, California’s electricity sector has followed an overall downward trend in emissions. In 2018, solar power generation has continued its rapid growth since 2013.
- Emissions from high-GWP gases increased 2.3 percent in 2018 (2000-2018 average year-over-year increase is 6.8 percent), continuing the increasing trend as they replace Ozone Depleting Substances (ODS) being phased out under the 1987 Montreal Protocol.

Figure 1 compares annual statewide GHG emissions to the 2020 GHG Limit.

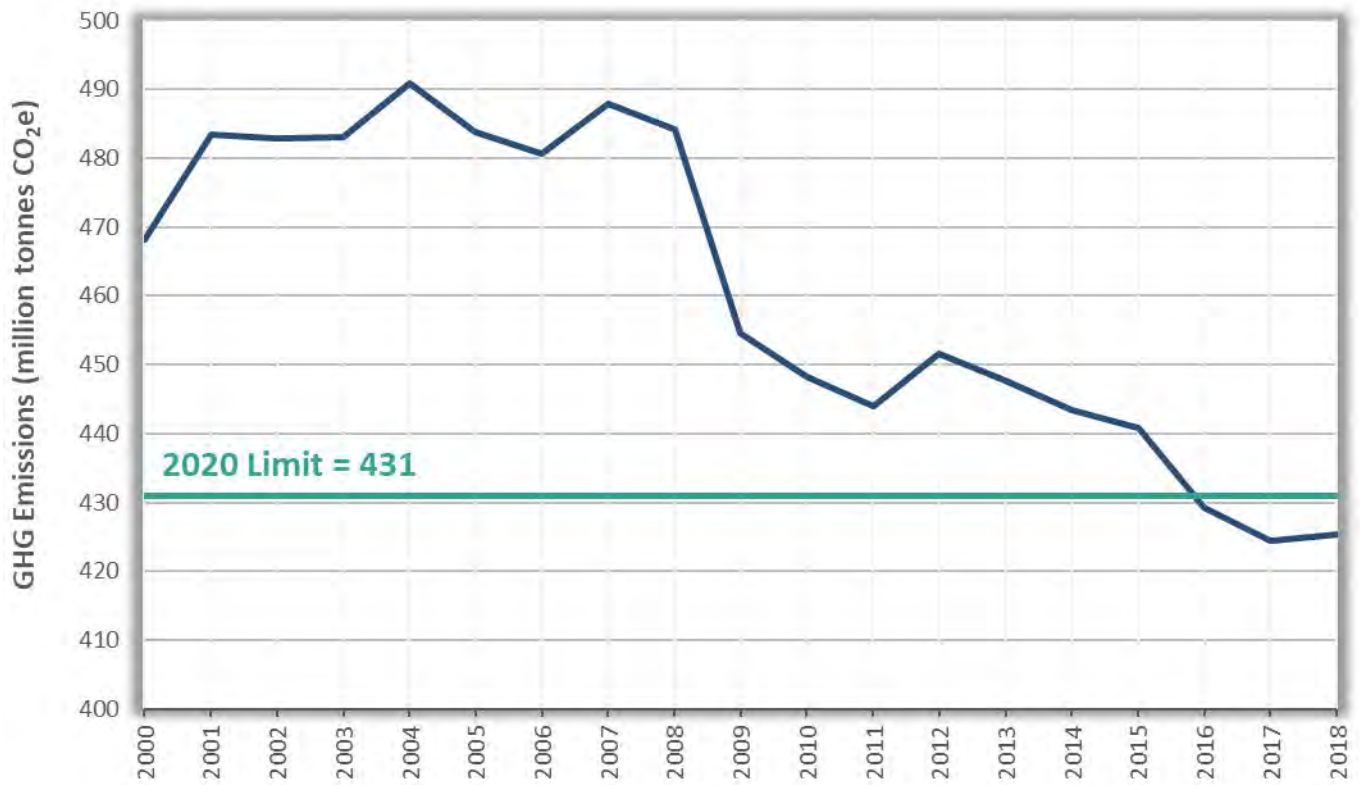


**Figure 1. California's GHG emissions, 2000-2018.** This graph shows California's annual GHG emissions from 2000 to 2018 in relation to the 2020 GHG Limit required by the California Global Warming Solutions Act (Assembly Bill 32). In 2016, California's GHG emissions dropped below the 2020 GHG Limit and have remained below the 2020 GHG Limit since that time.

## Introduction

The GHG inventory is an important tool in demonstrating the State's progress towards achieving the statewide GHG goals established by Assembly Bill 32 (AB 32) (reduce emissions to 1990 levels by 2020) and Senate Bill 32 (SB 32) (reduce emissions to at least 40 percent below 1990 levels by 2030). The GHG Inventory includes the following type of sources: emissions from fossil fuel combustion, GHG generated as by-product of chemical reactions in industrial processes, use of GHG-containing consumer products and human-made chemicals, and emissions from agricultural and waste sector operations. The exchange of ecosystem carbon between the atmosphere and the plants and soils in land is separately quantified in the Natural and Working Lands Ecosystem Carbon Inventory [1], which also includes wildfire emissions. For the emission sources included in the GHG Inventory, the inventory framework is consistent with international and national GHG inventory practices [2].

The 2020 edition of the GHG Inventory includes the emissions of the seven GHGs identified in AB 32 [3] for the years 2000 to 2018. There are additional climate pollutants that are not included in AB 32 that are tracked separately outside of the GHG inventory. These climate pollutants include black carbon and sulfuryl fluoride (SO<sub>2</sub>F<sub>2</sub>), which are discussed in the Short-Lived Climate Pollutant (SLCP) Strategy [4] and ozone depleting substances (ODS), which are being phased out under a 1987 international treaty [5]. ODS are now being substituted with hydrofluorocarbons, which are pollutants specified in AB 32 [3].

In this report, emission trends and indicators are presented in the categories outlined in the Initial AB 32 Scoping Plan [6]. There are alternative ways of organizing emission sources into categories, and the resulting percentages will be different depending on these categorization schemes. The *Additional Information* section at the end of this report provides further information on alternative categorization schemes. All emissions in this report are expressed in 100-year Global Warming Potential (GWP) from the Intergovernmental Panel on Climate Change (IPCC) 4th Assessment Report (AR4) [7], consistent with current international GHG inventory practices.

## Statewide Trends of Emissions and Indicators

In 2018, emissions from statewide emitting activities were 425 million metric tons of CO<sub>2</sub> equivalent (MMTCO<sub>2</sub>e, or million tonnes CO<sub>2</sub>e), 1.0 MMTCO<sub>2</sub>e higher than 2017 levels and 6 MMTCO<sub>2</sub>e below the 2020 GHG Limit of 431 MMTCO<sub>2</sub>e. Since the peak level in 2004, California's GHG emissions have generally followed a decreasing trend. In 2016, statewide GHG emissions dropped below the 2020 GHG Limit and have remained below the Limit since that time.

Per capita GHG emissions in California have dropped from a 2001 peak of 14.0 tonnes per person to 10.7 tonnes per person in 2018, a 24 percent decrease [8] [9]. Overall trends in the inventory also demonstrate that the carbon intensity of California's economy (the amount of carbon pollution per million dollars of gross domestic product (GDP)) is declining. From 2000 to 2018, the carbon intensity of California's economy decreased by 43 percent while the GDP increased by 59 percent. In 2018, GDP grew 4.3 percent while the emissions per GDP declined by 0.4 percent compared to 2017 [9] [10]. Figures 2(a)-(c) show California's growth alongside GHG emissions.

Figure 2a. Change in California GDP, Population, and GHG Emissions Since 2000

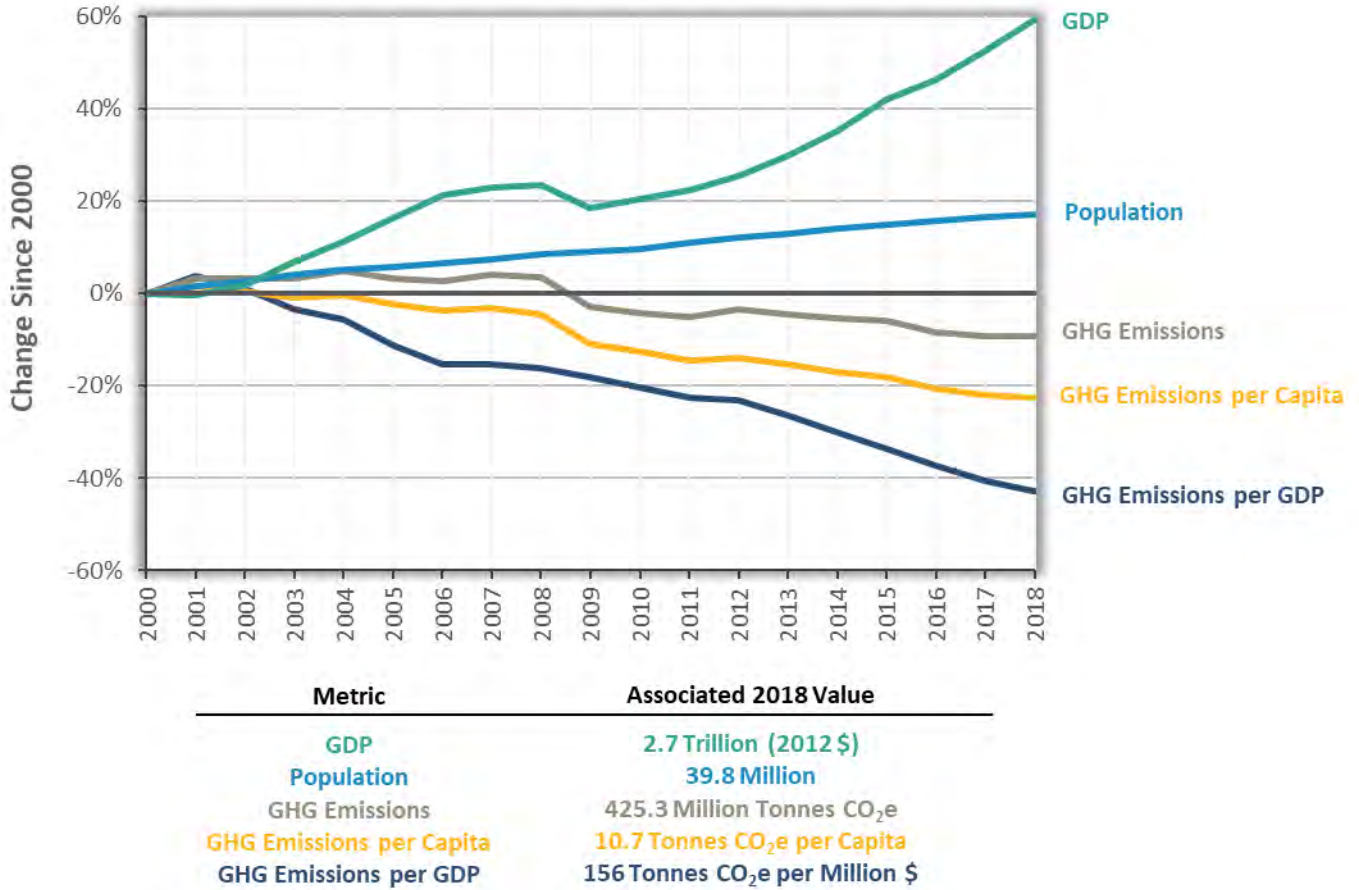


Figure 2b. California Total and Per Capita GHG Emissions

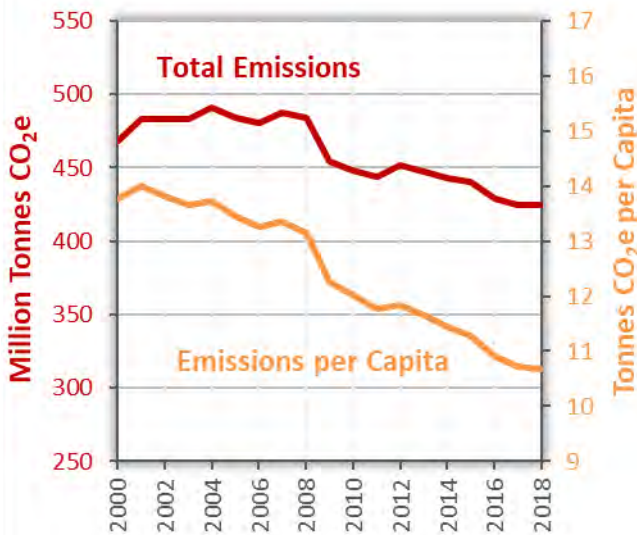
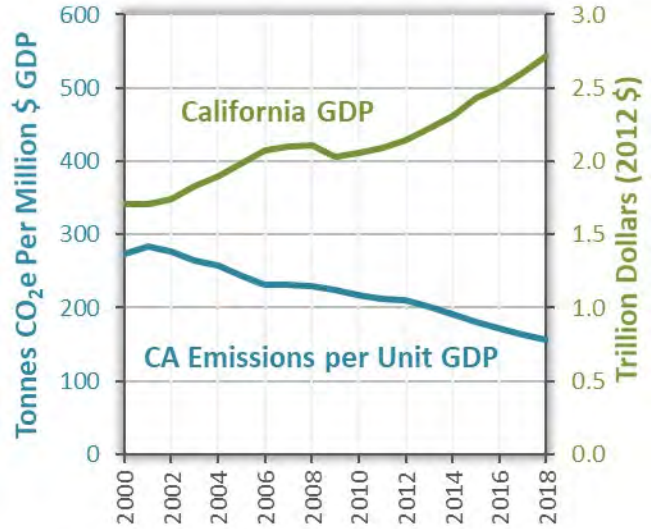


Figure 2c. Carbon Intensity of California's Economy



Figures 2(a)-(c). California's GHG emissions, population, GDP, GHG emissions per capita, and carbon intensity of the economy. Figure 2(a) shows percent change in GHG emissions relative to GDP and population since 2000. Figures 2(b) and 2(c) present these indicators in the original units. In the charts with 2 vertical axes, the color of a trend line matches the color of its corresponding vertical label.

## Overview of Emission Trends by Sector

The transportation sector remains the largest source of GHG emissions in the State. Direct emissions from vehicle tailpipe, off-road transportation sources, intrastate aviation, etc., account for 40 percent<sup>a</sup> of statewide emissions in 2018. Transportation emissions decreased in 2018 compared to the previous year, which is the first year over year decrease since 2013. Emissions from the electricity sector account for 15 percent of the inventory and showed a slight increase in 2018 due to less hydropower. The industrial sector trend has been relatively flat in recent years and remains at 21 percent of the inventory. Emissions from high-GWP gases have continued to increase as they replace ODS that are being phased out under the 1987 Montreal Protocol [5]. Emissions from other sectors have remained relatively constant in recent years. Figure 3 shows an overview of the emission trends by Scoping Plan sector. Figure 4 breaks out 2018 emissions by sector into an additional level of sub-sector categories.

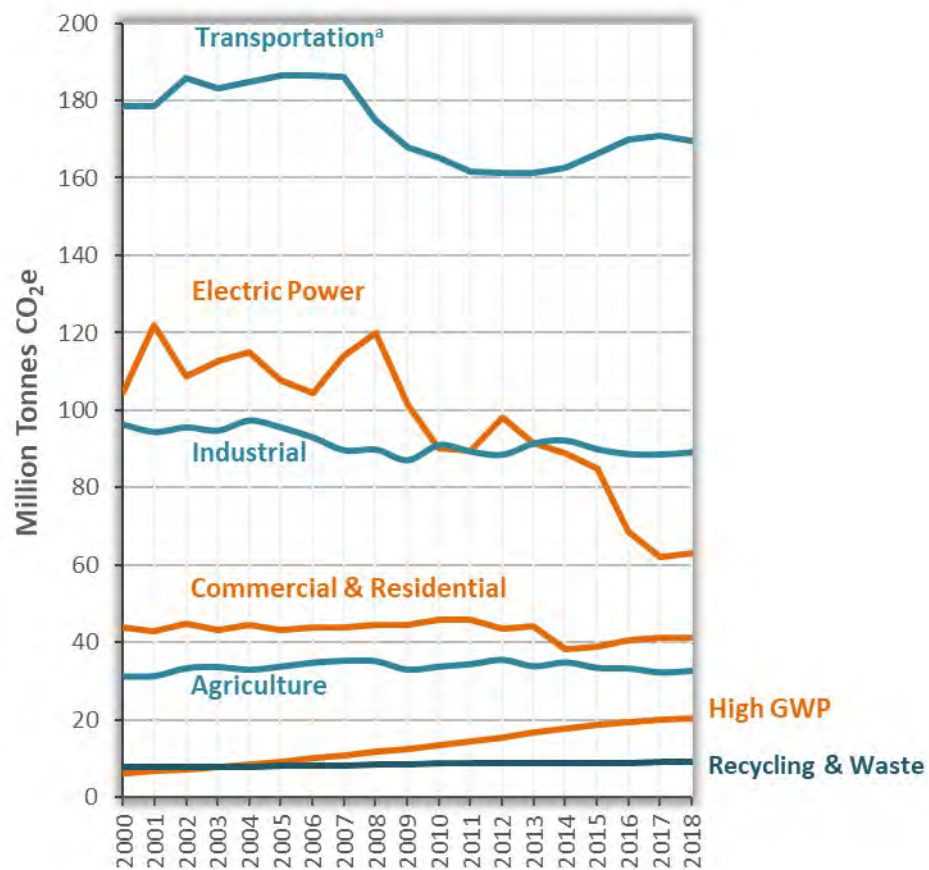


**Figure 3. Trends in California GHG Emissions.** This figure shows changes in emissions by Scoping Plan sector between 2000 and 2018. Emissions are organized by the categories in the AB 32 Scoping Plan.

<sup>a</sup> The transportation sector represents tailpipe emissions from on-road vehicles and direct emissions from other off-road mobile sources. It does not include emissions from petroleum refineries and oil extraction and production.

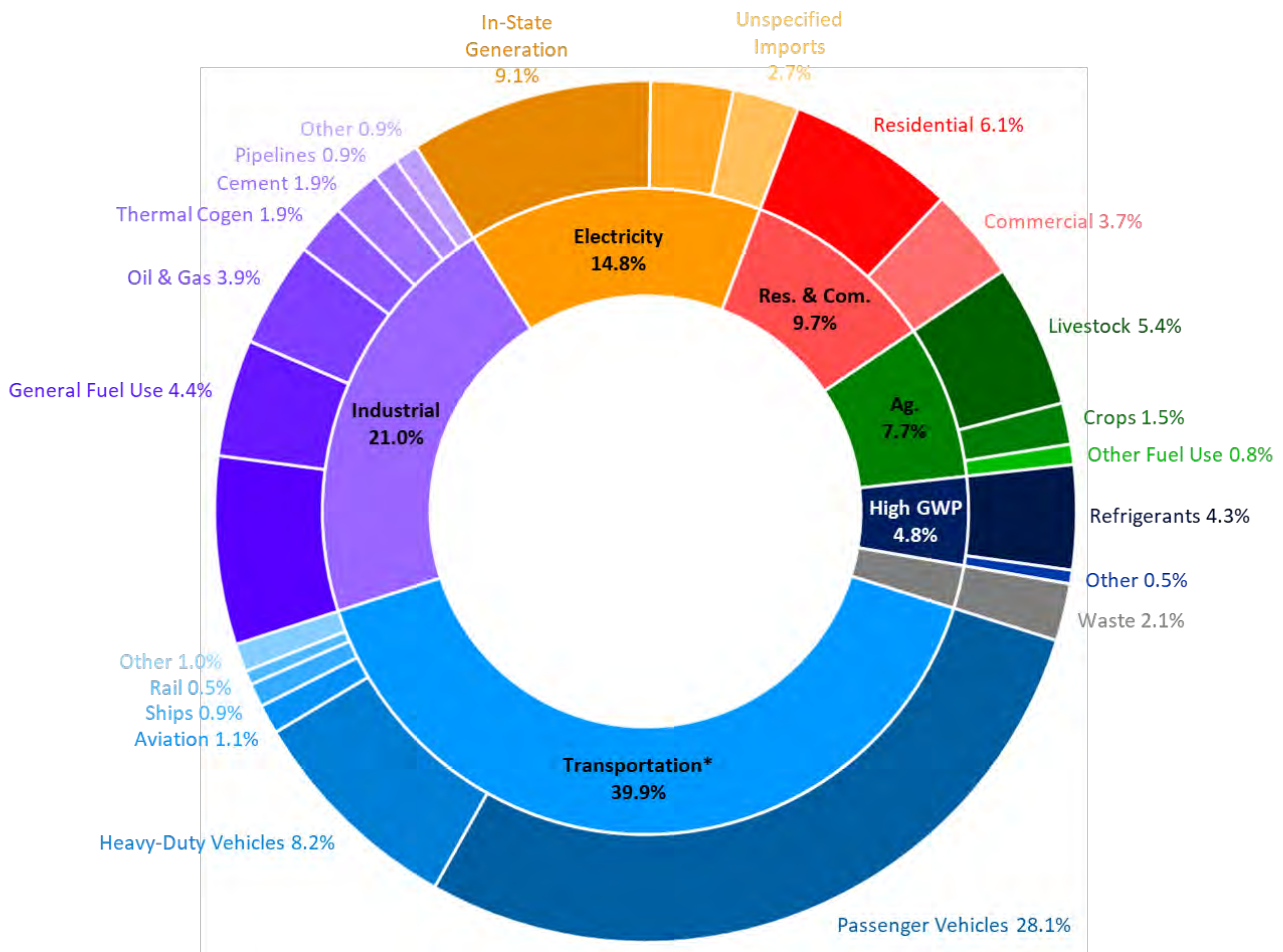


**Figure 4. 2018 GHG Emissions by Scoping Plan Sector and Sub-Sector Category.** This figure breaks out 2018 emissions by sector into an additional level of sub-sector categories. The inner ring shows the broad Scoping Plan sectors. The outer ring breaks out the broad sectors into sub-sectors or emission categories under each sector.

\*The transportation sector represents tailpipe emissions from on-road vehicles and direct emissions from other off-road mobile sources. It does not include emissions from petroleum refineries and oil extraction and production, which are included in the industrial sector.

## Transportation Sector

The transportation sector remains the largest source of GHG emissions in 2018, accounting for 40 percent<sup>b</sup> of California’s GHG inventory. Contributions from the transportation sector<sup>c</sup> include emissions from combustion of fuels in-state that are used by on-road and off-road vehicles, aviation, rail, and water-borne vehicles, as well as a few other smaller sources. (In this report, emissions from refrigerants used in vehicles, airplane, train, and ship and boat are shown in the High-GWP gases category.) Transportation emissions decreased in 2018 compared to the previous year, which is the first year over year decrease since 2013. Figure 5 shows emissions by transportation source categories and the sector total.

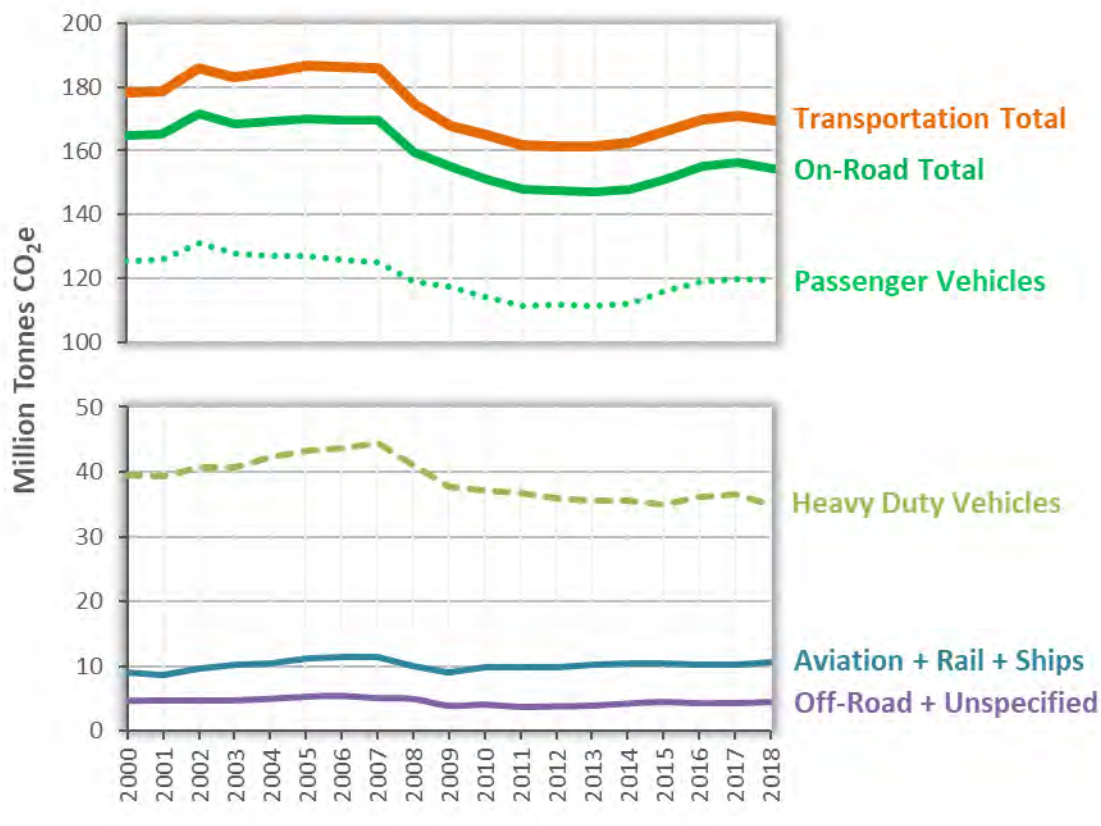


**Figure 5. Overview of GHG Emissions from the Transportation Sector.** “Transportation Total” is the sum of “On-Road Total,” “Aviation + Rail + Ships,” and “Off-Road + Unspecified.” “On-Road Total” is the sum of “Passenger Vehicles” and “Heavy Duty Vehicles.”

<sup>b</sup> The 40 percent figure represents tailpipe emissions from on-road vehicles and direct emissions from other non-road transportation sources. It does not include emissions from petroleum refineries and oil extraction and production, which are included in the industrial sector.

<sup>c</sup> Emissions from the following sources are not included in the GHG inventory for the purpose of comparing to the GHG Limit, but are tracked separately as informational items and are published with the GHG inventory: interstate and international aviation, diesel and jet fuel use at military bases, and a portion of bunker fuel purchased in California that is combusted by ships beyond 24 nautical miles from California’s shores. The following emissions are not included or tracked in the GHG inventory: emissions from the combustion of fuels purchased outside of California that are used in-state by passenger vehicles and trains crossing into California, and out-of-state upstream emissions tracked by the Low Carbon Fuel Standard (LCFS) program.

Figures 6 and 7 show the trends in emissions and fuel used in light-duty gasoline and heavy-duty diesel vehicles. Total fuel combustion emissions, inclusive of both fossil component (orange line) and bio-component (yellow shaded region) of the fuel blend, track trends in fuel sales. Consistent with the IPCC Guidelines [2] and the annual GHG inventories submitted by the U.S. and other nations to the United Nations Framework Convention on Climate Change (UNFCCC), carbon dioxide (CO<sub>2</sub>) emissions from biofuels (the biofuel components of fuel blends) are classified as “biogenic CO<sub>2</sub>.” They are tracked separately from the rest of the emissions in the inventory and are not included in the total emissions when comparing to California’s 2020 and 2030 GHG Limits. Biogenic CO<sub>2</sub> emissions data are available on the CARB webpage [9]. Emissions of methane (CH<sub>4</sub>) and nitrous oxide (N<sub>2</sub>O) from biofuel combustion are included in the inventory along with CO<sub>2</sub> from fossil fuel combustion.

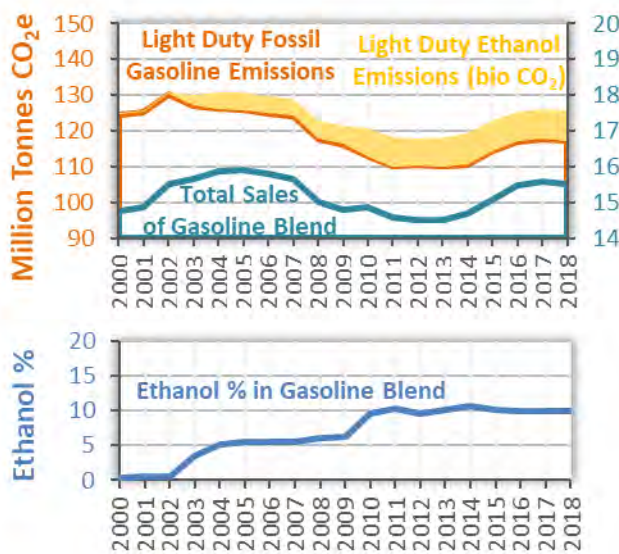


**Figure 6. Trends in On-Road Light Duty Gasoline Emissions.** In the top panel, the yellow shaded region represents CO<sub>2</sub> emissions from the ethanol-component of the gasoline fuel blend. The orange line includes all GHG emissions from the fossil gasoline component of the fuel blend, as well as the CH<sub>4</sub> and N<sub>2</sub>O emissions from the ethanol-component of the fuel blend. "Total Sales of Gasoline Blend" includes gasoline used in any types of vehicles, 93% of which are used in light duty vehicles. The color of a trend line matches the color of its corresponding vertical axes label. The bottom panel shows the percent of gasoline blend that is ethanol.

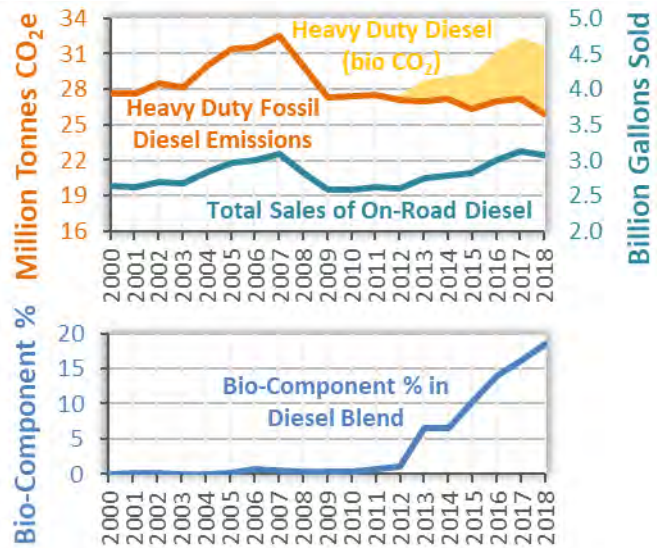


**Figure 7. Trends in On-Road Diesel Vehicle Emissions.** In the top panel, the yellow shaded region represents CO<sub>2</sub> emissions from the bio-component (biodiesel and renewable diesel) of the diesel fuel blend. The orange line includes all GHG emissions from the fossil diesel component of the fuel blend, as well as the CH<sub>4</sub> and N<sub>2</sub>O emissions from the bio-component of the fuel blend. "Total Sales of On-Road Diesel " includes diesel blends used in any types of vehicles, 97% of which are used in heavy duty vehicles. The color of a trend line matches the color of its corresponding vertical axes label. The bottom panel shows the percent of diesel blend that are biodiesel or renewable diesel.

Emissions from transportation sources declined from 2007 to 2013, followed by four consecutive years of annual increases through 2017. Transportation emissions dropped by 1.5 MMTCO<sub>2</sub>e in 2018. Sales of gasoline fuel blend decreased more than 60 million gallons, while ethanol blending increased by 15 million gallons. Diesel fuel blend sales decreased 50 million gallons, while sale and blending of biodiesel and renewable diesel increased by more than 60 million gallons. Emissions from gasoline used in on-road passenger cars, trucks, and SUVs are 74 percent of the transportation inventory and had been the main driver of the increases between 2013 and 2017.

A combination of factors influences on-road transportation emissions. Regulations, improved fuel efficiency of the state's vehicle fleet, and higher market penetration of zero-emission vehicles can drive down consumption and emissions over time; but population growth, lower fuel prices, more consumer activity, and higher overall employment are factors that may increase fuel use. Biofuels such as ethanol, biodiesel, and renewable diesel displace fossil fuels and reduce the amount of fossil-based CO<sub>2</sub> emissions released into the atmosphere. The percentages of biodiesel and renewable diesel in the total diesel blend have shown significant growth in recent years, growing from 0.5 percent in 2011 to 18.5 percent in 2018, due mostly to the implementation of the Low Carbon Fuel Standard.

## Electric Power

Emissions from the electric power sector comprise 15 percent of 2018 statewide GHG emissions. The GHG emission inventory divides the electric power sector into two broad categories: emissions from in-state power generation (including the portion of industrial and commercial cogeneration emissions attributed to electricity generation) and emissions from imported electricity.

Since the early 2000's, the development of renewable and less carbon-intensive resources have facilitated the continuing decline in fossil fuel electricity generation. The Renewable Portfolio Standard (RPS) Program and the Cap-and-Trade Program continue to incentivize the dispatch of renewables over fossil generation to serve California load. Higher energy efficiency standards also reduce growth in electricity consumption driven by a growing population and economy. However, year-to-year fluctuations in hydropower availability may result in small increases in carbon intensity in some years. Figures 8 and 9 show California's electricity emissions and GHG intensities of electricity generation over time.

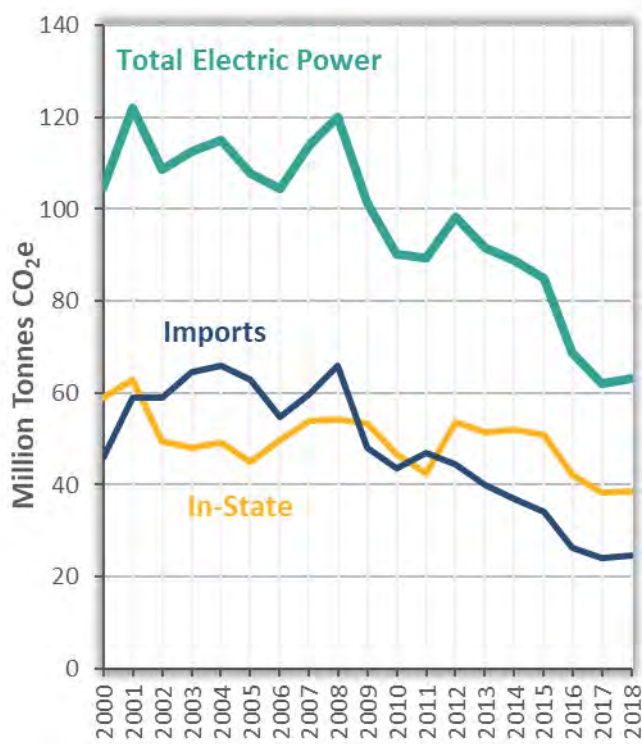


**Figure 8. GHG Emissions from the Electric Power Sector.** This figure shows trends in emissions of in-state electricity generation, emissions associated with electricity imported from outside of California, and the total electric power sector emissions, which is the sum of in-state generation and imports.

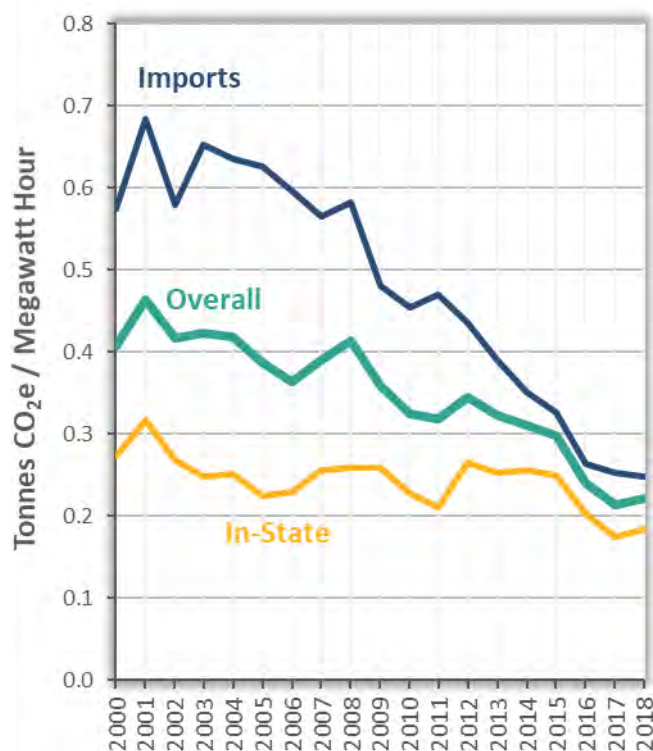


**Figure 9. GHG Intensity of Electricity Generation.<sup>d</sup>** This figure shows trends in GHG intensities of electricity generated by in-state power plants, electricity imported from outside of California, and the overall GHG intensities aggregating both in-state generation and electricity imports.

<sup>d</sup> All three GHG intensities account for renewables and exclude biogenic CO<sub>2</sub> emissions. For calculating in-state and overall intensities, in-state electricity emissions and generation (MWh) include on-site generation for on-site use, cogeneration emissions attributed to electricity generation, in-state generated electricity exported out of state, and rooftop solar. The denominator of overall intensity is the total electricity (MWh) consumed in and exported from California, and excludes electricity (MWh) lost during transmission and distribution.

From 2017 to 2018, electric power emissions increased by 1 MMTCO<sub>2e</sub>, primarily due to a 39 percent decrease in in-state hydropower generation (a result of lower precipitation levels in the 2017-2018 winter season) that was partially compensated by increases in solar generation and other lower GHG intensity resources. In 2018, 44 percent of total electricity generation (in-state generation plus imported electricity) came from solar, wind, hydropower, and nuclear power; and another five percent came from Asset Controlling Suppliers<sup>e</sup>, which imported low GHG intensity electricity consisting primarily hydropower.

In-state solar generation grew 14 percent in 2018 compared to 2017. Between 2011 and 2018, in-state solar generation saw significant growth as rooftop photovoltaic solar generation increased eight-fold [11] and total solar generation (commercial-scale plus rooftop solar) increased by a factor of 15 during that period [11] [12]. In-state wind energy generation ramped up through 2013, but its trend has remained relatively constant since 2013 [12]. Figure 10 shows trends in in-state hydro, solar, and wind electricity generation.

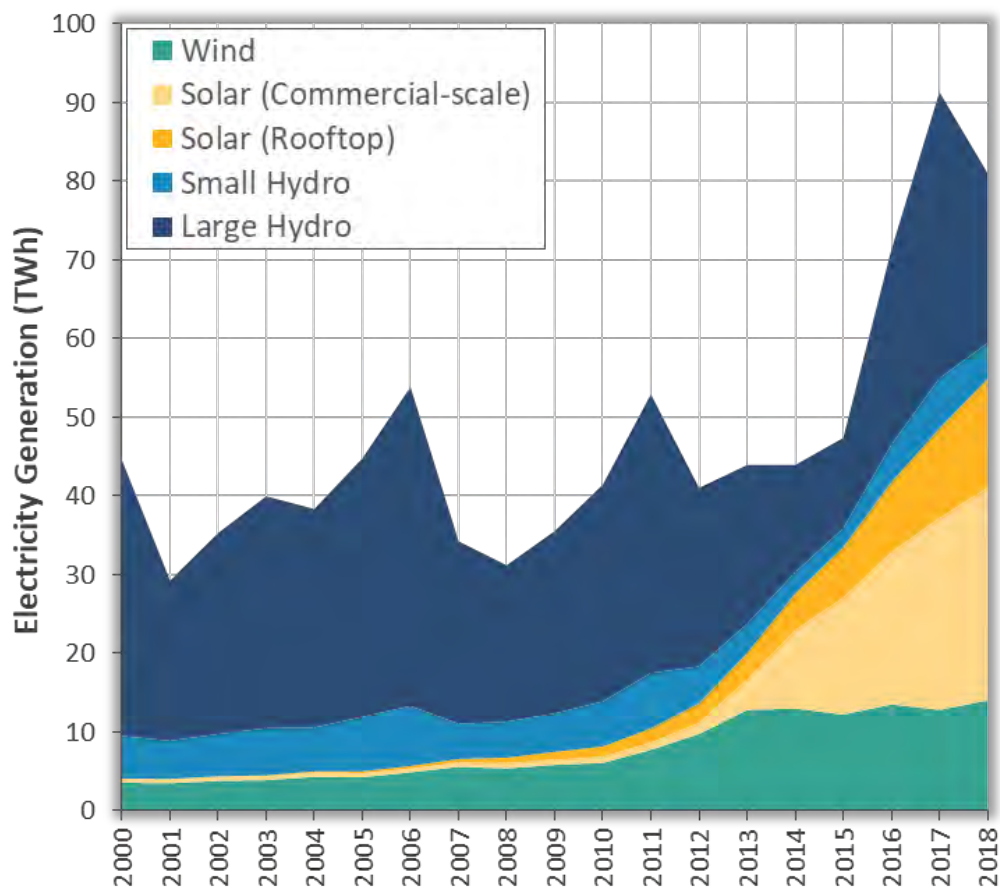


**Figure 10. In-State Hydro, Solar, and Wind Electricity Generation.** This figure shows the amounts of electricity generated by California’s in-state wind power projects, large commercial-scale solar power projects, rooftop solar panels, and hydropower generation stations. The units are in terawatt-hour (1 TWh = 10<sup>9</sup> kWh).

<sup>e</sup> “Asset Controlling Suppliers” are as defined by the Mandatory GHG Reporting Regulation (MRR). The term refers to an electric power entity that owns or operates inter-connected electricity generating facilities or serves as an exclusive marketer for these facilities even though it does not own them. Imports from ACS are primarily hydropower, but include some non-zero GHG power sources such as natural gas.

Trends in the types of in-state generation are presented in Figure 11. In-state natural gas generation complements the year-to-year fluctuations in hydro, solar, wind, and nuclear power, while generation from other fuel types gradually decline over time.

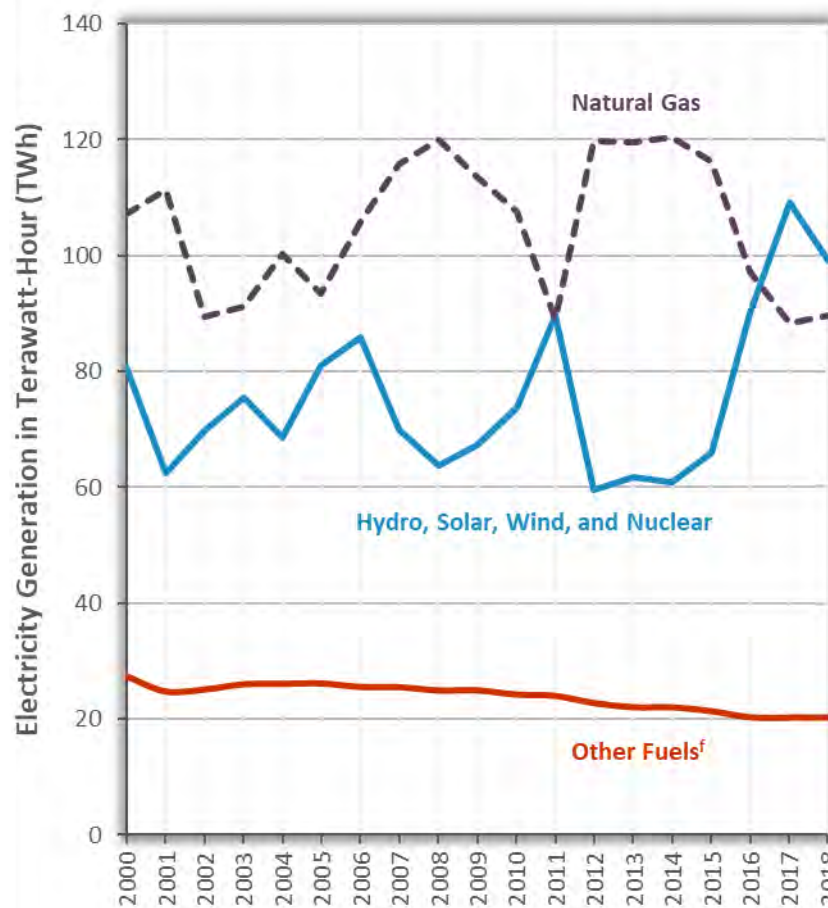


**Figure 11. In-State Electricity Generation by Fuel Type.** This figure shows the amounts of electricity generated by in-state natural gas power plants, hydro/solar/wind/nuclear resources, and other generation sources. The units are in terawatt-hour (1 TWh = 10<sup>9</sup> kWh).

<sup>f</sup> "Other Fuels" include energy generation from associated gas, biomass, coal, crude oil, digester gas, distillate, geothermal, jet fuel, kerosene, landfill gas, lignite coal, municipal solid waste (MSW), petroleum coke, propane, purchased steam, refinery gas, residual fuel oil, sub-bituminous coal, synthetic coal, tires, waste coal, waste heat, and waste oil. CO<sub>2</sub> and CH<sub>4</sub> emissions from geothermal power and CH<sub>4</sub> and N<sub>2</sub>O emissions from biomass power are included in the statewide total for comparing to the 2020 GHG Limit. Except for geothermal power, most of these fuels are combusted in industrial cogeneration facility.

Trends in the types of imported electricity are presented in Figure 12 [13]. In 2018, imports of hydro, solar, wind, and nuclear energy grew nine percent while imports of coal energy dropped 21 percent. Comparing to 2011 levels, imports of hydro, solar, wind, and nuclear energy nearly tripled, while imports of coal energy dropped by 67 percent.<sup>8</sup>

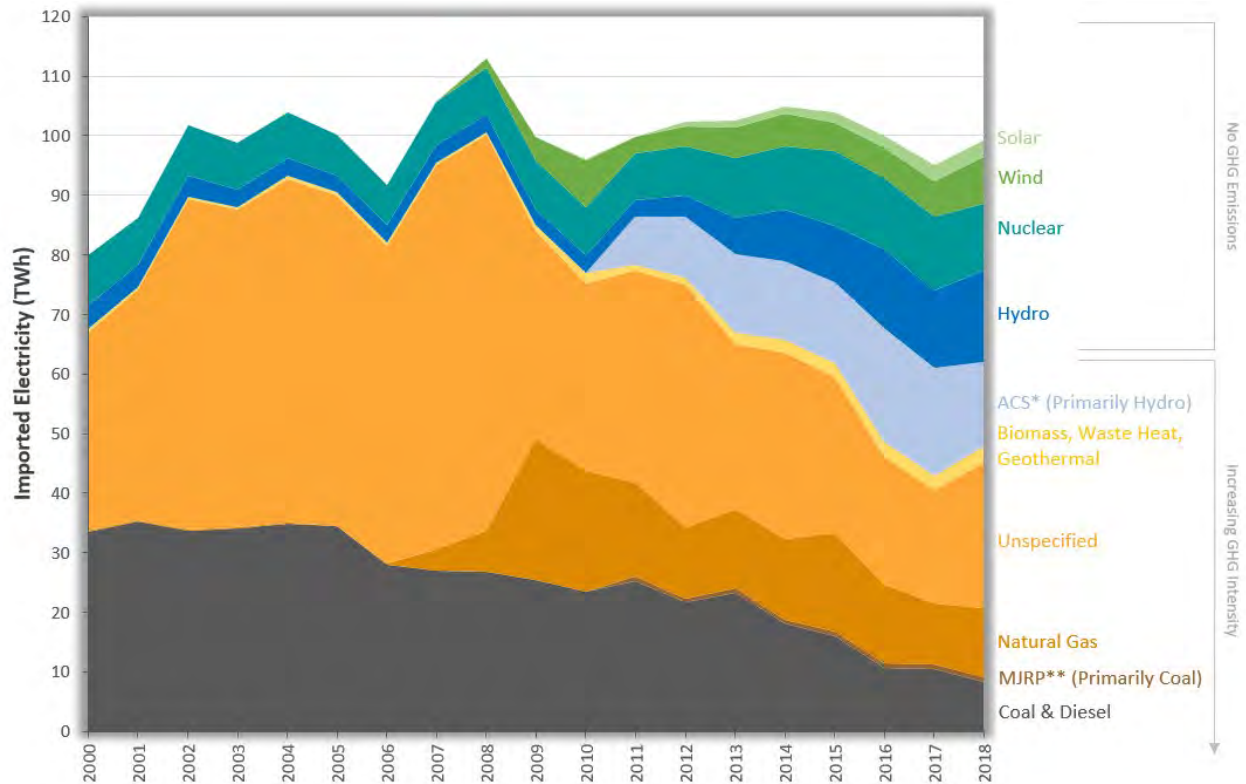


**Figure 12. Imported Electricity by Generation Type.** This figure shows the amounts of imported electricity by generation type. Non-emitting resources are on the top and include hydro, nuclear, wind, and solar. Asset Controlling Suppliers (ACS) and Multi-Jurisdictional Retail Provider (MJRP) are as defined by the Mandatory GHG Reporting Regulation (MRR) [13]. \*Imports from ACS are primarily hydropower, but include some GHG-emitting power sources such as natural gas. \*\*Imports from MJRP are primarily coal, but include other types of generation resources. The units are in terawatt-hour (1 TWh = 10<sup>9</sup> kWh).

<sup>8</sup> All claims of non-GHG-emitting imports are subject to third party verification to ensure against resource shuffling.

## Industrial

Emissions from the industrial sector contributed 21 percent of California’s total GHG emissions in 2018. Emissions in this sector are primarily driven by fuel combustion from sources that include refineries, oil & gas extraction, cement plants, and the portion of cogeneration emissions attributed to thermal energy output. Process emissions, such as from clinker production in cement plants and hydrogen production for refinery use, also contribute significantly to the total emissions. Refineries and hydrogen production represent the largest individual source in the industrial sector, contributing 34 percent of the sector’s total emissions. Refining and hydrogen production sector emissions have remained relatively constant in the past few years. Figure 13 shows emissions trends of the industrial sector over time.

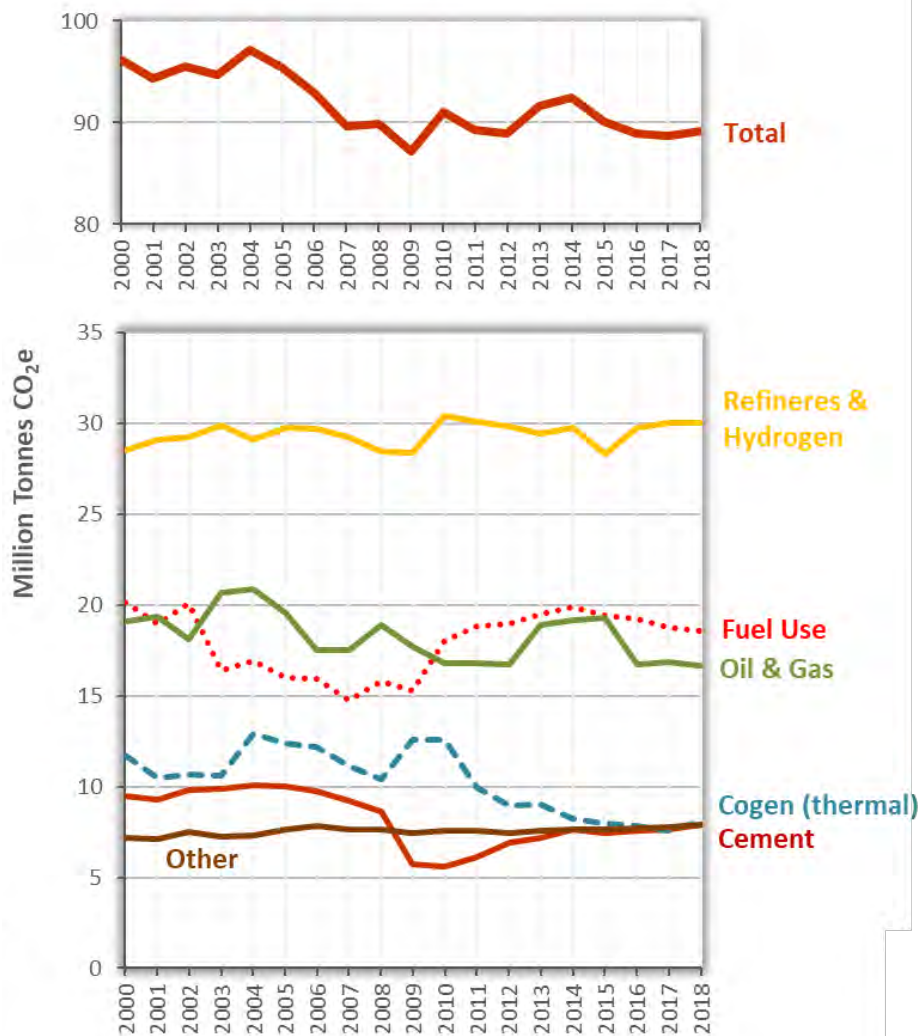


**Figure 13. Industrial Sector Emissions.** The top panel of this figure shows the overall emissions trend of the total industrial sector. The bottom panel shows emissions trends by sub-sector. Summing the bottom panel will equal the top panel. The “General Fuel Use” category includes emissions from combustion of fuels used by sectors not specifically broken out elsewhere in this figure. The “Other” category includes fugitive and process emissions (e.g., GHG released from chemical reaction during manufacturing process) from industrial sectors. In accordance with the IPCC Guidelines, the “Cogen (thermal)” category under the industrial sector includes only the portion of cogeneration emissions attributed to the total thermal output of cogeneration. The portion of cogeneration emissions attributed to electricity generation is assigned to the electric power sector and not shown in this graph.

## Commercial and Residential Fuel Combustion

Greenhouse gas emissions from the commercial and residential sectors are dominated by the combustion of natural gas and other fuels for household and commercial business use, such as space heating, cooking, and hot water or steam generation. Emissions from electricity used for cooling (air-conditioning) and appliance operation are accounted for in the Electric Power sector. In this report, using the Scoping Plan categorization, emissions from refrigerants use in commercial and residential buildings are presented in the high-GWP gases category. Changes in annual fuel combustion emissions are primarily driven by variability in weather conditions and the need for heating in buildings, as well as population growth. In 2018, emissions increased slightly compared to 2017 due to a rise in commercial natural gas use. Figure 14 presents emissions from the commercial and residential sectors, along with heating degree days, an estimate of the heating energy need in a given year.

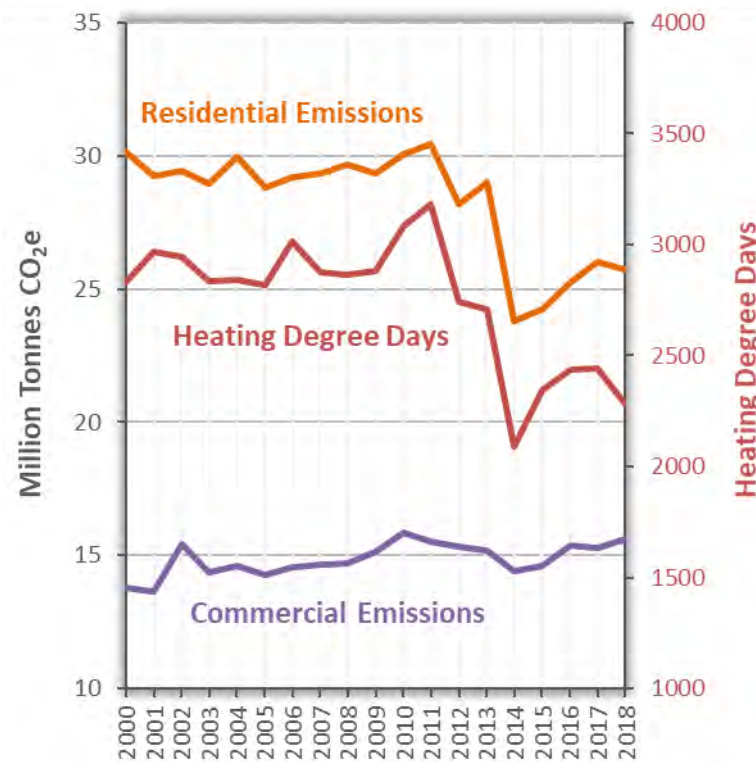


**Figure 14. Emissions from Residential and Commercial Sectors.** Emissions from the residential and commercial sectors are compared with heating degree days, an estimate of the heating energy need in a given year.

Emissions from fuel use by the commercial sector have grown by 13 percent since 2000; however, during the same period, commercial floor space grew by 27 percent. As a result, the commercial sector also exhibits a slight decline in fuel use per unit space. The number of occupied residential housing units grew steadily from 11.9 million units in 2000 to 13.1 million units in 2018 [14]. Emissions per housing unit generally fluctuate with the need for heating depending the winter temperatures of the given year, which is also illustrated by the heating degree day index in Figure 14 [15]. Figures 15a and 15b show emissions from these sectors and the related indicators.

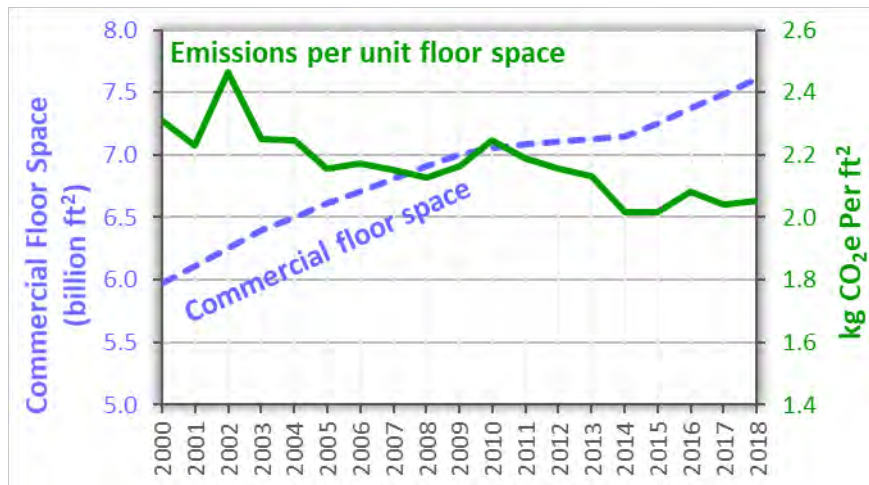


**Figure 15a. Emissions per Unit Floor Space.** The figure shows total square feet of commercial floor space and the emissions per square feet of commercial floor space.



**Figure 15b. Emissions per Residential Housing Unit.** The figure shows number of occupied residential housing units and emissions per housing unit.

## Agriculture

California's agricultural sector contributed approximately eight percent of statewide GHG emissions in 2018, mainly from CH<sub>4</sub> and N<sub>2</sub>O sources. Sources include enteric fermentation and manure management from livestock, crop production (fertilizer use, soil preparation and disturbance, and crop residue burning), and fuel combustion associated with agricultural activities (water pumping, cooling or heating buildings, and processing commodities).

Approximately 70 percent of agricultural sector greenhouse gases are emitted from livestock. Livestock emissions in 2018 are 19 percent higher than 2000 levels. Livestock emissions are almost entirely CH<sub>4</sub> generated from enteric fermentation and manure management, and most of the livestock emissions are from dairy operations. GHG emissions from dairy manure management and enteric fermentation followed an increasing trend between 2000 and 2007, and year-to-year changes since 2007 have been relatively small.

Crop production accounted for 20 percent of agriculture emissions in 2018. Emissions from the growing and harvesting of crops have generally followed a declining trend since 2000. The long-term trend of emissions reduction from 2000 to 2018 corresponds to a reduction in crop acreage (which leads to an associated decrease in synthetic fertilizer use) [16] and large-scale changes in irrigation management practices. Specifically, California agriculture has been shifting from flood irrigation towards sprinkler and drip irrigation. The increase from 2017 to 2018 is due to climatic factors that affect the amount of N<sub>2</sub>O produced from synthetic fertilizer (e.g. precipitation and min/max temperature). Figure 16 presents emissions from the livestock and crop production sectors.

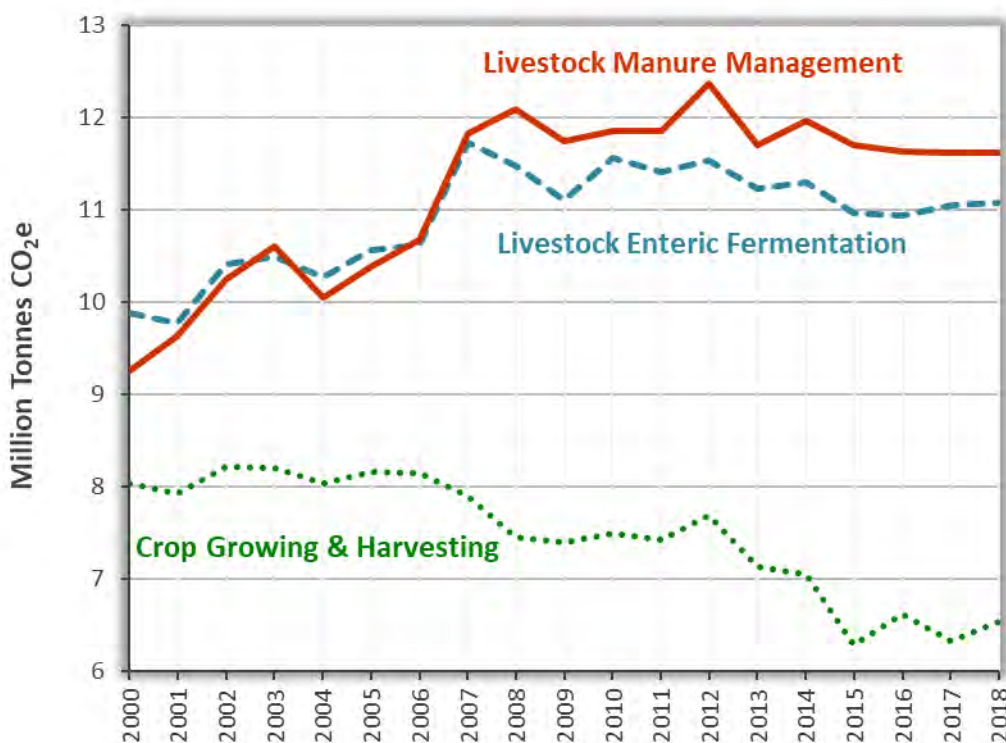


**Figure 16. Agricultural Emissions.** This figure presents the trends in emissions from livestock manure management and enteric fermentation, as well as emissions from crop growing and harvesting, which include fertilizer application, soil preparation and disturbances, and crop residue burning.

## High Global Warming Potential Gases

In 2018, High Global Warming Potential (high-GWP) gases comprised 4.8 percent of California's emissions. The GHG inventory tracks high-GWP gas emissions from releases of ozone depleting substance (ODS) substitutes, SF<sub>6</sub> emissions from the electricity transmission and distribution system, and gases that are emitted in the semiconductor manufacturing process. (ODSs are also high-GWP gases, but are outside the scope of the IPCC accounting framework and AB 32.) Of these tracked categories, 98 percent of high-GWP gas emissions are ODS substitutes, which are primarily hydrofluorocarbons (HFCs). ODS substitutes are used in refrigeration and air conditioning equipment, solvent cleaning, foam production, fire retardants, and aerosols. In 2018, refrigeration and air conditioning equipment contributed 91 percent of ODS substitutes emissions.

Emissions of ODS substitutes are expected to continue to grow as they replace ODS being phased out under the Montreal Protocol [5]. Emissions of ODS have decreased significantly since they began to be phased out in the 1990s and dropped below ODS substitutes emissions for the first time in 2015. ODS emissions continued to drop in 2018. The combined emissions of ODS and ODS substitutes have been steadily decreasing over time as ODS are phased out, even as emissions from ODS substitutes continue to increase. Of the four main sub-sectors within the ODS substitutes category (Transportation, Commercial, Industrial, and Residential), only the Transportation Sector has seen an emissions decrease. The transportation refrigeration units (TRU) Airborne Toxic Control Measure adopted in 2004 has reduced transportation sector emissions by limiting the charge size of TRUs beginning in January 2010, reducing leakage rates, and lowering end-of-life losses for passenger vehicle air conditioning systems [17]. Figures 17a and 17b show ODS substitute's emissions.

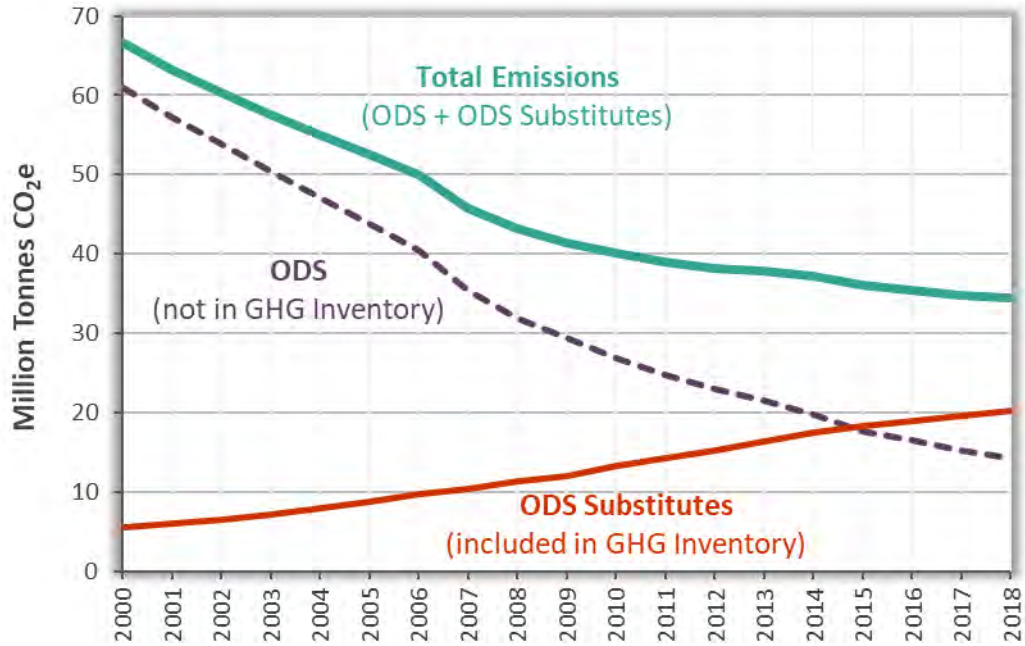


**Figure 17a. Trends in ODS and ODS Substitutes Emissions.** This figure presents the trends in emissions from ODS Substitutes, ODS, and their sum (“Total Emissions”). ODS Substitutes emissions are specified in IPCC Guidelines and AB 32 and are included in the inventory. ODS are also GHGs, but are tracked separately outside of the inventory.

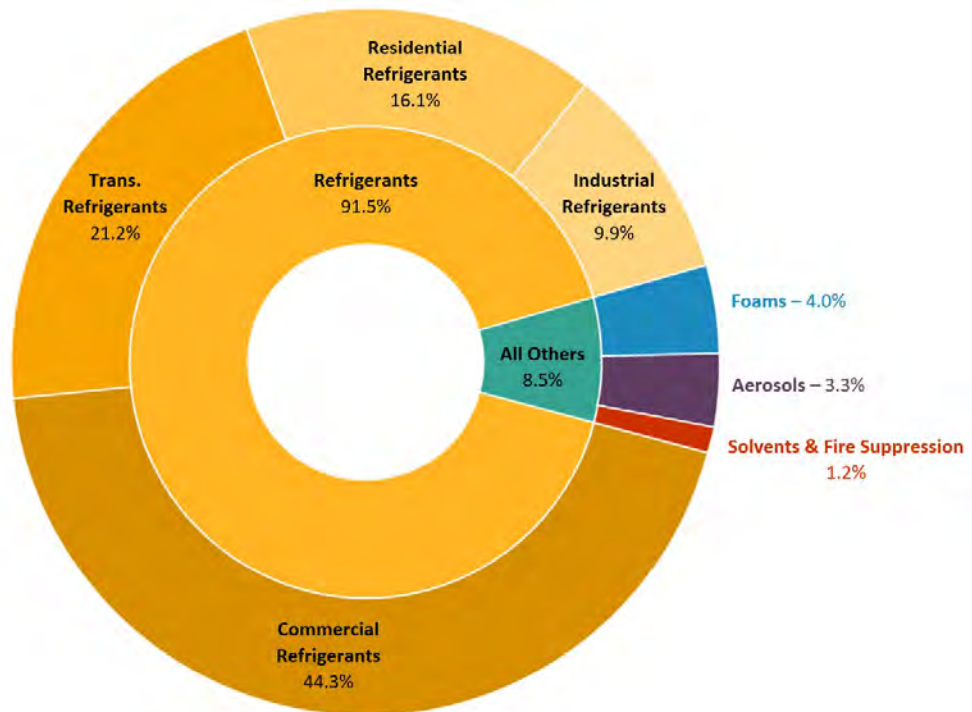


**Figure 17b. ODS Substitutes Emissions by Category.** This figure presents the breakdown of ODS substitutes emissions by product type and sector category in 2018. Refrigerants used in various sectors make up the majority of ODS substitutes emissions.

## Recycling and Waste

Emissions from the recycling and waste sector include CH<sub>4</sub> and N<sub>2</sub>O emissions from landfills and from commercial-scale composting. Emissions from recycling and waste, which comprise two percent of California’s GHG inventory, have grown by 19 percent since 2000. Landfill emissions are primarily CH<sub>4</sub>, and they account for 96 percent of the emissions in this sector,<sup>h</sup> while compost production facilities make up the remaining fraction of emissions.

The amount of emissions from a landfill is the difference between the methane generated from waste decomposition and the methane captured by landfill gas collection and control system. The annual amount of solid waste deposited in California’s landfills grew from 39 million short tons in 2000 to its peak of 46 million short tons in 2005, followed by a declining trend until 2012, after which deposited waste amounts have seen a steady rise over time [18]. Landfill methane generation is driven by the total waste-in-place, an accumulation of degradable carbon in the solid waste stream, rather than year-to-year fluctuation in annual deposition of solid waste [19]. Figures 18 and 19 show trends in landfill emissions and activities that drive emissions.

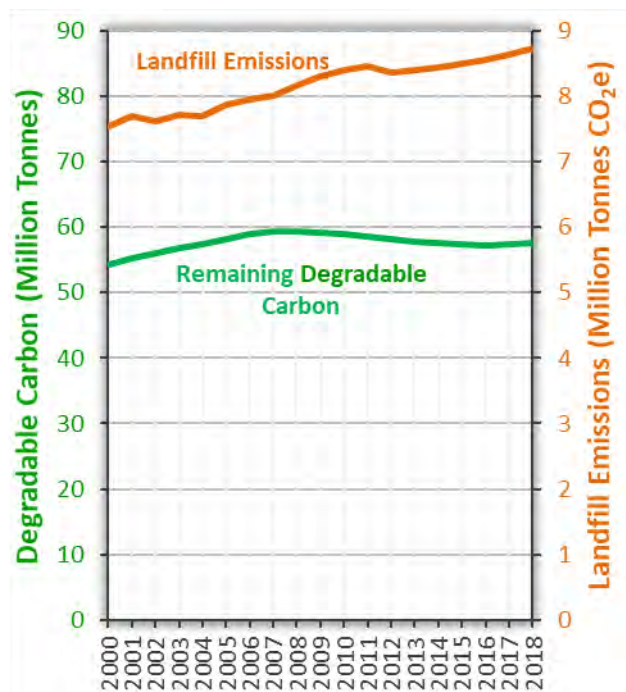


**Figure 18. Landfill Methane Emissions.** This figure presents trends in landfill emissions and the amount of degradable carbon remaining in California landfills. The latter drives the amount of emissions generated by landfills. The color of a trend line matches the color of its corresponding vertical axes label.

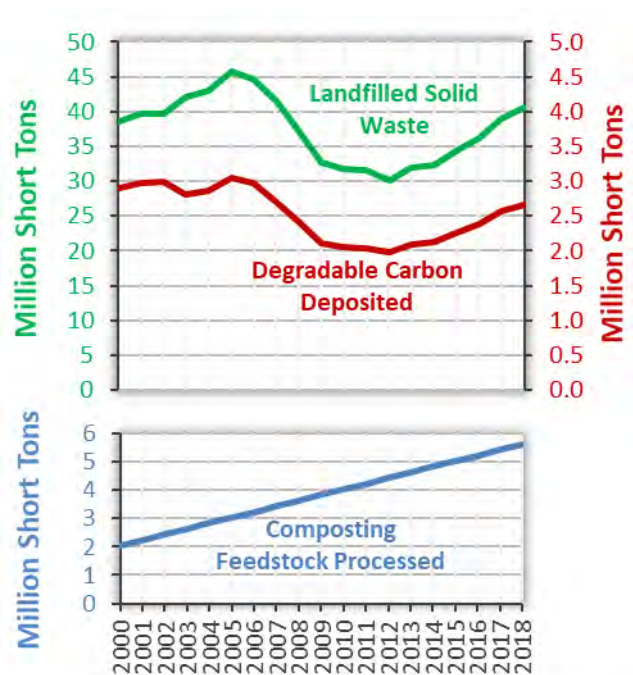


**Figure 19. Landfill Waste.** The top panel presents the annual amounts of solid waste deposited into California landfills and the amount of degradable carbon contained in the solid waste. The color of a trend line matches the color of its corresponding vertical axes label. The bottom panel shows estimated amounts of compost feedstock processed by the state’s composting facilities.

<sup>h</sup> CARB’s GHG inventory methodology has been using an assumption of 75 percent methane capture efficiency, consistent with common practice nationally.

## Additional Information

---

### ***International GHG Inventory Practice of Recalculating Emissions for Previous Years***

Consistent with the IPCC GHG inventory guidelines, recalculations are made to incorporate new methods or reflect updated data for all years from 2000 to 2017 to maintain a consistent inventory time series. Therefore, emission estimates for a given calendar year may be different between editions as methods and supplemental data are updated. For example, in the 2019 edition, total 2017 emissions were estimated to be 424.1 MMTCO<sub>2</sub>e. In the 2020 edition, recalculation revised the 2017 emissions to 424.3 MMTCO<sub>2</sub>e, reflecting refinements and updates to methodology and information gained since 2019. Analyses of emission trends, including the emissions increase of 1.0 MMTCO<sub>2</sub>e between 2017 and 2018, are based on the recalculated numbers in the 2020 edition of the inventory. A description of the method updates can be found here:

[https://ww3.arb.ca.gov/cc/inventory/pubs/reports/2000\\_2018/ghg\\_inventory\\_00-18\\_method\\_update\\_document.pdf](https://ww3.arb.ca.gov/cc/inventory/pubs/reports/2000_2018/ghg_inventory_00-18_method_update_document.pdf)

### ***Global Warming Potential Values***

In accordance with the IPCC GHG inventory guidelines, California's GHG Inventory uses the 100-year GWPs from the IPCC 4th Assessment Report, consistent with the national GHG inventories submitted by the U.S. and other nations to the UNFCCC. However, other CARB programs may use different GWP values. For example, the SLCP Reduction Strategy [4] uses a 20-year GWP because the SLCP has greater climate impact in the near-term compared to the longer-lived GHGs, such as CO<sub>2</sub>.

### ***Sources of Data Used in the GHG Emission Inventory***

Statewide GHG emissions are calculated using several data sources. One data source is from reports submitted to the California Air Resources Board (CARB) through the Regulation for the Mandatory Reporting of GHG Emissions (MRR). MRR requires facilities and entities with more than 10,000 metric tons CO<sub>2</sub>e per year of combustion and process emissions, all facilities belonging to certain industries, and all electricity importers to submit an annual GHG emissions data report directly to CARB. Reports from facilities and entities that emit more than 25,000 metric tons of CO<sub>2</sub>e per year are verified by a CARB-accredited third-party verification body. More information on MRR emissions reports can be found at: <https://ww2.arb.ca.gov/mrr-data>

CARB also relies on data from other California State and federal agencies to develop the annual statewide GHG emission inventory for the State of California. These additional sources include, but are not limited to, data from the California Energy Commission, California Department of Tax and Fee Administration, California Geologic Energy Management Division, Department of Food and Agriculture, CalRecycle, U.S. Energy Information Administration, and U.S. Environmental Protection Agency (U.S. EPA). All data sources used to develop the GHG Inventory are listed in the GHG Emission Inventory supporting documentation at:

<https://ww2.arb.ca.gov/ghg-inventory-data>

The main GHG inventory page is located at:

<https://ww2.arb.ca.gov/our-work/programs/ghg-inventory-program>

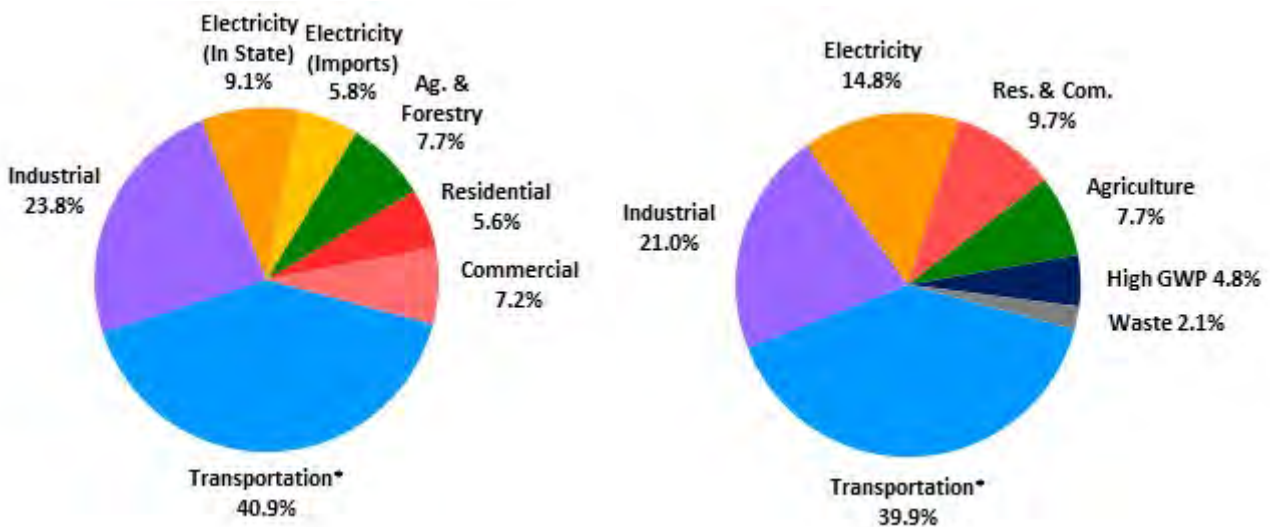
## Other Ways of Categorizing Emissions in the Inventory

There is more than one way of organizing emissions by category in an inventory. Each year, CARB makes the GHG inventory available in three categorization schemes:

- The Scoping Plan Categorization organizes emissions by CARB program structure. (This is the categorization scheme used in this report.)
- The Economic Sector/Activity Categorization generally aligns with how sectors are defined in the North America Industry Classification System (NAICS).
- The IPCC Categorization groups emissions into four broad categories of emission processes. This format conforms to international GHG inventory practice and is consistent with the national GHG inventory that U.S. EPA annually submits to the United Nations.

Although this report uses the Scoping Plan Categorization in the presentation and discussion of emissions, the Economic Sector/Activity Categorization is also often used by the public. The difference between the Scoping Plan Categorization and the Economic Sector/Activity Categorization are as follows: (1) High-GWP gases are shown as its own category under the Scoping Plan categorization, but under the economic sector categorization, they are included as part of the economic sectors where they are used. (2) The recycling and waste sector is shown as its own category under the Scoping Plan categorization but is included as part of the industrial sector under the Economic Sector/Activity Categorization.

The figures below show the Scoping Plan Categorization and the Economic Sector/Activity Categorization side-by-side. Detailed data for these categorization schemes can be accessed from CARB webpage at: <https://ww2.arb.ca.gov/ghg-inventory-data>



\*The transportation sector represents tailpipe emissions from on-road vehicles and direct emissions from other off-road mobile sources. It does not include emissions from petroleum refineries and oil production, which are included in the industrial sector.

\*\*Percentages may not add up to 100 percent due to rounding.

**Figure 20a\*\*. 2018 GHG Emissions by Economic Sector.** This figure shows the relative size of 2018 emissions by economic sector.

**Figure 20b. 2018 GHG Emissions by Scoping Plan Category.** This figure shows the relative size of 2018 emissions, organized by the categories in the AB32 Scoping Plan.

### ***Uncertainties in the Inventory***

CARB is committed to continually working to reduce the uncertainty in the inventory estimates. The uncertainty of emissions estimates in the inventory varies by sector. The data reported under MRR is subject to third-party verification, ensuring a high level of accuracy. Other non-MRR sources, mainly non-combustion, biochemical processes, have varying uncertainty depending on the input data and the emission processes.

### ***Natural and Working Lands Ecosystem Carbon Inventory and Wildfire Emissions***

CARB has also developed a Natural and Working Lands (NWL) Ecosystem Carbon Inventory (“the NWL Inventory”) separate from this GHG Inventory [1]. The NWL Inventory quantifies ecosystem carbon stored in plants and soils in California’s Natural and Working Lands (including forest, woodland, shrubland, grassland, wetland, orchard crop, urban forest, and soils) and tracks changes in carbon stock over time. The NWL inventory report can be accessed here: <https://ww2.arb.ca.gov/nwl-inventory>.

Fire has served a natural function in California's diverse ecosystems for millennia, such as facilitating germination of seeds for certain tree species, replenishing soil nutrients, clearing dead biomass to make room for living trees to grow, and reducing accumulation of fuel that lead to high-intensity wildfires. Fire also impacts human health and safety, and releases GHGs and other air pollutants. Greenhouse gas emissions from wildfires are tracked separately when compared to anthropogenic sources due to carbon cycling. Anthropogenic emissions from fossil fuels come from geological sources, which are part of the slow carbon cycle, where carbon pools change over the course of many millennia (e.g., fossil fuel formation). In contrast, the fast carbon cycle, in which carbon moves between pools over months to centuries, includes natural emission sources, such as wildfires, plant decomposition and respiration. The depletion of fossil fuels through their combustion has led to an increase in ambient CO<sub>2</sub> concentrations; however, wildfire emissions are part of a fast carbon cycle that is balanced by vegetation growth. In recent years the frequency and magnitude of wildfires have been prolific across California. In an effort to contextualize the GHG emissions from wildfires, emissions estimations are available here: <https://ww2.arb.ca.gov/wildfire-emissions>

## Figure References

Figure Number	Reference
Figure 1	[9]
Figure 2a	[8] [9] [10]
Figure 2b	[8] [9]
Figure 2c	[9] [10]
Figure 3	[9]
Figure 4	[9]
Figure 5	[9]
Figure 6	[9]
Figure 7	[9]
Figure 8	[9]
Figure 9	[9] [11] [12]
Figure 10	[11] [12]
Figure 11	[11] [12]
Figure 12	[13]
Figure 13	[9]
Figure 14	[9] [15]
Figure 15a	[9] [14]
Figure 15b	[9] [14]
Figure 16	[9]
Figure 17a & 17b	[9] [17]
Figure 18	[9]
Figure 19	[9] [18]
Figure 20a & 20b	[9]

## Reference

---

- [1] California Air Resources Board, "An Inventory of Ecosystem Carbon in California's Natural & Working Lands," 2018. [Online]. Available: [https://ww3.arb.ca.gov/cc/inventory/pubs/nwl\\_inventory.pdf](https://ww3.arb.ca.gov/cc/inventory/pubs/nwl_inventory.pdf).
- [2] Intergovernmental Panel on Climate Change, "IPCC Guidelines for National greenhouse Gas Inventories, Volume 1 - General Guidance and Reporting," [Online]. Available: <https://www.ipcc-nggip.iges.or.jp/public/2006gl/vol1.html>.
- [3] State of California, "California Health and Safety Code, Division 25.5, Part 1, Chapter 3, Section 38505(g)," 2006. [Online]. Available: [https://leginfo.legislature.ca.gov/faces/billNavClient.xhtml?bill\\_id=200520060AB32](https://leginfo.legislature.ca.gov/faces/billNavClient.xhtml?bill_id=200520060AB32).
- [4] California Air Resources Board, "Short-Lived Climate Pollutant (SLCP) Strategy," 2017. [Online]. Available: <https://www.arb.ca.gov/cc/shortlived/shortlived.htm>.
- [5] United Nations Environmental Programme, "Treaties and Decisions - The Montreal Protocol on Substances that Deplete the Ozone Layer," 2015. [Online]. Available: <http://ozone.unep.org/en/treaties-and-decisions/montreal-protocol-substances-deplete-ozone-layer>. [Accessed 14 June 2019].
- [6] California Air Resources Board, "First Update to the Climate Change Scoping Plan Building on the Framework Pursuant to AB32: California's Global Warming solutions Act 2006," 2014. [Online]. Available: [https://ww2.arb.ca.gov/sites/default/files/classic//cc/scopingplan/2013\\_update/first\\_update\\_climate\\_change\\_scoping\\_plan.pdf](https://ww2.arb.ca.gov/sites/default/files/classic//cc/scopingplan/2013_update/first_update_climate_change_scoping_plan.pdf).
- [7] Intergovernmental Panel on Climate Change, "Fourth Assessment Report," 2007. [Online]. Available: <https://www.ipcc.ch/assessment-report/ar4/>.
- [8] California Department of Finance, "E-6. Population estimates and components of change by county 2010-2019," 2019. [Online]. Available: <http://www.dof.ca.gov/Forecasting/Demographics/Estimates/E-6/>.
- [9] California Air Resources Board, "GHG Emissions Inventory (GHG EI) 2000-2018," 2020. [Online]. Available: <https://ww2.arb.ca.gov/ghg-inventory-data>.
- [10] California Department of Finance, "California Gross Domestic Product," 2020. [Online]. Available: [http://www.dof.ca.gov/Forecasting/Economics/Indicators/Gross\\_State\\_Product/](http://www.dof.ca.gov/Forecasting/Economics/Indicators/Gross_State_Product/).
- [11] Gautam, A, Personal Communication Between the California Air Resources Board (L. Hunsaker) and the California Energy Commission (A. Gautam), 2020.
- [12] U.S. Energy Information Administration, "Electricity - Form EIA-923 Detailed Data with Previous Form Data (EIA-906/920)," 2020. [Online]. Available: <https://www.eia.gov/electricity/data/eia923/>.

- [13] California Air Resources Board, "Summary of 2008 to 2018 Data from California's Greenhouse Gas Mandatory Reporting Program," 2019. [Online]. Available: <https://ww2.arb.ca.gov/mrr-data>.
- [14] U.S. Census Bureau, "Annual Estimates of Housing Units for the United States and States: April 1, 2020 to July 1, 2019," 15 May 2020. [Online]. Available: <https://www.census.gov/data/datasets/time-series/demo/popest/2010s-total-housing-units.html>.
- [15] National Oceanic and Atmospheric Administration, "Heating and Cooling Degree Days," 2020. [Online]. Available: [ftp://ftp.cpc.ncep.noaa.gov/htdocs/products/analysis\\_monitoring/cdus/degree\\_days/archives/Heating%20degree%20Days/monthly%20states/](ftp://ftp.cpc.ncep.noaa.gov/htdocs/products/analysis_monitoring/cdus/degree_days/archives/Heating%20degree%20Days/monthly%20states/).
- [16] U.S. Department of Agriculture, "National Agricultural Statistics Service," 2020. [Online]. Available: <https://quickstats.nass.usda.gov/>.
- [17] G. Gallagher, T. Zhan, Y.-K. Hsu, P. Gupta, J. Pederson, B. Croes, D. R. Blake, B. Barletta, S. Meindardi, P. Ashford, A. Vetter, S. Saba, R. Slim, L. Palandre, D. Clodic, P. Mathis, M. Wagner, J. Forgie, H. Dwyer and K. Wolf, "High-Global Warming Potential F-Gas Emissions in California: Comparison of Ambient-Based Versus Inventory-Based Emission Estimates, and Implications of Refined Estimates," *Environmental Science & Technology*, pp. 1084-1093, 21 January 201.
- [18] CalRecycle, "Landfill Tonnage Reports, 2000-2016," 2020. [Online]. Available: <https://www2.calrecycle.ca.gov/LandfillTipFees/>.
- [19] Intergovernmental Panel on Climate Change, "IPCC Guidelines for National Greenhouse Gas Inventories, Volume 5 - Waste: IPCC Waste Model," 2006. [Online]. Available: <https://www.ipcc-nggip.iges.or.jp/public/2006gl/vol5.html>.

## Solar Battery Comparison Chart



The comparison table below lists the latest Lithium battery systems available on the Australian, North American and Asian markets from the leading manufacturers. Table includes AC-coupled battery systems, high and low voltage DC-coupled batteries of the managed (CANbus) and self-managed varieties used for either hybrid or off-grid solar systems.

See the [detailed solar battery review here](#)

### Book Trusted Solar Pros

Ad Angi makes it simple to find the best contractors in your area. Just enter yo

Angi

[Learn More](#)

The four main types of hybrid and off-grid energy storage systems:

1. [Off-grid multi-mode inverters](#)
2. [All-in-one Battery Energy Storage Systems \(BESS\)](#)
3. [Hybrid Inverters](#)
4. [Battery systems - Energy storage \(shown\)](#)

## Battery System Comparison Chart 2021

Manufacturer	Pic	Model	Type	Use	Total Capacity	Usable Capacity	Power Output	Surge/peak Power	Battery Chemistry	Warranty	Compatible Inverters	Other Features	Cost per kWh**
Tesla		Powerwall 2	AC coupled Battery System	Back-up Solar storage	13.5kWh	90%	5.0kW	7.0kW	Lithium NMC	10 years 70% EOL capacity	N/A AC Coupled	Modular AC system, Liquid cooling system, Temp -20 to 50°C	\$1,022
												Integrated Inverter	

					10kWh				capacity		High cycle life		
Varta		Pulse 6	AC coupled Battery System	Solar storage	6.5kWh	90%	2.5kW	2.5kW	Lithium NMC	10 years 70% EOL capacity	N/A AC Coupled	Integrated Inverter, LG cells, IP33, Temp 5 to 45°C	\$1,236
Delta		BX6.3	AC coupled Battery System	Back-up Solar storage	6.3kWh	80%	3.0kW	3.0kW	Lithium NMC (Samsung cell)	10 years 60% EOL capacity	N/A AC Coupled	Modular up to 12.6kWh IP65 Temp -10 to 45°C	\$1,180
LG Chem		RESU Series	DC Battery System 48V	Back-up Solar storage Off-grid	3.3 kWh 6.5 kWh 9.8 kWh 13 kWh	90%	3.0kW 4.2kW 5.0kW	3.3kW 4.6kW 7.0kW	Lithium NMC	10 years 60% EOL capacity	SMA, Solax, Selectronic, Victron, Goodwe, Sungrow	Modular up to 26kWh, IP55 Temp 0 to 50°C	\$710
LG Chem		RESU H Series	DC Battery System 400V	Back-up Solar storage	6.5 kWh 9.8 kWh	90%	3.5kW 5.0kW	5.0kW 7.0kW	Lithium NMC	10 years 60% EOL capacity	SMA, SolarEdge, Solax, Huawei	IP55 Temp 0 to 50°C	\$795
BYD		LVS 4.0	DC Battery System 48V	Back-up Solar storage Off-grid	4.0kWh modules up to 256kWh	100%	3.3kW per module	4.6kW per module (5 sec)	Lithium LFP (LiFePO4)	10 years 60% EOL capacity	SMA, Solax, Selectronic, Victron, Goodwe	Modular IP55 Temp -10 to 50°C	\$840
BYD		LVL 15.4	DC Battery System 48V	Back-up Solar storage Off-grid	15.36kWh modules up to 983kWh	100%	12.8kW per module	19.2kW per module (5 sec)	Lithium LFP (LiFePO4)	10 years 60% EOL capacity	SMA, Solax, Selectronic, Victron, Goodwe	Modular IP55 Temp 0 to 50°C	\$750
BYD		Premium HVM	DC Battery System 150V - 400V	Back-up Solar storage	2.76kWh modules up to 66.2kWh	100%	2.0kW per modules	3.8kW per module (3 sec)	Lithium LFP (LiFePO4)	10 years 60% EOL capacity	Fronius, Goodwe, SMA, Kostal	Modular IP55 Temp 0 to 50°C	\$870
BYD		Premium HVS	DC Battery System 100V	Back-up Solar storage	2.56kWh modules up to 38.4kWh	100%	2.5kW per modules	5.0kW per module (3 sec)	Lithium LFP (LiFePO4)	10 years 60% EOL capacity	Fronius, Goodwe, SMA, Kostal	Modular IP55 Temp 0 to 50°C	\$935
Dyness		Powerbox	DC Battery System 48V	Back-up Solar storage Off-grid	2.4kWh modules up to 9.6kWh	90%	1.2kW per module	4.8kW per module (1 sec)	Lithium LFP (LiFePO4)	10 years 70% EOL capacity* (DOD 80%)	Solis, Victron, Goodwe, Growatt, Imeon, Sofar, Ningbo Dye	Modular IP65 Temp 0 to 50°C	\$690
Pylon Technology		U52000B	DC Battery System 48V	Back-up Solar storage Off-grid	2.4kWh	80%	2.0kW per module	2.2kW x No. of modules	Lithium LFP (LiFePO4)	10 years 70% EOL capacity	SMA, Solax, Victron, Redback, Goodwe	Integrated BMS	\$718
Huawei		Luna2000	DC Battery System HV	Back-up Solar storage	5.0kWh modules up to 30kWh	100%	TBA per module	TBA per module	Lithium LFP (LiFePO4)	10 years EOL capacity TBA*	Huawei Inverter Only	Modular 'string battery' IP65 Temp 0 to 50°C	N/A
Q Cells		Q.Save G2	DC Battery System 200V	Back-up Solar storage	4.0kWh modules up to 12kWh	90%	2.0kW per module	3.4kW per module	Lithium-Ion (Samsung SDI)	10 years 65% EOL capacity*	Q Cells Hybrid Inverter Only	Modular IP65 Temp 0 to 40°C	\$1,020
Soltaro		4.5kWh	DC Battery System 48V	Back-up Solar storage	4.5kWh	90%	4.5kW per module	6.1kW per module	Lithium LFP (LiFePO4)	10 years 80% EOL capacity*	Soltaro Inverters only	Modular IP65 Temp 0 to 50°C	\$786
Sungrow		SBP4K8	DC Battery System 48V	Back-up Solar storage	4.8kWh	90%	3.0kW per module	4.0kW per module	Lithium NMC	10 years 70% EOL capacity*	Sungrow Inverters only	Modular up to 14.4kWh, IP55 Temp -10 to 45°C	\$780
Growatt		GBLI 6532	DC Battery System 48V	Back-up Solar storage	6.5kWh	94%	5.0kW per module	5.3kW	Lithium-ion (TBA)	10 years 60% EOL capacity	Growatt inverters only	IP55 (Temp 0 to 50°C)	\$588
Delta		BX6	DC Battery System 95V	Back-up Solar storage	5.8kWh	80%	3.0kW per module	3.5kW	Lithium NMC	10 years 50% EOL capacity	Delta hybrid inverters only	IP54 (Temp 0 to 50°C)	\$840
Triple Power		T-BAT H 5.8	DC Battery System 115V	Back-up Solar storage	5.8kWh	90%	2.9kW per module	4.0kW	Lithium LFP (LiFePO4)	10 years 60% EOL capacity	Solax hybrid inverters only	Modular up to 25.2kWh IP55 (Temp 0 to 55°C)	\$662
FoxESS		HV2600	DC Battery System 52V	Back-up Solar storage	2.6kWh modules up to 20.8kWh	90%	2.6kW per module	3.1kW per module	Lithium NMC	10 years 60% EOL capacity	FoxESS inverters, TBA	Modular HV system up to 20.8kWh (Temp -10 to 50°C)	\$740
Simpliphi		PHI	Self-managed DC Battery System 24V, 48V	Back-up Solar storage Off-grid	3.8kWh modules up to 100kWh+	* 100%	1.9kW per module	4.8kW per module (10 min)	Lithium LFP (LiFePO4)	10 years 80% EOL capacity*	SMA, Victron, Selectronic, (any lead-acid hybrid or battery inverter)	Modular, lead-acid replacement, Temp 0 to 50°C	\$1,072

By using this website, you agree to our use of cookies. We use cookies to help our website run effectively.

OK

PowerPlus Energy		LiFe Premium	DC Battery System 24V, 48V, 120V	Back-up Solar storage Off-grid	modules up to 100kWh+	* 100%	3.2kW per module	3.2kW per module	Lithium LFP (LiFePO4)	10 years 80% EOL capacity*	Selectronic, (any lead-acid hybrid or battery inverter)	lead-acid replacement, Temp 0 to 55°C	\$908
PowerPlus Energy		ECO	Self-managed DC Battery System 48V	Back-up Solar storage Off-grid	4.0kWh modules up to 100kWh+	* 100%	2.0kW per module	3.2kW per module	Lithium LFP (LiFePO4)	10 years 70% EOL capacity*	SMA, Victron, Selectronic, (any lead-acid hybrid or battery inverter)	Modular, lead-acid replacement, Temp 0 to 55°C	\$705
GenZ		2RU	Self-managed DC Battery System 24V, 48V	Back-up Solar storage Off-grid	3.0kWh modules up to 100kWh+	* 100%	2.95kW per module	3.1kW per module	Lithium LFP (LiFePO4)	10 years 75% EOL capacity	SMA, Victron, Selectronic, (any lead-acid hybrid or battery inverter)	Integrated BMS Modular lead-acid replacement	\$854
Zenaji		Aeon	Self-managed DC Battery System 48V	Back-up Solar storage Off-grid	1.93kWh	100%	2.5kW per module	6.0kW per module (1 sec)	Lithium Titanate (LTO)	20 years 80% EOL capacity	SMA, Victron, Selectronic, Sungrow, MPP, Schneider	Modular, Temp range -20 to 60°C Very high cycle life (22,000)	\$1,436

Update Dec 2020 - V4.0

## Battery Features and Price Comparison

### Features:

- Weather ratings - IP20 to IP22 are suitable for indoor use only. IP55 and above is suitable for protected outdoor areas

### NOTES:

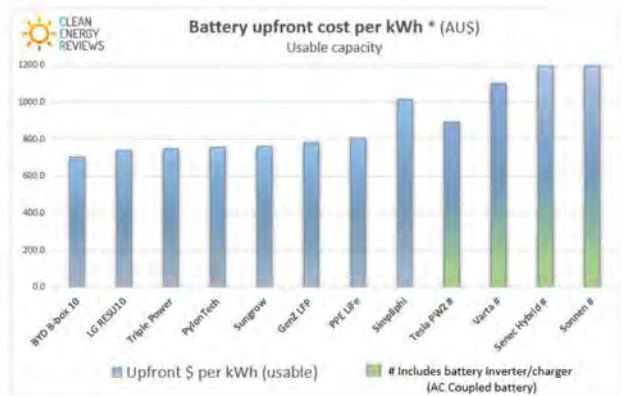
- \*\* Upfront cost estimate based on various Australian distributors and wholesalers
- AC coupled systems incorporate inverter/chargers which increases total cost, thus higher cost compared to DC batteries.
- \* DOD and cycle life values estimated based on manufactures specifications and rate of charge/discharge.

## Previous battery comparison and cost charts

Summary Comparison Table - Lithium Battery Systems\* \*Always refer to manufacturer specifications and data sheets. [www.CleanEnergyReviews.com.au](http://www.cleanenergyreviews.com.au)

Manufacturer	Model	Type	Low	Total Usable Capacity	Power Output	Charge (peak) Power	Battery Chemistry	Warranty	Compatible Inverters	Other Features	Cost per kWh**	Area 3 per kWh***
LG Chem	RESU10	Back up Solar storage (off-grid)	1.3 kW	2.5 kWh	3.5kW	4.2kW	Lithium NMC	10 years 80% EOL capacity	SMA, Victron, Selectronic, Sunspec	Integrated BMS Weather sealed IP55	\$138	\$111
LG Chem	RESU10	Back up Solar storage (off-grid)	1.3 kW	2.5 kWh	3.5kW	4.2kW	Lithium NMC	10 years 80% EOL capacity	SMA, Victron, Selectronic, Sunspec	Integrated BMS Weather sealed IP55	\$148	\$113
Tesla	Powerwall 2	Back up Solar storage	1.5kW	13.5kWh	5.0kW	12kW	Lithium NMC	10 years 70% EOL capacity	N/A AC Coupled	Integrated BMS Rapid temperature management	\$695	\$147
Sonnens	Home 100	Back up Solar storage	4.0kW	100%	3.0kW	30kW	Lithium LFP (SFP/PC)	10 years 80% EOL capacity	N/A AC Coupled	Integrated BMS Inverter high cycle life	\$1,380	\$233
BYD	Blue Plus	Back up Solar storage (off-grid)	2.5kW	2.5kWh up to 10.2kWh	2.5kW	1.5kW	Lithium LFP (SFP/PC)	10 years 80% EOL capacity	SMA, Victron, Selectronic, Sunspec	Integrated BMS Monitor up to 1000Vdc	\$730	\$186
BYD	Blue Plus	Back up Solar storage (off-grid)	2.5kW	2.5kWh up to 11.5kWh	2.5kW	1.5kW	Lithium LFP (SFP/PC)	10 years 80% EOL capacity	SMA, Victron, Selectronic, Sunspec	Integrated BMS Monitor up to 1000Vdc	\$745	\$112
Pylon Technology	10000	Back up Solar storage (off-grid)	1.2kW	1.2kWh up to 10.0kWh	1.2kW	2.4kW	Lithium LFP (SFP/PC)	8 years 80% EOL capacity	SMA, Victron, Selectronic, Sunspec	Integrated BMS Monitor and cell replacement	\$750	\$185
Energylight	10000	Back up Solar storage (off-grid)	1.2kW	1.2kWh up to 10.0kWh	1.2kW	2.4kW	Lithium LFP (SFP/PC)	10 years 80% EOL capacity	SMA, Victron, Selectronic, Sunspec	Integrated BMS Monitor and cell replacement	\$1,014	\$120
PowerPlus Energy	LiFe Premium	Back up Solar storage (off-grid)	1.3kW	2.5 kWh	3.5kW	4.2kW	Lithium LFP (SFP/PC)	10 years 80% EOL capacity	SMA, Victron, Selectronic, Sunspec	Integrated BMS Monitor and cell replacement	\$810	\$192
GenZ	2RU	Back up Solar storage (off-grid)	1.3kW	3.0 kWh	2.95kW	3.1kW	Lithium LFP (SFP/PC)	10 years 75% EOL capacity	SMA, Victron, Selectronic, Sunspec	Integrated BMS Monitor and cell replacement	\$788	\$182
Sonnec	Home 100	Back up Solar storage	2.5kW	100%	2.5kW	25kW	Lithium LFP (SFP/PC)	10 years 80% EOL capacity	N/A AC Coupled	Integrated BMS Inverter	\$1,185	\$183
Victron	Power 2	Back up Solar storage	2.5kW	100%	2.5kW	25kW	Lithium NMC	10 years 80% EOL capacity	N/A AC Coupled	Integrated BMS Inverter	\$1,100	\$181
Sungrow	10000	Back up Solar storage (off-grid)	1.2kW	1.2kWh up to 10.0kWh	1.2kW	4.0kW	Lithium ion	10 years 80% EOL capacity	Sungrow	Integrated BMS Monitor up to 1000Vdc	\$758	\$190
Triple Power	10000	Back up Solar storage (off-grid)	1.3 kW	2.5 kWh	2.5kW	12kW	Lithium LFP (SFP/PC)	8 years 80% EOL capacity	SMA, Victron, Selectronic, Sunspec	Integrated BMS Monitor up to 25,000Vdc	\$743	\$110

Lithium Battery Comparison Chart 2019 release



Battery cost comparison chart - Upfront cost per kWh of usable storage capacity. AC coupled systems include inverter/charger (retrofit) - 2019

By using this website, you agree to our use of cookies. We use cookies to help our website run effectively.

OK

---

[About Us](#)   [Privacy Policy](#)   [Terms Of Service](#)

---

---

By using this website, you agree to our use of cookies. We use cookies to help our website run effectively.

[OK](#)

Review

# A Review on the Thermal Hazards of the Lithium-Ion Battery and the Corresponding Countermeasures

Dongxu Ouyang<sup>1</sup>, Mingyi Chen<sup>2</sup> , Que Huang<sup>3</sup>, Jingwen Weng<sup>1</sup>, Zhi Wang<sup>1</sup> and Jian Wang<sup>1,\*</sup> 

<sup>1</sup> State Key Laboratory of Fire Science, University of Science and Technology of China, Hefei 230026, China; ouyang11@mail.ustc.edu.cn (D.O.); wengjw@mail.ustc.edu.cn (J.W.); ustc14wz@mail.ustc.edu.cn (Z.W.)

<sup>2</sup> School of Environment and Safety Engineering, Jiangsu University, Zhenjiang 212013, China; chenmy@ujs.edu.cn

<sup>3</sup> School of Environment and Safety Engineering, North University of China, Taiyuan 030051, China; que.huang@nuc.edu.cn

\* Correspondence: wangj@ustc.edu.cn

Received: 28 April 2019; Accepted: 12 June 2019; Published: 18 June 2019



**Abstract:** As one of the most promising new energy sources, the lithium-ion battery (LIB) and its associated safety concerns have attracted great research interest. Herein, a comprehensive review on the thermal hazards of LIBs and the corresponding countermeasures is provided. In general, the thermal hazards of the LIB can be caused or aggravated by several factors including physical, electrical and thermal factors, manufacturing defect and even battery aging. Due to the activity and combustibility of traditional battery components, they usually possess a relatively high thermal hazard and a series of side reactions between electrodes and electrolytes may occur under abusive conditions, which would further lead to the thermal failure of LIBs. Besides, the thermal hazards generally manifest as the thermal runaway behaviors such as high-temperature, ejection, combustion, explosion and toxic gases for a single battery, and it can even evolve to thermal failure propagation within a battery pack. To decrease these hazards, some countermeasures are reviewed including the application of safety devices, fire-retardant additives, battery management systems, hazard warnings and firefighting should a hazard occur.

**Keywords:** lithium-ion battery; thermal hazard; management and countermeasures

## 1. Introduction

In light of the steadily increasing energy demands and the consensus regarding the reduction of pollution, humans have paid great attention to the development of new energy such as solar energy, wind energy, tidal energy, lithium-ion battery (LIB) and fuel cell [1–5]. Advantages including high energy density, less pollution, stable performance and long-life cycle compared to many alternatives have made LIBs the dominant power sources for electrical applications [6,7]. Especially, with the approaching era of electric vehicles (EVs), it is foreseeable that the use of LIB will be more common in the future.

However, behind the boom, there exist challenges that must be faced. As a result of the high energy density of LIBs, they are sensitive to abusive conditions such as high temperature, crashing, overcharge, over-discharge and short-circuit, etc. [8–10]. Moreover, the typical components of a battery, e.g., plastic packing, separator and electrolyte are combustible. Thereby, the accidents induced by LIBs are frequently reported and can occur in a range of applications from mobile telephones, to EVs and even airplanes [11–14]. Especially with the increasing energy density, e.g., the popularity of  $\text{LiNi}_{0.8}\text{Mn}_{0.1}\text{Co}_{0.1}$  (NMC811), the problems will be exacerbated [15,16]. The abusive conditions

described above will destroy the original stable structure of battery, which triggers chain reactions inside battery and eventually leads to thermal runaway. Among, thermal runaway of a battery typically manifests as high temperature, gas ejection, violent combustion and even explosion, which will lead to catastrophic results.

Regarding the thermal hazards of the LIB, much research has been directed toward enhancing the inherent safety of battery and improving the thermal management to prevent thermal failure. For the former, it mainly focuses on enhancing the fire-retardant performance of battery components including the cathode, anode, electrolyte, additives and separator [17–27]. As for the latter, it includes the inclusion of battery safety devices, thermal management of LIBs during usage, thermal hazards warning and firefighting should a hazard occur. The thermal management of the LIB can usually be categorized into several types including air, liquid and phase change material (PCM) based systems [28–33]. Prior to the occurrence of a thermal hazard, LIBs are prone to experiencing evident increases in temperature and may also release representative gases such as CO, H<sub>2</sub> and SO<sub>2</sub>. Therefore, battery safety devices such as vents can be used to terminate the deterioration of failure, meanwhile a temperature sensor or gas sensor can also be applied to warn to the hazard [34–37]. Finally, if the thermal hazards are accompanied by severe combustion, it is necessary to fight the fire to impede its progression. Until now, researchers have paid great attention to firefighting methods and extinguishers so that the flame or combustion of the LIB can be extinguished effectively [38–41].

Although much work has been done on the thermal hazards of the LIB, comprehensive summaries on the thermal hazards of batteries involving battery components, a single battery and a battery pack are scarce. Besides, most researchers focus on the thermal management of battery during normal usage, countermeasures that suppress the thermal hazard require further study. The current work provides a comprehensive review on the thermal hazards of battery, and related thermal hazard prevention techniques. The Section 1 partially summarizes the safety-related LIB incidents that have occurred in recent years. The Section 2 is regarding the common causes of battery thermal hazard and the respective mechanism. The Section 3 demonstrates the thermal hazards of the LIB, involving typical battery components, a single battery and a battery pack. It is worthy to be noted that the influence of low-pressure environment and cathode chemistry on the thermal hazard is also involved. The Section 4 is concerning how to prevent the thermal hazard of a battery and improve its safety which can be divided into inherent safety methods and extra countermeasures.

## 2. Safety-Related Incidents Involving Lithium-Ion Batteries

Table 1 lists several representative incidents of LIB failure in recent years which can be divided into three main types including mobile telephone, EV and airplane [13,42–44]. With regard to safety-related battery incidents in mobile telephones, it is apparent that nearly all mainstream mobile telephones have experienced such incidents, e.g., Apple, Samsung and Huawei. Take the Samsung Note 7 as an example, it was released on 3 August 2016, and then its first reported explosion was on August 24, 2016. In the end, quantities of incidents forced Samsung to recall all Note 7 devices around the world on 2 September 2016. This greatly damaged consumer confidence in Samsung, and ultimately resulted in a sharp decrease in its market share and a loss of 17 billion dollars. The root reason of Note 7 incidents was attributed to the battery fault, i.e., Samsung adopted an excessively thin separator to increase the energy density of battery that substantially increased the possibility of the battery short-circuiting. Similar faults also occurred in the other failed batteries. For EVs, most safety-related battery incidents appeared under the conditions of crashing, charging, discharging and self-ignition, which subsequently led to the short-circuit of batteries. Although the failure rate of EV is approximately 1/10,000, which is much lower than that of traditional vehicles (7.6/10,000 [45]), this issue still significantly hinders the development of EVs. In the case of incidents on airplanes, these usually resulted from the failure of passengers' electronic equipment where the battery caught fire, filled the cabin with smoke and led to catastrophic results. These accidents forced civil aviation bureaus around the world to take strict administration regarding portable electronics. Research revealed that battery failures in airplanes

were generally the results of battery fault, aircraft vibration, pressure change and temperature change, which subsequently induced short-circuiting of the batteries.

**Table 1.** Selected incidents of lithium-ion battery failure in recent years.

Classification	No.	Date	Location	Accident Reply
Mobile telephone	1	2016.8.24	Korea	The first explosion of a Note 7 in the world [46]
	2	2016.9.18	China	The first explosion of a Note 7 in China [46]
	3	2016.10.10	China	An iPhone 7 exploded and hurt the user [47]
	4	2016.10.14	China	A Huawei P9 exploded during charging [48]
	5	2016.10.17	Australia	An iPhone 7 caught fire which then, burned a car [49]
	6	2018.1.9	Switzerland	An iPhone exploded when replacing the battery, which caused an injury and seven poisonings [50]
	7	2018.1.10	Spain	An iPhone exploded which caused thick smoke inside the store [50]
	8	2018.12.30	America	An iPhone XS Max self-ignited and burned the user [51]
EV	1	2016.1.1	Norway	A Tesla Model S caught fire during charging [52]
	2	2016.5.14	China	An EV bus caught fire because of battery pack short-circuit [52]
	3	2016.9.7	Netherlands	A Tesla Model S crashed to a tree which caused the battery to catch fire, resulting in the death of the driver [52]
	4	2017.1.15	China	An EV bus self-ignited during driving [53]
	5	2017.2.19	China	A Tesla Model X caught fire after crashing [53]
	6	2017.5.1	China	An EV bus self-ignited during charging [53]
	7	2018.3.24	America	A Tesla Model S caught fire whilst stationary [54]
	8	2018.5.21	China	An EV bus self-ignited during driving [54]
Airplane	1	2010.9.3	The United Arab Emirates	A Boeing 787 crashed due to the battery catching fire, which caused two deaths [55]
	2	2013.1.7	America	The battery pack caught fire and filled the cabin of a Boeing 787 with smoke [56]
	3	2013.1.16	Japan	The battery pack caught fire during a Boeing 787 flight from Yamaguchi-Ube to Tokyo [56]
	4	2014.4	Australia	A Boeing 737 caught fire due to the short-circuit of the battery inside a trunk [57]

As known, it is essential for LIB to pass several compulsory test standards, e.g., UN R100, SAE-J2464, IEC-62133 and GB/T 31485 etc. before its application. Therefore, it must be queried, why do incidents involving batteries still occur sporadically, even if these batteries have passed the test standards? The answers can be attributed to two factors: (1) the inherent possibility of battery failure and (2) the abusive conditions associated with their practical use. Similar to certain other equipment, an inherent possibility of self-induced failure exists for LIBs even if the probability of this is very low. In some cases, the working circumstances of LIBs are very complex and certain abusive conditions such as external forces, high temperature, low temperature, overcharging, over-discharging, etc. are typically experienced. Under the effects of abusive conditions, the manifestation of the battery failure will be more severe. Furthermore, the abusive conditions associated with batteries can typically be categorized into physical, electrical, and thermal factors even manufacturing defect and battery aging, which are reviewed in the next section.

### 3. The Causes of Thermal Hazards Associated with Lithium-Ion Batteries

Generally, LIB possesses stable structure in which lithium ions transfer between the cathode and the anode during charging/discharging such that it can be regularly cycled considerable times. Whereas, the original stable-structure of the LIB will become damaged due to the effect of abusive factors, generating thermal hazard. The factors can be summarized as several main types: physical, electrical and thermal factors, as well as manufacturing defect and battery aging [14,58–62].

#### 3.1. Physical Factor

The destructive deformation of battery caused by an applied force is a common feature of physical factor. Where, vehicle collision/crash and penetration of battery are the typical conditions for physical failure. Furthermore, the volume expansion of electrode materials and stress generation within battery may also lead to physical failure.

As seen in Table 1, many safety-related incidents involving the batteries of EVs took place after deformation. It reveals that during an accident involving the vehicle, it is possible for a single battery or a battery pack to deform under the effect of an external force. The deformation of battery may result in dangerous consequences: (1) the electrodes can come into contact causing an internal short circuit and (2) the flammable electrolyte leaks which may induce a fire.

Penetration, another common physical phenomenon may occur if the battery is affected by sharp objects. It is generally listed in the test standards of the LIB, i.e., GB/T 31485-2015, SAE J2464-2009 etc., to trigger the internal short circuit. Compared with collision or crash, penetration may result in more severe consequences due to the severity of the internal short circuit. In this case, severe short-circuit of the battery will rapidly take place and then severe heat release, combustion and even explosion may occur.

As known, the compressive stress reached during lithiation and the tensile stress reached during delithiation are significant inside battery [63,64]. Such large stress cycling over extended lithiation/delithiation cycles will invariably lead to fatigue damage, leaving battery materials susceptible to fracture and pulverization. Moreover, traditional electrode materials, such as silicon and transition metal oxides, may result in extreme volume changes during operation and further result in fracturing, electrical conductivity loss and mechanical integrity [65].

### 3.2. Electrical Factor

External short circuit, overcharge and over-discharge are common conditions of electrical failure. Where, the external short circuit of battery occurs once electrodes with a voltage difference are connected by conductors. It usually results from the deformation of battery, water immersion, conductor aging, improper usage and long-time charging, etc. During an external short circuit, the battery is in a state of fast discharging and the discharging current may be much larger than that of normal condition. Hereafter, the battery undergoes a violent temperature rise which may lead to serious consequence.

As the open circuit voltage of battery is charged above the cut-off voltage, overcharge occurs. The failure of battery management system is the ordinary reason of overcharge so that the charging of battery will proceed continuously. As a result, the internal pressure of battery increases, the deformation of battery and leakage of electrolytes occur, and the performance of battery also significantly decreases. Besides, severe heat and gas generation can also be seen during overcharge process. Compared to normal charging process, the heat generation behavior during overcharge will be much greater as a result of the side reactions inside battery and the increased internal resistance. In addition, excessive loss of lithium ions at the cathode during overcharging will lead to structural collapse of the cathode and subsequent oxygen release. The released oxygen accelerates the decomposition of electrolyte, and thereafter, gases are generated. Consequently, the thermal hazard associated with an overcharged battery is greatly heightened compared to that of a normal battery due to the excessive energy stored in the overcharged battery.

Similarly, when the open circuit voltage of battery is discharged below the cut-off voltage, over-discharge occurs and the failure of battery management system is also a typical reason for over-discharge. Over-discharge causes an excessive loss of lithium ions on the anode which will destroy the stable structure of the anode and cause irreversible damage. Meanwhile, gases such as CO and CO<sub>2</sub> can also be generated, resulting in battery swelling. Furthermore, over-discharge will cause the dissolution of copper collector. The dissolved copper migrates and deposits onto the surface of the anode, which will pierce the separator, causing a short circuit to form. Consistent with the other abusive conditions, substantial heat release also occurs upon over-discharge of the LIB.

### 3.3. Thermal Factor

Besides the overheating caused by physical or electrical factors, thermal failure can also be triggered by external high temperature and overheating. Thermal factor results in a fierce rise of battery temperature, the melting of separator, the decomposition of electrodes/electrolytes and numerous side

reactions etc., and finally leads to battery thermal runaway. In other words, thermal abuse is the root cause of battery thermal runaway. It should be noted that both physical and electrical factors also ultimately cause thermal runaway. Further, it can be found that almost all the abusive conditions are accompanied with internal short circuit, i.e., an internal short circuit is the most common feature of thermal runaway. It occurs when the cathode and the anode contact with each other due to the failure of battery separator. Once the internal short circuit is triggered, the electrochemical energy stored inside the battery spontaneously releases, generating large amounts of heat.

### 3.4. Manufacturing Defect and Aging

Apart from the external factors, battery internal defect due to poor manufacturing, such as a low-quality separator, material contaminant, and improperly arranged constituents, can also cause battery failure and result in thermally hazardous conditions [66]. As stated in Section 2, the main cause of incidents in the Samsung Note 7 was a battery fault, in other words, Samsung adopted an excessively thin separator to increase the energy density of battery which raised the possibility of battery short circuit [67]. Mohanty et al. [68] undertook a systematic investigation on several plausible cathode defects such as agglomeration, pinholes, metal particle contamination and non-uniformity. The findings showed that cathode agglomeration aggravated the cycle efficiency and resulted in faster capacity fading. Electrode pinholes showed substantially lower discharge capacities compared to the baseline of electrodes. Metal particle contaminants had an extremely negative effect on performance, and the electrodes with severe non-uniform coatings showed poor cycle life. In summary, cathode material defects decrease battery performance and increase the risk of thermal hazard. In addition, a low-quality separator will reduce the efficiency of  $\text{Li}^+$  passing through the separator and result in serious Li plating, which will further penetrate the separator and induce the internal short circuit [69]. The improper arrangement of constituents is also harmful to the operation of battery, deteriorates the heat generation and heat release, therefore decreases battery safety.

Finally, due to deterioration associated with battery aging, its thermal hazards will increase correspondingly. The aged battery will lose quantities of lithium and active materials [70,71]. Partially inactivated  $\text{Li}^+$  will transfer to Li metal and deposit onto the surface of electrodes and even the separator to form Li plating. Upon the progression of battery aging, the degree of Li plating will increase gradually and subsequently, dendrite is generated. The dendrite may penetrate the separator and form a bridge between the electrodes, which will cause micro-shorting inside the battery and eventually lead to failure of the battery. At the same time, the thickness of the solid electrolyte interface (SEI) layer will gradually increase with the aging of the battery, which will lead to increases in the battery resistance, heat generation and thermal hazards.

To better understand the thermal hazards of LIBs, some aspects regarding typical battery components, a single battery and a battery pack will be reviewed. In addition, the influence of certain parameters such as low pressure and cathode chemistry are also considered.

## 4. Thermal Hazards of Lithium-Ion Battery

### 4.1. Thermal Hazards of Typical Battery Components

In general, a LIB is mainly composed of electrodes, electrolytes and a separator. The electrodes can further be divided into the cathode and the anode. The thermal hazard of the LIB usually results from the destructive reactions of battery components such as the decomposition of electrode/electrolyte, the reaction between electrodes, the reaction between electrode and electrolyte, etc. In order to gain a comprehensive understanding on the thermal hazards of the LIB, the hazards of typical battery components will be discussed following.

#### 4.1.1. Thermal Hazards of the Electrolytes

Due to its relatively high content and liquidity, the combustion behavior of electrolyte is quite complicated. According to previous research, the initial decomposition temperature of electrolyte is approximately 80 °C [72,73], and large quantities of heat and gas are released, which easily lead to LIB leakage. In addition, the electrolyte will react with electrodes with the increasing temperature. At the meantime, leaked electrolyte will increase the liquid fire risk once ignition occurs. If the internal temperature of the LIB is higher, it will lead to a jet fire, and then noticeably accelerate the spread of fire.

Currently, among the commonly used commercial electrolytes, lithium salt is mainly used as lithium hexafluorophosphate (LiPF<sub>6</sub>) or lithium tetrafluoroborate (LiBF<sub>4</sub>). For the functional mechanism of the two kinds of lithium salts in electrolyte combustion process, Sloop et al. compared and analyzed the pyrolysis process of LiPF<sub>6</sub> and phosphorus pentafluoride (PF<sub>5</sub>) in ethylene carbonate/dimethyl carbonate (EC/DMC), and found that the products were almost the same [73]. Nagasubramanian et al. analyzed the thermal decomposition process of LiPF<sub>6</sub> in methyl ethyl carbonate (EC/EMC), and then put forward the pyrolysis mechanism of the LiPF<sub>6</sub> under high temperature [74–76]:

1. Lithium salt undergoes thermal decomposition to form PF<sub>5</sub>;
2. PF<sub>5</sub> reacts with water to generate hydrogen fluoride (HF);
3. PF<sub>5</sub> can also react with carbonate solution to form methyl fluoride (CH<sub>3</sub>F) and other substances.

In addition, it is generally regarded that LiBF<sub>4</sub> is superior to LiPF<sub>6</sub> with respect to factors such as high-temperature performance, reaction characteristics with water and chemical stability [77,78]. However, the anion of LiBF<sub>4</sub> is very small and it can be easily combined with lithium ions in solution, resulting in its weak ion transport ability. To overcome this weakness, researchers chelated lithium salt with oxygen to synthesize new large anionic lithium salts, such as lithium diethylborate (LiBOB) and lithium fluoroethylborate (LiDFOB) [79,80].

After a long period of development, some researchers believe that liquid electrolytes have inherent safety disadvantages. No matter how good the electrolyte additives and solutions are, they cannot prevent the formation of lithium dendrites. Therefore, researchers have started to develop solid-phase electrolytes [81–84].

#### 4.1.2. Thermal Hazards of the Electrodes

Nowadays, lithium nickel manganese cobalt oxide (NMC) ternary positive electrode material is one of the most widely used cathode materials, with high capacity, low cost and relatively good safety, which has been vigorously promoted in the current power battery industry [85]. The researchers found that with the higher content of Ni element, the cost would be significantly reduced, and the specific capacity would be higher [86]. However, the battery cycle life and the stability of electrode and electrolyte would be lower. Therefore, it is important to study the effect of element content in the NMC ternary material. Ma et al. compared the thermal runaway behavior of various NMC cathode materials with electrolytes at high temperature by accelerating calorimeter (ARC), while the results showed that under different cut-off voltages, using a traditional carbonate solution as the electrolyte, with the increase of Ni content, the initial temperature corresponding to the reactions between electrode and electrolyte was reduced, i.e., the fire risk of the LIB increased [16]. The material used in previous research was a common NMC cathode, made from a hydroxide precursor system, with a powder particle size of about 10 μm. The surface was not coated or modified to improve the performance. On the basis of traditional polycrystalline NMC materials, new single-crystal NMC materials have been developed, which are expected to improve battery stability at elevated temperatures [87].

For positive electrode materials, the amount of lithium embedded will directly affect the amount of heat produced. The more lithium that is embedded, the less heat the whole LIB system will generate. If there is only the electrode material without electrolyte, almost no heat will be released [88] and the reactivity between positive materials and different electrolytes will also be different. Wang et al. analyzed the heat production from the reaction between cobalt acid lithium batteries and different

electrolytes using a C80 micro-calorimeter, and the results showed that when compared with chain solvent, the annular solvent was more stable. Among the various chain carbonate solutions, DMC showed the highest reactivity, while diethyl carbonate (DEC) presented the lowest [89]. According to the above research, the heat production mechanism of positive electrode with electrolyte can be summarized as follows: The stability of electrode material will decrease and the temperature will increase, resulting in the decomposition of the positive electrode material and oxygen release during the charging process. The oxygen will react with the electrolyte and negative electrode leading to substantial heat release and gas generation, thus greatly increasing the risk of thermal failure.

For negative electrode materials, most of the commercial anode material is carbon such as graphite. On the anode surface, a layer of SEI would be formed during the first charge and discharge cycle. The SEI layer will not affect the lithium ion transport and can also prevent direct contact occurring between the anode and the electrolyte, which reduces the cycle performance. While the existence of the SEI will to some extent influence the capacity of LIBs, and its thermal stability under high temperature is poor. Barnett et al. investigated the graphite anode with organic electrolyte containing  $\text{LiPF}_6$  using ARC and differential scanning calorimetry (DSC), and the results indicated that the initial exothermal temperature of the system was about 80 °C, while the starting temperature of rapid heat production was about 150 °C, which was regarded as the thermal runaway temperature of the LIB. At the same time, other scholars have studied the pyrolysis of the SEI. With the increase of temperature, the initial structure of the SEI would be destroyed, thus losing its protective function, leading to the reaction between electrode and electrolyte and the release of heat [90–92].

#### 4.1.3. Thermal Hazards of the Separator

At present, the LIB separator is commonly made of polyethylene (PE), polypropylene (PP) or their composite materials. However, because of their low thermal deformation temperature (PE: within 85 °C, PP: within 100 °C) [93], the polyolefin separators will suffer severe thermal contraction when ambient temperature is relatively high, thus it is not suitable for the usage under high temperature environment. In order to meet the requirement of the complex working environment of the LIB, researchers have developed a variety of new composite separator materials and optimized their performance from the aspects such as preparation process improvement [94–96]. Among them, a new type of separator material obtained by the composite of polyaryl ether and thermoplastic resin has attracted extensive attention due to its superior ionic conductivity and high safety [97,98]. Zhong et al. developed a series of poly aryl ether materials, including poly aryl ether ketone (PPEK), poly aryl ether sulfone (PPES), poly (phthalazinone ether sulfone ketone) (PPESK) and so on. Their glass transition temperatures were over 260 °C, and the 5% thermal weightlessness temperatures were close to 500 °C. Upon analysis using an electrostatic spinning process, the poly aryl ether materials with polyvinylidene fluoride (PVDF) as a composite separator of a LIB showed excellent electrochemical performance and thermal stability [99,100].

Although the high-temperature resistant separator can significantly improve the safety condition of the LIB, it cannot completely inhibit the occurrence of thermal hazard. According to the previous research, although the mass ratio of the separator is approximately 3%, it can release up to 33% of heat in the combustion process, see Figure 1, indicating that the combustion characteristics of separator directly affect the fire risk of the LIB [76]. Therefore, the research and development of a new separator material with high thermal safety is essential.

#### 4.2. Thermal Hazards of a Single Battery and Battery Pack

Due to the high energy density of the LIB and the inherent hazards of battery components described above, it is common for the LIB to experience thermal hazards especially under abusive conditions. For a single battery, the thermal hazards are generally exhibited as high-temperature, ejection, combustion, explosion and toxic gases during thermal runaway. As for a battery pack, thermal failure propagation within the pack can also be observed.

Although the high-temperature resistant separator can significantly improve the safety condition of the LIB, it cannot completely inhibit the occurrence of thermal hazard. According to the previous research, although the mass ratio of the separator is approximately 3%, it can release up to 33% of heat in the combustion process, see Figure 1, indicating that the combustion characteristics of separator directly affect the fire risk of the LIB [76]. Therefore, the research and development of new separator material with high thermal safety is essential.

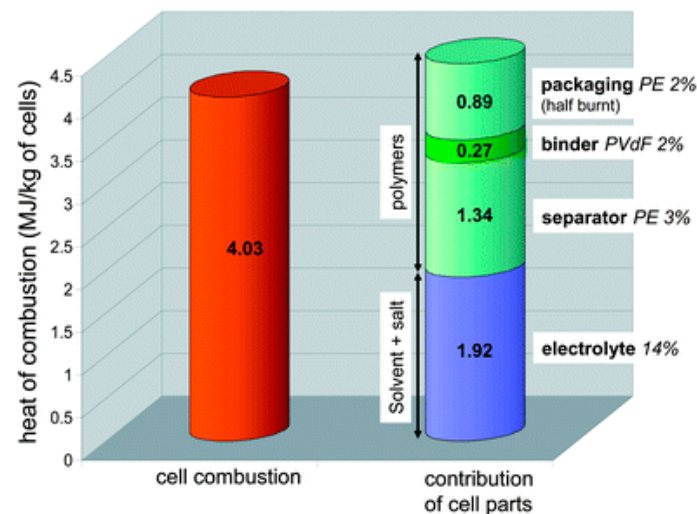


**Figure 1. The combustion heat distribution of lithium-ion battery: the overall combustion heat on the left was determined using experimental results, while the combustion heat of battery components on the right was obtained by the thermodynamic calculations.** Adopted from Ref. [76].

#### 4.2.1. Thermal Hazards of a Single Battery

With the proceeding of chain reactions inside battery during thermal runaway such as the decomposition of SEI layer, the decomposition of electrode and electrolyte, the reactions between electrode and electrolyte, and the combustion of electrolyte [101,102], substantial heat will be generated, which leads to the sharp increase of battery temperature. Figure 2 displays the typical curves of battery surface temperature and mass during the thermal runaway process, where the thermal runaway is triggered with a 2.5 kW electronic heater. As observed, the surface temperature of battery increases stably under the effect of the heater. The SEI layer decomposes at about 69 °C [90], which enables the reaction between electrolyte and anode to take place. As the temperature builds up, the intercalated lithium in the anode can also react with electrolyte and release heat [102]. At around 150 °C, the polymer separator will melt [105,104], resulting in the internal short circuit between cathode and anode, therefore a number of reactions take place that contribute to the accumulation of heat and pressure.

At approximately 150 °C, the safety vent of battery opens to decrease the pressure, hereafter gases releasing appears. As the continuous rising of battery temperature, the released combustible gases will be ignited, and then thermal runaway occurs. It can be observed that the surface temperature has a sharp increase to the peak value after thermal runaway, which ranges from 400–700 °C and it is related to battery chemistry, state of charge (SOC) and capacity etc. [105–107].

Once the safety vent cracks, quantities of gases will be ejected, which is accompanied by a clear sound [108,109]. The ejected gases are usually high-temperature, toxic and combustible, which will be ignited soon and exhibited as the first combustion. Furthermore, after thermal runaway appears, the second combustion will be generated. It is much more violent than the first one and is usually accompanied with the ejection of flame. The experimental phenomena during thermal runaway can be seen in Figure 3. According to the result of Fu et al., the axial flame temperature could reach as high as 800 °C [110]. Especially for the condition of overcharge, high-capacity and closed/semi-closed space, tremendous amounts of energy cannot be released effectively which may even result in the explosion of battery. Ouyang et al. researched the thermal runaway behavior of an overcharged 18,650 battery, and they found that the thermal runaway behavior of overcharged battery was much more violent than the normal battery. As depicted in Figure 4, where the safety vent of battery was blown away, the jellyroll was brought out and exposed to air [111]. With the help of an adiabatic calorimeter, vent sizing package 2 (VSP2), Jhu et al. found that the charged battery was prone to experiencing a thermal explosion compared to the uncharged battery, and the heat of reaction was calculated to be 26.2 kJ [112].

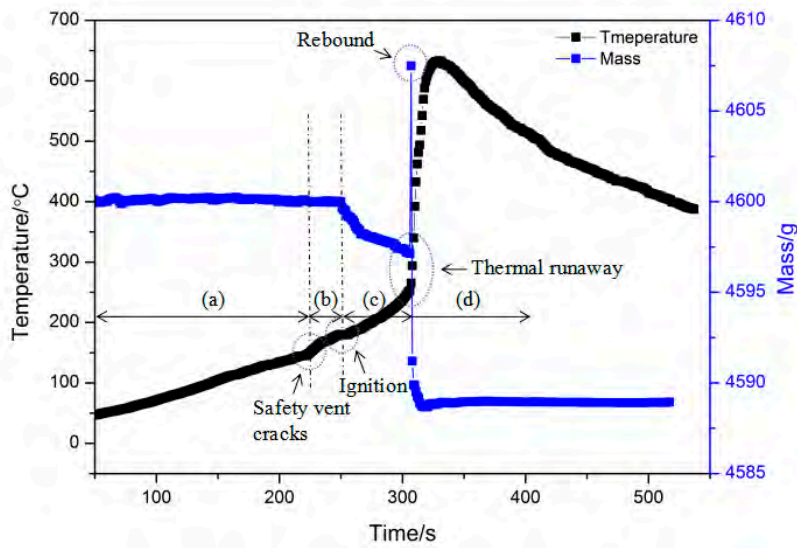


Figure 2. Typical curves of battery surface temperature and mass vs. time.

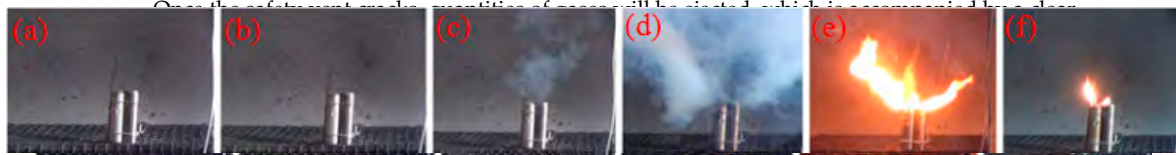


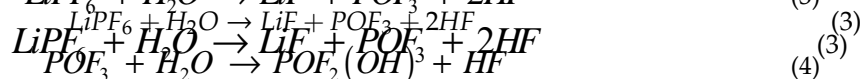
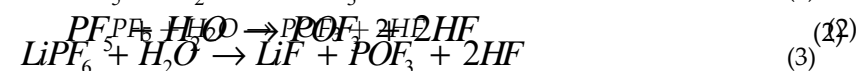
Figure 3. The experimental phenomenon during thermal runaway: (a) heating stage; (b) safety vent opening; (c) gas release; (d) ignition; (e) combustion; (f) abatement.



Figure 4. The photographs of the overcharged battery after thermal runaway test.

Figure 4. The photographs of the overcharged battery after thermal runaway test.

Commonly, quantities of toxic gases can be generated during the thermal runaway process such as  $\text{HF}$ , carbon monoxide ( $\text{CO}$ ), nitric oxide ( $\text{NO}$ ), sulfur dioxide ( $\text{SO}_2$ ), hydrogen chloride ( $\text{HCl}$ ) and hydrogen ( $\text{H}_2$ ) [76,115–116]. Due to the limited thermal stabilization of  $\text{LiPF}_6$ , it may decompose at elevated temperatures and it can be described as [117–118]:



On the other hand, the reaction between PVDF binder and lithiated graphite will occur in acidic medium and is as follows [119]:

On the other hand, the reaction between PVDF binder and lithiated graphite will occur in acidic medium and is as follows [119]:



On the other hand, the reaction between PVDF binder and lithiated graphite will occur in acidic medium and is as follows [119]:



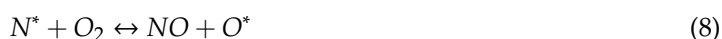
By means of fire calorimetry, Ribière et al. [76] carried out combustion experiments on pouch batteries and results revealed that an increasing amount of total HF emissions would be generated for the decreasing SOC value of battery. Besides, Ouyang et al. found that the generation of HF increased linearly with the increasing battery quantity and the burning of about 100 batteries (18,650) would release an amount of HF causing the immediate death of humans, 1.5 g [120,121].

In addition, resulting from the incomplete combustion of battery electrolyte as described in Equation (6), there will be some CO generated during thermal runaway [114]:



It is well-known that CO can bind with hemoglobin causing oxygen poisoning. By varying battery SOC and ambient pressure, Chen et al. [121] declared that with the increasing battery SOC, the amount of CO<sub>2</sub> decreased, while the amount of CO increased. The decreasing ratio of CO<sub>2</sub>/CO revealed that the combustion efficiency of battery would be lower for the high SOC battery. Besides, a low combustion efficiency could also be obtained under low-pressure conditions, and the battery with higher capacity would generate much more CO during thermal runaway [114].

Based on the research of Ribière et al. [76], NO may be produced as a reaction product of nitrogen (originating from air or fuel-bound nitrogen) and oxygen from air within the flame (thermal route of NO<sub>x</sub> production), which can be further expressed as:



NO will damage the peogaster of human and destroy the ozonosphere. Furthermore, it can be oxidized as corrosive nitrogen dioxide (NO<sub>2</sub>). With the increase of battery SOC, the amount of NO first ascends and then descends.

Additionally, sulfur-based compounds as additives are known to be used in electrolytes for their property in facilitating SEI formation [122,123]. Whereas, they will undergo degradation to form SO<sub>2</sub> at high temperatures. Similarly, SO<sub>2</sub> is harmful to the peogaster of human and it can also lead to acid rain. Moreover, the amount of SO<sub>2</sub> will ascend with the increasing battery SOC.

The generation of HCl originates from the combustion of polymers inside battery containing a binder, separator and package [124]. It is found that the amount of HCl is irrelevant to battery SOC.

Finally, one possible source of H<sub>2</sub> is the reaction between metal Li and the separator. Common separator materials are PVDF and carboxymethyl cellulose (CMC). As can be seen from the reaction detailed below, PVDF may react with metal Li and release H<sub>2</sub> under high-temperature conditions [124]:



A similar reaction of CMC and metal Li may take place to release H<sub>2</sub> which is as follows:



H<sub>2</sub> is highly reactive, and it may lead to violent combustion or explosion under external high-temperature.

### 4.2.2. Thermal Hazards of a Battery Pack

Battery packs are generally consisted of single batteries, in which the quantity of batteries depends on the application ranging from several to thousands. For example, one charge-pal usually contains 2–4 batteries (18,650), while there are more than 7000 batteries for the pack in a Tesla Model S. Consequently, battery pack possesses the thermal hazards of a single battery as described in Section 4.2.1. Whereas, different to a single battery, a battery pack possesses the hazard of thermal failure propagation, that is, the thermal failure of one or several batteries will propagate to the neighboring ones, resulting in catastrophic consequences. The thermal hazard will be heightened during the propagation; hence it is essential to pay attention to the issue of failure propagation within a battery pack [105,125–133].

Ouyang et al. carried out a set of failure propagation experiments in 18,650 packs with a size of 3 × 3 [128]. As depicted in Figure 5, the thermal failure of the battery in the lower right corner of the figure was induced by external heating, and then thermal failure propagated with a domino effect within the pack. Typically, the thermal failure of battery pack could be divided into several phases, i.e., the failure of the batteries in the former phase affected the batteries in the next phase and then caused the hierarchical propagation. Besides, they also researched the influence of several key factors such as the SOC, battery gap, failure location and pack size on the failure propagation. Results showed that higher SOC would worsen the propagation behavior of pack, in which the propagation speed grew linearly with the increasing pack SOC. It can be attributed to the fact that battery SOC affects the internal lithium ions distribution which will further influence the chain-reactions during thermal runaway. By increasing the battery gap, it was found that the risk of failure propagation within pack could be greatly reduced and the propagation speed exhibited a square index decline relationship with the battery gap, which was the result of radiation decay with squared distance. Upon further increasing

the battery gap, the propagation behavior would eventually be interrupted. If the battery close to the center of pack underwent thermal failure, the failure propagation was revealed to be aggravated significantly since the failure of the central battery would affect the surrounding batteries with the largest scope and lead to the thermal failure of the whole pack in a relatively short time. Moreover, if hazard of battery pack, some methods such as improving the separator property, enhancing the heat dissipation, adding an insulation board and decreasing the SOC may be considered.

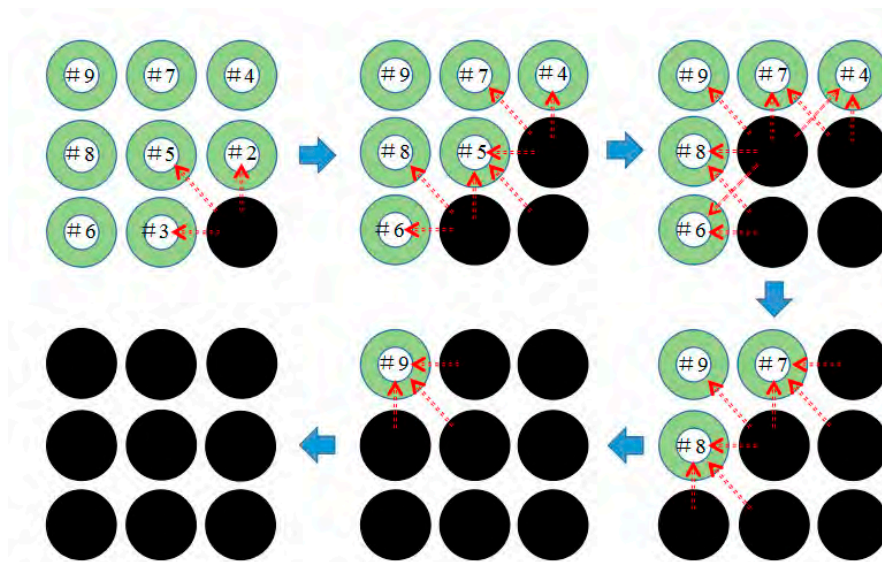
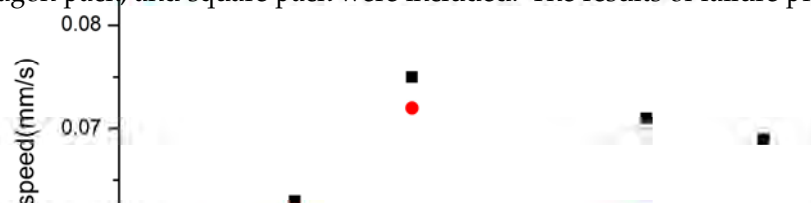


Figure 5. Schematic of thermal failure propagation.

Due to the application scenarios, it is common to see that batteries are generally arranged in various shapes or modes within battery packs. Ouyang et al. [125] compared the thermal failure propagation of battery packs with various shapes, where the triangle pack, rectangle pack, parallelogram pack, line pack, hexagon pack, and square pack were included. The results of failure propagation speed



are summar-  
propagation

revealed that the triangular pack might be the best choice of battery module due to its lower propagation hazard and higher space utilization.

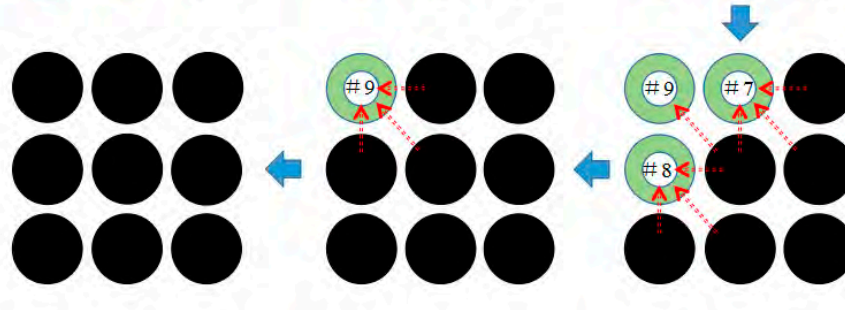


Figure 5. Schematic of thermal failure propagation.

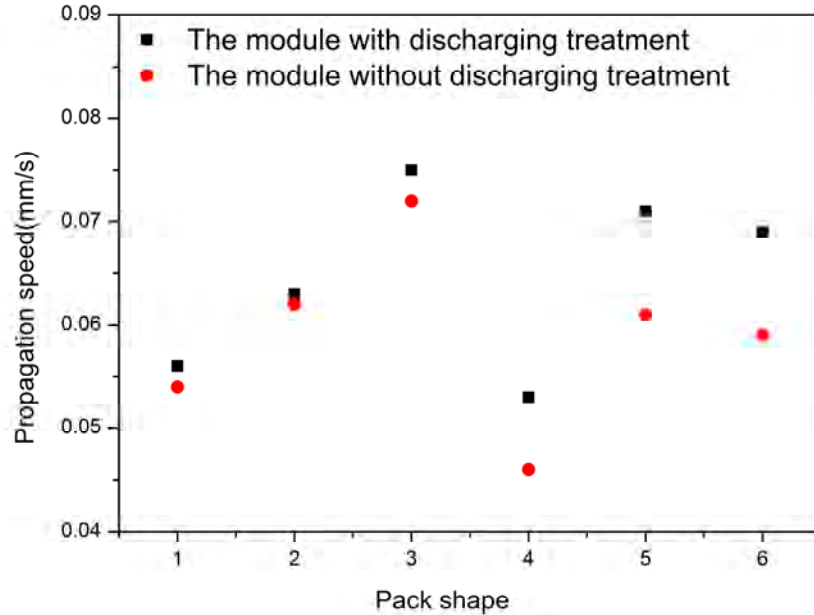


Figure 6. The propagation speed of packs with various shapes where the numbering 1, 2, 3, 4, 5 and 6 represents the triangle pack, rectangle pack, parallelogram pack, line pack, hexagon pack and square pack respectively.

Additionally, resulting from the disadvantages of traditional PCM such as low conductivity and diffusivity [134,135], it was found that the failure propagation behavior of a pack wrapped with PCM would be severer. The low conductivity and diffusivity of PCM caused a great deal of heat to be accumulated inside pack, and the close stacking of PCM reduced the heat release, therefore the propagation of thermal failure was accelerated. Besides, traditional PCM was flammable and it would be ignited by external heating which further aggravated the thermal failure propagation. In short, it is demanding to avoid the pack wrapped with traditional PCM being exposed to external heating or high temperature, especially for the flammable PCM. On the other hand, more work should be done to improve the thermal conductivity, diffusivity and fire resistance of PCM.

Apart from the factors above, it was determined that tab configuration also had a huge influence on the failure propagation behavior of the pack as a result of the heat transfer from the tab. According to the work of Lopez et al. [126], it was revealed that a branched style of tabbing as shown in Figure 7 improved the voltage retention as well as the safety of the pack over a serpentine style of tabbing as the shorted trigger battery was electrically better isolated from the rest of the pack when the tabs were branched. Lamb et al. [127] examined the failure propagation behavior of packs consisting of cylindrical and pouch batteries respectively, where the thermal failure was induced in a single battery. They observed that cylindrical batteries were less prone to propagation compared to the pouch batteries owing to the limited contact between neighboring batteries.

On the other hand, numerical simulation methods were also applied to investigate the failure propagation behaviors of battery packs [136–144]. Feng et al. [136] established a 3D thermal runaway propagation model for a large format LIB pack based on the energy balance equation. They proposed that the thermal failure propagation could be postponed by increasing the thermal runaway triggering temperature, which was generally reflected as the collapse temperature of battery separator. Furthermore, it was revealed that reducing the total electrical energy released during thermal



Hefei which mean that the primary batteries at lower pressure were less dangerous than those at higher pressure [163]. Fu et al. studied the ignition and combustion characteristics of LIBs under low atmospheric pressure using a low-pressure tank from 30 to 101 kPa. Results indicated that the low atmospheric pressure could largely extend the ignition and weakened the combustion intensity of LIBs [110]. In summary, the study of the combustion characteristics of LIBs under low-pressure conditions has scarcely been examined, while it is of great importance to the safety management of LIBs for air transport and more work on this issue are necessary to be conducted in the future.

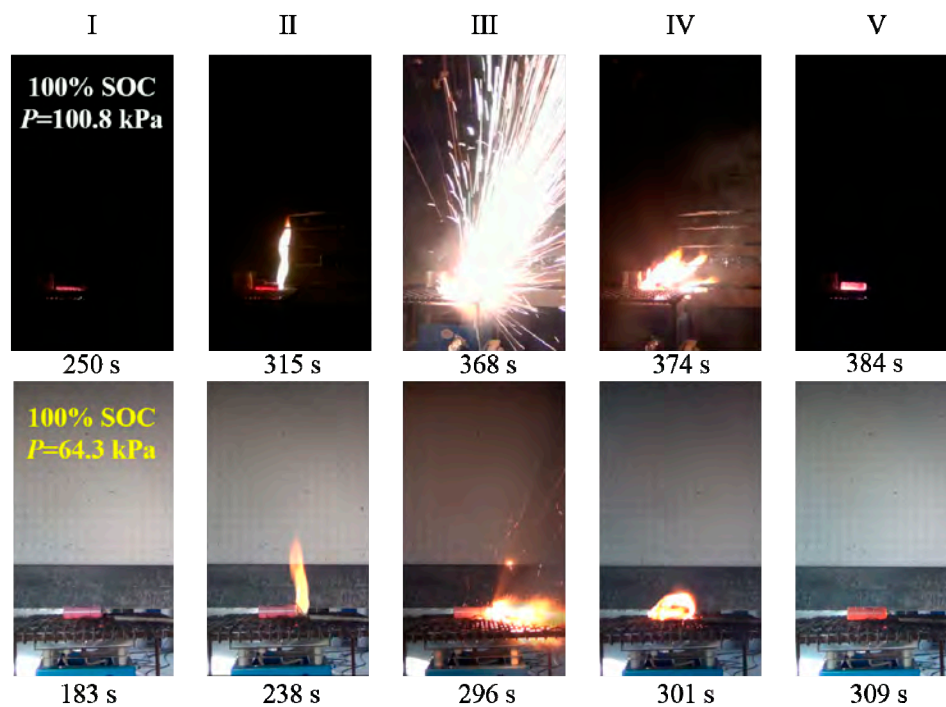


**Figure 8.** The burning process of 100% SOC (state of charge) 18,650 batteries at two pressures.

#### 4.4. Thermal Hazards of Typical Commercial Lithium-Ion Batteries

Lithium cobaltate oxide (LCO) cathode material was first put forward by the team of Prof. Goodenough in 1980, and it was also the first time that Li was introduced into the positive electrode in batteries, which promoted the application and development of a negative electrode without Li and, at the same time, improved the charging voltage of batteries. Most importantly, the lack of Li metal anode greatly improved the safety of batteries [164]. Furthermore, Prof. Goodenough's team proposed the lithium manganese oxide (LMO) cathode material in 1983. Although its theoretical capacity is only about half of that of LCO, its reversible specific capacity is excellent [165]. With the emergence of LCO and LMO, many lamellar and spinel LIB positive electrode materials based on transition metal oxides were developed in the following decade. Subsequently, in 1997, Goodenough's team reported the application of lithium iron phosphate (LFP) positive electrode materials, and, in further research, solved a series of problems of LFP positive electrode materials by carbon coating modification, so that LFP could be applied commercially on a large scale [166]. Therefore, the commercial cathode material structural system has been built, and the following positive electrode materials are improved on the basis of these three materials, while the NMC and lithium nickel cobalt aluminate oxide (NCA) materials improve the performance of the battery by regulating the content of the three elements in LCO.

##### 4.4.1. Lithium cobaltate oxide

At present, LCO cathode material still occupies a major part in the 3C field, while the safety is relatively poor, so it is gradually being replaced by other positive electrode materials [167,168]. The active surface of the LCO cathode material can catalyze the decomposition of the carbonate electrolyte then release a large amount of heat, thus causing the thermal runaway of battery [169,170]. Zhang et al. studied the overcharge capacity degradation mechanism of LCO/graphite battery and found that the dissolution of current collector led to changes in the structure of the SEI

#### 4.4.1. Lithium cobaltate oxide

At present, LCO cathode material still occupies a major part in the 3C field, while the safety is relatively poor, so it is gradually being replaced by other positive electrode materials [167,168]. The active surface of the LCO cathode material can catalyze the decomposition of the carbonate electrolyte then release a large amount of heat, thus causing the thermal runaway of battery [169,170]. Zhang et al. studied the overcharge capacity degradation mechanism of LCO/graphite battery and found that the dissolution of current collector led to changes in the structure of the SEI layer and electrodes, thereby reducing the battery capacity and increasing the risk of thermal runaway [171]. In view of the safety problem associated with LCO, researchers have proposed a variety of solutions. Ji et al. [172] recommended a phosphazene additive  $N_3P_3(OPh)F_5$  (PFPN), which could be oxidized to form a protective cathode electrolyte interface (CEI) before the electrolyte, greatly improving the safety of battery. Deng et al. [173] coated and doped LCO-positive electrode materials by adding Al and Ti elements, which greatly improved the thermal stability, increased the thermal runaway critical temperature and reduced the heat release. With the increasing demand for high-voltage LCO batteries, further studies are needed for the modification of LCO cathode materials, safe electrolytes and additives at high voltage.

#### 4.4.2. Lithium iron phosphate

LFP is the positive electrode with the best thermal stability among the current commercial LIB cathode materials. Yamada et al. compared the thermal stability of various electrode materials at high temperature, and LFP showed lower oxygen and heat release [174]. Jiang et al. used an ARC to analyze the thermal stability of LCO, NMC and LFP with LiBOB and  $LiPF_6$  electrolytes, and the thermal stability of LFP was found to be the best in both systems [175]. The high thermal stability of LFP is rooted in its strong structural stability during charging and discharging [176]. However, due to the poor conductivity of LFP, the migration rate of lithium ions is very low, therefore surface carbon coating, and  $Cu^{2+}$  or  $Mg^{2+}$  plasma doping are required for modification [177,178]. Furthermore, the modification of LFP is still a research focus. How to increase the electrochemical performance of LFP while maintaining the high level of safety is a key concern of researchers.

#### 4.4.3. Lithium nickel manganese cobalt oxide

NMC ternary material is developed on the basis of LCO positive electrode materials by adjusting the content of Ni, Mn and Co elements. Co element plays an important role in the electronic conductance of battery, while Ni element can improve the capacity. Mn element is responsible for stabilizing the structure of positive electrode material and preventing the capacity decline of battery [179,180]. With the rapid development of EVs, ternary materials have attracted extensive attention due to their high capacity, while ternary materials with a high Ni content have gradually replaced low-Ni materials due to the lower price. However, with the increase of Ni content, the safety of batteries is greatly compromised [181]. The content of Ni in NMC materials increases gradually, from NMC111 to NMC532 and NMC622, but this still cannot meet the current demand for power battery capacity and low cost. Therefore, NMC811 materials have received extensive attention in recent years, but the extremely high reactivity between positive electrode and electrolyte also brings great safety risks [16]. Ma et al. studied the effect of vinylene carbonate (VC) and fluoroethylene carbonate (FEC) additives on the reactivity of lithium intercalation carbon ( $Li_xC$ ) and electrolyte, and the results showed that the addition of FEC could reduce the self-heating rate between graphite and electrolyte [182]. Three component additives, such as VC211 and PES211, could improve the cycling performance and the chemical stability of electrode/electrolyte, and the effect was much better than that of single or binary additives [183]. According to the latest research results, the thermal runaway of NMC batteries is mainly caused by chemical crosstalk between the electrodes, the oxygen released by cathode diffuses to the anode, at which point, an oxidizing reaction occurs and emits a large amount of heat, causing

the thermal runaway of the NMC batteries. This is different from the traditional view that the main reason is the breakage of the diaphragm material, which leads to the internal short circuit then causes thermal runaway. Thus, it is possible to fundamentally solve the safety problem of high Ni ternary material [184].

#### 4.4.4. Lithium nickel cobalt aluminate oxide

Similar to NMC material, NCA ternary material was also developed on the basis of LCO positive electrode materials by adjusting the content of Ni, Co and Al elements. Within, Ni and Co elements are applied to improve the capacity and the electronic conductance, respectively. The main purpose of Al addition is to stabilize the lattice structure and avoid structural collapse during charging/discharging. So far, NCA materials are generally regarded as one of the most appealing materials due to their comparable operating voltage, energy density and ideal properties for practical applications [185]. Especially for the  $\text{LiNi}_{0.80}\text{Co}_{0.15}\text{Al}_{0.05}\text{O}_2$  cathode, which has achieved ubiquitous commercial success. The remaining problem for NCA material is the rapid capacity fading during cycling, which is due to the mixing of Li/Ni cations [186]. Because the radii of  $\text{Ni}^{2+}$  and  $\text{Li}^+$  are similar, it is easy for  $\text{Ni}^{2+}$  to enter the lithium layer, therefore results in capacity loss and thermal hazard. At present, several studies have been reported on the strategies to improve the stability of NCA materials [187–189]. These studies are mainly based on various cationic doping in Ni-rich cathode materials to cease the migration of  $\text{Ni}^{2+}$  towards the  $\text{Li}^+$  site. Moreover, doping in the  $\text{Li}^+$  intercalation site is also a very important strategy to reduce structural disorientation. Among, magnesium (Mg) and sodium (Na) are the most well-studied dopants that can be embedded into the  $\text{Li}^+$  site.

## 5. Management and Countermeasures

In view of the non-negligible thermal hazards of LIBs involving components, a single battery and a battery pack, management or countermeasures regarding these thermal hazards must be conducted. In the present study, the following is discussed: (1) the use of safety devices within battery; (2) the application of fire retardant (FR) additives; (3) the thermal management of battery; (4) provision of a warning once hazard occurs and (5) the firefighting after thermal hazard forms. The former three countermeasures aim to enhance the inherent safety of LIBs and decrease the possibility of hazard, and the others are applied to constrain the deterioration of thermal hazard, thereby reducing the damage.

### 5.1. Safety Devices within Battery

Due to the inherent hazards accompanied with LIB, manufacturers have developed several safety devices within the battery such as a safety vent, current interrupt device (CID) and positive temperature coefficient (PTC) to prevent the appearance of excessive current, temperature or pressure. Therefore, safety device can be regarded as a protective measure owed by the battery itself.

#### 5.1.1. Safety Vent

During the operation of the LIB, especially under abusive conditions, it is common to see that gases will be released inside battery. Thereby, the safety vent was proposed in response to the continuous increase of pressure inside battery, allowing the escape of excessive gases. Generally, a safety vent is composed of a gasket containing a puncture film and a spike. The spike is located at the top of the battery, while the gasket lies below it. Once the pressure inside battery builds up, the gasket squeezes upward and deforms, enabling the puncture film punctured by the spike, therefore the dangerous rupture of battery casing can be terminated [190–193]. Moreover, safety vents can be designed to operate at pre-set internal battery temperatures to meet the requirement of practices.

### 5.1.2. Current Interrupt Device

Another common safety device is called the CID, and it can be activated by high temperature. Under the conditions such as overheating, overcharging and short-circuiting, an increase of temperature can be seen inside the battery causing an increase in the vapor pressure of the electrolyte solvent; therefore, the solder joints welded to the aluminum sheet and the pressure relief sheet will fall off and the pressure relief sheet will turn over leading to the broken circuit inside battery [193]. Compared to the mechanism of safety vent releasing the internal pressure, the CID is used to interrupt battery current, which subsequently prevents the occurrence of hazard.

### 5.1.3. Positive Temperature Coefficient

Besides, the PTC based on materials are also widely used among LIBs, whose resistance increases dramatically in response to the rapid rise of temperature [194–199]. For example, if a large current flows across the PTC element, its temperature increases abruptly, while the PTC works. A concomitant and abnormally high resistance of the PTC element prevents current flow which limits the further deterioration of heat generation. Once the large current is removed, the battery and PTC element cool and the resistance of the latter drops, allowing the resumption of charge/discharge. Overall, the primary purpose of PTC devices is to protect batteries against abusive electrical conditions such as external short circuit and overcharge etc.

## 5.2. Fire Retardant

As known, the combustibility of conventional battery components, e.g., electrolyte and separator bring an inherent hazard to LIB which may induce the occurrence of fire or combustion. Thereby, an increasing number of researchers endeavor to investigate how to change flammable components into non-flammable ones or how to develop new substance to add into battery to reduce the combustibility. Herein, a summary is detailed on the studies on FR additives of electrolyte and separator in LIB.

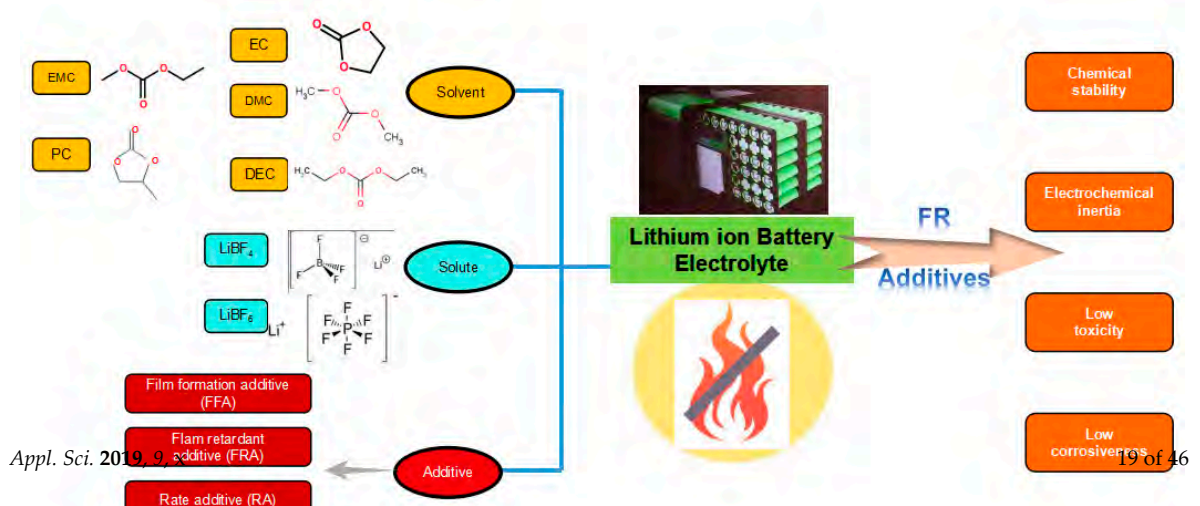
### 5.2.1. Fire-retardant Electrolyte

The electrolyte of a commercial LIB is a mixture of organic carbonates such as solvents and lithium salt, in which linear carbonates such as DMC, EMC or diethyl carbonate (DEC) and cyclic carbonates such as EC and propylene carbonate (PC) may be included. These organic carbonates are highly flammable which causes great concerns regarding their safety in LIB [200,201]. To solve this problem, the most straightforward way is to add FR components into solvents or thoroughly replace the flammable solvents [202].

However, some conflicts still exist between the property of FR additive and the electrochemical performance of LIB. In order to ensure the electrochemical performance of battery as much as possible, additives are necessary to meet the following requirements as depicted in Figure 9: (1) good chemical stability, no chemical reaction with battery components; (2) electrochemical inertia, no adverse electrochemical reactions within the normal operating voltage range of LIB; (3) suitable physical properties including conductivity, viscosity, boiling point, density, solubility etc.; (4) low toxicity, good machinability and appropriate cost [202].

Normally, the FR mechanism can be divided into two types: gas physical mechanism and chemical free-radical capture mechanism [203,204]. The former is based on oxygen isolation via the formation of a FR vapor and absorbing heat simultaneously, while the latter one is based on the additives capturing active free radicals and acids produced by combustion reaction to stop combustion development. Based on the elements contained and the working mechanism, currently studied FR additives for electrolytes can be divided into four main categories: phosphorus FR additives, fluoride FR additives, ionic liquid FR additives and composite FR additives, as illustrated in Figure 10.

possible, additives are necessary to meet the following requirements as depicted in Figure 9: (1) good chemical stability, no chemical reaction with battery components; (2) electrochemical inertia, no adverse electrochemical reactions within the normal operating voltage range of LIB; (3) suitable physical properties including conductivity, viscosity, boiling point, density, solubility etc.; (4) low toxicity, good machinability and appropriate cost [202].



studied FR additives for electrolytes can be divided into four main categories: phosphorus FR additives, fluorine FR additives, ionic liquid FR additives and composite FR additives, as illustrated in Figure 10.

Figure 9. The common constituents of LIB electrolytes and the requirement of FR additives.

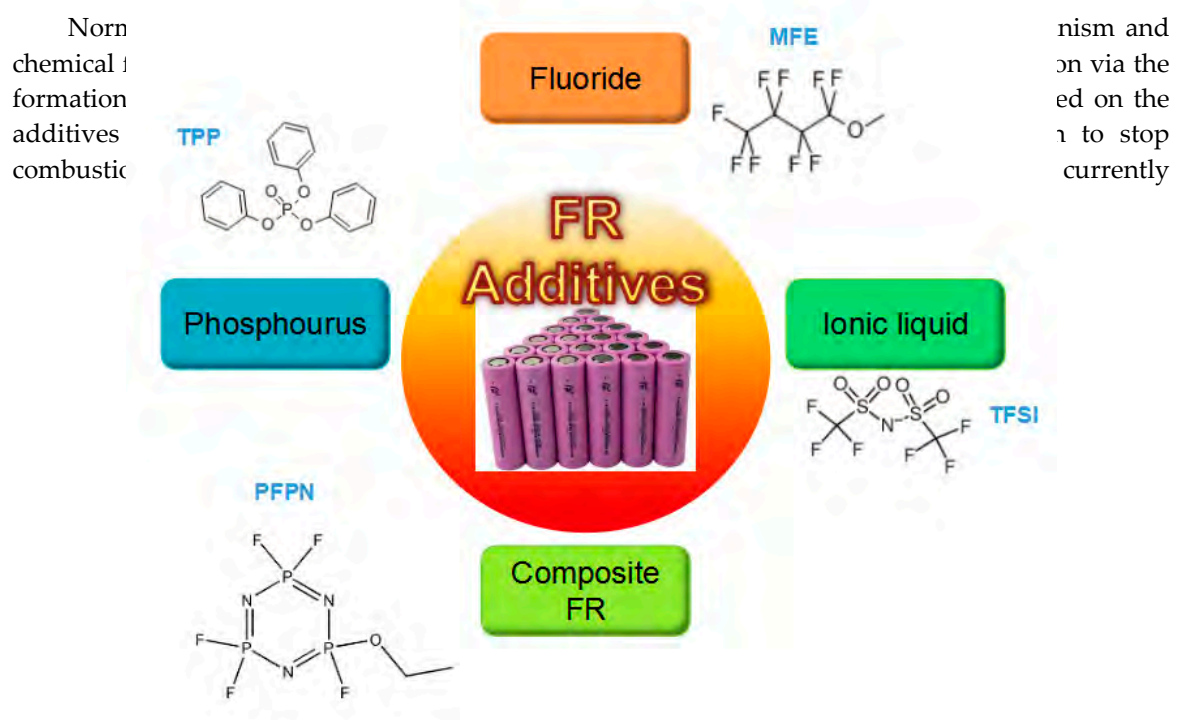
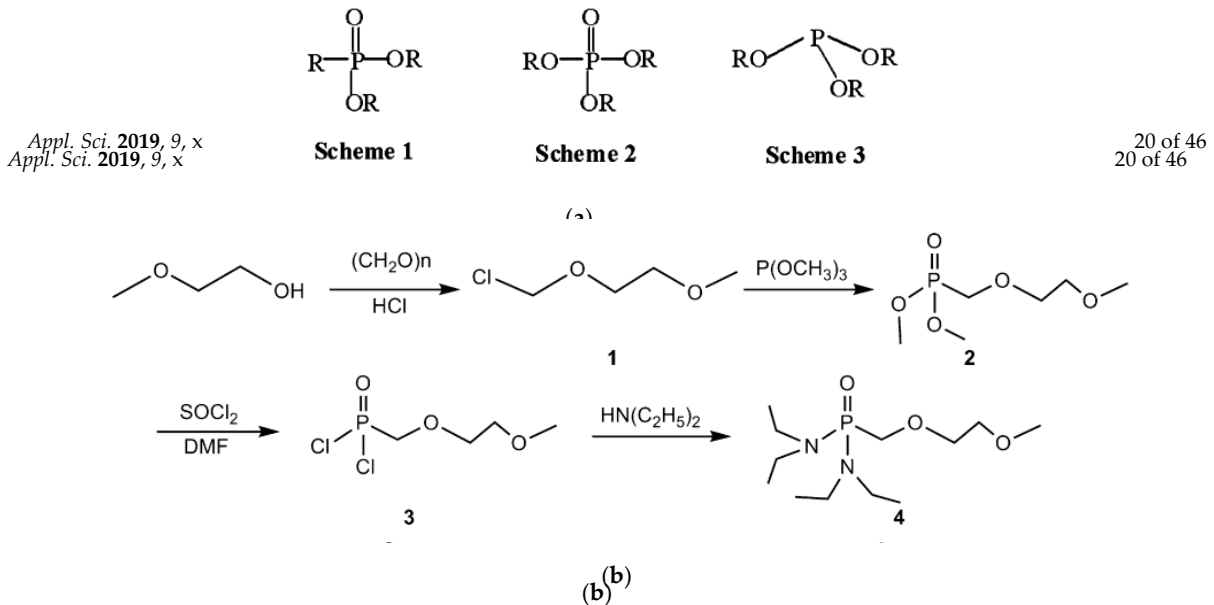


Figure 10. Typical FR additives in LIB electrolytes.

(1) Phosphorus Additives

Considering their advantages such as environmental persistence, ability to bioaccumulation and low toxicity, organophosphorus compounds are one of the most popular candidates for FR additives in LIBs [205]. They will decompose at high temperature to produce hydrogen phosphide (PH<sub>3</sub>) which will continue to transform into meta-phosphorous acid (HPO<sub>3</sub>), H<sub>2</sub>PO<sub>3</sub> will promote the carbonation reaction of carbonate, PO<sub>3</sub> and PO<sub>2</sub> will capture H<sub>2</sub> and H<sub>2</sub>O and therefore suppress the combustion of electrolytes. Until now, Xiang et al. [206] investigated the electrolyte with three kinds of dimethyl methyl phosphonate (DMMP) additives respectively (which could significantly suppress the flame ability while only causing a small decrease in the electrochemical performance of battery, see Figure 11(a). Hu et al. [207] synthesized a new phosphinamidate bis(N,N-diethyl) (2-methoxyethoxy) methylphosphonamidate (DEMEMPMA) as the N-P collaborative FR additive in electrolyte and found that 10 vol.% of DEMEMPMA to 0.9 M LiPF<sub>6</sub>/EC/DMC could significantly inhibit the burning of electrolytes and provide a wide electrochemical window, see Figure 11(b). Besides, Murmann et al. [203] performed studies on several phosphates with different fluorination concentrations to determine the influence of

(1B) will promote the carbonation reaction of carbonate, PO· and PO<sub>2</sub>· will capture H· and O· and; therefore suppress the combustion of electrolytes. Until now, Xiang et al. [206] investigated the electrolyte with three kinds of dimethyl methylphosphonate (DMMP) additives respectively which could significantly suppress the flammability while only causing a small decrease in the electrochemical performance of battery, see Figure 11(a). Hu et al. [207] synthesized a new phisohinamidate bis(N,N-diethyl) (2-methoxyethoxy) methylphosphonamidate (DEMEMP) as the FR additive. The FR additive DEMEMP as the FR additive DEMEMP and 90% LiPF<sub>6</sub>/EC/DMC of DEMEMP significantly inhibit the EC/DMC of delignification and provide a wide electrochemical window as depicted in Figure 11(b). Besides, Muryama et al. [203] performed studies [203] several phosphates with different phosphorus content to determine the difference of the fluorination degree within different phosphorus content. The results showed that the partially fluorinated phosphate offered the best FR results. FR results.



**Figure 11.** (a) Schemes for the three kinds of phosphorus. Adopted from Ref. [206]; (b) The synthetic route of DEMEMP. Adopted from Ref. [207].

(2) Fluoride Additives  
(2) Fluoride Additives  
(2) Fluoride Additives

Fluorinated substituents in organic molecules are known to suppress the flammability of molecules and reduce the boiling temperature and viscosity. By replacing hydrogen atoms with fluorine atoms, H<sub>2</sub> radicals can be reduced or eliminated to yield a non-flammable electrolyte. Ding et al. [208] introduced tris(2,2,2-trifluoroethyl) phosphite (TFP) as the FR additive into a LiPF<sub>6</sub>-based electrolyte containing EC/PC/EMC, and their results showed that the addition of TFP caused a continuous decrease in the dielectric constant and a continuous increase in the glass transition and the dielectric constant, therefore the flammability of the electrolyte was substantially reduced. Zeng et al. [209] synthesized a novel fluorinated alkyl phosphonate bis(2,2,2-trifluoroethyl) methylphosphonate (TFMP) as the FR additive to reduce the flammability of electrolyte. see Figure 12. Their experiments demonstrated that the addition of 20 vol.% TFMP could yield an electrolyte that was hardly flammable while having the least impact on the electrochemical performance.

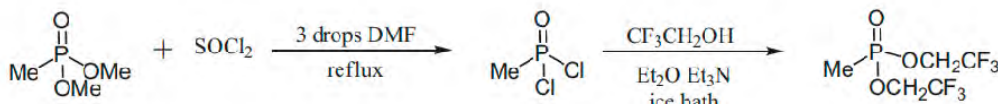


**Figure 12.** The synthetic route of bis(2,2,2-trifluoroethyl) methylphosphonate (TFMP). Adopted from Ref. [209].

(3B) Ionic Liquid  
(3) Ionic Liquid

An ionic liquid usually refers to a liquid salt at room temperature solely composed of anions and cations. It possesses certain characteristics such as it is non-volatile, nonflammable, pollution free and has a wide electrochemical window. Hence, the electrolyte with ionic liquid added is hoped to replace the traditional organic electrolyte to improve the safety of LIBs [210–214]. Rectenwald et al. [215] reported the successful design of a new class of lithium salts, phosphoryl-rich FR ions (FR-IONS) for safer LIB, see Figure 13. The thermogravimetric analysis of these lithium salts showed

An ionic liquid usually refers to a liquid salt at room temperature solely composed of anions and cations. It possesses certain characteristics such as it is non-volatile, nonflammable, pollution free and has a wide electrochemical window. Hence, the electrolyte with ionic liquid added is hoped to replace the traditional organic electrolyte to improve the safety of LIBs [210–214]. Rectenwald et al. [215] reported the successful design of a new class of lithium salts, phosphoryl-rich FR ions (FRIONs) for safer LIB, see Figure 13. The thermogravimetric analysis of these lithium salts showed that they were thermally stable up to around 200 °C. Moreover, the pyrolysis combustion flow calorimetry revealed that these salts would produce high char yields upon combustion which indicated the excellent FR property. Besides, the promising ionic liquid pentafluorocyclotriphosphazene (FPPN) is known to exhibit both an excellent FR performance and electrochemical properties. Dagger et al. [216] investigated a standard electrolyte mixed with 5 wt.% FPPN towards abuse tolerance in a 5 Ah battery and their results showed that FPPN significantly reduced the self-heating rate of the battery in the temperature range from 80 to 110 °C. Further, they conducted nail penetration and external short circuit experiments, but found no significant difference between standard and FPPN-containing batteries.

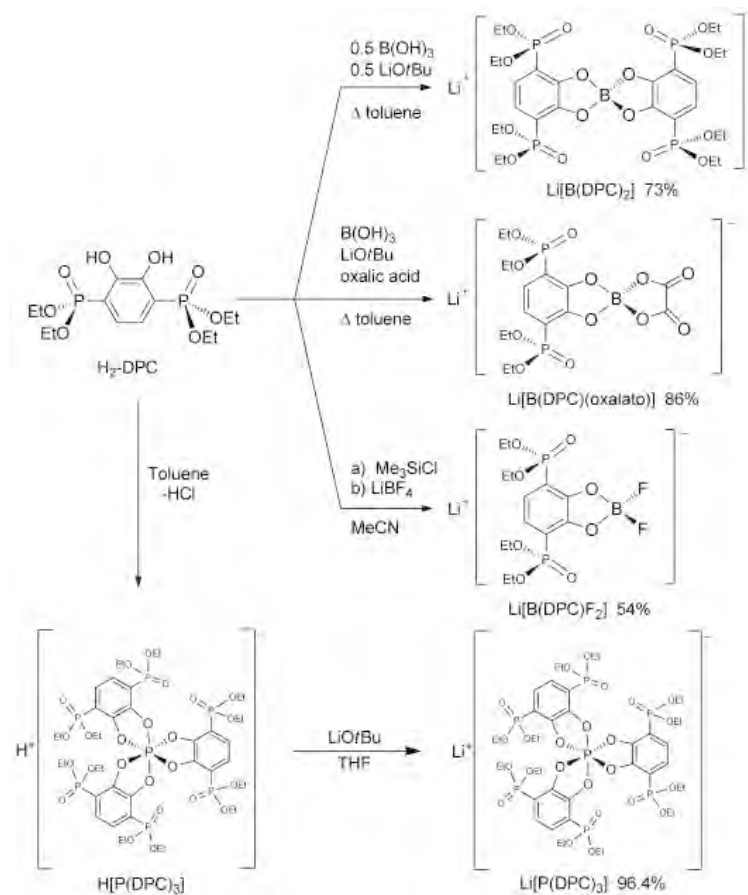


**Figure 13.** Conversion of 1,2-diphenylphosphinic acid into phosphor-rich FR ions (FRIONs) adopted from Ref. [215].

Adopted from Ref. [215].

#### (4) Composite Additives

Use of a single flame retardant generally requires adding a large amount. In addition, the solubility of the additive and the electrolyte compatibility are also relatively limited. Thus, it is necessary to use a composite approach by comparing the advantages and disadvantages of various types of retardant types of retardants to configure more suitable additives for LIB. Wu et al. [217] synthesized a phosphazene compound, triethoxyphosphazene-N-phosphoryl diethyl ester (PNP) by a facile method and characterized it as a FR electrolyte additive for LIB, see Figure 14. They found that the self-extinguishing time (SET) value of 10% PNP in the electrolyte was decreased by 40% compared to the base electrolyte, implying a strong inhibition to the flammability. Additionally, Li et al. [218] synthesized a multi-functional FR electrolyte additive pentafluoro cyclotriphosphazene (PFPN). The electrolyte with 5 vol.% of PFPN was found to be a non-flammable electrolyte, moreover it could reduce the charge transfer resistance of battery resulting in a decreased electrode polarization and enhanced electrochemical performance at lower temperatures. Finally, several representative

solubility of the additive and the electrolyte compatibility are also relatively limited. Thus, it is necessary to use a composite approach by comparing the advantages and disadvantages of various types of retardants to configure more suitable additives for LIB. Wu et al. [217] synthesized a phosphazene compound triethoxyphosphazene-N-phosphoryldiethylester (PNP) by a facile method and characterized it as a FR electrolyte additive for LIB, see Figure 14. They found that the self-extinguishing time (SET) value of 10% PNP in the electrolyte was decreased by 40% compared to the base electrolyte, implying a strong inhibition to the flammability. Additionally, Li et al. [218] synthesized a multi-functional FR electrolyte additive pentafluoro cyclotriphosphazene (PFPN). The electrolyte with 5 vol.% of PFPN was found to be a non-flammable electrolyte; moreover, it could reduce the charge transfer resistance of battery resulting in a decreased electrode polarization and enhanced electrochemical performance at low temperature. Finally, several representatives belonging to the four kinds of additives above are listed in Figure 15.

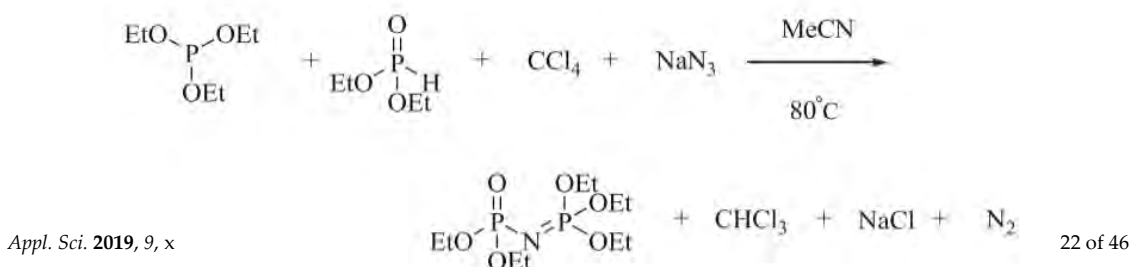


**Figure 14.** The synthetic route of triethoxyphosphazene-N-phosphoryldiethylester (PNP). Adopted from Ref. [217].

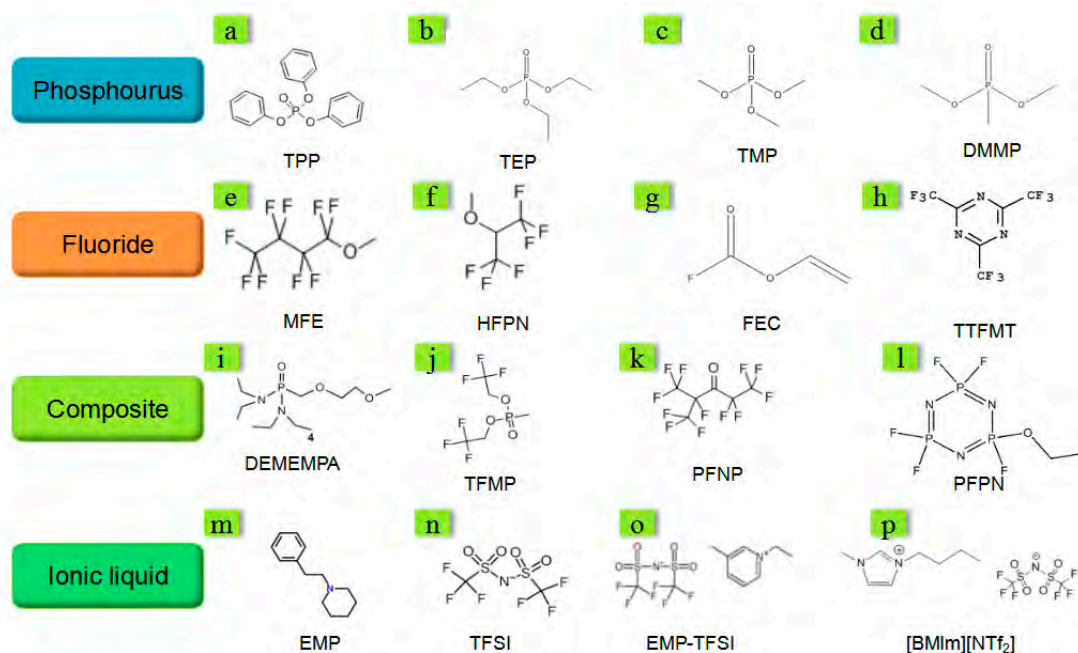


**Figure 15.** The chemical structures of several typical retardant electrolyte additives.

Commonly, the choice of FR electrolyte additive requires a comprehensive consideration including conductivity, solubility, retardant efficiency and cost etc. Table 2 summarizes the advantages/disadvantages of the typical FR additives stated above. It can be observed that the key challenges of these four kinds of FR additives which remain to be solved are: (1) the phosphorus FR needs to prevent reductive decomposition and coinsertion; (2) a better retardant efficiency and a lower cost are necessary for fluoride FR; (3) the ionic liquid FR shall be enhanced by reducing its cost while enhancing the electrochemical compatibility; (4) the composite FR must simplify their synthesis process and thus they can be obtained at a lower cost and in a shorter time. In brief, the development of FR additive aims to achieve a balance between the electrochemical performance and the retardant effect. Going forward, we will obtain knowledge of a more advanced substance and then make good use of synergistic effects to get a win-win situation.

**Table 2.** The comparison of several typical fire-retardant electrolyte additives.

Type	Advantages	Disadvantages
Phosphorus	Low cost; Simple synthesis process	Poor electrochemical compatibility; Low retardant efficiency
	Good electrochemical compatibility;	

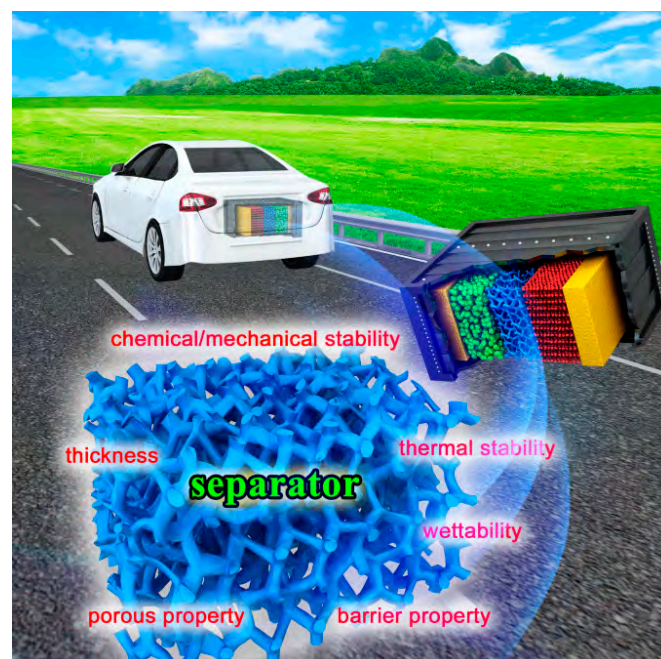
**Table 2.** The comparison of several typical fire-retardant electrolyte additives.

Type	Advantages	Disadvantages
Phosphorus	Low cost; Simple synthesis process	Poor electrochemical compatibility; Low retardant efficiency
Fluoride	Good electrochemical compatibility; Simple synthesis process	Low retardant efficiency; High cost
Ionic liquid	Appropriate to low-temperature environment	Complicated synthesis process; Low thermal stability; Low retardant efficiency
Composite	High retardant efficiency; Good electrochemical compatibility	Complicated synthesis process; High cost

### 5.2.5. Fire Retardant Separator

23 of 46

Within LIB, a separator is considered to be a critical component in securing battery safety [219–222]. It acts as the separation between the cathode and the anode while providing a pathway for lithium ion migration. Once the separator fails, an internal short circuit between electrodes may occur and lead to the thermal failure of LIBs [223–225]. As shown in Figure 16, a safe separator has strict demands on the following six factors: (1) chemical/mechanical stability, (2) thickness, (3) thermal stability, (4) wettability, (5) barrier property and (6) porous property.

**Figure 16.** The schematic diagram of separator and the requirement for safety.

As stated before, a commercialized separator typically consists of PE or PP, and has persistent drawbacks of a low melting temperature and poor wettability for liquid electrolyte, which make it difficult to widely adopt in large-scale LIB. To overcome these obstacles and enhance its thermal safety, a composite separator may be a feasible solution. Yeon et al. [226] synthesized several FR composites ( $\text{Al}_2\text{O}_3$ -sputtered PE separator, AA(OH)<sub>2</sub> composite, and (G-O)-composite) and verified in their experiments that these composites exhibited superior FR properties compared to traditional separator as they could reduce heat release at high temperatures. Meanwhile, another research group also synthesized a composite FR separator. Led et al. [227][228][229] developed and investigated a brominated poly(2,6-dimethyl-1,4-phenylene oxide) (BPPO)-based separator to improve the FR ability and thermal ability. Besides, Zhang et al. [229] developed a sustainable, heat-resistant and cellulose-based composite FR separator for high-performance LIB, namely FCCN, i.e., flame-retardant and thermal resistant cellulose-based composite nonwoven separator which showed superior heat tolerance and good mechanical strength.

ability. Besides, Zhang et al. [229] developed a sustainable, heat-resistant and cellulose-based composite FR separator for high-performance LIB, namely FCCN, i.e., flame-retardant and thermal resistant cellulose-based composite nonwoven separator which showed superior heat tolerance and good mechanical strength.

### 5.3. Battery Management System

In practical applications, LIBs are required to operate at different conditions where a complicated temperature environment such as high temperature, low temperature and a largely varying temperature etc. may be involved. As stated by many scholars, temperature greatly affects battery from both safety and performance points of view [230–234]. Hence, it is of great importance to configure an efficient battery management system (BMS) that allows for control of battery temperature and prevents the occurrence of thermal hazard.

BMS applied in EV is usually comprised of sensors, actuators and controllers, and it is used to achieve three main aims: (1) to protect battery from being damaged; (2) to make battery operate within the proper voltage and temperature interval; (3) to maintain the performance of battery to meet the requirement of vehicles [235]. Traditionally, BMS can be briefly divided into two categories: internal thermal management (ITM) and external thermal management (ETM) which is further displayed in Figure 17.

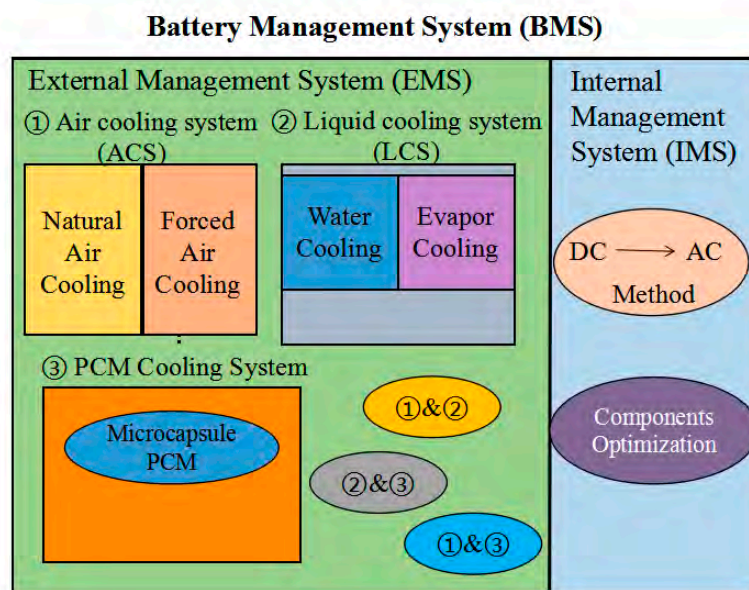


**Figure 17.** Summary of battery thermal management systems including the external management system (air cooling system, liquid cooling system, PCM cooling system) and the internal management system (alternating system, component optimization).

ITM, also known as intrinsic safety management, refers to those thermal management methods applied at the battery level in which the thermal management strategies exist in the core region of the battery monomer. One common approach is via optimizing battery components to be safer so that less heat is generated and better uniformity can be achieved. Choi et al. [236] proposed a cooling method to remove the heat generated within the lead-acid battery by means of controlling electrolyte circulation rate. Their results showed that such an approach could provide a desirable low temperature field and the temperature could be controlled to a desirable level. As shown in Figure 18a, Mohammadian et al. [237] introduced a particular type of internal cooling method, where liquid electrolyte served as a coolant and flowed through the micro-channels dispersed in electrodes. Besides, Bandhauer et al. [238] developed a novel system that utilized an internal evaporator with micro-channels incorporated in a thick current collector and then applied to side cooling, see Figure 18b.

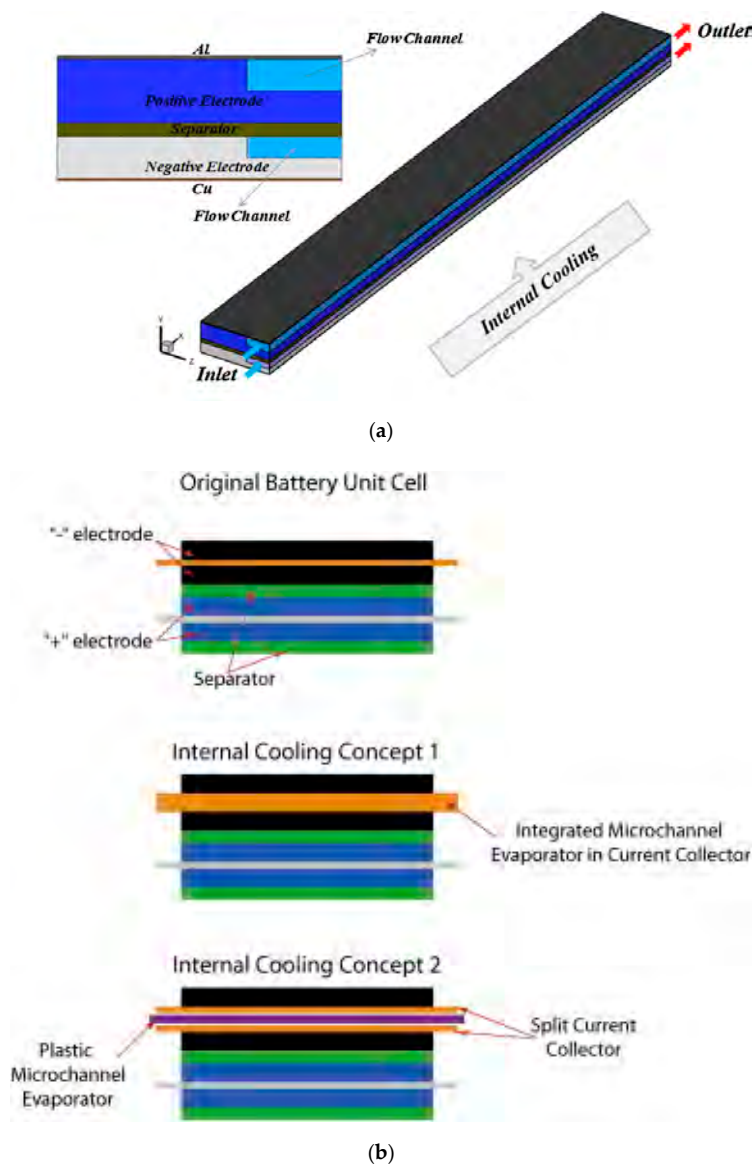


**Figure 18.** Internal thermal management: (a) internal cooling by micro-channel in electrode, adopted from Ref. [237]; (b) internal cooling by micro-channel evaporator in current collector, adopted from Ref. [238].

Another way to achieve ITM is via the application of alternating current (AC) that can efficiently heat battery without a substantial change of SOC. Stuart et al. [239] first proposed using AC to warm battery up rather than using an external heater. For this method, the heating rate increased with the increasing signal amplitude, however the effect of signal frequency on the heating performance was not taken into account. To address this problem, Ruan et al. [240] proposed an effective strategy to analyze the optimal frequency. Their results demonstrated that a constant frequency was more promising than variable frequency could be evaluated according to the intermediate temperature. Nevertheless, in practical applications, the ITM method is difficult to operate and some disadvantages such as low cooling efficiency and temperature gradient etc. also limit its usage [240]. Comparatively, another BMS, i.e., ETM has received a more universal application. Comparatively, another BMS, i.e., ETM has received a more universal application.

Corresponding to the ITM, ETM refers to the thermal management methods that improve heat dissipation from external environment. In order to promote heat dissipation, it is important to choose

Appl. Sci. 2019, 9, x 26 of 46

a suitable medium. On the basis of the medium, ETM can be further divided into three kinds: air cooling system (ACS), liquid cooling systems (LCS) and PCM cooling system (PCM-CS). heat dissipation from external environment. In order to promote heat dissipation, it is important to choose a suitable medium. On the basis of the medium, ETM can be further divided into three kinds: air cooling system (ACS), liquid cooling system (LCS) and PCM cooling system (PCM-CS). There are two types of air flow patterns in ACS: natural convection (NC) and forced convection (FC). For the ACS, air flow rate is an important factor in the promotion of the heat transfer coefficient, thus improving the efficiency of heat dissipation. Additionally, certain factors such as battery arrangement, flow path number and width also influence the performance. Wang et al. [241] investigated the behaviors of an air-cooled LIB. Their results showed that temperature non-uniformity caused by heat accumulation and concentration was mitigated by reciprocating air-flow with optimized reversing strategy and forward air-flow. Liu et al. [242] conducted a set of optimization methods in reciprocating air flow of LIB thermal management. They found that the reciprocating flow could achieve good dissipation, reduce the temperature difference of LIB, the temperature uniformity and effectively reduce the maximum temperature of battery. As displayed in Figure 19, Zhang et al. [243] proposed a novel battery pack with a wedge-shaped runner, optimizing the position of inlet/outlet, the width of the wedge-shaped flow path, the inclination angle of the battery and the clearance among batteries. Their results showed that the temperature distribution was exacerbated with the increase of the inlet temperature and improved with the increasing inlet velocity. However, despite the fact that the researchers have never stopped optimizing the structure of ACS, it is still hard for ACS to meet the demands of EV at present. Nelson et al. [244] argued that using an air-based system it was difficult to cool the battery to less than 52 °C when the battery temperature was above 66 °C.

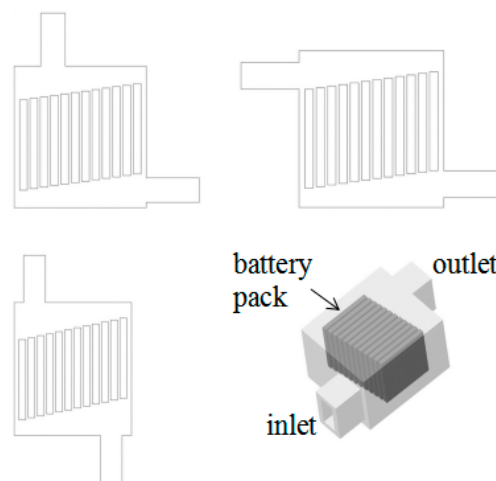


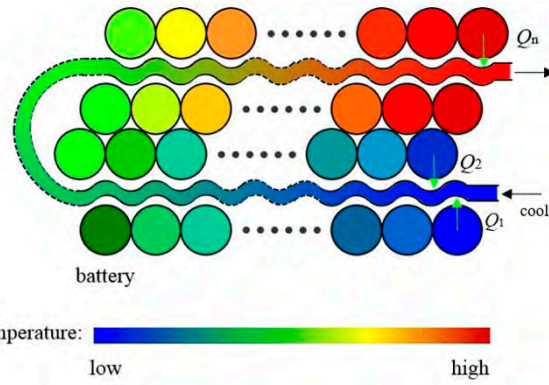
Figure 19. Air-cooled battery pack. Adopted from Ref. [243].

Compared to the ACS, a liquid-based cooling system possesses better performance due to its higher heat transfer coefficient. Normally, the LCS can be divided into two kinds according to whether a phase change occurs during the process, namely whether water changes into vapor which usually takes place in the heat pipe. Apparently, the phase change may be a driving force in heat absorption. Shang et al. [245] designed a LCS for LIB by changing the contact surface, and the results show it could not significantly improve the temperature uniformity. As shown in Figure 20, Zhao et al. [246] developed two cooling approaches via channelled liquid flow to minimize the thermal non-uniformity in a battery pack and found that the two LCSs could reduce the non-uniformity of battery under 5C discharging operation to values lower than 2 and 0.7, respectively. In addition, two cooling approaches via channelled liquid flow to minimize the thermal non-uniformity in a battery pack and found that the two LCSs could reduce the non-uniformity of battery under 5C discharging operation to values lower than 2.2 and 0.7 °C, respectively. In addition, Wang et al. [247] developed a new LCS based on thermal silica plates, which could greatly improve the cooling capacity and therefore decrease the maximum temperature difference within a battery.

Nevertheless, the fluidity of liquid is a huge barrier for electronic system which requires advanced and complicated design before application, therefore resulting in a high cost. Recently, Ren et al. [248] presented a novel method of employing water evaporation, as displayed in Figure 21. The thin sodium

Wang et al. [247] developed a new LCS based on thermal silica plates, which could greatly improve the cooling capacity and therefore decrease the maximum temperature difference within a battery.

film (SA-1 film) with a water content of 99 wt.% was prepared and their results revealed that under the condition of a cycle rate larger than 1C, the temperature rise rate of battery could be reduced by half. Meanwhile, the liquid barrier was successfully solved by the proposed SA-1 film such that there was not a large effect on the electronic system.



revealed that under the condition of a cycle rate larger than 1C, the temperature rise rate of battery could be reduced by half. Meanwhile, the liquid barrier was successfully solved by the proposed SA-1 film such that there was not a large effect on the electronic system.

Figure 20. The procedure of a representative liquid cooling method. Adopted from Ref. [246].

Nevertheless, the fluidity of liquid is a huge barrier for electronic system which requires advanced and complicated design before application, therefore resulting in a high cost. Recently, Ren et al. [248] presented a novel method of employing water evaporation, as displayed in Figure 21. The thin sodium film (SA-1 film) with a water content of 99 wt.% was prepared and their results revealed that under the condition of a cycle rate larger than 1C, the temperature rise rate of battery could be reduced by half. Meanwhile, the liquid barrier was successfully solved by the proposed SA-1 film such that there was not a large effect on the electronic system.

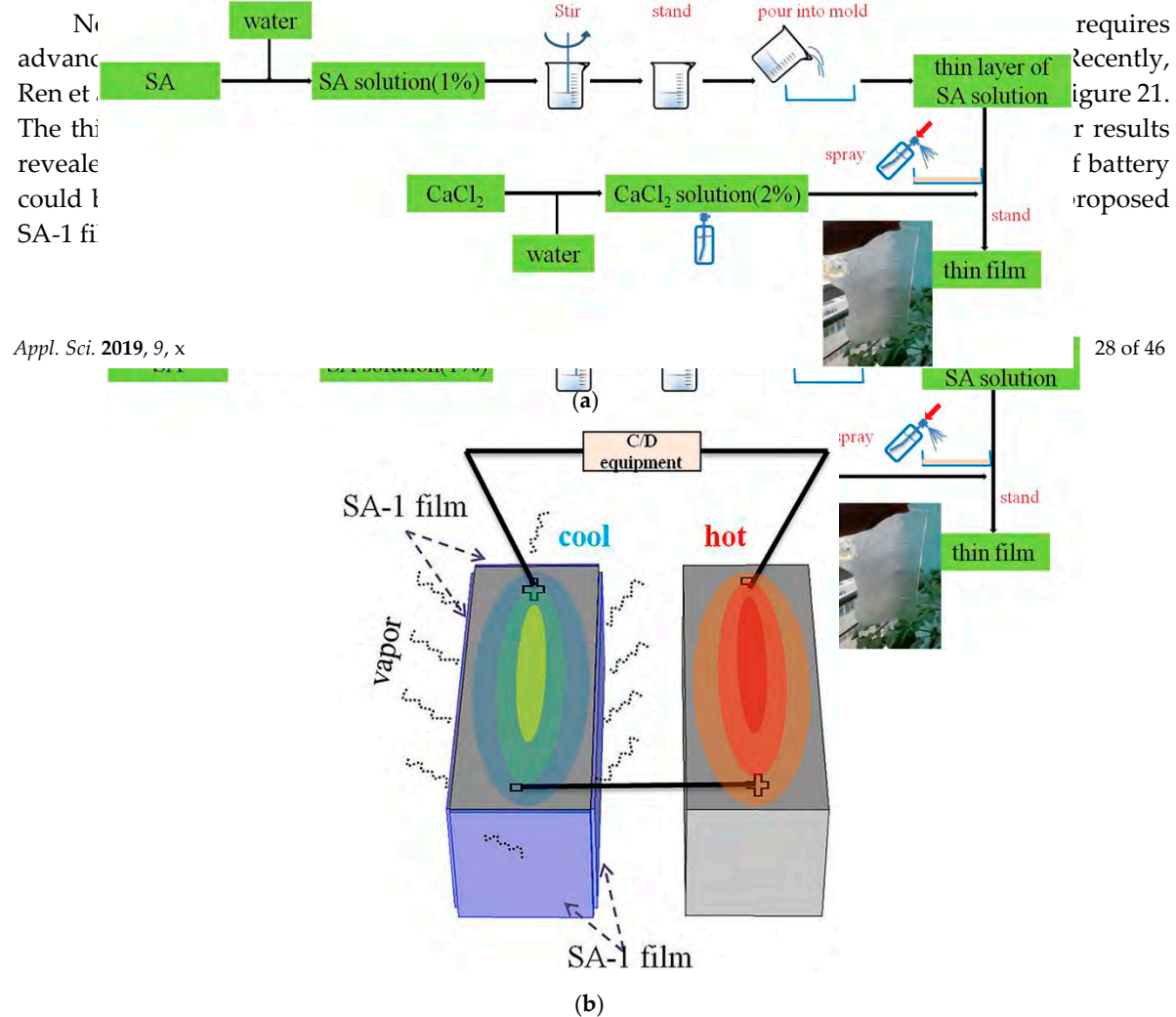


Figure 21. (a) The preparation process of thin sodium film (SA-1 film) (b) The application of SA-1 film in the system. Adopted from Ref. [248].

PCM is a type of material that is able to absorb thermal energy and then release it by a reverse process; hence, it is considered as a novel medium in BMS [249]. Commonly, it consists of three categories: the organic, the inorganic and the eutectic. The organic PCM contains carbon element, in which paraffin is the most common compound. For organic PCM, it possesses the advantage of not needing a container as their volume variation is relatively low, besides the chemical stability and

PCM is a type of material that is able to absorb thermal energy and then release it by a reverse process; hence, it is considered as a novel medium in BMS [249]. Commonly, it consists of three categories: the organic, the inorganic and the eutectic. The organic PCM contains carbon element, in which paraffin is the most common compound. For organic PCM, it possesses the advantage of no needing a container as their volume variation is relatively low, besides the chemical stability and non-corrosiveness [250]. The inorganic PCMs usually contain one or more metallic atoms. They have a good thermal conductivity and latent heat. Additionally, they are nonflammable and nontoxic. Nevertheless, some of them are corrosive and the reversibility of phase change is difficult to maintain in the long term. Moreover, the metals contained in inorganic PCM result in a high density which greatly limits its practical application. The eutectic PCM is a specific mixture of the previous PCMs, which permits the obtainment of a PCM with properties different to pure materials.

For most PCMs, their latent heat is large, while their thermal conductivity is relatively poor. Hence, considerable studies have been carried out to enhance the thermal conductivity of existing PCMs as displayed in Table 3, and some other materials with high thermal conductivity such as expanded graphite (EG), foamed metal and nanomaterials are also introduced to synthesize composite phase change material (CPCM). Wang et al. [251] developed an improved BMS based on the CPCM with aluminum boxes. Their results showed that the CPCM could significantly reduce the average temperature and improve temperature uniformity of a battery pack. Huang et al. [252] investigated the cooling effectiveness of CPCM on the thermal response of a battery under overcharge condition and found that the battery cooled down remarkably as compared to the natural convection condition when CPCM was attached to the pouch battery. Ling et al. [253] compared two CPCMs, a highly thermal conductive 60 wt.% RT44HC/EG composite and a 60 wt.% RT44HC/fumed silica composite with a lower thermal conductivity. Their results indicated that the low thermal conductivity of the CPCM would induce an even higher temperature difference over the battery pack in the absence of PCM.

**Table 3.** Research cases to enhance the thermal conductivity of phase change material.

Authors/Reference	CPCM/Proportions	Melting Temperature (°C)	Latent Heat (kJ/kg)	Thermal Conductivity (W/m·K)
Zhang et al. [254]	Alum/EG	87.9	214.9	0.95–5.88
Wang et al. [255]	Polyethylene glycol (PEG)/EG	61.5	161.2	0.30–1.32
Javieradrain et al. [256]	Alum foam/EG/paraffin	60.1	190.0	0.20–1.20
Kim et al. [257]	Octadecane (OD)/Expanded graphite (WEPC)	30.1	198.8	/
Sheng et al. [258]	Alum/Erythritol	118.0	/	4.00–30.00
Zhang et al. [259] (Figure 22a)	Diamond foam (DF)/paraffin	90.0	124.7	0.25–6.70
Darkwa et al. [260]	Alum/Hexadecane	24.9	167.0	0.15–1.25
Hasse et al. [261]	Paraffin	27.9	170.1	0.19
Yang et al. [262] (Figure 22b)	PEG/EG	25.9	98.6	/

In summary, each type of BMS has its own merits and drawbacks, herein a comparison is conducted among these different types of BMS, shown in Table 4. Most scholars agree on the fact that air cooling is easy to operate but is not enough to cope with the temperature elevation of battery. Liquid cooling is performant but complex and presents the shortest lifespan. As for PCM, the leakage danger is a problem in application, thus a container is necessary.

Nowadays, many researchers have focused on developing a combined battery management system (CBMS), in which more than one of the above thermal management methods are applied. In this way, different methods can complement mutual strengths and weaknesses to present excellent performance. Ling et al. [263] developed a hybrid thermal management system for LIB-integrated PCM with forced-air cooling, as depicted in Figure 23. This CBMS successfully prevented heat accumulation and maintained the maximum temperature under 50 °C, in which the PCM dictated the maximum temperature rise and temperature uniformity within the battery pack while forced air convection

Wang et al. [255]	Polyethylene glycol (PEG)/EG	61.5	161.2	0.30–1.32	
Javieradrain et al. [256]	Alum foam/EG/paraffin Octadecane	60.1	190.0	0.20–1.20	28 of 45
Kim et al. [257]	(OD)/Expanded graphite (WEG)	30.1	198.8	/	
Cheng et al. [258]	Alum/Expanded graphite (WEG)	90.0	124.7	0.25–6.70	
Zheng et al. [259]	(DE)/paraffin	24.9	167.0	0.15–1.25	
Darkwa et al. [260]	Alum/Hexadecane	27.9	170.1	0.19	
Hasse et al. [261]	Paraffin	25.9	98.6	/	
Yang et al. [262]	PEG/EG	25.9	98.6	/	

succeeded in recovering the thermal energy storage capacity of PCM. Fathabadi et al. [264] proposed a novel battery pack design including an active-passive thermal management system. Their developed BMS could be divided into two parts: the active part applied distributed thin ducts, air flow and natural convection as cooling media while the passive part utilized PCM/EG as the cooling component to optimize the thermal performance of the proposed battery pack. Xie et al. [265] developed a PCM-based thermal management system coupled with air cooling and their results showed that the cooling effect of the integrated system was evidently better than that of the air cooling system. Furthermore, it was more energy-efficient due to the relatively lower air flow rate.

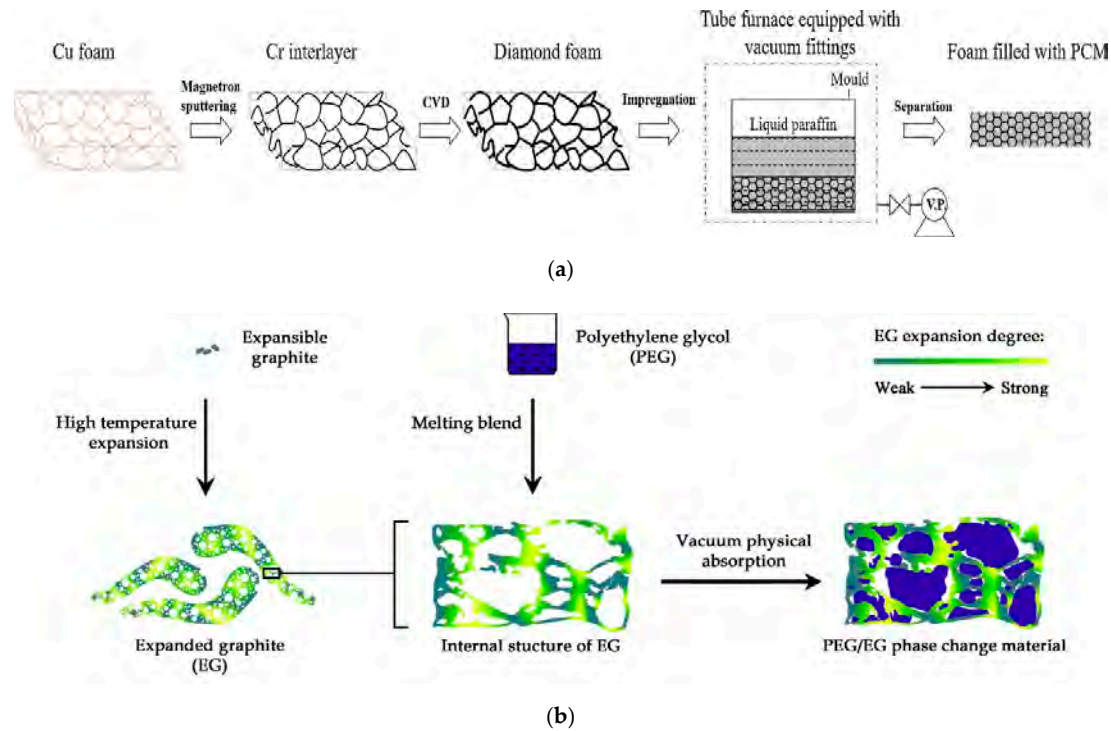


**Figure 22.** (a) The fabrication procedure of diamond foam and the generated composite phase change material (PCM) adopted from Ref. [259]; (b) The synthetic route of polyethylene glycol/expanded graphite (PEG/EG), adopted from Ref. [262].

In summary, each type of BMS has its own merits and drawbacks, herein a comparison is conducted among these different types of BMS, shown in Table 4. It was agreed on the fact that air cooling is easy to operate but is not enough to cope with the temperature elevation of battery.

BMS	Advantages	Disadvantages
LCS	Liquid cooling	Low cost; Easy to maintain
ACS	Vapor cooling	Low cost; Simple structure; Easy to integrate; Little electricity consumption
PCM-CS	Organic Inorganic Eutectic	Low heat transfer coefficient; Dependent on ambient temperature; Uneven temperature distribution; Low efficiency; Dependent on ambient environment; Insufficient for extreme condition

**Table 4.** Comparison among different kinds of battery management systems.

As shown in Figure 24, Song et al. [266] investigated a CBMS that integrated liquid cooling and PCM together. Their results demonstrated that both the battery temperature ramp-up rate and the battery steady-state temperature were significantly reduced by the conjugated cooling, in comparison

system (CBMS), in which more than one of the above thermal management methods are applied. In this way, different methods can complement mutual strengths and weaknesses to present excellent performance. Ling et al. [263] developed a hybrid thermal management system for LIB-integrated PCM with forced-air cooling, as depicted in Figure 23. This CBMS successfully prevented heat accumulation and maintained the maximum temperature under 50 °C, in which the PCM dictated the maximum temperature rise and temperature uniformity within the battery pack while forced air convection succeeded in recovering the thermal energy storage capacity of PCM. Fathabadi et al. [264] developed a liquid battery pack design in which all [264] investigated an optimization method, the response surface methodology (RSM) with PCM and liquid cooling integrated for LIB, which helped retain the PCM mass by up to 94.1% and the volume by up to 55.6%. Compared with the conventional LCC, the hybrid system is not only highly efficient but lightweight and flexible for the batteries with arbitrary shapes. Xie et al. [265] developed a CPCM-based thermal management system coupled with air cooling and their results showed that the cooling effect of the integrated system was evidently better than that of the air cooling system. Furthermore, it was more energy-efficient due to the relatively lower air flow rate.

Appl. Sci. 2019, 9, 2483

29 of 45

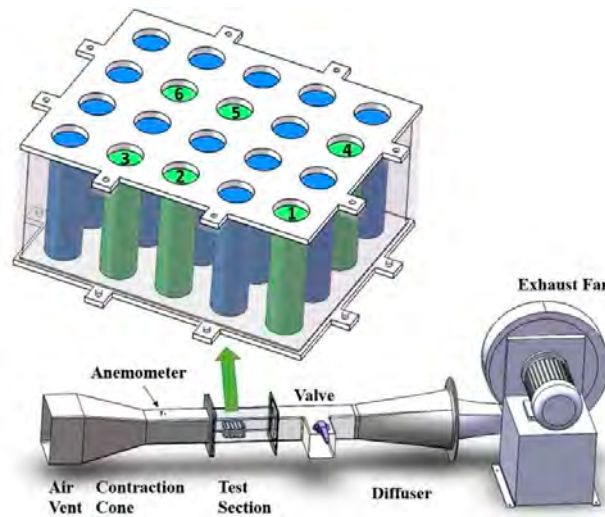


**Figure 23.** Schematic of a combined battery management system (CBMS) integrated phase change material (PCM) with forced-air cooling. Adopted from Ref. [263].

Appl. Sci. 2019, 9, x

32 of 46

As shown in Figure 24, Song et al. [266] investigated a CBMS that integrated liquid cooling and

P  
b

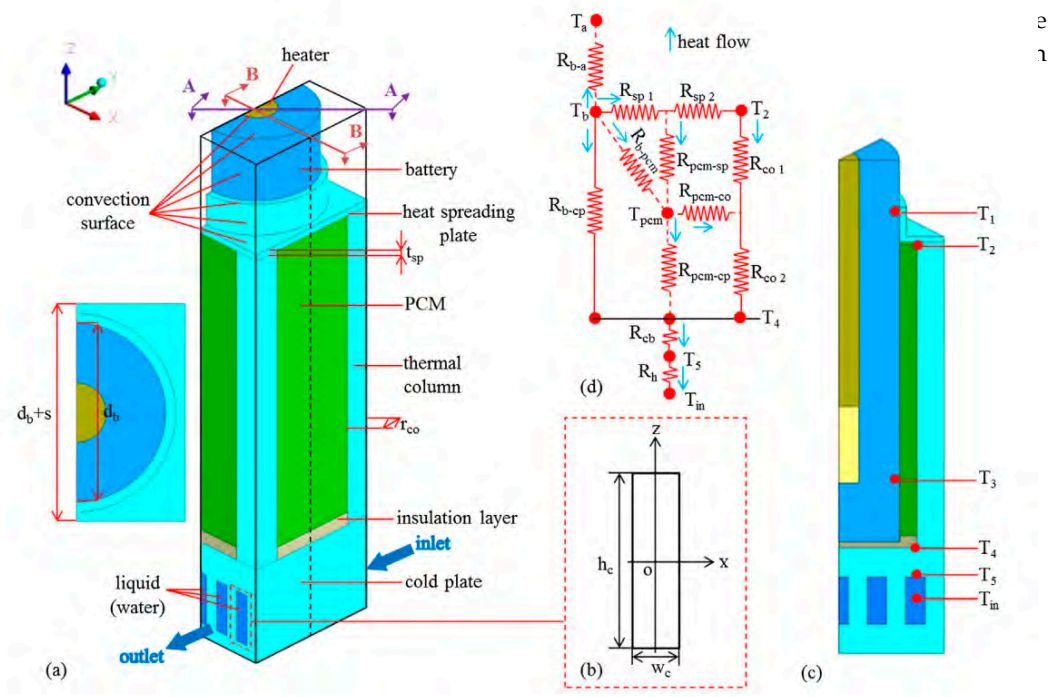


**Figure 24.** Schematic of a CBMS combining PCM and liquid cooling techniques. Adopted from Ref. [266]: (a) the numerical model of single battery; (b) cross-section of the flow channel; (c) temperature monitoring points in A-A cross-section; (d) the simplified thermal resistance network at steady state, with the total thermal path, absent for the liquid cooling condition.

5.5. Firefighting

As displayed in Table 5, fires are generally classified into five different kinds (classes A, B, C, D and K) [276]. Nevertheless, due to the complexity of battery components and the diversity of usage conditions, the classification of LIB fire is controversial and it may vary among classes A, B, and C. In view of the uncertainty, there are currently no unified and specific requirements for the suppression of LIB fires. The fire suppression of LIBs will be discussed in detail in the following sections.

To conclude, it is worth noting that both the application of FR additives and the thermal management on battery are compliant before the appearance of battery hazard, that is, the normal operation process. Even the safety device acts as a protective method for battery thermal hazard. Whereas, once thermal hazard occurs, it is essential to take certain countermeasures such as the warning of hazard and subsequent firefighting methods to reduce the damage inflicted by the hazard and suppress further deterioration.

#### 5.4. Warning

There are two aspects from the perspective of early warning in order to solve the safety problem associated with LIB. The first is for a single battery; real-time monitoring of voltage, current, resistance and other data should take place prior to the occurrence of thermal hazard, allowing for an alarm to be raised when an abnormality appears. The second is to carry out management monitoring for a battery pack, that is, to analyze and alarm the abnormalities occurring during the operation of the entire battery pack. The early warning includes monitoring the changes in voltage, current, resistance and other electrical performance parameters, the temperature change and the escaping gases. An early warning and monitoring system is disclosed by Xie et al. [269] for battery packs. During normal cycling of a battery, surface temperature, voltage, current and impedance may be monitored to determine if abnormalities exist in the battery. Hermann invented a method for detecting LIB failure within a battery pack based on variations in the measured electrical isolation resistance of the battery pack [270]. Besides, escaping gas from LIB is becoming a growing concern since the volatile organics emitted are flammable and their unpredictable release represents a safety risk. Davion et al. [271] illustrated the results that the sensor could detect escaping gas prior to thermal events. With enough prior warning from the sensor, there is a desire to determine whether it provides suitable control at the fringes of battery performance. Somov et al. [272] applied an autonomous wireless sensor system for early fire and gas leak detection of LIBs. The system consisted of two modules: a gas sensor module and a power management module. At the same time, there have been more studies on the thermal runaway and fire releasing gases of LIBs; therefore, the number of gas detection methods that can be used for thermal runaway and fire warning has also increased [273–275]. The problem of thermal runaway and fire in LIBs is now more serious, therefore some advanced means are needed to predict the occurrence of disasters. Accurate warning of thermal runaway and fire shall be achieved through more quantitative data analysis.

#### 5.5. Firefighting

As displayed in Table 5, fires are generally classified into five different kinds (classes A, B, C, D and K) [276]. Nevertheless, due to the complexity of battery components and the diversity of usage conditions, the classification of LIB fire is controversial and it may vary among classes A, B, and C. In view of the uncertainty, there are currently no unified and specific requirements for the suppression of LIB fires, and effective fighting technology for LIB fire is still a challenge. Suppressing LIB fire involves extinguishing the open flame and decreasing the battery temperature. If the battery temperature is sufficiently high after the open flame is extinguished, there is still a possibility that the battery will reignite.

To investigate how LIB fire can be suppressed effectively, researchers and institutions have conducted extensive studies to date. The National Technical Information Service (NTIS) assessed the fire hazards of LIBs and tested the extinguishing effect of different Halon products on battery fire [277,278]. Their results showed that the Halon extinguishing agents could suppress the open fire, while the battery temperature would still increase after the flame was extinguished. Later, Egelhaaf et al. studied the fighting effect of water combined with a surfactant and a gelling agent on battery fire [279]. They measured the battery temperature and the water consumption and found that water was capable of extinguishing the battery fire and additives helped to apparently reduce the amount of water required to fight the fire. Additionally, the Fire Protection Research Foundation (FPRF) performed a

full-scale suppression test for the fire involving EV battery [280]. They proposed that although the water jet could quickly extinguish the battery fire, the toxic or flammable smoke and gas would still release after suppression. The FAA conducted experiments to screen the effective fire extinguishing agent for battery fire [281]. Experimental results indicated that water-based extinguishing agents (water, AF-31, AF-21, A-B-D, and Novec 1230 (C<sub>6</sub>F<sub>12</sub>O)) were the most effective, especially the evident cooling effect, while nonaqueous extinguishing agents (gas, dry powder, etc.) were the least effective. The Det Norske Veritas and Germanischer Lloyd (DNVGL) carried out a series experiments to evaluate the extinguishing effect of the F500, Fireice, PyroCool, aerosol and water on battery fire respectively [282]. Their results showed that all extinguishers used in this work could put down battery fire if they were sprayed immediately upon the detection of a thermal spike. Among, water exhibited the best cooling effect for a battery with thermal runaway. Hui et al. selected carbon dioxide, superfine powder and heptafluoropropane to conduct the battery fire suppression test series [283] in which heptafluoropropane was verified to be the most effective in controlling battery fires and suppressing the thermal runaway reactions. Further, Wang et al. investigated the efficiency of heptafluoropropane fire extinguishing agent (HFC-227ea), and they found that heptafluoropropane could suppress individual battery and even small-format battery pack fire [284]. However, the battery might be reignited due to the fiercely exothermic reactions inside battery after the fire was extinguished. Liu et al. investigated the suppression efficiency of dodecafluoro-2-methylpentan-3-one (C<sub>6</sub>F<sub>12</sub>O) in large-capacity battery fires [39]. They proposed that C<sub>6</sub>F<sub>12</sub>O first showed a negative inhibitory effect, which was then transformed into an inhibitory effect as the dose increased, and they also calculated the proper dose of C<sub>6</sub>F<sub>12</sub>O under their conditions. Besides, Luo et al. studied the fire extinguishing effect of a water mist containing additives system on a power battery [285]. Their results indicated that 5% F-500 solution and 5% self-made solution yielded a more significant extinguishing effect than pure water on battery fire.

**Table 5.** Classification of fires.

Class	Description
A	Fires in ordinary combustible materials such as wood, cloth, paper, rubber and many plastics.
B	Fires in flammable liquids, combustible liquids, petroleum greases, tars, oils, oil-based paints, solvents, lacquers, alcohols and flammable gases.
C	Fires that involve energized electrical equipment.
D	Fires in combustible metals such as magnesium, titanium, zirconium, sodium, lithium and potassium.
K	Fires in cooking appliances that involve combustible cooking media.

In summary, the previous studies mainly focused on the comparison of fire extinguishing effects among different extinguishing agents, such as Halon, water, carbon dioxide, foam, dry powders and so on. However, some deficiencies still exist and challenging questions are being proposed regarding fighting battery fire. For example, the spray time of the agent, dose of agent, damage degree of the battery, cost and scenario, etc. shall be quantitatively or qualitatively estimated. Furthermore, standard specifications and guidelines for the firefighting of battery fire shall be formulated and promulgated as soon as possible to meet the requirements of the market.

## 6. Summary and Outlook

With the global energy policy transitioning from fossil energy to renewable energy, LIBs, as a type of energy storage method, show great advantages over other kinds of batteries. Therefore, they have attracted considerable attention. However, the safety concerns regarding LIB are still a main obstacle that hinder large-scale applications of LIBs in many fields. Benefiting from the fast spread of information today, incidents of fire or explosions induced by LIBs are often reported ranging from

mobile telephones and EVs to airplanes. These incidents greatly threaten consumers' lives and property, while damage human's confidence on LIBs, thereby restricting the progression of their use. Therefore, paying more attention to the thermal hazards of LIBs and the corresponding countermeasures is of great importance.

Generally, the thermal hazards of LIBs can be caused by several abusive factors, e.g., physical, electrical and thermal factors, manufacturing defect and battery aging. The physical factor can trigger electrical abuse, and the electrical abuse releases heat which will further induce thermal abuse; namely, thermal hazard and even thermal runaway. During the process of battery thermal hazard, a series of destructive reactions among battery components such as the decomposition of electrodes/electrolytes, the reaction between electrodes, the reaction between electrode and electrolyte, etc. are induced, substantial heat is released and quantities of combustible gases are generated. Besides battery components, the thermal hazards of a single battery and a battery pack are also reviewed. For the former, the thermal hazards that are generally exhibited are high-temperature, ejection, combustion, explosion and toxic gases during thermal runaway. While for a battery pack, thermal failure propagation provides a thermal hazard in addition to thermal runaway. Thermal failure propagation will aggravate the thermal hazard further, resulting in a serious incident. In addition, the influence of low-pressure environment and cathode chemistry on the thermal hazard of LIBs is discussed here. However, it still lacks sufficient examinations on the thermal behavior of LIBs under low pressure, the hazard difference between normal condition and low-pressure condition is worth noting in future research.

In an aim to decrease the thermal hazards of LIBs as much as possible, certain management or countermeasures must be implemented. In current work, the measures discussed were (1) the usage of safety devices inside battery; (2) the application of FR additives; (3) the thermal management of battery; (4) the warning of thermal hazard and (5) firefighting upon the occurrence of a hazard. However, challenges still remain. Effective FR additives and thermal management systems still need to be developed to meet the requirement of practices including performance, cost and so on. The current warning method is not sufficiently sensitive to give the humans the time necessary to escape danger or take the appropriate measurements. Moreover, standard guidelines for the fighting of battery fire remain to be formulated and promulgated. In short, to decrease the challenges of battery thermal hazards and create LIBs that better benefit humankind, there is still a lot of work to do.

**Author Contributions:** D.O., M.C., Q.H., J.W., Z.W. and J.W. wrote this paper together.

**Funding:** This work was supported by the National Key R&D Program of China (No. 2018YFC0808600) and the Open Project Program of the State Key Laboratory of Fire Science (No. HZ2019-KF10).

**Conflicts of Interest:** The authors declare no conflict of interest.

## References

1. Kannan, N.; Vakeesan, D. Solar energy for future world: A review. *Renew. Sustain. Energy Rev.* **2016**, *62*, 1092–10111. [[CrossRef](#)]
2. Lewis, N.S. Research opportunities to advance solar energy utilization. *Science* **2016**, *351*, aad1920. [[CrossRef](#)] [[PubMed](#)]
3. Pérez-Collazo, C.; Greaves, D.; Iglesias, G. A review of combined wave and offshore wind energy. *Renew. Sustain. Energy Rev.* **2015**, *42*, 141–153. [[CrossRef](#)]
4. Lewis, M.; Neill, S.P.; Robins, P.E.; Hashemi, M.R. Resource assessment for future generations of tidal-stream energy arrays. *Energy* **2015**, *83*, 403–415. [[CrossRef](#)]
5. Dyer, C.K. Fuel cells for portable applications. *J. Power Sources* **2002**, *106*, 31–34. [[CrossRef](#)]
6. Saevarsdottir, G.; Tao, P.; Stefansson, H.; Harvey, W. Potential use of geothermal energy sources for the production of lithium-ion batteries. *Renew. Energy* **2014**, *61*, 17–22. [[CrossRef](#)]
7. Richter, F.; Vie, P.J.S.; Kjelstrup, S.; Burheim, O.S. Measurements of ageing and thermal conductivity in a secondary NMC-hard carbon Li-ion battery and the impact on internal temperature profiles. *Electrochim. Acta* **2017**, *250*, 228–237. [[CrossRef](#)]

8. Maleki, H.; Howard, J.N. Effects of overdischarge on performance and thermal stability of a Li-ion cell. *J. Power Sources* **2006**, *160*, 1395–1402. [[CrossRef](#)]
9. Doughty, D.H.; Roth, E.P. A general discussion of Li ion battery safety. *Electrochem. Soc. Interface* **2012**, *21*, 37–44. [[CrossRef](#)]
10. Belov, D.; Yang, M.H. Failure mechanism of Li-ion battery at overcharge conditions. *J. Solid State Electrochem.* **2008**, *12*, 885–894. [[CrossRef](#)]
11. Kim, T.H.; Park, J.S.; Chang, S.K.; Choi, S.; Ryu, J.H.; Song, H.K. The current move of lithium ion batteries towards the next phase. *Adv. Energy Mater.* **2012**, *2*, 860–872. [[CrossRef](#)]
12. Lisbona, D.; Snee, T. A review of hazards associated with primary lithium and lithium-ion batteries. *Process Saf. Environ. Prot.* **2011**, *89*, 434–442. [[CrossRef](#)]
13. Feng, X.; Ouyang, M.; Liu, X.; Lu, L.; Xia, W.; He, X. Thermal runaway mechanism of lithium ion battery for electric vehicles: A review. *Energy Storage Mater.* **2018**, *10*, 246–267. [[CrossRef](#)]
14. Wang, Q.; Ping, P.; Zhao, X.; Chu, G.; Sun, J.; Chen, C. Thermal runaway caused fire and explosion of lithium ion battery. *J. Power Sources* **2012**, *208*, 210–224. [[CrossRef](#)]
15. Huang, Q.; Ma, L.; Liu, A.; Ma, X.W.; Li, J.; Wang, J.; Dahn, J.R. The reactivity of charged positive  $\text{Li}_{1-n}[\text{Ni}_x\text{Mn}_y\text{Co}_z]\text{O}_2$  electrodes with electrolyte at elevated temperatures using accelerating rate calorimetry. *J. Power Sources* **2018**, *390*, 78–86. [[CrossRef](#)]
16. Ma, L.; Nie, M.; Xia, J.; Dahn, J.R. A systematic study on the reactivity of different grades of charged Li  $[\text{Ni}_x\text{Mn}_y\text{Co}_z]\text{O}_2$  with electrolyte at elevated temperatures using accelerating rate calorimetry. *J. Power Sources* **2016**, *327*, 145–150. [[CrossRef](#)]
17. Xia, L.; Li, S.L.; Ai, X.P.; Yang, H.X.; Cao, Y.L. Temperature-sensitive cathode materials for safer lithium-ion batteries. *Energy Environ. Sci.* **2011**, *4*, 2845–2848. [[CrossRef](#)]
18. Zhong, H.; Kong, C.; Zhan, H.; Zhan, C.; Zhou, Y. Safe positive temperature coefficient composite cathode for lithium ion battery. *J. Power Sources* **2012**, *216*, 273–280. [[CrossRef](#)]
19. Kovalenko, I.; Zdyrko, B.; Magasinski, A.; Benjamin, H. A major constituent of brown algae for use in high-capacity Li-ion batteries. *Science* **2011**, *334*, 75–79. [[CrossRef](#)]
20. Ryou, M.H.; Kim, J.; Lee, I.; Kim, S.J. Mussel-inspired adhesive binders for high-performance silicon nanoparticle anodes in lithium-ion batteries. *Adv. Mater.* **2013**, *25*, 1571–1576. [[CrossRef](#)]
21. Wu, H.; Chan, G.; Choi, J.W.; Ryu, I. Stable cycling of double-walled silicon nanotube battery anodes through solid–electrolyte interphase control. *Nat. Nanotechnol.* **2012**, *7*, 310–315. [[CrossRef](#)] [[PubMed](#)]
22. Kim, Y.S.; Kim, T.H.; Lee, H.; Song, H.K. Electronegativity-induced enhancement of thermal stability by succinonitrile as an additive for Li ion batteries. *Energy Environ. Sci.* **2011**, *4*, 4038–4045. [[CrossRef](#)]
23. Kim, G.Y.; Dahn, J.R. The effect of some nitriles as electrolyte additives in Li-ion batteries. *J. Electrochem. Soc.* **2015**, *162*, A437–A447. [[CrossRef](#)]
24. Chen, R.; Liu, F.; Chen, Y.; Ye, Y.; Huang, Y. An investigation of functionalized electrolyte using succinonitrile additive for high voltage lithium-ion batteries. *J. Power Sources* **2016**, *306*, 70–77. [[CrossRef](#)]
25. Zhu, Y.; Wang, F.; Liu, L.; Xiao, S. Composite of a nonwoven fabric with poly (vinylidene fluoride) as a gel membrane of high safety for lithium ion battery. *Energy Environ. Sci.* **2013**, *6*, 618–624. [[CrossRef](#)]
26. Zhang, J.; Liu, Z.; Kong, Q. Renewable and superior thermal-resistant cellulose-based composite nonwoven as lithium-ion battery separator. *ACS Appl. Mater. Interfaces* **2012**, *5*, 128–134. [[CrossRef](#)] [[PubMed](#)]
27. Kang, S.M.; Ryou, M.H.; Choi, J.W. Mussel- and diatom-inspired silica coating on separators yields improved power and safety in Li-ion batteries. *Chem. Mater.* **2012**, *24*, 3481–3485. [[CrossRef](#)]
28. Saw, L.H.; Ye, Y.; Tay, A.A.O. Computational fluid dynamic and thermal analysis of Lithium-ion battery pack with air cooling. *Appl. Energy* **2016**, *177*, 783–792. [[CrossRef](#)]
29. Huo, Y.; Rao, Z.; Liu, X. Investigation of power battery thermal management by using mini-channel cold plate. *Energy Convers. Manag.* **2015**, *89*, 387–395. [[CrossRef](#)]
30. Li, K.; Yan, J.; Chen, H. Water cooling based strategy for lithium ion battery pack dynamic cycling for thermal management system. *Appl. Thermal Eng.* **2018**, *132*, 575–585. [[CrossRef](#)]
31. Zhao, J.; Rao, Z.; Huo, Y. Thermal management of cylindrical power battery module for extending the life of new energy electric vehicles. *Appl. Thermal Eng.* **2015**, *85*, 33–43. [[CrossRef](#)]
32. Wang, Z.; Li, X.; Zhang, G. Experimental study of a passive thermal management system for three types of battery using copper foam saturated with phase change materials. *RSC Adv.* **2017**, *7*, 27441–27448. [[CrossRef](#)]

33. Al-Zareer, M.; Dincer, I.; Rosen, M.A. Novel thermal management system using boiling cooling for high-powered lithium-ion battery packs for hybrid electric vehicles. *J. Power Sources* **2017**, *363*, 291–303. [[CrossRef](#)]
34. Lee, C.Y.; Lee, S.J.; Tang, M.S. In situ monitoring of temperature inside lithium-ion batteries by flexible micro temperature sensors. *Sensors* **2011**, *11*, 9942–9950. [[CrossRef](#)] [[PubMed](#)]
35. Wu, C.; Yin, P.; Zhu, X. Synthesis of hematite ( $\alpha$ -Fe<sub>2</sub>O<sub>3</sub>) nanorods: Diameter-size and shape effects on their applications in magnetism, lithium ion battery, and gas sensors. *J. Phys. Chem. B* **2006**, *110*, 17806–17812. [[CrossRef](#)] [[PubMed](#)]
36. Mutyala, M.S.K.; Zhao, J.; Li, J.; Pan, H.; Yuan, C.; Li, X. In-situ temperature measurement in lithium ion battery by transferable flexible thin film thermocouples. *J. Power Sources* **2014**, *260*, 43–49. [[CrossRef](#)]
37. Chen, J.; Xu, L.; Li, W.; Gou, X.  $\alpha$ -Fe<sub>2</sub>O<sub>3</sub> nanotubes in gas sensor and lithium-ion battery applications. *Adv. Mater.* **2005**, *17*, 582–586. [[CrossRef](#)]
38. Reif, R.H.; Liffers, M.; Forrester, N.; Peal, K. Lithium Battery Safety: A look at Woods Hole Oceanographic Institution's Program. *Prof. Saf.* **2010**, *55*, 32–37.
39. Liu, Y.; Duan, Q.; Xu, J. Experimental study on the efficiency of dodecafluoro-2-methylpentan-3-one on suppressing lithium-ion battery fires. *RSC Adv.* **2018**, *8*, 42223–42232. [[CrossRef](#)]
40. Williard, N.; He, W.; Hendricks, C.; Pecht, M. Lessons learned from the 787 dreamliner issue on lithium-ion battery reliability. *Energies* **2013**, *6*, 4682–4695. [[CrossRef](#)]
41. Kolly, J.M.; Panagiotou, J.; Czech, B.A. *The Investigation of a Lithium-Ion Battery Fire Onboard a Boeing 787 by the US National Transportation Safety Board*; Safety Research Corporation of America: Dothan, AL, USA, 2013; pp. 1–18.
42. Goto, N. *Aircraft Serious Incident Investigation Report: All Nippon Airways Co. Ltd. JA804A*; Report No. AI2014-4; Japan Transport Safety Board: Tokyo, Japan, 25 September 2014.
43. *Aircraft Incident Report: Auxiliary Power Unit Battery Fire, Japan Airlines Boeing 787, JA 829 J, Boston, Massachusetts, January 7, 2013*; Report No. PB2014-108867; National Transportation Safety Board: Washington, DC, USA, 21 November 2014.
44. Abraham, D.P.; Roth, E.P.; Kostecki, R. Diagnostic examination of thermally abused high-power lithium-ion cells. *J. Power Sources* **2006**, *161*, 648–657. [[CrossRef](#)]
45. Karter, M.J. *Fire Loss in the United States During 2013*; National Fire Protection Association: Quincy, MA, USA, 2014.
46. The Samsung Note7 Exploded. Available online: [http://www.sohu.com/a/125020048\\_467791/](http://www.sohu.com/a/125020048_467791/) (accessed on 23 January 2017).
47. Is the Heart of the Distortion or Moral Bankruptcy? Available online: <https://www.caishimv.com/party/1476152753.html/> (accessed on 11 October 2016).
48. Huawei P9 Plus Exploded and the Attitude Was Worse than Samsung Note7. Available online: [http://www.sohu.com/a/116273061\\_162764/](http://www.sohu.com/a/116273061_162764/) (accessed on 16 October 2016).
49. An iPhone 7 Took Fire and Burned a Car in Australia. Available online: <http://news.mydrivers.com/1/504/504106.htm/> (accessed on 21 October 2016).
50. Too Scary! Suddenly, the iPhone Battery Exploded and Seven People Were Hospitalized. Available online: <https://baijiahao.baidu.com/s?id=1589274155032747498&wfr=spider&for=pc/> (accessed on 11 January 2018).
51. An iPhone XS Max Caught Fire for the First Time and the Users Said They Might Sue Apple. Available online: [http://www.sohu.com/a/285734633\\_499322/](http://www.sohu.com/a/285734633_499322/) (accessed on 30 December 2018).
52. A Summary Analysis on the 35 Fire Accidents of New Energy Vehicles in 2016. Available online: [http://www.sohu.com/a/123335110\\_526255/](http://www.sohu.com/a/123335110_526255/) (accessed on 4 January 2017).
53. Electric Vehicle Fire Accident Inventory in the First Half of 2017. Available online: [https://www.sohu.com/a/155869592\\_118021/](https://www.sohu.com/a/155869592_118021/) (accessed on 10 July 2017).
54. Electric Vehicle Fire Accident Inventory in the First Half of 2018. Available online: <http://www.evpartner.com/news/8/detail-36915.html/> (accessed on 8 June 2018).
55. Flight UPS6 Crashed in Dubai on 3 September 2010. Available online: <http://m.yzwb.net/a/180910225943473.html/> (accessed on 10 September 2018).
56. The Boeing 787's Lithium Battery Troubles. Available online: [http://www.360doc.com/content/13/0522/10/7536781\\_287205631.shtml/](http://www.360doc.com/content/13/0522/10/7536781_287205631.shtml/) (accessed on 22 May 2013).

57. Why Lithium Batteries Are 'Frowned Upon' by Aircraft? Available online: <http://www.fx361.com/page/2017/0731/2112773.shtml/> (accessed on 31 July 2017).
58. Wen, J.; Yu, Y.; Chen, C. A Review on Lithium-Ion Batteries Safety Issues: Existing Problems and Possible Solutions. *Mater. Express* **2012**, *2*, 197–212. [[CrossRef](#)]
59. Lyon, R.E.; Walters, R.N. Energetics of lithium ion battery failure. *J. Hazard. Mater.* **2016**, *318*, 164–172. [[CrossRef](#)] [[PubMed](#)]
60. Liu, X.; Stolarov, S.I.; Denlinger, M.; Masias, A.; Snyder, K. Comprehensive calorimetry of the thermally-induced failure of a lithium ion battery. *J. Power Sources* **2015**, *280*, 516–525. [[CrossRef](#)]
61. Ouyang, D.; He, Y.; Chen, M.; Liu, J.; Wang, J. Experimental study on the thermal behaviors of lithium-ion batteries under discharge and overcharge conditions. *J. Thermal Anal. Calorim.* **2018**, *132*, 65–75. [[CrossRef](#)]
62. Wang, Z.; Ouyang, D.; Chen, M.; Wang, X.; Zhang, Z.; Wang, J. Fire behavior of lithium-ion battery with different states of charge induced by high incident heat fluxes. *J. Thermal Anal. Calorim.* **2019**, *136*, 2239–2247. [[CrossRef](#)]
63. Zhang, J.; Lu, B.; Song, Y.; Ji, X. Diffusion induced stress in layered Li-ion battery electrode plates. *J. Power Sources* **2012**, *209*, 220–227. [[CrossRef](#)]
64. Riley, L.A.; Cavanagh, A.S.; George, S.M.; Jung, Y.S.; Yan, Y.; Lee, S.H.; Dillon, A.C. Conformal Surface Coatings to Enable High Volume Expansion Li-Ion Anode Materials. *ChemPhysChem* **2010**, *11*, 2124–2130. [[CrossRef](#)] [[PubMed](#)]
65. Basu, S.; Suresh, S.; Ghatak, K.; Bartolucci, S.; Gupta, T.; Hundekar, P.; Kumar, R.; Lu, T.; Datta, D.; Shi, Y. Utilizing van der Waals slippery interfaces to enhance the electrochemical stability of Silicon film anodes in lithium-ion batteries. *ACS Appl. Mater. Interfaces* **2018**, *10*, 13442–13451. [[CrossRef](#)]
66. Wu, Y.; Saxena, S.; Xing, Y.; Wang, Y.; Li, C.; Yung, W.; Pecht, M. Analysis of manufacturing-induced defects and structural deformations in Lithium-ion batteries using computed tomography. *Energies* **2018**, *11*, 925. [[CrossRef](#)]
67. Samsung Expands Recall to All Galaxy Note7 Devices. Available online: <http://www.samsung.com/us/note7recall/> (accessed on 20 August 2017).
68. Mohanty, D.; Hockaday, E.; Li, J.; Hensley, D.K.; Daniel, C.; Wood, D.L., III. Effect of electrode manufacturing defects on electrochemical performance of lithium-ion batteries: Cognizance of the battery failure sources. *J. Power Sources* **2016**, *312*, 70–79. [[CrossRef](#)]
69. Cannarella, J.; Arnold, C.B. The effects of defects on localized plating in lithium-ion batteries. *J. Electrochem. Soc.* **2015**, *162*, A1365–A1373. [[CrossRef](#)]
70. Kong, D.; Wen, R.; Ping, P.; Peng, R.; Zhang, J.; Chen, G. Study on degradation behavior of commercial 18650 LiAlNiCoO<sub>2</sub> cells in over-charge conditions. *Int. J. Energy Res.* **2019**, *43*, 552–567. [[CrossRef](#)]
71. Wu, W.; Wu, W.; Qiu, X.; Wang, S. Low-temperature reversible capacity loss and aging mechanism in lithium-ion batteries for different discharge profiles. *Int. J. Energy Res.* **2019**, *43*, 243–253. [[CrossRef](#)]
72. Kawamura, T.; Kimura, A.; Egashira, M.; Okada, S.; Yamaki, J.I. Thermal stability of alkyl carbonate mixed-solvent electrolytes for lithium ion cells. *J. Power Sources* **2002**, *104*, 260–264. [[CrossRef](#)]
73. Sloop, S.E.; Kerr, J.B.; Kinoshita, K. The role of Li-ion battery electrolyte reactivity in performance decline and self-discharge. *J. Power Sources* **2003**, *119*, 330–337. [[CrossRef](#)]
74. Nagasubramanian, G. Comparison of the thermal and electrochemical properties of LiPF<sub>6</sub> and LiN(SO<sub>2</sub>C<sub>2</sub>F<sub>5</sub>)<sub>2</sub> salts in organic electrolytes. *J. Power Sources* **2003**, *119*, 811–814. [[CrossRef](#)]
75. Wang, Q.; Sun, J.; Yao, X.; Chen, C. C80 Calorimeter Studies of the Thermal Behavior of LiPF<sub>6</sub> Solutions. *J. Solut. Chem.* **2006**, *35*, 179–189. [[CrossRef](#)]
76. Ribière, P.; Grugeon, S.; Morcrette, M.; Boyanov, S.; Laruelle, S.; Marlair, G. Investigation on the fire-induced hazards of Li-ion battery cells by fire calorimetry. *Energy Environ. Sci.* **2012**, *5*, 5271–5280. [[CrossRef](#)]
77. Takata, K.; Morita, M.; Matsuda, Y.; Matsui, K. Cycling characteristics of secondary Li electrode in LiBF<sub>4</sub>/mixed ether electrolytes. *J. Electrochem. Soc.* **1985**, *132*, 126–128. [[CrossRef](#)]
78. Zhang, S.S.; Xu, K.; Jow, T.R. A new approach toward improved low temperature performance of Li-ion battery. *Electrochem. Commun.* **2002**, *4*, 928–932. [[CrossRef](#)]
79. Xu, K.; Zhang, S.S.; Lee, U.; Allen, J.L.; Jow, T.R. LiBOB: Is it an alternative salt for lithium ion chemistry? *J. Power Sources* **2005**, *146*, 79–85. [[CrossRef](#)]
80. Xu, W.; Angell, C.A. LiBOB and Its Derivatives: Weakly Coordinating Anions, and the Exceptional Conductivity of Their Nonaqueous Solutions. *Electrochem. Solid State Lett.* **2001**, *4*, E1–E4. [[CrossRef](#)]

81. Li, Y.; Wang, Z.; Li, C.; Cao, Y.; Guo, X. Densification and ionic-conduction improvement of lithium garnet solid electrolytes by flowing oxygen sintering. *J. Power Sources* **2014**, *248*, 642–646. [[CrossRef](#)]
82. Zhang, Y.; Chen, F.; Tu, R.; Shen, Q.; Zhang, L. Field assisted sintering of dense Al-substituted cubic phase  $\text{Li}_7\text{La}_3\text{Zr}_2\text{O}_{12}$  solid electrolytes. *J. Power Sources* **2014**, *268*, 960–964. [[CrossRef](#)]
83. Kobayashi, Y.; Miyashiro, H.; Takeuchi, T.; Shigemura, H.; Balakrishnan, N.; Tabuchi, M.; Kageyama, H.; Iwahori, T. All-solid-state lithium secondary battery with ceramic/polymer composite electrolyte. *Solid State Ion.* **2002**, *s152–s153*, 137–142. [[CrossRef](#)]
84. Mei, A.; Wang, X.L.; Lan, J.L.; Feng, Y.C.; Geng, H.X.; Lin, Y.H.; Nan, C.W. Role of amorphous boundary layer in enhancing ionic conductivity of lithium–lanthanum–titanate electrolyte. *Electrochim. Acta* **2010**, *55*, 2958–2963. [[CrossRef](#)]
85. Nelson, K.J.; d’Eon, G.L.; Wright, A.T.B.; Ma, L.; Xia, J.; Dahn, J.R. Studies of the effect of high voltage on the impedance and cycling performance of  $\text{Li}[\text{Ni}_{0.4}\text{Mn}_{0.4}\text{Co}_{0.2}]\text{O}_2$ /graphite lithium-ion pouch cells. *J. Electrochem. Soc.* **2015**, *162*, A1046–A1054. [[CrossRef](#)]
86. Kim, H.; Oh, S.-M.; Scrosati, B.; Sun, Y.-K. High-performance electrode materials for lithium-ion batteries for electric vehicles. *Adv. Battery Technol. Electr. Veh.* **2015**, 191–241. [[CrossRef](#)]
87. Li, J.; Cameron, A.R.; Li, H.; Glazier, S.; Xiong, D.; Chatzidakis, M.; Allen, J.; Botton, G.A.; Dahn, J.R. Comparison of Single Crystal and Polycrystalline  $\text{LiNi}_{0.5}\text{Mn}_{0.3}\text{Co}_{0.2}\text{O}_2$  Positive Electrode Materials for High Voltage Li-Ion Cells. *J. Electrochem. Soc.* **2017**, *164*, A1534–A1544. [[CrossRef](#)]
88. Zhang, Z.; Fouchard, D.; Rea, J.R. Differential scanning calorimetry material studies: Implications for the safety of lithium-ion cells. *J. Power Sources* **1998**, *70*, 16–20. [[CrossRef](#)]
89. Wang, Q.; Sun, J.; Chen, X.; Chu, G.; Chen, C. Effects of solvents and salt on the thermal stability of charged  $\text{LiCoO}_2$ . *Mater. Res. Bull.* **2009**, *44*, 543–548. [[CrossRef](#)]
90. Wang, Q.; Sun, J.; Yao, X.; Chen, C. Thermal Behavior of Lithiated Graphite with Electrolyte in Lithium-Ion Batteries. *J. Electrochem. Soc.* **2006**, *153*, A329–A333. [[CrossRef](#)]
91. Yamaki, J.I.; Takatsuji, H.; Kawamura, T.; Egashira, M. Thermal stability of graphite anode with electrolyte in lithium-ion cells. *Solid State Ion.* **2002**, *148*, 241–245. [[CrossRef](#)]
92. Zinigrad, E.; Larush-Asraf, L.; Gnanaraj, J.S.; Gottlieb, H.E.; Sprecher, M.; Aurbach, D. Calorimetric studies of the thermal stability of electrolyte solutions based on alkyl carbonates and the effect of the contact with lithium. *J. Power Sources* **2005**, *146*, 176–179. [[CrossRef](#)]
93. Bowden, P.B.; Young, R.J. Deformation mechanisms in crystalline polymers. *J. Mater. Sci.* **1974**, *9*, 2034–2051. [[CrossRef](#)]
94. Liu, N.; Wu, H.; Mcdowell, M.T.; Yao, Y.; Wang, C.; Cui, Y. A yolk-shell design for stabilized and scalable Li-ion battery alloy anodes. *Nano Lett.* **2012**, *12*, 3315–3321. [[CrossRef](#)]
95. Wagemaker, M.; Mulder, F.M. Properties and promises of nanosized insertion materials for Li-ion batteries. *Acc. Chem. Res.* **2012**, *46*, 1206–1215. [[CrossRef](#)]
96. Zhong, Y.J.; Li, J.T.; Wu, Z.G.; Guo, X.D.; Zhong, B.H.; Sun, S.G.  $\text{LiMn}_{0.5}\text{Fe}_{0.5}\text{PO}_4$  solid solution materials synthesized by rheological phase reaction and their excellent electrochemical performances as cathode of lithium ion battery. *J. Power Sources* **2013**, *234*, 217–222. [[CrossRef](#)]
97. Lu, C.; Qi, W.; Li, L.; Xu, J.; Chen, P.; Xu, R.; Han, L.; Yu, Q. Electrochemical performance and thermal property of electrospun PPESK/PVDF/PPESK composite separator for lithium-ion battery. *J. Appl. Electrochem.* **2013**, *43*, 711–720. [[CrossRef](#)]
98. Gong, W.; Wei, S.; Ruan, S.; Shen, C. Electrospun coaxial PPESK/PVDF fibrous membranes with thermal shutdown property used for lithium-ion batteries. *Mater. Lett.* **2019**, *244*, 126–129. [[CrossRef](#)]
99. Zhang, S.; Liu, P.; Chen, Y.; Jin, J.; Hu, L.; Jian, X. Preparation of thermally stable composite forward osmosis hollow fiber membranes based on copoly (phthalazinone biphenyl ether sulfone) substrates. *Chem. Eng. Sci.* **2017**, *166*, 91–100. [[CrossRef](#)]
100. Wang, G.; Zhang, H.; Qian, B.; Wang, J.; Jian, X.; Qiu, J. Preparation and characterization of electrospun poly (phthalazinone ether nitrile ketone) membrane with novel thermally stable properties. *Appl. Surf. Sci.* **2015**, *351*, 169–174. [[CrossRef](#)]
101. Kim, G.H.; Pesaran, A.; Spotnitz, R. A three-dimensional thermal abuse model for lithium-ion cells. *J. Power Sources* **2007**, *170*, 476–489. [[CrossRef](#)]
102. Spotnitz, R.; Franklin, J. Abuse behavior of high-power, lithium-ion cells. *J. Power Sources* **2003**, *113*, 81–100. [[CrossRef](#)]

103. Venugopal, G. Characterization of thermal cut-off mechanisms in prismatic lithium-ion batteries. *J. Power Sources* **2001**, *101*, 231–237. [[CrossRef](#)]
104. Wang, Q.; Sun, J. Enhancing the safety of lithium ion batteries by 4-isopropyl phenyl diphenyl phosphate. *Mater. Lett.* **2007**, *61*, 3338–3340. [[CrossRef](#)]
105. Ouyang, D.; Liu, J.; Chen, M.; Weng, J.; Wang, J. An experimental study on the thermal failure propagation in lithium-ion battery pack. *J. Electrochem. Soc.* **2018**, *165*, A2184–A2193. [[CrossRef](#)]
106. Huang, P.; Wang, Q.; Li, K.; Ping, P.; Sun, J. The combustion behavior of large scale lithium titanate battery. *Sci. Rep.* **2015**, *5*, 7788. [[CrossRef](#)]
107. Ouyang, D.; Liu, J.; Chen, M.; Wang, J. Investigation into the Fire Hazards of Lithium-Ion Batteries under Overcharging. *Appl. Sci.* **2017**, *7*, 1314. [[CrossRef](#)]
108. Ping, P.; Wang, Q.S.; Huang, P.F.; Li, K.; Sun, J.H.; Kong, D.P.; Chen, C.H. Study of the fire behavior of high-energy lithium-ion batteries with full-scale burning test. *J. Power Sources* **2015**, *285*, 80–89. [[CrossRef](#)]
109. Chen, M.; Zhou, D.; Chen, X.; Zhang, W.; Liu, J.; Yuen, R.; Wang, J. Investigation on the thermal hazards of 18650 lithium ion batteries by fire calorimeter. *J. Therm. Anal. Calorim.* **2015**, *122*, 755–763. [[CrossRef](#)]
110. Fu, Y.; Lu, S.; Shi, L.; Cheng, X.; Zhang, H. Ignition and combustion characteristics of lithium ion batteries under low atmospheric pressure. *Energy* **2018**, *161*, 38–45. [[CrossRef](#)]
111. Ouyang, D.; Chen, M.; Liu, J.; Wei, R.; Weng, J.; Wang, J. Investigation of a commercial lithium-ion battery under overcharge/over-discharge failure conditions. *RSC Adv.* **2018**, *8*, 33414–33424. [[CrossRef](#)]
112. Jhu, C.Y.; Wang, Y.W.; Shu, C.M.; Chang, J.C.; Wu, H.C. Thermal explosion hazards on 18650 lithium ion batteries with a VSP2 adiabatic calorimeter. *J. Hazard. Mater.* **2011**, *192*, 99–107.87. [[CrossRef](#)]
113. Larsson, F.; Andersson, P.; Blomqvist, P.; Lorén, A.; Mellander, B.E. Characteristics of lithium-ion batteries during fire tests. *J. Power Sources* **2014**, *271*, 414–420. [[CrossRef](#)]
114. Golubkov, A.W.; Fuchs, D.; Wagner, J.; Wiltsche, H.; Stangl, C.; Fauler, G.; Voitic, G.; Thaler, A.; Hacher, V. Thermal-runaway experiments on consumer Li-ion batteries with metal-oxide and olivin-type cathodes. *RSC Adv.* **2014**, *4*, 3633–3642. [[CrossRef](#)]
115. Sun, J.; Li, J.; Zhou, T.; Yang, K.; Wei, S.; Tang, N.; Dang, N.; Li, H.; Qiu, X.; Chen, L. Toxicity, a serious concern of thermal runaway from commercial Li-ion battery. *Nano Energy* **2016**, *27*, 313–319. [[CrossRef](#)]
116. Yang, H.; Zhuang, G.V.; Ross, P.N. Thermal stability of LiPF<sub>6</sub> salt and Li-ion battery electrolytes containing LiPF<sub>6</sub>. *J. Power Sources* **2006**, *161*, 573–579. [[CrossRef](#)]
117. Maleki, H.; Deng, G.; Anani, A. Thermal Stability Studies of Li-Ion Cells and Components. *J. Electrochem. Soc.* **1999**, *146*, 3224–3229. [[CrossRef](#)]
118. Gray, F.M. *Solid Polymer Electrolytes*; VCH: New York, NY, USA, 1991.
119. Braun, J.; Stöss, H.; Zober, A. Intoxication following the inhalation of hydrogen fluoride. *Arch. Toxicol.* **1984**, *56*, 50–54. [[CrossRef](#)] [[PubMed](#)]
120. Ouyang, D.; Chen, M.; Wei, R.; Wang, Z.; Wang, J. A study on the fire behaviors of 18650 battery and batteries pack under discharge. *J. Therm. Anal. Calorim.* **2019**, *136*, 1915–1926. [[CrossRef](#)]
121. Chen, M.; Liu, J.; He, Y.; Yuen, R.; Wang, J. Study of the fire hazards of lithium-ion batteries at different pressures. *Appl. Therm. Eng.* **2017**, *125*, 1061–1074. [[CrossRef](#)]
122. Wagner, M.W.; Liebenow, C.; Besenhard, J.O. Effect of polysulfide-containing electrolyte on the film formation of the negative electrode. *J. Power Sources* **1997**, *68*, 328–332. [[CrossRef](#)]
123. Wrodnigg, G.H.; Besenhard, J.O.; Winter, M. Cyclic and acyclic sulfites: New solvents and electrolyte additives for lithium ion batteries with graphitic anodes? *J. Power Sources* **2001**, *97*, 592–594. [[CrossRef](#)]
124. Lee, J.H.; Paik, U.; Hackley, V.A.; Choi, Y.M. Effect of carboxymethyl cellulose on aqueous processing of natural graphite negative electrodes and their electrochemical performance for lithium batteries. *J. Electrochem. Soc.* **2005**, *152*, A1763–A1769. [[CrossRef](#)]
125. Ouyang, D.; Liu, J.; Chen, M.; Weng, J.; Wang, J. Thermal Failure Propagation in Lithium-Ion Battery Modules with Various Shapes. *Appl. Sci.* **2018**, *8*, 1263. [[CrossRef](#)]
126. Lopez, C.F.; Jeevarajan, J.A.; Mukherjee, P.P. Experimental analysis of thermal runaway and propagation in lithium-ion battery modules. *J. Electrochem. Soc.* **2015**, *162*, A1905–A1915. [[CrossRef](#)]
127. Lamb, J.; Orendorff, C.J.; Steele, L.A.M.; Spangler, S.W. Failure propagation in multi-cell lithium ion batteries. *J. Power Sources* **2015**, *283*, 517–523. [[CrossRef](#)]

128. Larsson, F.; Anderson, J.; Andersson, P.; Mellander, B.E. Thermal modelling of cell-to-cell fire propagation and cascading thermal runaway failure effects for lithium-ion battery cells and modules using fire walls. *J. Electrochem. Soc.* **2016**, *163*, A2854–A2865. [[CrossRef](#)]
129. Feng, X.; He, X.; Ouyang, M.; Lu, L.; Wu, P.; Kulp, C.; Prasser, S. Thermal runaway propagation model for designing a safer battery pack with 25 Ah LiNi<sub>x</sub>Co<sub>y</sub>Mn<sub>z</sub>O<sub>2</sub> large format lithium ion battery. *Appl. Energy* **2015**, *154*, 74–91. [[CrossRef](#)]
130. Wilke, S.; Schweitzer, B.; Khateeb, S.; Al-Hallaj, S. Preventing thermal runaway propagation in lithium ion battery packs using a phase change composite material: An experimental study. *J. Power Sources* **2017**, *340*, 51–59. [[CrossRef](#)]
131. Spinner, N.S.; Field, C.R.; Hammond, M.H.; Williams, B.A.; Myers, K.M.; Lubrano, A.L.; Rose-Pehrsson, S.L.; Tuttle, S.G. Physical and chemical analysis of lithium-ion battery cell-to-cell failure events inside custom fire chamber. *J. Power Sources* **2015**, *279*, 713–721. [[CrossRef](#)]
132. Gao, S.; Feng, X.; Lu, L. Thermal Runaway Propagation Assessment of Different Battery Pack Designs Using the TF5 Draft as Framework. *J. Electrochem. Soc.* **2019**, *166*, A1653–A1659. [[CrossRef](#)]
133. Feng, X.; Sun, J.; Ouyang, M.; Wang, F.; He, X.; Lu, L.; Peng, H. Characterization of penetration induced thermal runaway propagation process within a large format lithium ion battery module. *J. Power Sources* **2015**, *275*, 261–273. [[CrossRef](#)]
134. Alshaer, W.G.; Nada, S.A.; Rady, M.A.; Le Bot, C.; Del Barrio, E.P. Numerical investigations of using carbon foam/PCM/Nano carbon tubes composites in thermal management of electronic equipment. *Energy Convers. Manag.* **2015**, *89*, 873–884. [[CrossRef](#)]
135. Şahan, N.; Fois, M.; Paksoy, H. Improving thermal conductivity phase change materials—A study of paraffin nanomagnetite composites. *Sol. Energy Mater. Sol. Cells* **2015**, *137*, 61–67. [[CrossRef](#)]
136. Feng, X.; Lu, L.; Ouyang, M.; Li, J.; He, X. A 3D thermal runaway propagation model for a large format lithium ion battery module. *Energy* **2016**, *115*, 194–208. [[CrossRef](#)]
137. Coman, P.T.; Darcy, E.C.; Veje, C.T.; White, R.E. Numerical analysis of heat propagation in a battery pack using a novel technology for triggering thermal runaway. *Appl. Energy* **2017**, *203*, 189–200. [[CrossRef](#)]
138. Coman, P.T.; Rayman, S.; White, R.E. A lumped model of venting during thermal runaway in a cylindrical Lithium Cobalt Oxide lithium-ion cell. *J. Power Sources* **2016**, *307*, 56–62. [[CrossRef](#)]
139. Richard, M.N.; Dahn, J.R. Accelerating rate calorimetry study on the thermal stability of lithium intercalated graphite in electrolyte. I. Experimental. *J. Electrochem. Soc.* **1999**, *146*, 2068–2077. [[CrossRef](#)]
140. Richard, M.N.; Dahn, J.R. Accelerating rate calorimetry study on the thermal stability of lithium intercalated graphite in electrolyte. II. Modeling the results and predicting differential scanning calorimeter curves. *J. Electrochem. Soc.* **1999**, *146*, 2078–2084. [[CrossRef](#)]
141. Guo, G.; Long, B.; Cheng, B. Three-dimensional thermal finite element modeling of lithium-ion battery in thermal abuse application. *J. Power Sources* **2010**, *195*, 2393–2398. [[CrossRef](#)]
142. Hatchard, T.D.; MacNeil, D.D.; Basu, A.; Dahn, J.R. Thermal model of cylindrical and prismatic lithium-ion cells. *J. Electrochem. Soc.* **2001**, *148*, A755–A761. [[CrossRef](#)]
143. Yeow, K.F.; Teng, H. Characterizing thermal runaway of lithium-ion cells in a battery system using finite element analysis approach. *Sae Int. J. Altern. Powertrains* **2013**, *2*, 179–186. [[CrossRef](#)]
144. Spotnitz, R.M.; Weaver, J.; Yeduvaka, G.; Doughty, D.H.; Roth, E.P. Simulation of abuse tolerance of lithium-ion battery packs. *J. Power Sources* **2007**, *163*, 1080–1086. [[CrossRef](#)]
145. Kieler, A. At Least 17 Lithium-Ion Batteries Have Exploded on Planes This Year. Available online: <https://consumerist.com/2017/06/09/at-least-17-lithium-ion-batteries-have-exploded-on-planes-this-year/> (accessed on 6 September 2017).
146. Yafei, W.; Lizhong, Y.; Xiaodong, Z.; Jiakun, D.; Yupeng, Z.; Zhihua, D. Experiment study of the altitude effects on spontaneous ignition characteristics of wood. *Fuel* **2010**, *89*, 1029–1034. [[CrossRef](#)]
147. Niu, Y.; He, Y.; Hu, X.; Zhou, D.; Lin, C.; Yin, J.; Yao, W. Experimental study of burning rates of cardboard box fires near sea level and at high altitude. *Proc. Combust. Inst.* **2013**, *34*, 2565–2573. [[CrossRef](#)]
148. Yao, W.; Hu, X.; Rong, J.; Wang, J.; Zhang, H. Experimental study of large-scale fire behavior under low pressure at high altitude. *J. Fire Sci.* **2013**, *31*, 481–494. [[CrossRef](#)]
149. Li, Z.; He, Y.; Zhang, H.; Wang, J. Combustion characteristics of n-heptane and wood crib fires at different altitudes. *Proc. Combust. Inst.* **2009**, *32*, 2481–2488. [[CrossRef](#)]

150. McAllister, S.; Fernandez-Pello, C.; Urban, D.; Ruff, G. The combined effect of pressure and oxygen concentration on piloted ignition of a solid combustible. *Combust. Flame* **2010**, *157*, 1753–1759. [[CrossRef](#)]
151. Zarzecki, M.; Quintiere, J.G.; Lyon, R.E.; Rossmann, T.; Diez, F.J. The effect of pressure and oxygen concentration on the combustion of PMMA. *Combust. Flame* **2013**, *160*, 1519–1530. [[CrossRef](#)]
152. Weng, W.G.; Hasemi, Y.; Fan, W.C. Predicting the pyrolysis of wood considering char oxidation under different ambient oxygen concentrations. *Combust. Flame* **2006**, *145*, 723–729. [[CrossRef](#)]
153. Liu, J.; He, Y.; Zhou, Z.; Yao, W.; Yuen, R.; Wang, J. The burning behaviors of pool fire flames under low pressure. *Fire Mater.* **2016**, *40*, 318–334. [[CrossRef](#)]
154. Hu, X.; He, Y.; Li, Z.; Wang, J. Combustion characteristics of n-heptane at high altitudes. *Proc. Combust. Inst.* **2011**, *33*, 2607–2615. [[CrossRef](#)]
155. Tu, R.; Fang, J.; Zhang, Y.M.; Zhang, J.; Zeng, Y. Effects of low air pressure on radiation-controlled rectangular ethanol and n-heptane pool fires. *Proc. Combust. Inst.* **2013**, *34*, 2591–2598. [[CrossRef](#)]
156. Tao, C.; He, Y.; Li, Y.; Wang, X. Effects of oblique air flow on burning rates of square ethanol pool fires. *J. Hazard. Mater.* **2013**, *260*, 552–562. [[CrossRef](#)] [[PubMed](#)]
157. Yin, J.; Yao, W.; Liu, Q.; Zhou, Z.; Wu, N.; Zhang, H.; Lin, C.H.; Wu, T.; Meier, O.C. Experimental study of n-Heptane pool fire behavior in an altitude chamber. *Int. J. Heat Mass Transf.* **2013**, *62*, 543–552. [[CrossRef](#)]
158. Jiusheng, Y.; Wei, Y.; Quanyi, L.; Wu, N.; Zhou, Z.; Wu, Y.; Zhang, H. Experimental study of n-heptane pool fire behaviors under dynamic pressures in an altitude chamber. *Procedia Eng.* **2013**, *52*, 548–556. [[CrossRef](#)]
159. Yao, J.; Liu, J.; Chen, X.; Li, H.; Niu, Y.; Zhou, Z.; Wang, J. Experimental study of small scale n-heptane pool fire with water bath in an altitude chamber. *Int. J. Heat Mass Transf.* **2015**, *90*, 1153–1159. [[CrossRef](#)]
160. Fang, J.; Tu, R.; Guan, J.; Wang, J.; Zhang, Y. Influence of low air pressure on combustion characteristics and flame pulsation frequency of pool fires. *Fuel* **2011**, *90*, 2760–2766. [[CrossRef](#)]
161. Liu, J.; He, Y.; Zhou, Z.; Yuen, R.; Wang, J. Investigation of enclosure effect of pressure chamber on the burning behavior of a hydrocarbon fuel. *Appl. Therm. Eng.* **2016**, *101*, 202–216. [[CrossRef](#)]
162. Zeng, Y.; Fang, J.; Tu, R.; Wang, J.; Zhang, Y. Study on burning characteristics of small-scale ethanol pool fire in closed and open space under low air pressure. In *ASME 2011 International Mechanical Engineering Congress and Exposition*; American Society of Mechanical Engineers: New York, NY, USA, 2011; pp. 1423–1430.
163. Chen, M.; Liu, J.; Lin, X.; Huang, Q.; Yuen, R.; Wang, J. Combustion characteristics of primary lithium battery at two altitudes. *J. Therm. Anal. Calorim.* **2016**, *124*, 865–870. [[CrossRef](#)]
164. Mizushima, K.; Jones, P.; Wiseman, P.; Goodenough, J.B.  $\text{Li}_x\text{CoO}_2$  ( $0 < x < -1$ ): A new cathode material for batteries of high energy density. *Mater. Res. Bull.* **1980**, *15*, 783–789.
165. Thackeray, M.; David, W.; Bruce, P.; Goodenough, J.B. Lithium insertion into manganese spinels. *Mater. Res. Bull.* **1983**, *18*, 461–472. [[CrossRef](#)]
166. Padhi, A.K.; Nanjundaswamy, K.S.; Goodenough, J.B. Phospho-olivines as positive-electrode materials for rechargeable lithium batteries. *J. Electrochem. Soc.* **1997**, *144*, 1188–1194. [[CrossRef](#)]
167. Kraysberg, A.; Ein-Eli, Y. Higher, Stronger, Better ... A Review of 5 Volt Cathode Materials for Advanced Lithium-Ion Batteries. *Adv. Energy Mater.* **2012**, *2*, 922–939. [[CrossRef](#)]
168. Takahashi, Y.; Tode, S.; Kinoshita, A.; Fujimoto, H.; Nakane, I.; Fujitani, S. Development of Lithium-Ion Batteries with a  $\text{LiCoO}_2$  Cathode Toward High Capacity by Elevating Charging Potential. *J. Electrochem. Soc.* **2008**, *155*, A537–A541. [[CrossRef](#)]
169. Yin, R.-Z.; Kim, Y.-S.; Shin, S.-J.; Jung, I.; Kim, J.S.; Jeong, S.K. In situ XRD investigation and thermal properties of Mg doped  $\text{LiCoO}_2$  for lithium ion batteries. *J. Electrochem. Soc.* **2012**, *159*, A253–A258. [[CrossRef](#)]
170. Ahn, S.; Kim, H.-S.; Yang, S.; Do, J.Y.; Kim, B.H.; Kim, K. Thermal stability and performance studies of  $\text{LiCo}_{1/3}\text{Ni}_{1/3}\text{Mn}_{1/3}\text{O}_2$  with phosphazene additives for Li-ion batteries. *J. Electroceram.* **2009**, *23*, 289–294. [[CrossRef](#)]
171. Zhang, L.; Ma, Y.; Cheng, X.; Du, C.; Guan, T.; Cui, Y.; Sun, S.; Zuo, P.; Gao, Y.; Yin, G. Capacity fading mechanism during long-term cycling of over-discharged  $\text{LiCoO}_2$ /mesocarbon microbeads battery. *J. Power Sources* **2015**, *293*, 1006–1015. [[CrossRef](#)]
172. Ji, Y.; Zhang, P.; Lin, M.; Zhao, W.; Zhang, Z.; Zhao, Y.; Yang, Y. Toward a stable electrochemical interphase with enhanced safety on high-voltage  $\text{LiCoO}_2$  cathode: A case of phosphazene additives. *J. Power Sources* **2017**, *359*, 391–399. [[CrossRef](#)]

173. Deng, Y.; Kang, T.; Ma, Z.; Tan, X.; Song, X.; Wang, Z.; Pang, P.; Shu, D.; Zuo, X.; Nan, J. Safety influences of the Al and Ti elements modified LiCoO<sub>2</sub> materials on LiCoO<sub>2</sub>/graphite batteries under the abusive conditions. *Electrochim. Acta* **2019**, *295*, 703–709. [[CrossRef](#)]
174. Yamada, A.; Chung, S.-C.; Hinokuma, K. Optimized LiFePO<sub>4</sub> for lithium battery cathodes. *J. Electrochem. Soc.* **2001**, *148*, A224–A229. [[CrossRef](#)]
175. Jiang, J.; Dahn, J. ARC studies of the thermal stability of three different cathode materials: LiCoO<sub>2</sub>; Li[Ni<sub>0.1</sub>Co<sub>0.8</sub>Mn<sub>0.1</sub>]O<sub>2</sub>; and LiFePO<sub>4</sub>, in LiPF<sub>6</sub> and LiBoB EC/DEC electrolytes. *Electrochem. Commun.* **2004**, *6*, 39–43. [[CrossRef](#)]
176. Bazzi, K.; Nazri, M.; Naik, V.; Garg, V.K.; Oliveira, A.C.; Nazri, G.A.; Naik, R. Enhancement of electrochemical behavior of nanostructured LiFePO<sub>4</sub>/Carbon cathode material with excess Li. *J. Power Sources* **2016**, *306*, 17–23. [[CrossRef](#)]
177. Johnson, I.D.; Lübke, M.; Wu, O.Y.; Makwana, N.M.; Smales, G.J.; Islam, H.U.; Dedigama, R.Y.; Guar, R.I.; Tighe, C.J.; Scanlon, D.O.; et al. Pilot-scale continuous synthesis of a vanadium-doped LiFePO<sub>4</sub>/C nanocomposite high-rate cathodes for lithium-ion batteries. *J. Power Sources* **2016**, *302*, 410–418. [[CrossRef](#)]
178. Huang, Y.; Liu, H.; Gong, L.; Hou, Y.; Li, Q. A simple route to improve rate performance of LiFePO<sub>4</sub>/reduced graphene oxide composite cathode by adding Mg<sup>2+</sup> via mechanical mixing. *J. Power Sources* **2017**, *347*, 29–36. [[CrossRef](#)]
179. Ohzuku, T.; Makimura, Y. Layered lithium insertion material of LiCo<sub>1/3</sub>Ni<sub>1/3</sub>Mn<sub>1/3</sub>O<sub>2</sub> for lithium-ion batteries. *Chem. Lett.* **2001**, *30*, 642–643. [[CrossRef](#)]
180. Liu, Z.; Yu, A.; Lee, J.Y. Synthesis and characterization of LiNi<sub>1-x-y</sub>Co<sub>x</sub>Mn<sub>y</sub>O<sub>2</sub> as the cathode materials of secondary lithium batteries. *J. Power Sources* **1999**, *81*, 416–419. [[CrossRef](#)]
181. Myung, S.-T.; Maglia, F.; Park, K.-J.; Yoon, C.S.; Lamp, P.; Kim, S.J.; Sun, Y.K. Nickel-rich layered cathode materials for automotive lithium-ion batteries: Achievements and perspectives. *ACS Energy Lett.* **2016**, *2*, 196–223. [[CrossRef](#)]
182. Ma, L.; Xia, J.; Xia, X.; Dahn, J.R. The impact of vinylene carbonate, fluoroethylene carbonate and vinyl ethylene carbonate electrolyte additives on electrode/electrolyte reactivity studied using accelerating rate calorimetry. *J. Electrochem. Soc.* **2014**, *161*, A1495–A1498. [[CrossRef](#)]
183. Ma, L.; Xia, J.; Dahn, J. Ternary electrolyte additive mixtures for Li-ion cells that promote long lifetime and less reactivity with charged electrodes at elevated temperatures. *J. Electrochem. Soc.* **2015**, *162*, A1170–A1174. [[CrossRef](#)]
184. Liu, X.; Ren, D.; Hsu, H.; Feng, X.; Xu, G.L.; Zhuang, M.; Gao, H.; Lu, L.; Han, X.; Chu, Z.; et al. Thermal runaway of lithium-ion batteries without internal short circuit. *Joule* **2018**, *2*, 2047–2064. [[CrossRef](#)]
185. Hwang, S.; Chang, W.; Kim, S.M.; Su, D.; Kim, D.H.; Lee, J.Y.; Chung, K.Y.; Stach, E.A. Investigation of changes in the surface structure of Li<sub>x</sub>Ni<sub>0.8</sub>Co<sub>0.15</sub>Al<sub>0.05</sub>O<sub>2</sub> cathode materials induced by the initial charge. *Chem. Mater.* **2014**, *26*, 1084–1092. [[CrossRef](#)]
186. Cai, L.; Liu, Z.; An, K.; Liang, C. Probing Li-Ni Cation Disorder in Li<sub>1-x</sub>Ni<sub>1+x-y</sub>Al<sub>y</sub>O<sub>2</sub> Cathode Materials by Neutron Diffraction. *J. Electrochem. Soc.* **2012**, *159*, A924–A928. [[CrossRef](#)]
187. Lee, M.J.; Noh, M.; Park, M.H.; Jo, M.; Kim, H.; Nam, H.; Cho, J. The role of nanoscale-range vanadium treatment in LiNi<sub>0.8</sub>Co<sub>0.15</sub>Al<sub>0.05</sub>O<sub>2</sub> cathode materials for Li-ion batteries at elevated temperatures. *J. Mater. Chem. A* **2015**, *3*, 13453–13460. [[CrossRef](#)]
188. Muto, S.; Tatsumi, K.; Kojima, Y.; Oka, H.; Kondo, H.; Horibuchi, K.; Ukyo, Y. Effect of Mg-doping on the degradation of LiNiO<sub>2</sub>-based cathode materials by combined spectroscopic methods. *J. Power Sources* **2012**, *205*, 449–455. [[CrossRef](#)]
189. Huang, B.; Li, X.; Wang, Z.; Guo, H.; Xiong, X. Synthesis of Mg-doped LiNi<sub>0.8</sub>Co<sub>0.15</sub>Al<sub>0.05</sub>O<sub>2</sub> oxide and its electrochemical behavior in high-voltage lithium-ion batteries. *Ceram. Int.* **2014**, *40*, 13223–13230. [[CrossRef](#)]
190. Wang, Q.; Mao, B.; Stolarov, S.I. A review of lithium ion battery failure mechanisms and fire prevention strategies. *Prog. Energy Combust. Sci.* **2019**, *73*, 95–131. [[CrossRef](#)]
191. Kong, L.; Li, C.; Jiang, J.; Pecht, M.G. Li-ion battery fire hazards and safety strategies. *Energies* **2018**, *11*, 2191. [[CrossRef](#)]
192. Mier, F.A.; Hargather, M.J.; Ferreira, S.R. *Experimental Quantification of Vent Mechanism Flow Parameters in 18650 Format Lithium Ion Batteries*; Sandia National Lab.(SNL-NM): Albuquerque, NM, USA, 2019.
193. Balakrishnan, P.G.; Ramesh, R.; Kumar, T.P. Safety mechanisms in lithium-ion batteries. *J. Power Sources* **2006**, *155*, 401–414. [[CrossRef](#)]

194. Meyer, J. Glass transition temperature as a guide to selection of polymers suitable for PTC materials. *Polym. Eng. Sci.* **1973**, *13*, 462–468. [[CrossRef](#)]
195. Johnson, B.A.; White, R.E. Characterization of commercially available lithium-ion batteries. *J. Power Sources* **1998**, *70*, 48–54. [[CrossRef](#)]
196. Huo, W.; Qu, Y. Effects of  $\text{Bi}_{1/2}\text{Na}_{1/2}\text{TiO}_3$  on the Curie temperature and the PTC effects of  $\text{BaTiO}_3$ -based positive temperature coefficient ceramics. *Sens. Actuators A Phys.* **2006**, *128*, 265–269. [[CrossRef](#)]
197. Ding, S.W.; Jia, G.; Wang, J.; He, Z.Y. Electrical properties of Y-and Mn-doped  $\text{BaTiO}_3$ -based PTC ceramics. *Ceram. Int.* **2008**, *34*, 2007–2010. [[CrossRef](#)]
198. Zhao, S.; Li, G.; Liu, H.; Dai, K.; Zheng, G.; Yan, X.; Liu, C.; Chen, J.; Shen, C.; Guo, Z. Positive Temperature Coefficient (PTC) Evolution of Segregated Structural Conductive Polypropylene Nanocomposites with Visually Traceable Carbon Black Conductive Network. *Adv. Mater. Interfaces* **2017**, *4*, 1700265. [[CrossRef](#)]
199. Zhao, S.; Lou, D.; Zhan, P.; Li, G.; Dai, K.; Guo, J.; Zheng, G.; Liu, C.; Shen, C.; Guo, Z. Heating-induced negative temperature coefficient effect in conductive graphene/polymer ternary nanocomposites with a segregated and double-percolated structure. *J. Mater. Chem. C* **2017**, *5*, 8233–8242. [[CrossRef](#)]
200. Dunn, B.; Kamath, H.; Tarascon, J.M. Electrical energy storage for the grid: A battery of choices. *Science* **2011**, *334*, 928–935. [[CrossRef](#)]
201. Mönnighoff, X.; Murmann, P.; Weber, W.; Winter, M.; Nowak, S. Post-mortem investigations of fluorinated flame retardants for lithium ion battery electrolytes by gas chromatography with chemical ionization. *Electrochim. Acta* **2017**, *246*, 1042–1051. [[CrossRef](#)]
202. Wang, Q.; Jiang, L.; Yu, Y.; Sun, J. Progress of enhancing the safety of lithium ion battery from the electrolyte aspect. *Nano Energy* **2019**, *55*, 93–114. [[CrossRef](#)]
203. Murmann, P.; Mönnighoff, X.; von Aspern, N.; Janssen, P.; Kalinovich, N.; Shevchuk, M.; Kazakova, O.; Rösenthale, G.V.; Cekic-Laskovic, I.; Winter, M. Influence of the fluorination degree of organophosphates on flammability and electrochemical performance in lithium ion batteries: Studies on fluorinated compounds deriving from triethyl phosphate. *J. Electrochem. Soc.* **2016**, *163*, A751–A757. [[CrossRef](#)]
204. Xu, K.; Ding, M.S.; Zhang, S.; Allen, J.L.; Jow, T.R. An attempt to formulate nonflammable lithium ion electrolytes with alkyl phosphates and phosphazenes. *J. Electrochem. Soc.* **2002**, *149*, A622–A626. [[CrossRef](#)]
205. Laoutid, F.; Bonnaud, L.; Alexandre, M.; Lopez-Cuesta, J.M.; Dubois, P. New prospects in flame retardant polymer materials: From fundamentals to nanocomposites. *Mater. Sci. Eng. R Rep.* **2009**, *63*, 100–125. [[CrossRef](#)]
206. Xiang, H.F.; Xu, H.Y.; Wang, Z.Z.; Chen, C. Dimethyl methylphosphonate (DMMP) as an efficient flame retardant additive for the lithium-ion battery electrolytes. *J. Power Sources* **2007**, *173*, 562–564. [[CrossRef](#)]
207. Hu, J.; Jin, Z.; Zhong, H.; Zhan, H.; Zhou, Y.; Li, Z. A new phosphoramidate as flame retardant additive in electrolytes for lithium ion batteries. *J. Power Sources* **2012**, *197*, 297–300. [[CrossRef](#)]
208. Ding, M.S.; Xu, K.; Jow, T.R. Effects of tris (2, 2, 2-trifluoroethyl) phosphate as a flame-retarding cosolvent on physicochemical properties of electrolytes of LiPF<sub>6</sub> in EC-PC-EMC of 3, 3, 4 weight ratios. *J. Electrochem. Soc.* **2002**, *149*, A1489–A1498. [[CrossRef](#)]
209. Zeng, Z.; Jiang, X.; Wu, B.; Xiao, L.; Ai, X.; Yang, H.; Cao, Y. Bis (2, 2, 2-trifluoroethyl) methylphosphonate: An novel flame-retardant additive for safe lithium-ion battery. *Electrochim. Acta* **2014**, *129*, 300–304. [[CrossRef](#)]
210. Moreno, M.; Simonetti, E.; Appetecchi, G.B.; Carewska, M.; Montaninoc, M.; Kim, G.T.; Loeffler, N.; Passerini, S. Ionic Liquid Electrolytes for Safer Lithium Batteries I. Investigation around Optimal Formulation. *J. Electrochem. Soc.* **2017**, *164*, A6026–A6031. [[CrossRef](#)]
211. Chawla, N.; Bharti, N.; Singh, S. Recent advances in non-flammable electrolytes for safer lithium-ion batteries. *Batteries* **2019**, *5*, 19. [[CrossRef](#)]
212. Shi, P.; Zheng, H.; Liang, X.; Sun, Y.; Cheng, S.; Chen, C.; Xiang, H. A highly concentrated phosphate-based electrolyte for high-safety rechargeable lithium batteries. *Chem. Commun.* **2018**, *54*, 4453–4456. [[CrossRef](#)] [[PubMed](#)]
213. Safa, M.; Chamaani, A.; Chawla, N.; El-Zahab, B. Polymeric ionic liquid gel electrolyte for room temperature lithium battery applications. *Electrochim. Acta* **2016**, *213*, 587–593. [[CrossRef](#)]
214. Guo, Q.; Han, Y.; Wang, H.; Xiong, S.; Sun, W.; Zheng, C.; Xie, K. Flame Retardant and Stable  $\text{Li}_{1.5}\text{Al}_{0.5}\text{Ge}_{1.5}(\text{PO}_4)_3$ -Supported Ionic Liquid Gel Polymer Electrolytes for High Safety Rechargeable Solid-State Lithium Metal Batteries. *J. Phys. Chem. C* **2018**, *122*, 10334–10342. [[CrossRef](#)]

215. Rectenwald, M.F.; Gaffen, J.R.; Rheingold, A.L.; Morgan, A.B.; Protasiewicz, J.D. Phosphoryl-Rich Flame-Retardant Ions (FRIONS): Towards Safer Lithium-Ion Batteries. *Angew. Chem.* **2014**, *126*, 4257–4260. [[CrossRef](#)]
216. Dagger, T.; Meier, V.; Hildebrand, S.; Brüggemann, D.; Winter, M.; Schappacher, F.M. Safety Performance of 5 Ah Lithium Ion Battery Cells Containing the Flame Retardant Electrolyte Additive (Phenoxy) Pentafluorocyclotriphosphazene. *Energy Technol.* **2018**, *6*, 2001–2010. [[CrossRef](#)]
217. Wu, B.; Pei, F.; Wu, Y.; Mao, R.; Ai, X.; Yang, H.; Cao, Y. An electrochemically compatible and flame-retardant electrolyte additive for safe lithium ion batteries. *J. Power Sources* **2013**, *227*, 106–110. [[CrossRef](#)]
218. Li, X.; Li, W.; Chen, L.; Lu, Y.; Su, Y.; Bao, L.; Wang, J.; Chen, R.; Chen, S.; Wu, F. Ethoxy (pentafluoro) cyclotriphosphazene (PPFN) as a multi-functional flame retardant electrolyte additive for lithium-ion batteries. *J. Power Sources* **2018**, *378*, 707–716. [[CrossRef](#)]
219. Wu, H.; Zhuo, D.; Kong, D. Improving battery safety by early detection of internal shorting with a bifunctional separator. *Nat. Commun.* **2014**, *5*, 5193. [[CrossRef](#)]
220. Ryou, M.H.; Lee, D.J.; Lee, J.N.; Lee, J.K.; Park, J.K.; Choi, J.W. Excellent cycle life of lithium-metal anodes in lithium-ion batteries with mussel-inspired polydopamine-coated separators. *Adv. Energy Mater.* **2012**, *2*, 645–650. [[CrossRef](#)]
221. Kim, J.H.; Kim, J.H.; Choi, K.H.; Yu, H.K.; Kim, J.H.; Lee, J.S.; Lee, S.Y. Inverse opal-inspired, nanoscaffold battery separators: A new membrane opportunity for high-performance energy storage systems. *Nano Lett.* **2014**, *14*, 4438–4448. [[CrossRef](#)]
222. Orendorff, C.J. The role of separators in lithium-ion cell safety. *Electrochem. Soc. Interface* **2012**, *21*, 61–65. [[CrossRef](#)]
223. Xiang, Y.; Li, J.; Lei, J.; Liu, D.; Xie, Z.; Qu, D.; Li, K.; Deng, T.; Tang, H. Advanced separators for lithium-ion and lithium-sulfur batteries: A review of recent progress. *ChemSusChem* **2016**, *9*, 3023–3039. [[CrossRef](#)] [[PubMed](#)]
224. Arora, P.; Zhang, Z. Battery separators. *Chem. Rev.* **2004**, *104*, 4419–4462. [[CrossRef](#)] [[PubMed](#)]
225. Ryou, M.H.; Lee, J.N.; Lee, D.J.; Kim, W.K.; Jeong, Y.K.; Choi, J.W.; Park, J.K.; Lee, Y.M. Effects of lithium salts on thermal stabilities of lithium alkyl carbonates in SEI layer. *Electrochim. Acta* **2012**, *83*, 259–263. [[CrossRef](#)]
226. Yeon, D.; Lee, Y.; Ryou, M.H.; Lee, Y.M. New flame-retardant composite separators based on metal hydroxides for lithium-ion batteries. *Electrochim. Acta* **2015**, *157*, 282–289. [[CrossRef](#)]
227. Lee, T.; Kim, W.K.; Lee, Y.; Ryou, M.H.; Lee, Y.M. Effect of Al<sub>2</sub>O<sub>3</sub> coatings prepared by RF sputtering on polyethylene separators for high-power lithium ion batteries. *Macromol. Res.* **2014**, *22*, 1190–1195. [[CrossRef](#)]
228. Lee, J.Y.; Shin, S.H.; Moon, S.H. Flame retardant coated polyolefin separators for the safety of lithium ion batteries. *Korean J. Chem. Eng.* **2016**, *33*, 285–289. [[CrossRef](#)]
229. Zhang, J.; Yue, L.; Kong, Q.; Liu, Z.; Zhou, X.; Zhang, C.; Xu, Q.; Zhang, B.; Ding, G.; Qin, B.; et al. Sustainable, heat-resistant and flame-retardant cellulose-based composite separator for high-performance lithium ion battery. *Sci. Rep.* **2014**, *4*, 3935. [[CrossRef](#)]
230. Wu, W.; Wang, S.; Wu, W.; Chen, K.; Hong, S.; Lai, Y. A critical review of battery thermal performance and liquid based battery thermal management. *Energy Convers. Manag.* **2019**, *182*, 262–281. [[CrossRef](#)]
231. Ramadass, P.; Haran, B.; White, R.; Popov, B. Capacity fade of Sony 18650 cells cycled at elevated temperatures: Part II. Capacity fade analysis. *J. Power Sources* **2002**, *112*, 614–620. [[CrossRef](#)]
232. Smart, M.C.; Ratnakumar, B.V.; Whitcanack, L.D.; Chin, K.B.; Surampudi, S.; Croft, H.; Tice, D.; Staniewicz, R. Improved low-temperature performance of lithium-ion cells with quaternary carbonate-based electrolytes. *J. Power Sources* **2003**, *119*, 349–358. [[CrossRef](#)]
233. Ouyang, M.; Chu, Z.; Lu, L.; Li, J.; Han, X.; Feng, X.; Liu, G. Low temperature aging mechanism identification and lithium deposition in a large format lithium iron phosphate battery for different charge profiles. *J. Power Sources* **2015**, *286*, 309–320. [[CrossRef](#)]
234. Feng, X.; Xu, C.; He, X.; Wang, L.; Zhang, G.; Ouyang, M. Mechanisms for the evolution of cell variations within a LiNi<sub>x</sub>Co<sub>y</sub>Mn<sub>z</sub>O<sub>2</sub>/graphite lithium-ion battery pack caused by temperature non-uniformity. *J. Clean. Prod.* **2018**, *205*, 447–462. [[CrossRef](#)]
235. Lu, L.; Han, X.; Li, J.; Hua, J.; Ouyang, M. A review on the key issues for lithium-ion battery management in electric vehicles. *J. Power Sources* **2013**, *226*, 272–288. [[CrossRef](#)]
236. Choi, K.W.; Yao, N.P. Heat Transfer in Lead-Acid Batteries Designed for Electric-Vehicle Propulsion Application. *J. Electrochem. Soc.* **1979**, *126*, 1321–1328. [[CrossRef](#)]

237. Mohammadian, S.K.; He, Y.L.; Zhang, Y. Internal cooling of a lithium-ion battery using electrolyte as coolant through microchannels embedded inside the electrodes. *J. Power Sources* **2015**, *293*, 458–466. [[CrossRef](#)]
238. Bandhauer, T.M.; Garimella, S. Passive, internal thermal management system for batteries using microscale liquid–vapor phase change. *Appl. Therm. Eng.* **2013**, *61*, 756–769. [[CrossRef](#)]
239. Stuart, T.A.; Hande, A. HEV battery heating using AC currents. *J. Power Sources* **2004**, *129*, 368–378. [[CrossRef](#)]
240. Ruan, H.; Jiang, J.; Sun, B.; Zhang, W.; Gao, W.; Wang, L.; Ma, Z. A rapid low-temperature internal heating strategy with optimal frequency based on constant polarization voltage for lithium-ion batteries. *Appl. Energy* **2016**, *177*, 771–782. [[CrossRef](#)]
241. Wang, S.; Li, K.; Tian, Y.; Wang, J.; Wu, Y.; Ji, S. Improved thermal performance of a large laminated lithium-ion power battery by reciprocating air flow. *Appl. Therm. Eng.* **2019**, *152*, 445–454. [[CrossRef](#)]
242. Liu, Y.; Ouyang, C.; Jiang, Q.; Liang, B. Design and parametric optimization of thermal management of lithium-ion battery module with reciprocating air-flow. *J. Cent. South Univ.* **2015**, *22*, 3970–3976. [[CrossRef](#)]
243. Zhang, J.; Kang, H.; Wu, K.; Li, J.; Wang, Y. The impact of enclosure and boundary conditions with a wedge-shaped path and air cooling for battery thermal management in electric vehicles. *Int. J. Energy Res.* **2018**, *42*, 4054–4069. [[CrossRef](#)]
244. Nelson, P.; Dees, D.; Amine, K.; Henriksen, G. Modeling thermal management of lithium-ion PNGV batteries. *J. Power Sources* **2002**, *110*, 349–356. [[CrossRef](#)]
245. Shang, Z.; Qi, H.; Liu, X.; Ouyang, C.; Wang, Y. Structural optimization of lithium-ion battery for improving thermal performance based on a liquid cooling system. *Int. J. Heat Mass Transf.* **2019**, *130*, 33–41. [[CrossRef](#)]
246. Zhao, C.; Sousa, A.C.M.; Jiang, F. Minimization of thermal non-uniformity in lithium-ion battery pack cooled by channeled liquid flow. *Int. J. Heat Mass Transf.* **2019**, *129*, 660–670. [[CrossRef](#)]
247. Wang, C.; Zhang, G.; Li, X.; Huang, J.; Wang, Z.; Lv, Y.; Meng, L.; Situ, W.; Rao, M. Experimental examination of large capacity LiFePO<sub>4</sub> battery pack at high temperature and rapid discharge using novel liquid cooling strategy. *Int. J. Energy Res.* **2018**, *42*, 1172–1182. [[CrossRef](#)]
248. Ren, Y.; Yu, Z.; Song, G. Thermal management of a Li-ion battery pack employing water evaporation. *J. Power Sources* **2017**, *360*, 166–171. [[CrossRef](#)]
249. Ianniciello, L.; Biwolé, P.H.; Achard, P. Electric vehicles batteries thermal management systems employing phase change materials. *J. Power Sources* **2018**, *378*, 383–403. [[CrossRef](#)]
250. Fan, Y.F.; Zhang, X.X.; Wang, X.C.; Li, J.; Zhu, Q.B. Super-cooling prevention of microencapsulated phase change material. *Thermochim. Acta* **2004**, *413*, 1–6. [[CrossRef](#)]
251. Wang, W.; Zhang, X.; Xin, C.; Rao, Z. An experimental study on thermal management of lithium ion battery packs using an improved passive method. *Appl. Therm. Eng.* **2018**, *134*, 163–170. [[CrossRef](#)]
252. Huang, P.; Verma, A.; Robles, D.J.; Wang, Q.; Mukherjee, P.; Sun, J. Probing the cooling effectiveness of phase change materials on lithium-ion battery thermal response under overcharge condition. *Appl. Therm. Eng.* **2018**, *132*, 521–530. [[CrossRef](#)]
253. Ling, Z.; Wen, X.; Zhang, Z.; Fang, X.; Gao, X. Thermal management performance of phase change materials with different thermal conductivities for Li-ion battery packs operated at low temperatures. *Energy* **2018**, *144*, 977–983. [[CrossRef](#)]
254. Zhang, S.; Wu, W.; Wang, S. Experimental investigations of Alum/expanded graphite composite phase change material for thermal energy storage and its compatibility with metals. *Energy* **2018**, *161*, 508–516. [[CrossRef](#)]
255. Wang, W.; Yang, X.; Fang, Y.; Ding, J.; Yan, J. Preparation and thermal properties of polyethylene glycol/expanded graphite blends for energy storage. *Appl. Energy* **2009**, *86*, 1479–1483. [[CrossRef](#)]
256. Ruiz, J.; Ganatra, Y.; Bruce, A.; Howarter, J.; Marconnet, A.M. Investigation of aluminum foams and graphite fillers for improving the thermal conductivity of paraffin wax-based phase change materials. In Proceedings of the 2017 16th IEEE Intersociety Conference on Thermal and Thermomechanical Phenomena in Electronic Systems (ITherm), Orlando, FL, USA, 30 May–2 June 2017; pp. 384–389.
257. Kim, D.; Jung, J.; Kim, Y.; Lee, M.; Seo, J.; Khan, S.B. Structure and thermal properties of octadecane/expanded graphite composites as shape-stabilized phase change materials. *Int. J. Heat Mass Transf.* **2016**, *95*, 735–741. [[CrossRef](#)]
258. Sheng, N.; Dong, K.; Zhu, C.; Akiyama, T.; Nomura, T. Thermal conductivity enhancement of erythritol phase change material with percolated aluminum filler. *Mater. Chem. Phys.* **2019**, *229*, 87–91. [[CrossRef](#)]

259. Zhang, L.; Zhou, K.; Wei, Q.; Ma, L.; Ye, W.; Li, H.; Zhou, B.; Yu, Z.; Lin, C.; Luo, J.; et al. Thermal conductivity enhancement of phase change materials with 3D porous diamond foam for thermal energy storage. *Appl. Energy* **2019**, *233*, 208–219. [[CrossRef](#)]
260. Darkwa, J.; Zhou, T. Enhanced laminated composite phase change material for energy storage. *Energy Convers. Manag.* **2011**, *52*, 810–815. [[CrossRef](#)]
261. Hasse, C.; Grenet, M.; Bontemps, A.; Dendievel, R.; Sallée, H. Realization, test and modelling of honeycomb wallboards containing a Phase Change Material. *Energy Build.* **2011**, *43*, 232–238. [[CrossRef](#)]
262. Yang, Y.; Pang, Y.; Liu, Y.; Guo, H. Preparation and thermal properties of polyethylene glycol/expanded graphite as novel form-stable phase change material for indoor energy saving. *Mater. Lett.* **2018**, *216*, 220–223. [[CrossRef](#)]
263. Ling, Z.; Wang, F.; Fang, X.; Gao, X.; Zhang, Z. A hybrid thermal management system for lithium ion batteries combining phase change materials with forced-air cooling. *Appl. Energy* **2015**, *148*, 403–409. [[CrossRef](#)]
264. Fathabadi, H. High thermal performance lithium-ion battery pack including hybrid active–passive thermal management system for using in hybrid/electric vehicles. *Energy* **2014**, *70*, 529–538. [[CrossRef](#)]
265. Xie, Y.; Tang, J.; Shi, S.; Xing, Y.; Wu, H.; Hu, Z.; Wen, D. Experimental and numerical investigation on integrated thermal management for lithium-ion battery pack with composite phase change materials. *Energy Convers. Manag.* **2017**, *154*, 562–575. [[CrossRef](#)]
266. Song, L.; Zhang, H.; Yang, C. Thermal analysis of conjugated cooling configurations using phase change material and liquid cooling techniques for a battery module. *Int. J. Heat Mass Transf.* **2019**, *133*, 827–841. [[CrossRef](#)]
267. Ling, Z.; Cao, J.; Zhang, W.; Fang, X.; Gao, X. Compact liquid cooling strategy with phase change materials for Li-ion batteries optimized using response surface methodology. *Appl. Energy* **2018**, *228*, 777–788. [[CrossRef](#)]
268. Zheng, Y.; Shi, Y.; Huang, Y. Optimisation with adiabatic interlayers for liquid-dominated cooling system on fast charging battery packs. *Appl. Therm. Eng.* **2019**, *147*, 636–646. [[CrossRef](#)]
269. Xie, J.; Chen, J. Battery Early Warning and Monitoring System. U.S. Patent 8,952,823, 10 February 2015.
270. Hermann, W.A. Method for Detecting Battery Thermal Events Via Battery Pack Isolation Monitoring. U.S. Patent 8,168,315, 1 May 2012.
271. Hill, D.; Gully, B.; Agarwal, A.; Nourai, A.; Thrun, L.; Swartz, S.; Koslowski, M.; Cumming, S.; Butkowski, J.; Moore, B. Detection of off gassing from Li-ion batteries. In Proceedings of the 2013 IEEE Energytech, Cleveland, OH, USA, 21–23 May 2013; pp. 1–7.
272. Somov, A.; Spirjakin, D.; Ivanov, M.; Khromushin, I.; Passerone, R.; Baranov, A.; Savkin, A. Combustible gases and early fire detection: An autonomous system for wireless sensor networks. In *Proceedings of the 1st International Conference on Energy-Efficient Computing and Networking*; ACM: New York, NY, USA, 2010; pp. 85–93.
273. Lecocq, A.; Eshetu, G.G.; Grugeon, S.; Martin, N.; Laruelle, S.; Marlair, G. Scenario-based prediction of Li-ion batteries fire-induced toxicity. *J. Power Sources* **2016**, *316*, 197–206. [[CrossRef](#)]
274. Larsson, F.; Andersson, P.; Blomqvist, P.; Mellander, B.E. Toxic fluoride gas emissions from lithium-ion battery fires. *Sci. Rep.* **2017**, *7*, 10018. [[CrossRef](#)]
275. Andersson, P.; Blomqvist, P.; Lorén, A.; Larsson, F. Using Fourier transform infrared spectroscopy to determine toxic gases in fires with lithium-ion batteries. *Fire Mater.* **2016**, *40*, 999–1015. [[CrossRef](#)]
276. Keane, R.E.; Cary, G.J.; Davies, I.D.; Flannigan, M.D.; Gardner, R.H.; Lavorel, S.; Lenihan, J.M.; Li, C.; Rupp, T.S. A classification of landscape fire succession models: Spatial simulations of fire and vegetation dynamics. *Ecol. Model.* **2004**, *179*, 3–27. [[CrossRef](#)]
277. Summer, S.M. *Flammability Assessment of Lithium-Ion and Lithium-Ion Polymer Battery Cells Designed for Aircraft Power Usage*, US Department of Transportation; Federal Aviation Administration: Washington, DC, USA, 2010.
278. Ditch, B.; de Vries, J. *Flammability Characterization of Lithium-Ion Batteries in Bulk Storage*; FM Global: Johnston, RI, USA, 2013.
279. Egelhaaf, M.; Kress, D.; Wolpert, D.; Lange, T.; Justen, R.; Wilstermann, H. Fire Fighting of Li-Ion Traction Batteries. *Sae Int. J. Altern. Powertrains* **2013**, *2*, 37–48. [[CrossRef](#)]
280. Long, R.T.; Blum, A.F.; Bress, T.J.; Cotts, B.R. *Best Practices for Emergency Response to Incidents Involving Electric Vehicles Battery Hazards: A Report on Full-Scale Testing Results*; National Fire Protection Research Foundation: Quincy, MA, USA, 2013.

281. Maloney, T. *Extinguishment of Lithium-Ion and Lithium-Metal Battery Fires*, US Department of Transportation; Federal Aviation Administration: Washington, DC, USA, 2014; pp. 46–51.
282. Edison, C. *Considerations for ESS Fire Safety*; DNV GL: Oslo, Norway, 2017.
283. Rao, H.; Huang, Z.; Zhang, H.; Xiao, S. Study of fire tests and fire safety measures on lithiumion battery used on ships. In Proceedings of the 2015 International Conference on Transportation Information and Safety (ICTIS), Wuhan, China, 25–28 June 2015; pp. 865–870.
284. Wang, Q.; Shao, G.; Duan, Q.; Chen, M.; Li, Y.; Wu, K.; Liu, B.; Peng, P.; Sun, J. The efficiency of heptafluoropropane fire extinguishing agent on suppressing the lithium titanate battery fire. *Fire Technol.* **2016**, *52*, 387–396. [[CrossRef](#)]
285. Luo, W.; Zhu, S.; Gong, J.; Zhou, Z. Research and Development of Fire Extinguishing Technology for Power Lithium Batteries. *Procedia Eng.* **2018**, *211*, 531–537. [[CrossRef](#)]



© 2019 by the authors. Licensee MDPI, Basel, Switzerland. This article is an open access article distributed under the terms and conditions of the Creative Commons Attribution (CC BY) license (<http://creativecommons.org/licenses/by/4.0/>).



# Evaluating the thermal failure risk of large-format lithium-ion batteries using a cone calorimeter

Journal of Fire Sciences  
2019, Vol. 37(1) 81–95  
© The Author(s) 2018  
Article reuse guidelines:  
sagepub.com/journals-permissions  
DOI: 10.1177/0734904118816616  
journals.sagepub.com/home/jfs



Zhi Wang<sup>1</sup>, Xiaoyao Ning<sup>1</sup>, Kang Zhu<sup>2</sup>,  
Jian Wang<sup>3</sup>, Han Yang<sup>4</sup> and Jian Wang<sup>1</sup> 

Date received: 10 October 2018; accepted: 11 November 2018

## Abstract

A series of experiments were conducted to study the thermal failure hazard of large-format commercial lithium-ion batteries with typical states of charge in a calorimeter apparatus. The results indicate that the thermal failure penetration of the lithium-ion battery with 70% state of charge is faster than the lithium-ion battery with 50% state of charge. Two typical thermal failure modes, “Gas-driven mode” and “Flame-driven mode,” were also observed, corresponding to lithium-ion battery with 70% state of charge and 50% state of charge, respectively. Significant heat release, accompanied by large amount of carbon dioxide (CO<sub>2</sub>) release, took place for lithium-ion battery with 50% state of charge. Inversely, lithium-ion battery with 70% state of charge presented a lower heat release while more carbon monoxide (CO) generation and obvious mass loss trend. This study may serve as a reference for safe storage, application, and transportation in lithium-ion batteries.

## Keywords

Lithium-ion battery, thermal failure, states of charge, safety

---

<sup>1</sup>State Key Laboratory of Fire Science, University of Science and Technology of China, Hefei, P.R. China

<sup>2</sup>China Aviation Lithium Battery Co., Ltd., Changzhou, P.R. China

<sup>3</sup>China CEPREI Laboratory, Guangzhou, P.R. China

<sup>4</sup>Hangzhou Fire Detachment, Hangzhou, P.R. China

## Corresponding author:

Jian Wang, State Key Laboratory of Fire Science, University of Science and Technology of China, Hefei 230026, Anhui, P.R. China.

Email: wangj@ustc.edu.cn

## Introduction

As is well known, advanced lithium-ion batteries (LIBs) providing several advantages of high energy density, large output power, long service life, high operating voltage, no memory effect, and environmental protection have been used in a wide range of electronic components, such as mobile phones, cameras, and laptops.<sup>1,2</sup> In recent years, large-format LIBs are becoming more commonly applied as the energy storage devices,<sup>3</sup> involving electric vehicles, building energy reserves, backup powers, renewable energy sources, and military reserve powers.<sup>2</sup> However, LIBs are still facing the thermal failure issues leading to serious fires and explosions,<sup>4</sup> which has become one of the most important limitations for their application. Incidents related to the severe thermal failure of LIB have been reported. Besides, the large-format LIB contains more energetic materials and flammable chemical electrolyte, and thus, the thermal failure of an individual battery, bulk batteries, or even battery pack becomes more vigorous and fierce. State of charge (SOC) is considered to be the main factor that impacts the thermal failure and the ensuing fire and explosion of LIBs. 50% SOC is usually recommended as the normal SOC in storage or transportation to ensure the capacity of LIB, whereas some users demand that the LIB must hold the 70% SOC before delivery.<sup>5,6</sup> Thus, it is required to investigate and compare thermal failure characteristics of large-format LIBs with 50% SOC and 70% SOC. The external heating as a most common trigger of thermal failure of LIB was employed in this work.

Various research works have been done to better understand the thermal stability of the battery materials using differential scanning calorimetry (DSC),<sup>7–11</sup> thermogravimetric analysis (TG/TGA),<sup>9,12,13</sup> accelerating rate calorimeter (ARC),<sup>12,14,15</sup> adiabatic calorimetry vent sizing package 2 (VSP2),<sup>11,12,16,17</sup> and C80 calorimetry.<sup>18,19</sup> For instance, Richard and Dahn<sup>20</sup> proposed that the onset decomposition temperature of the solid electrolyte interface (SEI) was about 90°C–120°C using an ARC. Jhu et al.<sup>16</sup> used a VSP2 adiabatic calorimetry to investigate the thermal abuse of the 18,650 LIBs employed LiCoO<sub>2</sub> as cathodes and reported that the uncharged batteries were less dangerous than charged ones. In addition, more research focused on the thermal runaway behavior, mechanism, and propagation in LIBs, taking into account factors such as SOC,<sup>21,22</sup> over/charging,<sup>23,24</sup> over/discharging,<sup>25,26</sup> internal/external short circuit,<sup>27,28</sup> heating mode/power,<sup>22,29</sup> aging level,<sup>30</sup> battery module,<sup>31</sup> arrangement,<sup>32</sup> and ambient pressure.<sup>33</sup>

Moreover, some scholars concerned the combustion/fire behaviors of LIBs. Ribière et al.<sup>34</sup> performed fire calorimetry experiments to study the fire hazards of single 2.9-Ah LiMn<sub>2</sub>O<sub>4</sub> LIBs and found that the released toxic gases and heat mainly depended on the battery SOC. The fire tests of commercial lithium-ion cells and battery packs were carried out by Larsson et al.<sup>35</sup> It was observed that the LIB with higher SOC presented lower total HF emission and higher heat release rate (HRR) peaks. Fu et al.<sup>36</sup> evaluated the burning behaviors of 18,650 LIBs using a cone calorimeter, and the effects of SOC and incident heat flux were also discussed. Chen et al.<sup>33</sup> employed an in-suit calorimetry to explore the fire hazards of 18,650 LIBs at different pressures and established empirical correlations to relate the hazard parameter with pressure. To estimate of the flammability of small-size batteries in a rack storage array and the effectiveness of a protection system, FM Global performed a large number of large-scale burning and extinguishing tests of 18,650 LiCoO<sub>2</sub>-based cells with 2.6 Ah capacity.<sup>37</sup> Liu et al.<sup>38</sup> and Said et al.<sup>39</sup> employed a novel technique to investigate the widely used small-format LIBs at different SOCs. It was determined that the total energy yielded inside the LIB increased as the SOC increased. In addition, these studies

combined Copper Slug Battery Calorimetry (CSBC) with the cone calorimeter to measure the energy released due to combustion of ejected battery materials. Zhong et al.<sup>40</sup> used a modified cone calorimeter to study the thermal runaway and fire behavior of 18,650 LIBs and found that the production of CO showed an increasing trend as SOC increases. Huang et al.<sup>41</sup> investigated the burning behavior of large-format titanate battery with the capacity of 50 Ah, and the results indicated that the thermal hazard of battery increased with the SOC. Ping et al.<sup>42</sup> conducted a full-scale burning test to estimate the fire safety of a 50-Ah lithium iron phosphate/graphite battery pack. They found that the total heat production, maximum heat release, and the mass loss of the battery relied on the SOC of LIB to some extent.

However, limited work has been done to investigate the thermal hazards of a large-format LIB. In this study, the 50-Ah  $\text{LiNi}_x\text{Co}_y\text{Mn}_{1-x-y}\text{O}_2$ /graphite battery, one of the most promising composition schemes for large-scale battery, was picked to experimentally investigate the thermal failure characteristics and combustion behaviors. The main information, including battery temperature, experimental photograph, heat release, gas release, and mass loss, was recorded and analyzed to provide critical data for the thermal failure issues of LIB. The effect of SOC on the thermal failure was also examined and discussed.

## Materials and methods

### Materials

The batteries used in this work are the prismatic LIBs (produced by China Aviation Lithium Battery Co., Ltd., Changzhou, China), which are 148 mm in length, 27 mm in width, and 98 mm in height. The normal capacity and voltage are 50 Ah and 3.65 A, respectively. Two different SOCs (50% SOC and 70% SOC) corresponding to the recommended SOCs in storage or transportation to reduce the attenuation of the capacity are adopted. The LIBs employ  $\text{LiNi}_x\text{Co}_y\text{Mn}_{1-x-y}\text{O}_2$  as the positive and graphite as the negative. The detailed components of LIB sample are lithium nickel cobalt manganese oxide (NCM), natural graphite, PVDF, PE, EC, LiPF<sub>6</sub>, Al, Cu, and so on. The distribution of mass fractions of the main components is shown in Figure 1. The previous studies have reported that the thermal failure of LIBs is ascribed to several exothermic chemical reactions including the decomposition SEI layer, thermal decomposition of electrode materials, exothermic reaction between the electrode materials and electrolyte melting of separator materials, and so on. The active components provide approximately more than 60% of the mass fraction and more than 80% of heat fraction. Figure 2 presents the typical scanning electron microscopy (SEM) micrograph and energy-dispersive spectrometer (EDS) analysis of cathode materials scraped from the original electrode piece. It indicates that the NCM has a feature of layer structure, and its particles are approximately in sphere-like shape. Besides, the elements of Ni, Co, Mn, and O have also been detected using EDS analysis.

### Methods

All experiments were carried out in an in-suit calorimeter, and the schematic diagram of the test apparatus is illustrated in Figure 3(a). The LIB is placed in the steel mesh surrounded by a quartz tube. The steel mesh was consisted of 10 fine wires with diameter of 2 mm. The mesh size was 48 mm × 48 mm. A 0.4-kW cylindrical heater (150 mm in length, 8 mm in diameter) was selected as the external heating source to ignite the battery. It was fixed on the

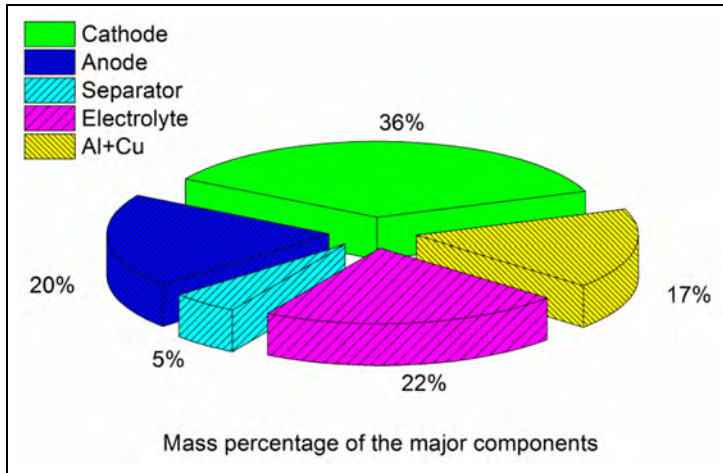


**Figure 1.** Mass distribution of the LIBs.

right-side surface of battery, the distance between heater axis line and upper surface of battery where electrode located is about 4 mm. Several K-type thermocouples (diameter of 1 mm, maximum range of 1300°C, and measurement precision of 0.1°C) were used to record the surface temperature and flame temperature. The lowest thermocouple to measure flame temperature was 100 mm above the top of the battery, and the spacing between two adjacent thermocouples was 100 mm. Besides, nine thermocouples on the left-side surface of the battery were used to measure the surface temperature distribution. Schematic diagram of the thermocouples is shown in Figure 3(b). The mass loss was measured by a load cell Mettler Toledo XP10002S, Zurich, Switzerland (maximum range of 9 kg and resolution of 0.01 g). A gas analyzer (Servomex 4100, East Sussex, UK) was applied to obtain the contents of CO<sub>2</sub>, CO, and O<sub>2</sub> in the exhaust duct, and these were further used to estimate the HRR based on the oxygen depletion method. The thermal failure process was recorded with a digital camera (JVC, Victor Company of Japan, Limited, Yokohama, Japan, 25 fps).

## Results

### *Temperature profiles*

The typical temperature profiles on the left-side surface of LIBs at different SOCs are plotted in Figure 4. It can be found that there is an obvious temperature penetration process along battery surface, which is different from the previous researches for small-scale LIBs. The LIB temperature increases slowly via the heat conduction and radiation because of the cylindrical heater at the initial stage. The temperature at all measurement points has a similar trend with time. However, the temperature increasing rate for 70% SOC LIB is slightly larger than that for 50% SOC LIB. When the surface temperature values raise to 100°C–300°C, the thermal failure occurs. Hereafter, the LIB surface temperature skyrockets steeply. The maximum surface temperature reaches approximately 800°C for 70% LIB and 700°C for 50% LIB. Some temperature measurement points demonstrate the apparent decrease, eventually to room temperature due to the thermal expansion or the thermocouple shedding. The onset time and temperature of thermal failure decrease with the SOC, accompanied by

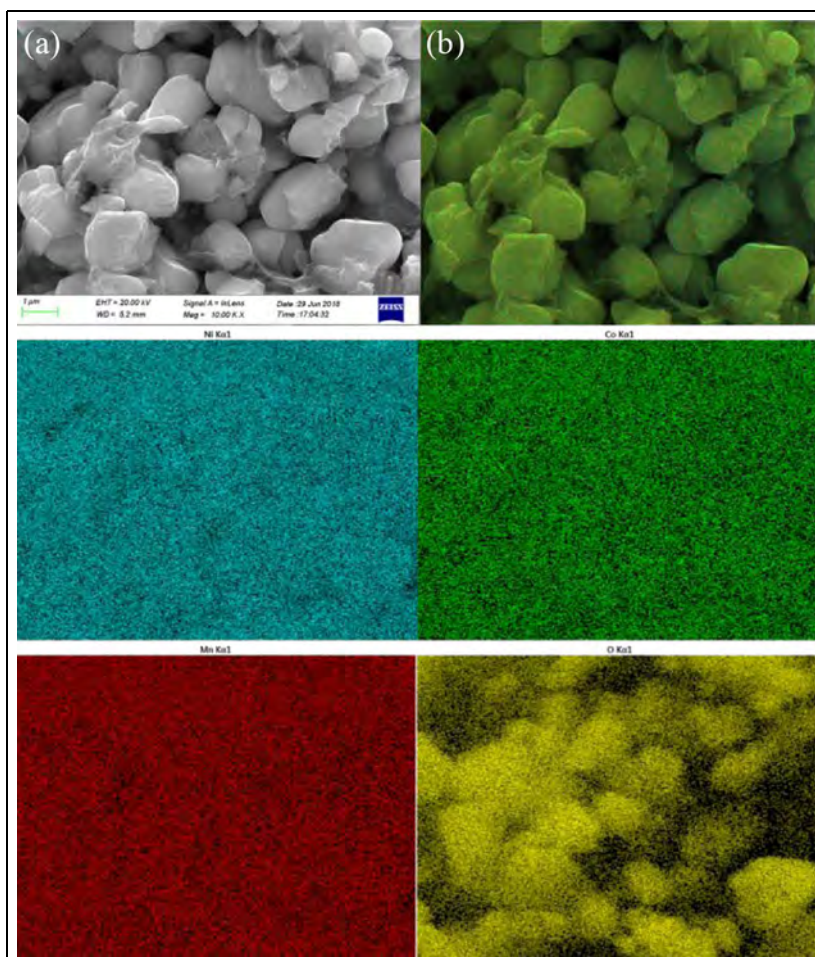


**Figure 2.** Typical SEM micrograph and EDS analysis of cathode.

severe intense exothermic reactions under a higher SOC. Figure 5 gives the typical center temperature on the left-side surface of LIBs at different SOCs. The thermal failure process consists of several stages, and the number of stages depends on the SOC. The initial temperature of thermal failure on LIBs surface center is almost close to 200°C for both 50% and 70% SOC LIBs. The maximum thermal failure temperature increases with the SOC, as shown in Figure 5, 603.4°C for 50% SOC LIB and 630.1°C for 70% SOC LIB. All above indicates that the thermal stability of LIB decreases with the increase in the SOCs, agreeing well with the previous studies.<sup>4,22</sup>

### General observations

Figure 6 shows the typical combustion process of the LIBs at different SOCs. The burning behavior of the 50% SOC LIB can be roughly divided into the following stages: the continuous heating, open of safety valve and ignition, violent ejection, first stable combustion,

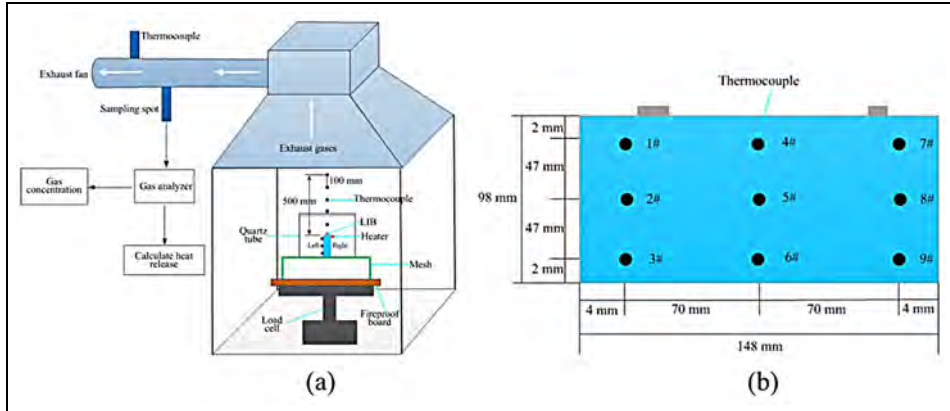


**Figure 3.** Schematic diagram of experimental setup: (a) test apparatus and (b) the thermocouples on the left-side surface of the battery.

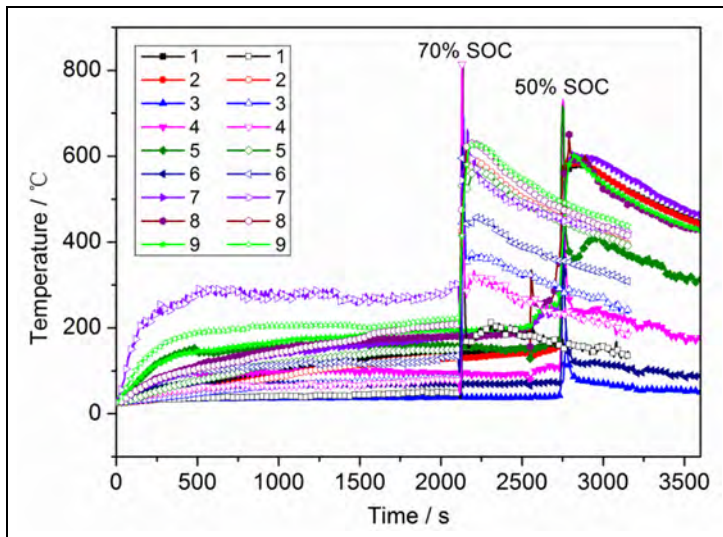


**Figure 4.** Temperature profiles of LIBs (50% SOC: Solid symbol; 70% SOC: Hollow symbol).

intense explosion and jet fire, second stable combustion, extinguishment and abatement. However, compared with the 50% SOC LIB, the burning behavior of the 70% SOC LIB can be summarized into the completely different stages: the continuous heating, open of safety valve, gas release and splash spark, heavy gas and white smoke spilled with hissing sound, fierce explosion and combustion, flame weakening and extinguishing. The 70% SOC LIB went into thermal failure with a large amount of gases due to high-speed gas ejection, which might blow out the flame. At 2551 s, the 50% SOC LIB got into thermal failure, while the thermal failure of 70% SOC LIB occurred at 2110 s. Shortly after that, the

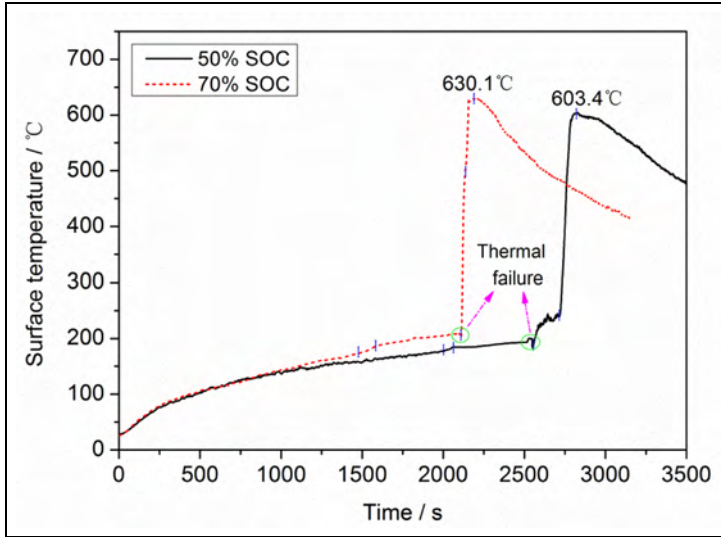


**Figure 5.** Surface temperature of LIBs center at different SOC.

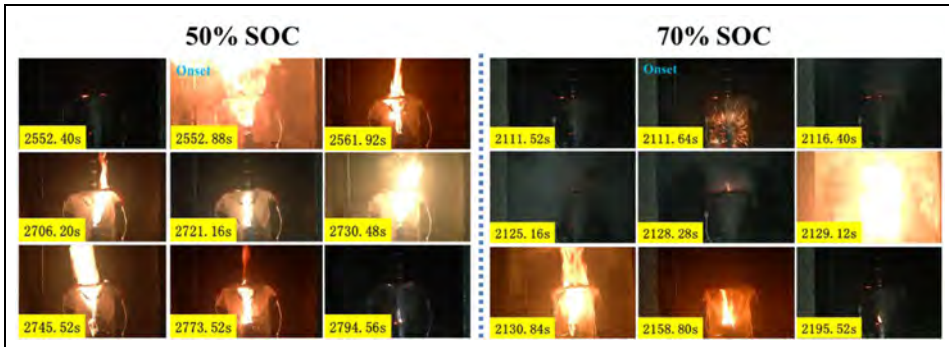


**Figure 6.** Typical photographs of thermal failure of LIBs at different SOC.

thermal failure completely went out of control and chemical reactions became more vigorous, accompanied with gas or smoke venting, materials jet, bright flame, violent explosion, and so on. Finally, all combustibles were consumed and the flame became smaller and jumped, and eventually, extinguished. In summary, “Gas-driven mode” and “Flame-driven mode” proposed are responsible for the 70% SOC LIB and 50% SOC LIB, respectively. In addition, the values of maximum flame temperature are 803.2°C and 1101.9°C for 50% SOC and 70% SOC LIBs, respectively. Figure 7 plots the flame temperature of LIBs fire at different SOC, where the maximum flame temperature is observed. The change of flame temperature for 50% SOC LIB is different from that of 70% SOC LIB, which is identical with the different combustion behaviors.

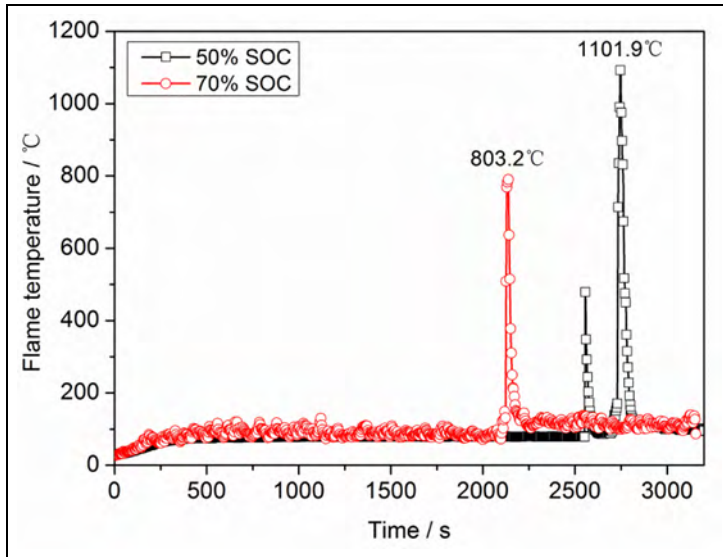


**Figure 7.** Flame temperature of LIBs fire at different SOC.

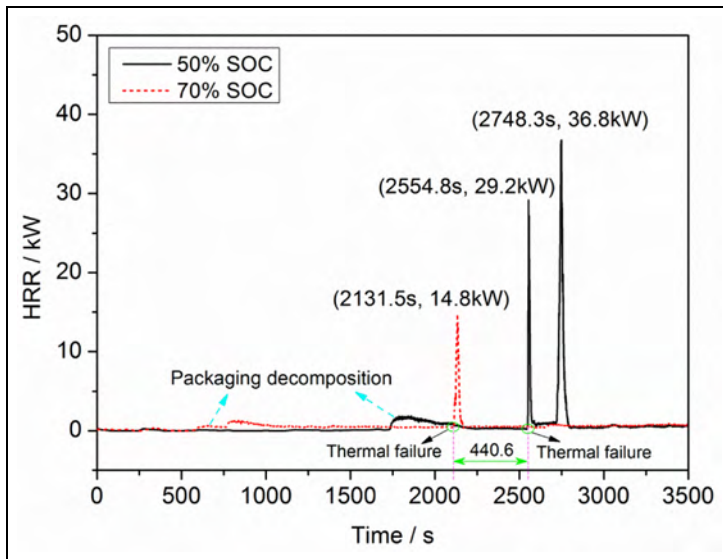


**Figure 8.** HRR profiles of LIBs at different SOC.

### Heat release and gas emissions

The estimated HRR in this work is based on the oxygen depletion,<sup>43</sup> which considers that all consumed oxygen comes from the local air. Figure 8 presents the typical HRR curves of the combustion of the individual 50% SOC LIB and 70% SOC LIB. It should be noted that

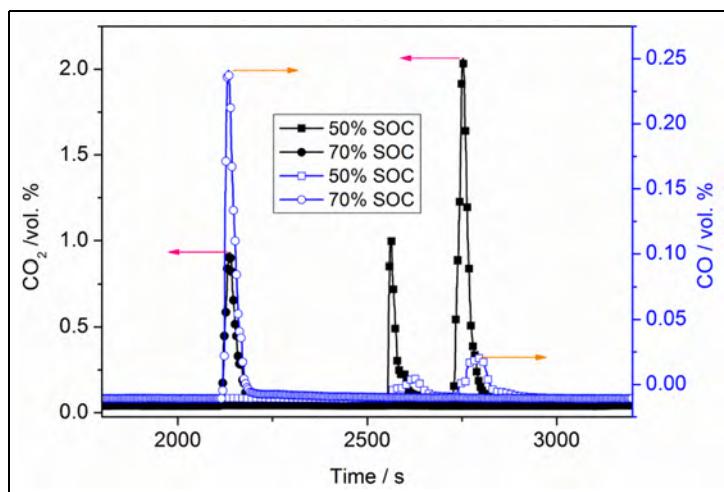


**Figure 9.** Gases production profiles of LIBs at different SOC levels.

there are two HRR peaks for 50% SOC LIB. And, the values of HRR peaks are 29.2 and 36.8 kW at 2554.8 and 2748.3 s, respectively. While the HRR curve of 70% SOC LIB shows a single lower HRR peak of 14.8 kW at 2131.5 s. These correspond to the above thermal failure and combustion behaviors. Two peak HRR values for 50% SOC LIB reflect two violent combustion stages, which may be ascribed to the specific internal or external conditions of battery including the vigorous electrochemical reactions, high-speed ejection, flame quenching and self-igniting, and so on.

The gases released in the process of thermal failure are generally combustible and toxic including  $\text{CO}_2$ ,  $\text{CO}$ ,  $\text{CH}_4$ ,  $\text{HF}$ , and  $\text{POF}_3$ .<sup>34,36</sup> In this work, the gas analyzer can only detect  $\text{CO}_2$  and  $\text{CO}$  gases. The typical gaseous emission curves are shown in Figure 9. The concentration of  $\text{CO}_2$  and  $\text{CO}$  increased sharply to peaks while the thermal failure occurred. The maximum concentrations of  $\text{CO}_2$  and  $\text{CO}$  are 2.06 and 0.02 vol.% for 50% SOC LIB, respectively. However, the 70% SOC LIB presents the maximum concentration of  $\text{CO}_2$  and  $\text{CO}$  of 0.93 and 0.24 vol.%. It can be noted that the maximum concentration and generation of  $\text{CO}$  show a significant increasing trend with the increase in the SOC. Inversely, the production of  $\text{CO}_2$  for 50% SOC LIB is even higher than that of 70% SOC LIB. That is in agreement with the above combustion and HRR analysis. In addition, the higher  $\text{CO}$  and lower  $\text{CO}_2$  during the thermal failure of 70% SOC LIB are due to the fact that the high-velocity release gas cannot be ignited immediately, further resulting in the incomplete combustion. The results can be evidenced by a large amount of gas and smoke.

### Mass loss and residue

Figure 10 shows the mass loss curves of LIBs at different SOC levels. The multiple representative thermal failure stages of 50% SOC LIB and 70% SOC LIB could also be seen in the mass curves, respectively. During the initial stage, there was negligible mass loss for all tests. When the safety valve opened and gas released, the mass decreased gradually. Then, the mass

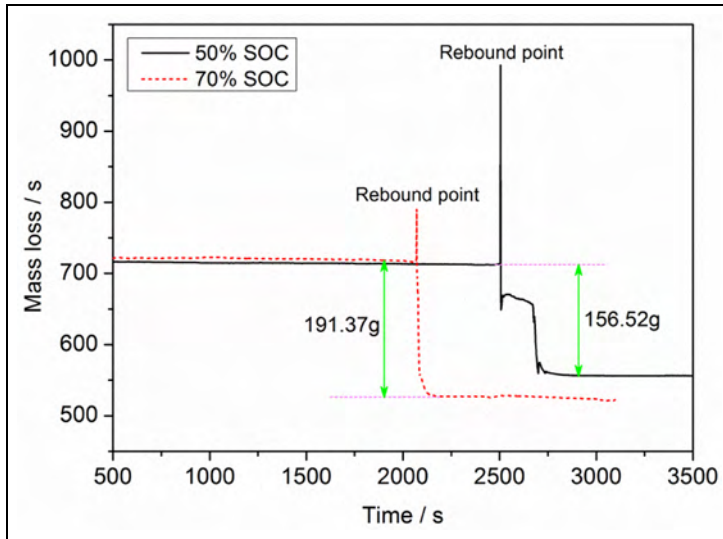


**Figure 10.** Mass loss of LIBs at different SOC.

demonstrated a significant reduction once the thermal failure occurred. It is obvious that there exist two distinct mass loss stages in the mass plot of 50% SOC LIB, which relates to the two stages of thermal failure. For the 70% SOC LIB, there is only one obvious mass loss phase corresponding to individual thermal failure stage. In addition, it can be seen that the mass curve includes several rebound points, which is caused by the high-speed gas release, producing a positive pulse to the load cell, immediately. The LIB has a total mass loss of 156.52 and 191.37 g, relating to the 50% SOC and 70% SOC. This result indicates that the 70% SOC LIB undergoes a quite more significant mass loss, which ascribed to the deteriorated thermal failure. Figure 11 gives the images of LIBs before and after thermal failure. These LIBs after thermal failure are similar, but differ in terms of bulging. It should be observed that the expansion of 70% SOC LIB is more obvious than that of 50% SOC LIB. That can be explained by the violent chemical reactions and aggravated thermal failure under the higher SOC.

## Discussion

Table 1 lists the thermal failure characteristics of two batteries. The SOC can be found as a key factor for battery thermal runaway and combustion. Recall that the stored electric energy in the battery related to the SOC reported in Said et al.<sup>39</sup> and Ping et al.<sup>42</sup> affected the thermal behavior. Theoretically, the heat release should have an increasing tendency with increasing SOC of battery. However, LIB with 70% SOC gave a smaller heat release in this work. This variation can be ascribed to the incomplete combustion behavior, which was caused by the high hydrodynamic strain rates of the ejecting materials or the low temperature of the space. The results of mass loss and CO emission supported the above analysis. Mass loss of LIB increased with SOC. The materials combustion, gas ejection, and



**Figure 11.** The images of LIBs before and after thermal failure.

**Table I.** The summary of thermal failure characteristics for two batteries.

State of charge	50% SOC	70% SOC
Mean upper surface temperature at failure (°C)	183.4	204.1
Maximum upper surface temperature (°C)	603.4	630.1
Maximum flame temperature (°C)	1101.9	803.2
Time to thermal failure (s)	2551	2110
Peak HRR (kW)	29.2	14.8
	36.8	
Total heat release (MJ)	2.34	2.04
Peak concentration of CO (ppm)	50	2400
	200	
Peak concentration of CO <sub>2</sub> (vol.%)	1.00	0.93
	2.06	
Total mass loss (g)	156.52	191.37
Maximum mass loss rate (g s <sup>-1</sup> )	-9.39	-24.45

SOC: state of charge; HRR: heat release rate.

electrolyte leakage were responsible for the total mass loss. Meanwhile, more CO released was also corresponding to the insufficient reactions and presented gas toxicity.

**Table 2.** Results of thermal risk classification and toxicity index.

State of charge	THR (MJ m <sup>-2</sup> )	$x$ parameter (kW m <sup>-2</sup> s <sup>-1</sup> )	FED (-)	LC <sub>50</sub> (g m <sup>-3</sup> )
50% SOC	234	1.44	0.04	2264.5
70% SOC	204	0.70	0.48	230.7

THR: total heat release; FED: fractional effective dose; SOC: state of charge.

Thermal properties and gas toxicity should be combined to assess the fire hazard of the large-scale batteries under storage and transportation process. Two evaluation methods, proposed by Petrella<sup>44</sup> and Han and Chow,<sup>45</sup> were employed to classify the danger of the battery with different SOCs. Four important parameters, total heat release (THR),  $x$  parameter, fractional effective dose (FED), and the lethal concentration for 50% of the population ( $LC_{50}$ ) within a 30-min exposure plus 14 days post-exposure. The calculated values are shown in Table 2. It can be concluded that the LIB with 70% SOC exhibited lower heat risk and higher toxicity in this work, compared with the one with 50% SOC. However, we should be conservative with this conclusion, because this may not be valid when battery is exposed to different conditions. Certainly, this conclusion is consistent with the previous observation (“Gas-driven mode” for 70% SOC and “Flame-driven mode” for 50% SOC). It may also be possible to guide the fire rescue of LIB.

## Conclusion

In this study, a series of thermal failure experiments of large-format LIBs at different SOCs were conducted on an in-suit calorimeter. Specific parameters, including the temperature, experimental photograph, HRR, gas release, mass loss, and residue were measured. The experimental results are qualitatively analyzed and discussed, and some essential conclusions gained are generalized as follows:

1. The surface temperature of LIB is driven by the heat transport from the external heater and the inner exothermic reactions. The LIB with higher SOC generates more heat due to more vigorous reactions, resulting in higher temperature of battery. It indicates that the thermal failure of higher SOC LIB is triggered early and aggravates rapidly than that of lower one.
2. The thermal failure process can be divided into multiple progressive stages. The number and characteristics of each stage change with the SOC of battery. Two typical modes including “Gas-driven mode” and “Flame-driven mode” were proposed to be responsible for the battery thermal failure at different SOCs. The maximum flame temperature of 50% SOC LIB is also larger than 70% SOC LIB.
3. The 50% SOC LIB shows two significant HRR peaks, while just one peak for 70% SOC LIB. The maximum value of HRR for 50% SOC LIB is larger than that of 70% SOC LIB; whereas, the combustion of materials ejected from 70% SOC LIB releases large amounts of toxic gases, especially carbon monoxide during the thermal failure. Also, the higher SOC LIB presents larger mass loss and expansion than the lower one after thermal failure. It should be stressed that incomplete combustion exists due to

the instantaneously fierce and massive ejection of flammable materials from higher SOC LIB.

4. The LIB with 50% SOC has a higher heat risk than the one with 70% SOC in this work, while the latter shows a higher smoke toxicity than the former. Thus, it is suggested that thermal hazard and toxicity should be taken into account comprehensively for the choice of proper SOC of LIBs in storage and transportation. Besides, once the thermal failure appears, some effective strategies including cooling, insulation, and suffocation should be applied to prevent the risk propagation based on the thermal failure mode and phase.

### Declaration of conflicting interests

The author(s) declared no potential conflicts of interest with respect to the research, authorship, and/or publication of this article.

### Funding

The author(s) disclosed receipt of the following financial support for the research, authorship, and/or publication of this article: This work was supported by the National Key R&D Program of China (No. 2018YFC0809500) and the Changzhou Sci&Tech Program (No. CE20185001).

### ORCID iD

Jian Wang  <https://orcid.org/0000-0002-3106-5638>

### References

1. Etacheri V, Marom R, Elazari R, et al. Challenges in the development of advanced Li-ion batteries: a review. *Energ Environ Sci* 2011; 4(9): 3243–3262.
2. Liu K, Liu Y, Lin D, et al. Materials for lithium-ion battery safety. *Sci Adv* 2018; 4(6): eaas9820.
3. Koksang R, Olsen II and Shackle D. Review of hybrid polymer electrolytes and rechargeable lithium batteries. *Solid State Ionics* 1994; 69(3–4): 320–335.
4. Wang Q, Ping P, Zhao X, et al. Thermal runaway caused fire and explosion of lithium ion battery. *J Power Sources* 2012; 208: 210–224.
5. T/CIAPS0002-2017. *Specification of lithium-ion battery enterprise safety production*. Tianjin, China: CIAPS, 2017.
6. <https://wenku.baidu.com/view/46c0a85784868762cbaed59c.html>
7. Yang H, Bang H, Amine K, et al. Investigations of the exothermic reactions of natural graphite anode for Li-ion batteries during thermal runaway. *J Electrochem Soc* 2005; 152(1): A73–A79.
8. Biensan P, Simon B, Peres J, et al. On safety of lithium-ion cells. *J Power Sources* 1999; 81: 906–912.
9. Maleki H, Deng G, Anani A, et al. Thermal stability studies of Li-ion cells and components. *J Electrochem Soc* 1999; 146(9): 3224–3229.
10. Roth E and Doughty D. Thermal abuse performance of high-power 18650 Li-ion cells. *J Power Sources* 2004; 128(2): 308–318.
11. Wen C-Y, Jhu C-Y, Wang Y-W, et al. Thermal runaway features of 18650 lithium-ion batteries for LiFePO<sub>4</sub> cathode material by DSC and VSP2. *J Therm Anal Calor* 2012; 109(3): 1297–1302.
12. Mancini M, Fleischhammer M, Fleischmann S, et al. Investigation on the thermal stability of Li<sub>2</sub>MnSiO<sub>4</sub>-based cathodes for Li-ion batteries: effect of electrolyte and state of charge. *Energ Technol* 2017; 5(9): 93–97.
13. Nasef MM and Saidi H. Structural, thermal and ion transport properties of radiation grafted lithium conductive polymer electrolytes. *Mater Chem Phys* 2006; 99(2–3): 361–369.
14. Maleki H and Howard JN. Role of the cathode and anode in heat generation of Li-ion cells as a function of state of charge. *J Power Sources* 2004; 137(1): 117–127.
15. Von Sacken U, Nodwell E, Sundher A, et al. Comparative thermal stability of carbon intercalation anodes and lithium metal anodes for rechargeable lithium batteries. *J Power Sources* 1995; 54(2): 240–245.
16. Jhu C-Y, Wang Y-W, Shu C-M, et al. Thermal explosion hazards on 18650 lithium ion batteries with a VSP2 adiabatic calorimeter. *J Hazard Mater* 2011; 192(1): 99–107.
17. Jhu C-Y, Wang Y-W, Wen C-Y, et al. Thermal runaway potential of LiCoO<sub>2</sub> and Li(Ni<sub>1/3</sub>Co<sub>1/3</sub>Mn<sub>1/3</sub>)O<sub>2</sub> batteries determined with adiabatic calorimetry methodology. *Appl Energy* 2012; 100: 127–131.
18. Wang Q, Sun J, Yao X, et al. Micro calorimeter study on the thermal stability of lithium-ion battery electrolytes. *J Loss Prev Process Ind* 2006; 19(6): 561–569.

19. Wang Q, Ping P, Sun J, et al. Improved thermal stability of lithium ion battery by using cresyl diphenyl phosphate as an electrolyte additive. *J Power Sources* 2010; 195(21): 7457–7461.
20. Richard M and Dahn J. Accelerating rate calorimetry study on the thermal stability of lithium intercalated graphite in electrolyte. I. Experimental. *J Electrochem Soc* 1999; 146(6): 2068–2077.
21. Golubkov AW, Scheikl S, Planteu R, et al. Thermal runaway of commercial 18650 Li-ion batteries with LFP and NCA cathodes—impact of state of charge and overcharge. *RSC Adv* 2015; 5(70): 57171–57186.
22. Liu J, Wang Z, Gong J, et al. Experimental study of thermal runaway process of 18650 lithium-ion battery. *Mater* 2017; 10(3): E230.
23. Ye J, Chen H, Wang Q, et al. Thermal behavior and failure mechanism of lithium ion cells during overcharge under adiabatic conditions. *Appl Energ* 2016; 182: 464–474.
24. Wang Z, Liu K, Liu J, et al. Influence of the charging and discharging of the 18650 lithium-ion battery thermal runaway. *J Loss Prev Process Ind.* Epub ahead of print 26 November 2017. DOI: 10.1016/j.jlp.2017.11.008.
25. Erol S, Orazem ME and Muller RP. Influence of overcharge and over-discharge on the impedance response of LiCoO<sub>2</sub>/C batteries. *J Power Sources* 2014; 270: 92–100.
26. Jeon DH and Baek SM. Thermal modeling of cylindrical lithium ion battery during discharge cycle. *Energ Convers Manage* 2011; 52(8–9): 2973–2981.
27. Zhao R, Liu J and Gu J. Simulation and experimental study on lithium ion battery short circuit. *Appl Energ* 2016; 173: 29–39.
28. Hatchard T, MacNeil D, Basu A, et al. Thermal model of cylindrical and prismatic lithium-ion cells. *J Electrochem Soc* 2001; 148(7): A755–A761.
29. Wu T, Chen H, Wang Q, et al. Comparison analysis on the thermal runaway of lithium-ion battery under two heating modes. *J Hazard Mater* 2018; 344(Suppl. C): 733–741.
30. Larsson F, Bertilsson S, Furlani M, et al. Gas explosions and thermal runaways during external heating abuse of commercial lithium-ion graphite-LiCoO<sub>2</sub> cells at different levels of ageing. *J Power Sources* 2018; 373: 220–231.
31. Lopez CF, Jeevarajan JA and Mukherjee PP. Experimental analysis of thermal runaway and propagation in lithium-ion battery modules. *J Electrochem Soc* 2015; 162(9): A1905–A1915.
32. Chen M, Yuen R and Wang J. An experimental study about the effect of arrangement on the fire behaviors of lithium-ion batteries. *J Therm Anal Calor* 2017; 129(1): 181–188.
33. Chen M, Liu J, He Y, et al. Study of the fire hazards of lithium-ion batteries at different pressures. *Appl Therm Eng* 2017; 125: 1061–1074.
34. Ribière P, Grugeon S, Morcrette M, et al. Investigation on the fire-induced hazards of Li-ion battery cells by fire calorimetry. *Energ Environ Sci* 2012; 5(1): 5271–5280.
35. Larsson F, Andersson P, Blomqvist P, et al. Characteristics of lithium-ion batteries during fire tests. *J Power Sources* 2014; 271: 414–420.
36. Fu Y, Lu S, Li K, et al. An experimental study on burning behaviors of 18650 lithium ion batteries using a cone calorimeter. *J Power Sources* 2015; 273: 216–222.
37. Ditch B and De Vries J. *Flammability characterization of lithium-ion batteries in bulk storage*. Massachusetts, USA: FM Global, 2013.
38. Liu X, Wu Z, Stoliarov SI, et al. Heat release during thermally-induced failure of a lithium ion battery: impact of cathode composition. *Fire Saf J* 2016; 85: 10–22.
39. Said AO, Lee C, Liu X, et al. Simultaneous measurement of multiple thermal hazards associated with a failure of prismatic lithium ion battery. *Proc Combust Inst.* Epub ahead of print 15 June 2018. DOI: 10.1016/j.proci.2018.05.066.
40. Zhong G, Mao B, Wang C, et al. Thermal runaway and fire behavior investigation of lithium ion batteries using modified cone calorimeter. *J Therm Anal Calor.* Epub ahead of print 16 August 2018. DOI: 10.1007/s10973-018-7599-7.
41. Huang P, Wang Q, Li K, et al. The combustion behavior of large scale lithium titanate battery. *Sci Rep* 2015; 5: 7788.
42. Ping P, Wang Q, Huang P, et al. Study of the fire behavior of high-energy lithium-ion batteries with full-scale burning test. *J Power Sources* 2015; 285: 80–89.
43. Thornton WM. XV. The relation of oxygen to the heat of combustion of organic compounds. *Lond Edinb Dublin Philos Mag J Sci* 1917; 33(194): 196–203.
44. Petrella RV. The assessment of full-scale fire hazards from cone calorimeter data. *J Fire Sci* 1994; 12(1): 14–43.
45. Han SS and Chow WK. Calculating FED and LC50 for testing toxicity of materials in bench-scale tests with a cone calorimeter. *Polym Test* 2005; 24(7): 920–924.

## Author biographies

**Zhi Wang** is a Ph.D. candidate student who works on fire safety of new energy and thermal behavior of lithium ion battery, at the State Key Laboratory of Fire Science of University of Science and Technology of China.

**Xiaoyao Ning** is a postgraduate student worked on fire science at the State Key Laboratory of Fire Science of University of Science and Technology of China.

**Kang Zhu** is a Construction Safety Chief Engineer who works on fire safety in the production of lithium ion battery at the China Aviation Lithium Battery Co., Ltd..

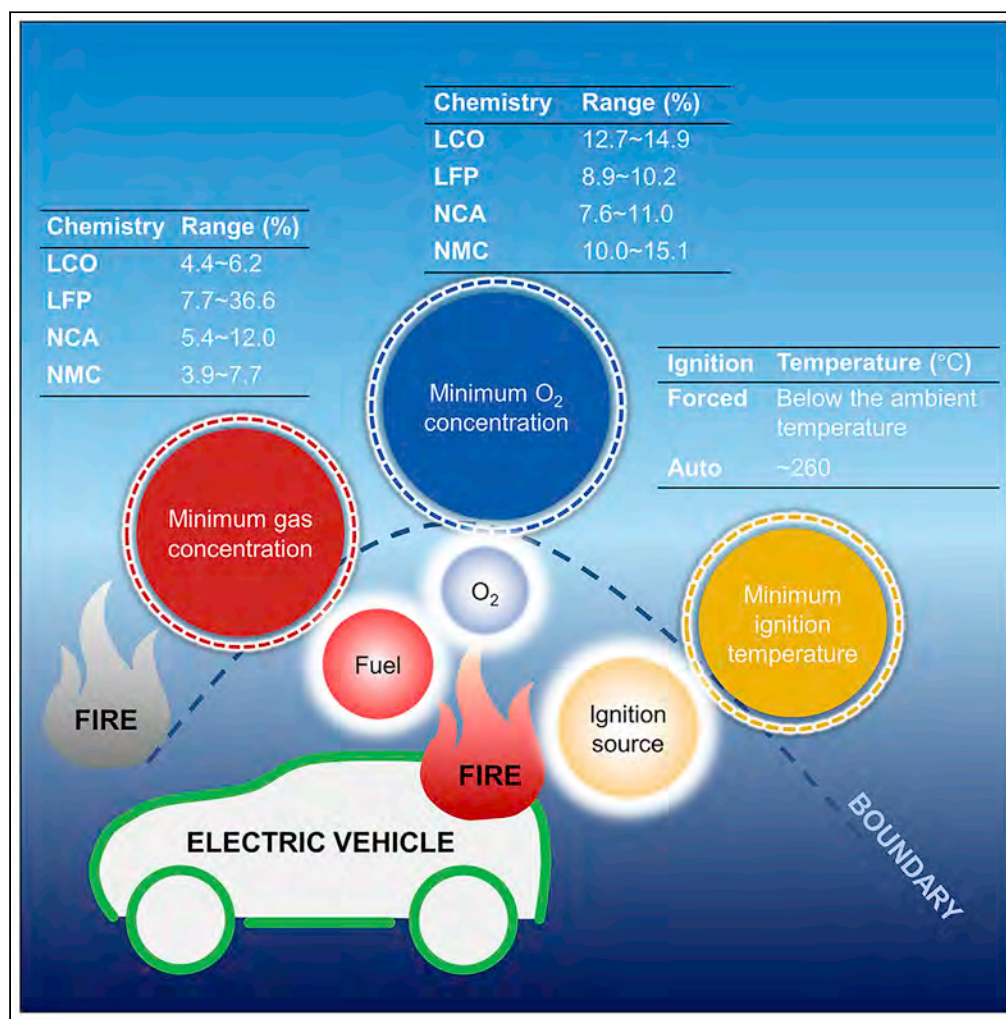
**Jianyao Hu** is a Ph.D. worked on evaluation of new energy vehicle and safety assessment of lithium ion battery at the China CEPREI Laboratory.

**Han Yang** is a professional Firefighter who works on fire extinguishing technology at the Hangzhou Fire Detachment.

**Jian Wang** is a Professor worked on fire dynamics, combustion mechanism and lithium ion battery safety at the State Key Laboratory of Fire Science of University of Science and Technology of China.

## Article

## Fire boundaries of lithium-ion cell eruption gases caused by thermal runaway



Weifeng Li, Shun Rao, Yang Xiao, Zhenhai Gao, Yupeng Chen, Hewu Wang, Minggao Ouyang

gaozh@jlu.edu.cn (Z.G.)  
ypchen0727@buaa.edu.cn (Y.C.)  
ouymg@tsinghua.edu.cn (M.O.)

**Highlights**

We clarified the three fire boundaries of LIBs corresponding to the fire triangle

Batteries are prone to ignition with forced ignition sources

Batteries are hard to autoignite when temperatures are low enough

LIB ignition modes can be controlled by changing temperatures and ignition sources

Li et al., iScience 24, 102401  
May 21, 2021 © 2021 The Author(s).  
<https://doi.org/10.1016/j.isci.2021.102401>

## Article

## Fire boundaries of lithium-ion cell eruption gases caused by thermal runaway

Weifeng Li,<sup>1</sup> Shun Rao,<sup>1</sup> Yang Xiao,<sup>1</sup> Zhenhai Gao,<sup>1,4,\*</sup> Yupeng Chen,<sup>2,\*</sup> Hewu Wang,<sup>3</sup> and Minggao Ouyang<sup>3,\*</sup>

## SUMMARY

Lithium-ion batteries are applied in electric vehicles to mitigate climate change. However, their practical applications are impeded by poor safety performance owing mainly to the cell eruption gas (CEG) fire triangle. Here, we report quantitatively the three fire boundaries corresponding to the CEG fire triangle of four types of mainstream cells with the state of charge (SOC) values ranging from 0% to 143% based on 29 thermal runaway tests conducted in an inert atmosphere in open literature. Controlling the SOC and/or selecting a reasonable cell type can alter the minimum CEG and oxygen concentrations required for ignition, thereby changing the probability of a battery fire. The ignition temperature varies greatly according to the type of ignition source type. Temperature and ignition source type play a leading role in the ignition mode. Breaking any fire boundary will stop the ignition of CEG, thus significantly improving the battery safety performance.

## INTRODUCTION

Electric vehicles are paid much attention to mitigate climate change (Stephan et al., 2021; Han et al., 2019; Gourley et al., 2020). After many years of development, lithium-ion batteries (LIBs) have become increasingly acceptable as the main power source of electric vehicles, given their higher energy density and longer life cycle (EIA, 2020; Liu et al., 2018). However, the safety aspects concerning electric vehicles have received increasing attention due to the hazards of possible fires, usually caused by the failure of on-board large capacity power batteries (Sun et al., 2020).

As one of the main energetic failures, thermal runaway refers to the rapid self-heating of a cell, resulting from the exothermic chemical reaction between the highly oxidizing positive electrode and highly reducing negative electrode of the cell. This can occur in batteries with almost any chemistry (Mikolajczak et al., 2011). With the occurrence of LIB thermal runaway, more and more gases are generated inside the cells. Then, when the pressure inside a cell reaches a certain value, the cell's safety valve is released, or the area at the aluminum-plastic film with the lower allowable pressure for the pouch cell develops a crack. Then, the cell erupts and releases gaseous emissions, i.e., cell eruption gases (CEGs) (Finegan et al., 2015; Wang et al., 2019a; Li et al., 2019b; Zhang et al., 2019). These gases are among the main combustion materials that lead to fires (Xu and Hui, 2017; Bi et al., 2015).

Because CEGs are generally released from the inside of a cell to the battery pack and the external environment, the main combustion-supporting material is oxygen (O<sub>2</sub>) in air. The parameters corresponding to the first two boundaries are the lower flammability limit (LFL) and upper flammability limit (UFL) of the CEGs, which are expressed by the CEG concentration in the CEG-air mixture. When the CEG concentration is lower than the LFL, the CEGs are too thin for ignition. Therefore, the LFL is the  $c_{\text{CEG, ignition}}$ . When the CEG concentration is greater than the UFL, because it is too rich, meaning that the surrounding O<sub>2</sub> is too thin, ignition cannot occur. The O<sub>2</sub> concentration in the CEG-air mixture corresponding to the UFL is the minimum O<sub>2</sub> concentration ( $c_{\text{O}_2, \text{ ignition}}$ ) required for ignition. When the CEG concentration is between the LFL and UFL, there is neither a lack of fuel nor O<sub>2</sub> and ignition can occur.

It should be noted that the  $c_{\text{O}_2, \text{ ignition}}$  mentioned here refers to the O<sub>2</sub> concentration in the CEG-air mixture at the LFL (Liu et al., 2004). It is due to the too rich fuel and too lean O<sub>2</sub> for ignition

<sup>1</sup>State Key Laboratory of Automotive Simulation and Control, Jilin University, Changchun 130025, China

<sup>2</sup>Key Laboratory of Bio-inspired Smart Interfacial Science and Technology of Ministry of Education, School of Chemistry, Beihang University, Beijing 100191, P.R. China

<sup>3</sup>State Key Laboratory of Automotive Safety and Energy, Tsinghua University, Beijing 100084, PR China

<sup>4</sup>Lead contact

\*Correspondence: gaozh@jlu.edu.cn (Z.G.), ypch0727@buaa.edu.cn (Y.C.), ouymg@tsinghua.edu.cn (M.O.)

<https://doi.org/10.1016/j.isci.2021.102401>



to take place. Another similar concept is the critical  $O_2$  concentration (Fairweather et al., 1999), which refers to the  $O_2$  concentration in the fuel-air dilution mixture when the LFL coincides with the UFL using inert gas to dilute the fuel-air mixture. In fact, the critical  $O_2$  concentration is a special case of  $c_{CO_2, \text{ignition}}$ .

To obtain the flammability limit of the CEG, three research methods are generally used. In the first method, thermal runaway is triggered in an inert atmosphere until eruption, and the CEG components are then detected. Afterward, calculations are performed on the basis of the detected components. Based on the existing results (Somandepalli et al., 2014), Guo et al. (Guo and Zhang., 2016) calculated the flammability limits of CEGs and found that the flammability range increases with an increase in the state of charge (SOC). In our open study (Li et al., 2019b), the flammability limits of the CEGs released by commercial 18,650 LIBs with lithium nickel cobalt aluminum oxide (NCA) and lithium iron phosphate (LFP) cathodes at 0%–143% SOCs were calculated using available data in open literature (Golubkov et al., 2015). We found that the UFL and LFL curves of CEGs form a peninsula shape for both cell types with a decrease in the SOC, where the flammability range did not essentially change at first and then dramatically decreased. For the LFP cell, the LFL of the CEGs was higher, and the flammability range was lower than that of the NCA cell at the same SOC.

In the second method, a thermal runaway test is performed in a vacuum environment, and the released cell gases are collected. Then, the flammability limit of the gases is directly tested through an experimental method using a combustion chamber. By using this method, Somandepalli et al. (Somandepalli et al., 2014) found that the LFL of CEGs is about 6.3% and the UFL is between 30 and 40% for cases of 100% and 150% SOCs.

The third method is similar to the second but is conducted in an air environment. In this case, the detected gas is the product of the reaction between CEGs and the air in the test container rather than the CEGs alone. However, the results are of important reference value for evaluating whether CEGs are flammable in the atmosphere after being released from battery packs. Long et al. (Long et al., 2014) subjected a 100 Ah 3.3 V cell to thermal runaway by overcharging it and then collected the CEGs. They opened the valve of the gas collection bag, ignited the gas using an igniter in a laboratory, and found that the CEGs continued to burn. Chen et al. (Chen et al., 2020) used a cell in a closed container filled with air to conduct a thermal runaway test and then tested the LFL of the CEG. They found that the LEL of the CEG increased at the initial stage and then decreased with an increase in the SOC. Moreover, they reported that batteries should be stored at 60% SOC in non-extremely dry environments to reduce the risk of explosion and that keeping the SOC at 100%, which has the lowest LEL, poses a high risk of danger caused by thermal runaway.

### However, some problems remain regarding cell eruptions and fires

First, there are few comparisons of the  $c_{CEG, \text{ignition}}$  for different types of cells, which makes it difficult to provide better guidance for cell selection and battery pack design. Baird et al. (Baird et al., 2020) evaluated the LFL of CEGs to quantify the cell chemistry effect and SOC using three modeling methods. They found that the LFL was 7.6–9.0, 8.6–10.0, 6.1–8.8, and 6.7–11.8 for lithium nickel cobalt manganese oxide (NMC), LFP, lithium cobalt oxide (LCO), and NCA cells, respectively. The results showed that the CEG of LFP generally had higher LFL values at 100% SOC, allowing for more gases to accumulate before reaching deflagration or a fire hazard compared with that of NCA or LCO cells. However, these calculation results were based on gases detected in air, vacuum, and inert atmospheres. It is difficult to distinguish which results were based on the CEG and which results were based on the reaction products of the CEG and air. CEGs are generally ejected from the inside of a cell to the battery pack and subsequently react with the air in the pack before being released to the atmosphere. Therefore, it is still difficult to directly provide guidance for the design of battery packs based on these results.

Second, insufficient data are available (Garche and Brandt, 2018) on the minimum  $O_2$ /air concentration (without the introduction of other inert gases) required for CEG ignition for different types of cells. This makes it difficult to provide better guidance for battery pack design. If the amount of air inside a battery pack can be changed to make the  $O_2$  content below the  $c_{CO_2, \text{ignition}}$ , ignition can be avoided, thus slowing the spread of heat and the resultant damage to the pack components, cells, circuits, and other parts.

**Table 1. Equipment used to detect the cell eruption gases in the summarized works**

Literature	Equipment	Model	Gas detected
Somandepalli et al. (2014)	GC-MS	–	CO, CO <sub>2</sub> , H <sub>2</sub> , and hydrocarbons
Golubkov et al. (2014)	GC	Agilent 3000 Micro GC, two columns, Mol Sieve and PLOTU	H <sub>2</sub> , O <sub>2</sub> , N <sub>2</sub> , CO, CO <sub>2</sub> , CH <sub>4</sub> , C <sub>2</sub> H <sub>2</sub> , C <sub>2</sub> H <sub>4</sub> , and C <sub>2</sub> H <sub>6</sub>
	TCD	–	Permanent gases
Golubkov, et al., 2015	GC	Agilent 3000 Micro GC, two columns, Mol Sieve and PLOTU	H <sub>2</sub> , O <sub>2</sub> , N <sub>2</sub> , CO, CO <sub>2</sub> , CH <sub>4</sub> , C <sub>2</sub> H <sub>2</sub> , C <sub>2</sub> H <sub>4</sub> , and C <sub>2</sub> H <sub>6</sub>
	TCG	–	Permanent gases
Lammer et al., 2017	GC	Agilent Micro-GC 3000A	H <sub>2</sub> , CO, CO <sub>2</sub> , CH <sub>4</sub> , C <sub>2</sub> H <sub>2</sub> , C <sub>2</sub> H <sub>4</sub> , and C <sub>2</sub> H <sub>6</sub>
Zhang et al., 2019	GC	Agilent 7890A	H <sub>2</sub> , CO, CO <sub>2</sub> , and hydrocarbons
	GC-MS	Agilent 7890B-5977A	DEC, EMC
	IC	Metrohm 930 Compact	HCl
Essl et al., 2020	FTIR	Bruker MATRIX-MG01	CO, CO <sub>2</sub> , CH <sub>4</sub> , C <sub>2</sub> H <sub>6</sub> , C <sub>2</sub> H <sub>4</sub> , C <sub>2</sub> H <sub>2</sub> , DEC, DMC, EC, EMC, H <sub>2</sub> O, C <sub>6</sub> H <sub>14</sub> , HF, C <sub>4</sub> H <sub>10</sub> , and C <sub>3</sub> H <sub>8</sub>
	GC	3000 Micro GC (G2802A) with three columns and TCD detectors	H <sub>2</sub> , O <sub>2</sub> , N <sub>2</sub> , CH <sub>4</sub> , CO, CO <sub>2</sub> , C <sub>2</sub> H <sub>6</sub> , C <sub>2</sub> H <sub>4</sub> , C <sub>2</sub> H <sub>2</sub>

For more information, refer to Zhang et al. (2019); Somandepalli et al. (2014); Golubkov et al. (2015); Golubkov et al. (2014); Lammer et al. (2017); and Essl et al. (2020).

Third, few analysis results (Garcke and Brandt, 2018) have been presented for  $T_{\text{ignition}}$ . If this boundary is known, the CEG temperature can be reduced to a value below the boundary through thermal management, thus avoiding the possibility of CEG ignition after their release.

Therefore, based on our previous research on the generation reasons (Li et al., 2019a), eruption characteristics (Wang et al., 2019a; Zhang et al., 2020), component identification (Zhang et al., 2019), ignition sources (Zhang et al., 2019), and flammability analyses (Li et al., 2019b) of CEGs, we summarize the CEG component identification results of 29 thermal runaway tests conducted in an inert atmosphere, as presented in the literature (Zhang et al., 2019; Somandepalli et al., 2014; Golubkov et al., 2014, 2015; Lammer et al., 2017; Essl et al., 2020). According to the results, a time sequence diagram of CEG generation is drawn, and the three fire boundaries of CEGs, including  $C_{\text{CEG}}$ ,  $T_{\text{ignition}}$ ,  $T_{\text{CO}_2}$ , and  $T_{\text{ignition}}$ , are analyzed on the basis of thermal ignition theory. Overall, this research can provide theoretical guidance for cell selection, pack design, and fire safety design.

### Review of the cell eruption gas components

This study focuses on summarizing the performed works (Zhang et al., 2019; Somandepalli et al., 2014; Golubkov et al., 2014, 2015; Lammer et al., 2017; Essl et al., 2020) in the last 10 years regarding the identification of CEG in an inert atmosphere because triggered thermal runaway in an inert atmosphere avoids chemical changes as much as possible after the CEG is ejected from the cell.

Table 1 shows equipment used in the summarized works (Zhang et al., 2019; Somandepalli et al., 2014; Golubkov et al., 2014, 2015; Lammer et al., 2017; Essl et al., 2020) and the types of gases detected. The used instruments mainly included gas chromatography-mass spectrometers (GC-MSs), gas chromatographers (GCs), thermal conductivity detectors (TCGs), ion chromatographs (ICs), and Fourier transform infrared spectrometers (FTIRs). The types of detected gases mainly included hydrogen (H<sub>2</sub>), oxygen (O<sub>2</sub>), nitrogen (N<sub>2</sub>), carbon monoxide (CO), carbon dioxide (CO<sub>2</sub>), methane (CH<sub>4</sub>), ethyne (C<sub>2</sub>H<sub>2</sub>), ethylene (C<sub>2</sub>H<sub>4</sub>), ethane (C<sub>2</sub>H<sub>6</sub>), and other hydrocarbons. In addition, diethyl carbonate (DEC), methyl ethyl carbonate (EMC),

**Table 2. Details of the cells used in the thermal runaway tests in inert atmosphere in the summarized works**

Test no.	Literature	Legend	Chemistry	Format	Nominal capacity (Ah)	SOC (%)					
1	<a href="#">Somandepalli et al. (2014)</a>	LCO_2.1 Ah	LiCoO <sub>2</sub>	–	2.1	50					
2						100					
3						150					
4	<a href="#">Golubkov et al. (2014)</a>	LFP_1.1 Ah (2014)	LiFePO <sub>4</sub>	18650	1.1	100					
5	<a href="#">Golubkov, et al., 2015</a>	LFP_1.1 Ah (2015)	Li <sub>0.882</sub> FePO <sub>4</sub>	18650	1.1	0					
6						25					
7						50					
8						75					
9						100					
10						115					
11						130					
12						<a href="#">Lammer et al. (2017)</a>	NCA_3.2 Ah	LiNi <sub>0.8</sub> Co <sub>0.15</sub> Al <sub>0.05</sub> O <sub>2</sub>	18650	3.2	100
13						<a href="#">Golubkov et al. (2015)</a>	NCA_3.35 Ah	Li <sub>0.925</sub> (Ni <sub>0.80</sub> Co <sub>0.15</sub> Al <sub>0.05</sub> )O <sub>2</sub>	18650	3.35	0
14											25
15											50
16	75										
17	100										
18	112										
19	120										
20	127										
21	132										
22	143										
23	<a href="#">Lammer et al. (2017)</a>	NCA_3.5 Ah (47.68 g)	LiNi <sub>0.8</sub> Co <sub>0.15</sub> Al <sub>0.05</sub> O <sub>2</sub>	18650	3.5	100					
24		NCA_3.5 Ah (46.35 g)				100					
25	<a href="#">Golubkov et al. (2014)</a>	NMC_1.5 Ah	Li(Ni <sub>0.45</sub> Mn <sub>0.45</sub> Co <sub>0.10</sub> )O <sub>2</sub>	18650	1.5	100					
26	<a href="#">Zhang et al. (2019)</a>	NMC_50 Ah	Li(Ni <sub>0.6</sub> Mn <sub>0.2</sub> Co <sub>0.2</sub> )O <sub>2</sub>	Prismatic	50	100					
27	<a href="#">Golubkov et al. (2014)</a>	NMC/LCO_2.6 Ah	LiCoO <sub>2</sub> /	18650	2.6	100					
			Li(Ni <sub>0.50</sub> Mn <sub>0.25</sub> Co <sub>0.25</sub> )O <sub>2</sub>								
28	<a href="#">Essl et al. (2020)</a>	NMC/LMO_41Ah	LiNiMnCoO <sub>2</sub> /LiMn <sub>2</sub> O <sub>4</sub>	Pouch	41	100					
29						30					

For more information, refer to [Zhang et al. \(2019\)](#); [Somandepalli et al. \(2014\)](#); [Golubkov et al. \(2015\)](#); [Golubkov et al. \(2014\)](#); [Lammer et al. \(2017\)](#); and [Essl et al. \(2020\)](#).

dimethyl carbonate (DMC), hydrogen chloride (HCl), ethylene carbonate (EC), hydrogen fluoride (HF), etc., were also detected.

Table 2 shows the details of the cells used in the summarized works ([Zhang et al., 2019](#); [Somandepalli et al., 2014](#); [Golubkov et al., 2014, 2015](#); [Lammer et al., 2017](#); [Essl et al., 2020](#)). The cell chemistries include common types, such as LCO, LFP, NCA, and NMC. The cell capacity ranged from 1.1 Ah to 50 Ah, and the cell formats included square, 18650, and pouch. The SOC values varied from 0% to 143%.

Figure 1 shows the main CEG components detected in the summarized works ([Zhang et al., 2019](#); [Somandepalli et al., 2014](#); [Golubkov et al., 2014, 2015](#); [Lammer et al., 2017](#); [Essl et al., 2020](#)), which were H<sub>2</sub>, CO<sub>2</sub>, CO, CH<sub>4</sub>, C<sub>2</sub>H<sub>4</sub>, and C<sub>2</sub>H<sub>6</sub>. In addition, the components included electrolyte vapor, HF, and other gases. The formation reactions of the main CEG components are summarized in detail in the study by ([Wang et al., 2019b](#)).

Figure 2 shows the time sequence of the CEG generation. In addition to the electrolyte vaporization (90°C–248°C) caused by physical changes, the CEG also contains new gases generated by chemical reactions, which

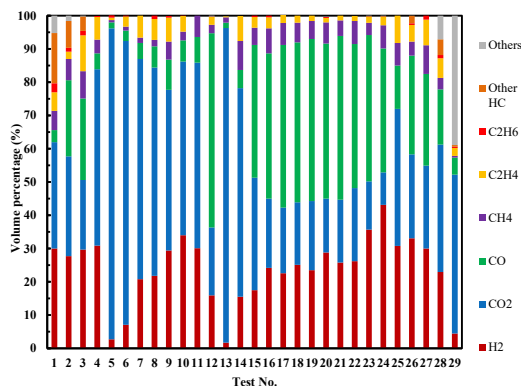


**Figure 1. Variations of the volume percentage of the CEG components in the summarized works vs. test number**

CEG identification result is based on 29 thermal runaway tests conducted in an inert atmosphere in open literature.

can be explained by the thermal decomposition and reactions of the electrolyte, binder, and electrode materials (Golubkov et al., 2014; Wang et al., 2012; Roth and Orendorff., 2012; Fleischhammer and Döring., 2013; Pfrang et al., 2017), as mentioned in the summarized works (Golubkov et al., 2014, 2015; Kocha et al., 2018).

The solid electrolyte interphase (SEI) is a reaction layer that is formed by electrolyte reduction during the first charging cycle on the surfaces of carbon-based anodes (Garche and Brandt, 2018). During the formation of the primary SEI, gases including phosphorus pentafluoride (PF<sub>5</sub>), HF, H<sub>2</sub>, C<sub>2</sub>H<sub>4</sub>, etc., are produced (Agubra and Fergus, 2014; Aurbach et al., 1999; Watanabe and Yamaki, 2006). In general, the SEI consists of inorganic and organic compounds. The organic compounds are metastable at around 80°C, and they start to react and form the so-called secondary SEIs (Wang et al., 2006; Yang et al., 2005; Richard and Dahn, 1999; Andersson and Edström, 2001). The secondary SEI mainly consists of lithium carbonate (Li<sub>2</sub>CO<sub>3</sub>) and lithium fluoride (LiF) (Yang et al., 2005). It has been suggested that besides the formation of secondary SEIs, new organic SEIs are formed by solvent reduction. These complex processes of SEI formation and change occur up to a temperature of ~200°C (Wang et al., 2006; Zhou et al., 2012). During the formation of secondary SEIs, gases including HF, C<sub>2</sub>H<sub>4</sub>, CO<sub>2</sub>, O<sub>2</sub>, C<sub>2</sub>H<sub>4</sub>, etc., are produced (Agubra and Fergus, 2014; Aurbach et al., 1999; Zhou et al., 2012). The initial decomposition of SEI occurs at 80°C–120°C (Spotnitz and Franklin, 2003) with a peak at ~100°C (Richard and Dahn, 1999). An SEI layer may decompose at relatively lower temperatures, such as 69°C (Wang et al., 2006) or 57°C (Wang et al., 2005). C<sub>2</sub>H<sub>4</sub>, CO<sub>2</sub>, O<sub>2</sub>, and other gases are produced during the thermal decomposition of SEI (Yang et al., 2005).

The differential scanning calorimetry traces of the lithiated carbon anodes and electrolytes become very complex at the following peaks: ~100°C, ~150°C, ~270°C, and ~300°C (Spotnitz and Franklin, 2003).

Organic solvents (EC, PC, DMC, etc.) can also react with intercalated lithium to release flammable hydrocarbons, such as C<sub>2</sub>H<sub>4</sub>, C<sub>3</sub>H<sub>6</sub>, and C<sub>2</sub>H<sub>6</sub> (Spotnitz and Franklin, 2003; Aurbach et al., 1997; Gachot et al., 2010, 2012; Yoshida et al., 1997; Onuki et al., 2008; Shin et al., 2002).

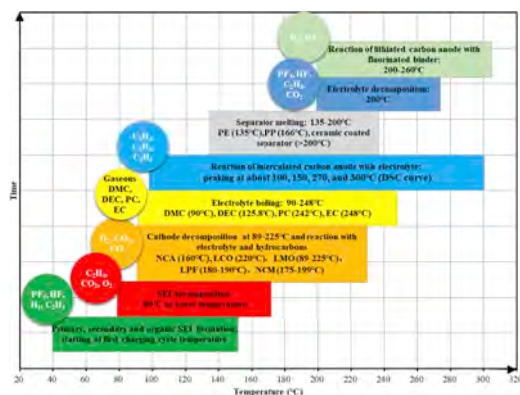


**Figure 2. Time sequence of CEG generation**

Temperature without special explanations refers to the onset temperature of reaction, decomposing, boiling, or melting.

The PE and PP separators melt at 135°C and 166°C, respectively, while some ceramic-coated separators may maintain their structural integrity even above 200°C (Mao et al., 2018; Orendorff, 2012). It has not been previously reported in open literature that gas can be produced during this process.

The initial decomposition of cathodes occurs at 89°C–225°C (Biensan et al., 1999; Wang et al., 2007a, 2007b; Huang et al., 2016; Zhang et al., 1998; Martha et al., 2011; Joachin et al., 2009), and then, O<sub>2</sub> is released (Dahn et al., 1994; Li et al., 2006). The release of O<sub>2</sub> can lead to a further reduction of the generated hydrocarbons down to CO<sub>2</sub>. Since this O<sub>2</sub> generation from the cathodes inside the cells and the other O<sub>2</sub> sources are both limited, some hydrocarbons only get reduced to CO (Golubkov et al., 2014; Roth and Orendorff, 2012).

LiPF<sub>6</sub> salt decomposes at 200°C to LiF and PF<sub>5</sub> (Ravdel et al., 2003). The decomposition of the electrolyte is a multistage reaction and mainly takes place in the ranges of 200°C–220°C, 220°C–250°C, and 250°C–300°C, generating gases such as PF<sub>5</sub>, HF, CO<sub>2</sub>, and C<sub>2</sub>H<sub>4</sub> (Ribiere et al., 2012; Wang et al., 2019b; Campion et al., 2004; Gnanaraj et al., 2003; Kawamura et al., 2006).

When a carbon anode is intercalated with lithium-ions, it can react with PVDF, generating HF and H<sub>2</sub> (Pasquier et al., 1998). The temperatures at which the reaction begins were reported to be 200°C (Maleki et al., 1999), 240°C (Biensan et al., 1999), and 260°C (Pasquier et al., 1998).

## RESULTS AND DISCUSSION

Gas can be divided into two types: non-flammable and flammable. In the former case, no gas ignition will occur regardless of the conditions. As determined in tests 5 and 13 shown in Table 2 and Figure 1, CEGs are non-flammable when the SOC is 0% owing to the high CO<sub>2</sub> content (Li et al., 2019b). However, the CEGs were flammable in the other 27 tests. It should be noted that flammable does not guarantee ignition. To achieve fire, combustibles need an oxidizer, an ignition source, ignition energy, ignition critical diameter, etc (Xu and Hui, 2017; Bi et al., 2015; Turns and Haworth, 2021). The main conditions for ignition are collectively known as the fire triangle, i.e., a combustible, an oxidizer, and an ignition source. The three fire boundaries corresponding to the fire triangle are  $c_{CEG, ignition}$ ,  $c_{CO_2, ignition}$  and  $T_{ignition}$ . According to the thermal ignition theory, these three boundaries are necessary for fire but not sufficient (Xu and Hui, 2017; Bi et al., 2015; Turns and Haworth, 2021). When one of the fire boundaries is met, a fire may occur or not. But when any one of the fire boundaries is not met, a fire cannot occur. This means that if any one of fire boundaries is broken, no fire will occur. This is of great significance for battery fire suppression. This section analyzes the three fire boundaries of flammable CEGs in a cell fire based on the thermal ignition theory. When analyzing the impact of a certain boundary, it is assumed that the other fire boundaries are available. Considering the limited amount of data in open literature (Zhang et al., 2019; Somandepalli et al., 2014; Golubkov et al., 2014, 2015; Lammer et al., 2017; Essl et al., 2020), when discussing the changes in  $c_{CEG, ignition}$  and  $c_{CO_2, ignition}$  with SOC, only the trends of LFP\_1.1 Ah (2015), NCA\_3.35 Ah (2015), and LCO\_2.1 Ah were discussed. In addition, to compare the differences between cell types, cells using NMC, NMC/LCO, and NMC/LMO as positive electrodes were collectively classified as NMC cells.

### Minimum CEG concentration required for ignition

Figure 3 shows the variation in  $c_{CEG, ignition}$  with the SOC for different types of cells. The calculation method of  $c_{CEG, ignition}$  is shown in the supplemental information section. It decreases with an increase in the SOC for the LFP\_1.1 Ah (2015) cell at the discharged state, especially when the SOC is below 50%. This shows that the probability of fire increases with the SOC value. Also,  $c_{CEG, ignition}$  remains almost unchanged at the full and overcharged stages. However, from the discharged (25% SOC) to the fully charged (100% SOC) to the overcharged (130% SOC) stages, it successively decreases by 79.0% and increases by 13.0%.

Compared with  $c_{CEG, ignition}$  for the LFP\_1.1 Ah (2015) cell,  $c_{CEG, ignition}$  for the NCA\_3.35 Ah (2015) cell has a similar variety trend with an increase in the SOC. From the discharged (25% SOC) to the fully charged (100% SOC) to the overcharged (143% SOC) stages, it successively decreases by 35.8% and increases by 2.6%.

For the LCO\_2.1 Ah cell,  $c_{CEG, ignition}$  first increases and then slightly decreases with an increase in the SOC. From the discharged (25% SOC) to the fully charged (100% SOC) to the overcharged (143% SOC) stages, it successively increases by 40.9% and decreases by 12.9%.

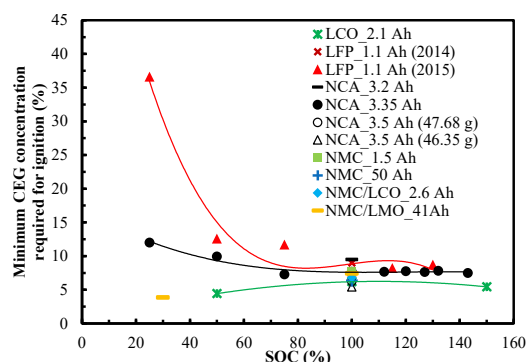


**Figure 3. Variations in the minimum CEG concentration required for ignition vs. SOC**

Thus, for these three types of cells, at the same SOC, the LFP\_1.1 Ah (2015) cell requires the highest  $c_{CEG, ignition}$ , followed by the NCA\_3.35 Ah (2015) cell and then the LCO\_2.1 Ah cell. It successively decreases by 21.4% and 55.6% at the discharged state (50% SOC). Then, it successively decreases by 0.8% and 19.5% at the fully charged state (100% SOC). This shows that when the other fire conditions are the same, the LFP\_1.1 Ah (2015) cell has the lowest fire possibility, followed by the NCA\_3.35 Ah (2015) cell and then the LCO\_2.1 Ah cell.

Table 3 shows the range of  $c_{CEG, ignition}$  under different charging states. The respective  $c_{CEG, ignition}$  for the LCO, LFP, NCA, and NMC cells is 4.4%, 11.7%–36.3%, 7.3%–12.0%, and 3.9% when not fully charged and 6.2%, 7.7%, 5.4%–9.5%, and 6.4%–7.7% for the case of being fully charged, respectively. When LCO, LFP and NCA are overcharged, the values are 5.4%, 8.2%–8.7%, and 7.5%–7.9%, respectively. Overall, the  $c_{CEG, ignition}$  for the LCO, LFP, NCA, and NMC cells is 4.4%–6.2%, 7.7%–36.6%, 5.4%–12.0%, and 3.9%–3.9%, respectively. The  $c_{CEG, ignition}$  for the LFP cell is highest, followed by the NCA and LCO cells and then the NMC cell, as shown in Figure 4. This shows that the fire probability for these types of cells successively increases and that the difficulty of their fire suppression by controlling the CEG concentration also successively increases.

The above analysis results show that by controlling the SOC and/or selecting a reasonable cell type, the  $c_{CEG, ignition}$  of a cell can be changed, thereby changing the probability of battery fire.

### Minimum O<sub>2</sub> concentration required for ignition

Figure 5 shows the variation in  $c_{O_2, ignition}$  with the SOC for different types of cells. The calculation method of  $c_{O_2, ignition}$  is shown in the supplemental information section. For the LFP\_1.1 Ah (2015) cell, as the SOC value increases, it does not significantly change. From the discharged (25% SOC) to the fully charged (100% SOC) to the overcharged (130% SOC) stages, it successively increases by 8.5% and decreases by 5.9%.

For the NCA\_3.35 Ah (2015) cell, as the SOC value increases,  $c_{O_2, ignition}$  decreases at the discharged state but remains almost unchanged at the fully charged and overcharged stages. From the discharged (25% SOC) to the fully charged (100% SOC) to the overcharged (143% SOC) stages, it successively decreases by 16.4% and increases by 1.1%.

The LCO\_2.1 Ah cell has a similar trend to that of the NCA\_3.35 Ah (2015) cell. From the discharged (50% SOC) to the fully charged (100% SOC) to the overcharged (150% SOC) stages,  $c_{O_2, ignition}$  successively decreases by 13.4% and increases by 1.6%.

**Table 3. Minimum CEG concentration required for ignition for different cell types.**

Chemistry	Not fully charged	Fully charged	Overcharged	Range
LCO	4.4	6.2	5.4	4.4–6.2
LFP	11.7–36.6	7.7	8.2–8.7	7.7–36.6
NA	7.3–12.0	5.4–9.5	7.5–7.9	5.4–12.0
NMC	3.9	6.4–7.7	–	3.9–7.7

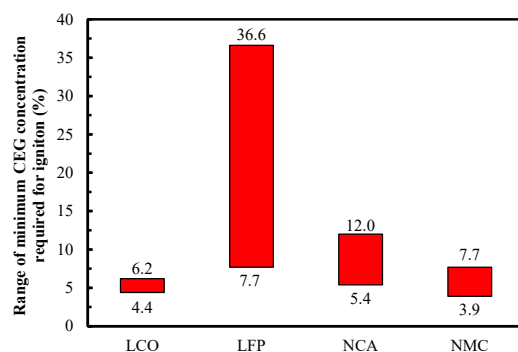


**Figure 4. Variations in the range of the minimum CEG concentration required for ignition vs. cell type**

For these three types of cells, at the same SOC, the LCO\_2.1 Ah cell requires higher  $c_{O_2, \text{ignition}}$  than that of the other two cell types. For the same SOC value, the NCA\_3.35 Ah (2015) cell requires higher  $c_{O_2, \text{ignition}}$  than that of the LFP\_1.1 Ah (2015) cell at the discharged state. However, there is no obvious difference in  $c_{O_2, \text{ignition}}$  at the fully and overcharged states for these two cells. From the LCO\_2.1 Ah cell to the NCA\_3.35 Ah (2015) cell to the LFP\_1.1 Ah (2015) cell,  $c_{O_2, \text{ignition}}$  successively decreases by 37.6% and 4.3% at the discharged state (50% SOC) and successively decreases by 30.2% and increases by 10.9% at the fully charged state (100% SOC), respectively. This shows that when the other fire conditions are the same, the LCO\_2.1 Ah cell has the lowest fire possibility among these three types of cells.

Table 4 shows the range of  $c_{O_2, \text{ignition}}$  under different charging states. For the LCO, LFP, NCA, and NMC cells, the respective values are 14.9%, 8.9%–9.4%, 9.3%–11.0%, and 15.1% for the case of being not fully charged and 12.9%, 10.2%, 7.6%–9.3%, and 10.0%–11.5% when fully charged, respectively. For the overcharged LCO, LFP, NCA cells, the values are 12.7%, 8.9%–9.6%, and 8.5%–9.3%, respectively. In general,  $c_{O_2, \text{ignition}}$  for the LCO, LFP, NCA, and NMC cells is 12.7%–14.9%, 8.9%–10.2%, 7.6%–11.0%, and 10.0%–15.1%, respectively. Thus, the LCO cell requires the highest  $c_{O_2, \text{ignition}}$  to ignite, followed by the NMC and LFP cells and then NCA cell, as shown in Figure 6. This shows that the fire hazard of these types of cells increases in turn and that the difficulty of their fire suppression by controlling the  $O_2$  concentration also successively increases.

The above analysis results show that by controlling the SOC and/or selecting a reasonable cell type, the  $c_{O_2, \text{ignition}}$  of the cell can be changed, thereby changing the probability of battery fire.

It should be noted that the results of evaluating the cell safety based on  $c_{CEG, \text{ignition}}$  and  $c_{O_2, \text{ignition}}$  are different. Based on the former, the order of safety from high to low is LFP > NCA > LCO > NMC. Based on the latter, the order of safety from high to low is LCO > NMC > LFP > NCA. This shows that a cell should be selected based on its application; for different types of cells, different fire prevention and control strategies should be selected.

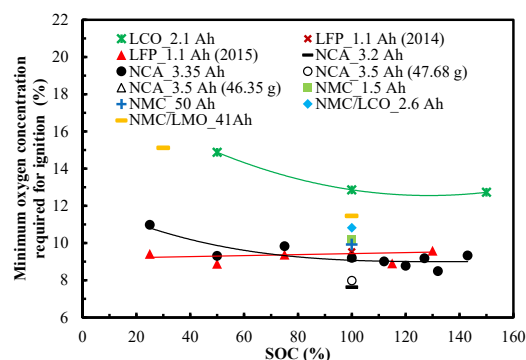


**Figure 5. Variations in the minimum oxygen concentration required for ignition vs. SOC**

**Table 4. Minimum oxygen concentration required for ignition for different types of cells.**

Chemistry	Not fully charged	Fully charged	Overcharged	Range
LCO	14.9	12.9	12.7	12.7–14.9
LFP	8.9–9.4	10.2	8.9–9.6	8.9–10.2
NA	9.3–11.0	7.6–9.3	8.5–9.3	7.6–11.0
NMC	15.1	10.0–11.5	–	10.0–15.1

The higher the  $c_{\text{CEG, ignition}}$ , the easier it is to suppress battery fire by controlling the CEG concentration. The same case applies for  $c_{\text{O}_2, \text{ ignition}}$ . For example,  $c_{\text{CEG, ignition}}$  for NMC cells is relatively low, while  $c_{\text{O}_2, \text{ ignition}}$  is relatively high. This shows that to suppress NMC battery ignition, it is easier to control the  $\text{O}_2$  concentration than to control the CEG concentration. From the perspectives of  $c_{\text{CEG, ignition}}$  and  $c_{\text{O}_2, \text{ ignition}}$  for four different types of cells, to achieve fire suppression, it is recommended to control the CEG concentration for the LFP and NCA cells and the  $\text{O}_2$  concentration for the LCO and NMC cells.

However, actual scenarios should also be considered to select appropriate control methods. For example, for the inside of a closed battery box, the CEG and  $\text{O}_2$  concentrations can be reduced by filling incombustible gas or the  $\text{O}_2$  concentration can be reduced by reducing the internal pack space (after a cell erupts). It is difficult to control the  $\text{O}_2$  concentration in the atmosphere, so it should be mixed with incombustible gas before CEGs are released and reduced to a value below  $c_{\text{CEG, ignition}}$  to avoid fires.

Notably, because  $c_{\text{O}_2, \text{ ignition}}$  refers to the concentration of  $\text{O}_2$  in the CEG-air mixture, it is lower than the  $\text{O}_2$  content in the air (21%). In an open environment, sufficient air will continuously dilute the flammable CEG and can easily meet the  $\text{O}_2$  concentration boundary (Xu and Hui, 2017; Bi et al., 2015; Turns and Haworth, 2021). Therefore, if all other fire conditions are met, a fire will occur in an open environment. However, this does not mean that all CEGs will ignite in air because some CEGs are nonflammable (test 5 and 13 shown in Table 2 and Figure 1). In a closed environment, such as inside a battery box or a closed battery transport space, it is easier to control the  $\text{O}_2$  content. The  $\text{O}_2$  concentration boundary can be broken by reducing the amount of air by lowering the pressure, reducing the volume, and filling with inert gas to avoid the occurrence of fire (Li et al., 2019b; Turns and Haworth, 2021; Chen et al., 2017; Xie et al., 2020; Dong et al., 2019).

### Minimum ignition temperature required for ignition

Table 5 shows the main components of CEGs in open literature (Zhang et al., 2019; Somandepalli et al., 2014; Golubkov et al., 2014, 2014, 2015; Golubkov et al., 2014; Essl et al., 2020). In addition to  $\text{CO}_2$ ,  $\text{H}_2\text{O}$ , and  $\text{O}_2$ , 33 flammable substances have been found so far, such as  $\text{CO}$ ,  $\text{H}_2$ , alkane, alkene, alkyne, aromatic HC, electrolyte, etc. Based on the substances marked with \*, the ignition mode and  $T_{\text{ignition}}$  of cells were analyzed in this section.

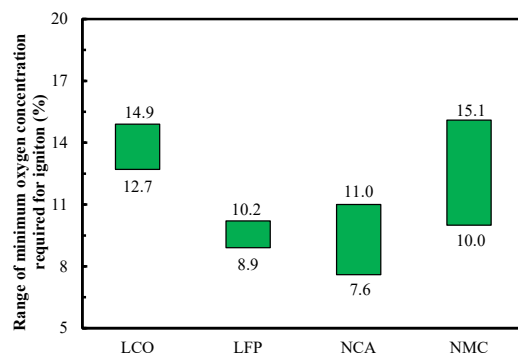


**Figure 6. Variations of the range of the minimum  $\text{O}_2$  concentration required for ignition vs. cell type**

**Table 5. Main components of CEGs found in open literature**

Category	No.	Name	Formular	Essl et al. (2020)	Zhang et al. (2019)	Lammer et al. (2017)	Golubkov et al. (2015)	Golubkov et al. (2014)	Somandepalli et al. (2014)
Non-HC	1	Carbon dioxide	CO <sub>2</sub>	√	√	√	√	√	√
	2	Carbon monoxide	CO	√	√*	√	√	√	√
	3	Hydrogen	H <sub>2</sub>	√	√*	√	√	√	√
Alkane	4	Methane	CH <sub>4</sub>	√	√*	√	√	√	√
	5	Ethane	C <sub>2</sub> H <sub>6</sub>	√	√*	√	√	√	√
	6	Propane	C <sub>3</sub> H <sub>8</sub>	√	√*				√
	7	n-Butane	C <sub>4</sub> H <sub>10</sub>	√	√*				√
	8	Isobutane	C <sub>4</sub> H <sub>10</sub>						√
	9	n-Pentane	C <sub>5</sub> H <sub>12</sub>		√*				√
	10	Isopentane	C <sub>5</sub> H <sub>12</sub>						√
Alkene	11	Ethylene	C <sub>2</sub> H <sub>4</sub>	√	√*	√	√	√	√
	12	Propylene	C <sub>3</sub> H <sub>6</sub>		√*				
	13	1-Butylene	C <sub>4</sub> H <sub>8</sub>		√*				√#
	14	2-Methyl propene	C <sub>4</sub> H <sub>8</sub>		√				√#
	15	trans-2-Butene	C <sub>4</sub> H <sub>8</sub>		√				√#
	16	cis-2-Butene	C <sub>4</sub> H <sub>8</sub>		√				√#
	17	1-Pentene	C <sub>5</sub> H <sub>10</sub>		√*				
	18	cis-2-Pentene	C <sub>5</sub> H <sub>10</sub>		√				
	19	trans-2-Pentene	C <sub>5</sub> H <sub>10</sub>		√				
	20	2-Methyl-1-butene	C <sub>5</sub> H <sub>10</sub>		√				
	21	2-Methyl-2-butene	C <sub>5</sub> H <sub>10</sub>		√				
	22	3-Methyl-1-butene	C <sub>5</sub> H <sub>10</sub>		√				
	23	2-Methyl-1-pentene	C <sub>6</sub> H <sub>12</sub>		√*				
Alkyne	24	Ethyne	C <sub>2</sub> H <sub>2</sub>	√	√*	√			
	25	Propyne	C <sub>3</sub> H <sub>4</sub>		√*				√
	26	1,3-Butadiene	C <sub>4</sub> H <sub>6</sub>		√*				
Aromatic HC	27	Benzene	C <sub>6</sub> H <sub>6</sub>		√*				√
	28	Methylbenzene	C <sub>7</sub> H <sub>8</sub>						√*
	29	Ethylbenzene	C <sub>8</sub> H <sub>10</sub>						√*
	30	m & p-xylene	C <sub>8</sub> H <sub>10</sub>						√
Electrolyte	31	DMC	C <sub>3</sub> H <sub>6</sub> O <sub>3</sub>		√*				
	32	EMC	C <sub>4</sub> H <sub>8</sub> O <sub>3</sub>		√*				
	33	DEC	C <sub>5</sub> H <sub>10</sub> O <sub>3</sub>	√	√*				

(Continued on next page)

Table 5. Continued

Category	No.	Name	Formular	Essl et al. (2020)	Zhang et al. (2019)	Lammer et al. (2017)	Golubkov et al. (2015)	Golubkov et al. (2014)	Somandepalli et al. (2014)
Others	34	2,4-Dimethyl-1-heptene	C <sub>9</sub> H <sub>18</sub>		√*				
	35	Oxidane	H <sub>2</sub> O	√	√				
	36	Hydrogen chloride	HCl		√				
	37	Oxygen	O <sub>2</sub>	√					

\* Substance was used to analyze the temperature boundary and ignition mode.

# The type of isomer cannot be determined.

For more information, refer to Essl et al. (2020); Zhang et al. (2019); Golubkov et al. (2014, 2015); and Somandepalli et al. (2014).

According to thermal ignition theory, the ignition of CEG is divided into forced ignition and autoignition, as shown in Table 6. Forced ignition signifies that the CEG is heated locally by forced ignition sources, and the local CEG ignites first. Then, the produced flame spreads from the ignition zone to the others. A forced ignition source often has high temperature. Common forced ignition sources include sparks, hot spots, and flames, as shown in Table 6. The electrification of automobiles creates conditions for the generation of electric sparks, and the maximum temperature of electric sparks can be close to 10,000°C. The minimum temperature required for a substance to be forced to ignite is defined as the forced ignition point ( $T_{\text{forced-ignition}}$ ).

Autoignition signifies that all CEGs are heated by autoignition sources and then ignite. An autoignition source does not require a high temperature but needs to have enough energy to heat the CEG. According to the energy source, autoignition sources are divided into self-heating and nonself-heating sources, as shown in Table 6. The main difference between a nonself-heating source and a forced ignition source is whether the ignition source is in direct contact with combustibles, and whether it can increase the temperature of the overall combustibles. The lowest temperature required for a substance to spontaneously ignite without forced ignition sources is defined as the autoignition point ( $T_{\text{autoignition}}$ ).

Forced ignition and autoignition are essentially the same. After heat accumulates to a certain extent, the chemical reaction rate is automatically and continuously accelerated until a higher chemical reaction rate is reached. The main difference is that the former is local heating, and the latter is overall heating. To facilitate the analysis, the following assumptions were made:

- $T_{\text{forced-ignition}}$  is usually 5°C–20°C higher than the flash point ( $T_{\text{flash}}$ , the minimum temperature required for a substance to flash), but the  $T_{\text{forced-ignition}}$  data are incomplete and are related mainly to testing methods and boundaries. Therefore,  $T_{\text{flash}}$  is used to measure the  $T_{\text{forced-ignition}}$  of CEG components.
- The influences of the pressure and temperature inside a cell on the physical and chemical properties of the CEG components were not considered.
- The cell jet area temperature was used to represent the CEG temperature during eruption.
- For the convenience of analysis, it was considered that the CEG temperature, i.e.,  $T_{\text{eruption}}$ , is about 350°C (Zhang et al., 2019) and that the ambient temperature ( $T_{\text{ambient}}$ ) is ~25°C.

When there is a forced ignition source, the temperature boundary is  $T_{\text{flash}}$ . That is, when the CEG temperature exceeds  $T_{\text{flash}}$ , the CEG may be forced ignited. Figure 7 shows the  $T_{\text{flash}}$  of the CEG main components. As the number of carbon atoms increases,  $T_{\text{flash}}$  increases for alkanes (carbon atoms fewer than 6), alkenes (carbon atoms less than 7), and aromatic hydrocarbons (carbon atoms fewer than 9), but it decreases for alkynes (carbon atoms fewer than 5). The  $T_{\text{flash}}$  values of the three electrolytes are not significantly different. Among the detected substances, the substance with the lowest  $T_{\text{flash}}$  is CH<sub>4</sub>, which is

**Table 6. Ignition source and its temperature**

	Definition	Ignition source		$T_{\text{Ignition source}}$ °C
Forced ignition	The CEG is heated locally by forced ignitions, and the local CEG ignites first, and then, the flame spreads to the others. Forced ignition sources often have high temperatures.	Spark	(1) Electric spark caused by too small electric clearance between conductive parts	3000–6000
			(2) Electric arc caused by lots of sparks	8700–9700
			(3) Static electric spark caused by invalid equipotential bonding	–
			(4) Mechanical spark caused by friction between the eruption flow and the wall	~1200
			(5) Spark from the ICE pipe	600–800
		Hot spot	(6) High temperature surface of the cell	~1000
			(7) High temperature cable with short circuit or overcurrent	–
			(8) Cigarette butts	250–800
		Flame	(9) Gas flame	1600–2100
			(10) Gasoline flame	~1200
			(11) Match flame	500–650
Autoignition	The CEG is heated whole by autoignition sources and then ignites. The autoignition source does not need to have a high temperature but needs to have enough energy to heat the CEG.	Self-heating	(1) Heats from the chemical reactions during the generating process of CEGs	200–1000
			(2) Heats from slow chemical reactions of CEGs caused by lighting, catalytic reactions by cathode materials, etc.	–
		Non-self-heating	(3) Heats from high temperature autoignition sources often with indirect contact with the CEG, such as the high temperature surface of a cell with thermal runaway, the high temperature surface of the ICE of another vehicle, a heater, etc. They can make the temperature of all the CEG be increased.	–
			(4) An energy source that converts other forms of energy into heat, such as friction, compression, etc.	–

around  $-200^{\circ}\text{C}$ , and the substance with the highest  $T_{\text{flash}}$  is the electrolyte, which is higher than  $0^{\circ}\text{C}$ . When there is a forced ignition source, there are two typical situations:

- When a cell erupts, the CEG is easily ignited if other ignition boundaries are available, as shown in [Figure 7A](#), because the  $T_{\text{flash}}$  values of all of the substances are lower than  $T_{\text{eruption}}$  (about  $350^{\circ}\text{C}$  ([Zhang et al., 2019](#))).
- If the CEG is cooled to  $T_{\text{ambient}}$ , substances with  $T_{\text{flash}}$  lower than  $T_{\text{ambient}}$  can easily ignite. Among the CEG components, CO, hydrogen, small molecular alkanes, small molecular olefins, and other substances generally have a flash point lower than the  $T_{\text{ambient}}$  (about  $25^{\circ}\text{C}$ ), so they are easily ignited first. The electrolyte, macromolecular alkanes, macromolecular alkenes, small molecular alkynes, benzene, and other substances may have a higher flash point than  $T_{\text{ambient}}$  (e.g., cold winter), so these substances may be ignited by the other substances that were already ignited first, as shown in [Figure 7B](#).

When there is no forced ignition source, the temperature boundary is  $T_{\text{autoignition}}$ . That is, when the fuel temperature exceeds  $T_{\text{auto-ignition}}$ , CEGs may be autoignited. [Figure 8](#) shows the  $T_{\text{autoignition}}$  of the main

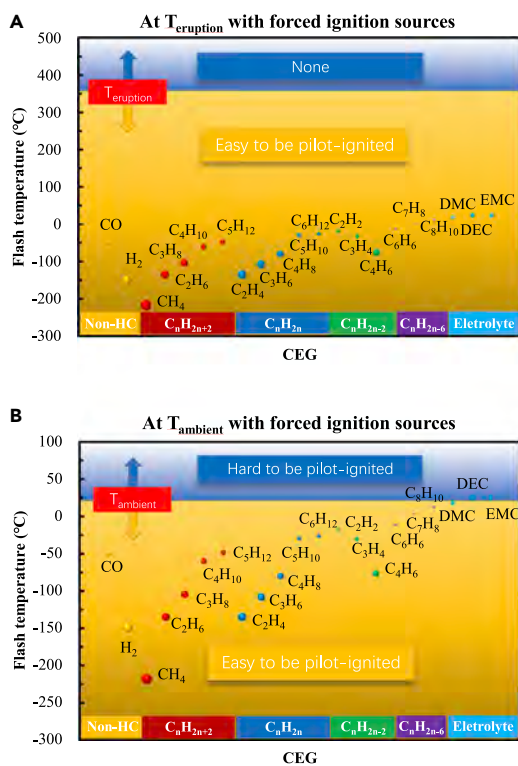


**Figure 7. Flash temperatures of the main CEG components**

When there is a forced ignition source, the temperature boundary is  $T_{flash}$ . That is, when the CEG temperature exceeds  $T_{flash}$ , the CEG may be forced ignited.

(A) When a cell erupts, the CEG is easily ignited if other ignition boundaries are available.

(B) If the CEG is cooled to  $T_{ambient}$ , substances with  $T_{flash}$  lower than  $T_{ambient}$  can easily ignite.

CEG components. For the alkanes (carbon atoms less than 6), alkenes (carbon atoms less than 7), and aromatic hydrocarbons (carbon atoms less than 9), as the number of carbon atoms increases, the overall  $T_{autoignition}$  shows a downward trend, but it increases for the alkynes (the number of carbon atoms is less than 5). Among the detected substances, CO has the highest  $T_{autoignition}$ , followed by  $C_6H_6$ ,  $H_2$  and  $CH_4$  (all above  $500^\circ\text{C}$ ); the substances with lower  $T_{autoignition}$  (around  $300^\circ\text{C}$ ) are mainly macromolecule alkanes (e.g.,  $C_4H_{10}$ ,  $C_5H_{12}$ ), macromolecule alkenes (e.g.,  $C_6H_{12}$ ,  $C_5H_{10}$ ), and small-molecule alkynes (e.g.,  $C_2H_2$ ). The  $T_{autoignition}$  of  $C_5H_{12}$  is lowest at  $260^\circ\text{C}$ . When there are no forced ignition sources, there are two typical situations:

- When a cell erupts, the substances with  $T_{auto-ignition}$  lower than  $T_{eruption}$  are easy to autoignite first (e.g., macromolecular alkanes, macromolecular alkenes, and small molecular alkynes), and then, they ignite the substances with  $T_{auto-ignition}$  higher than  $T_{eruption}$  (e.g., CO,  $H_2$ , small molecular alkanes, macromolecular alkynes, benzene, and electrolyte), as shown in Figure 8A.
- If the CEGs are cooled below the minimal value of autoignitions of all components in the CEG ( $T_{auto-ignition, min}$ ) of  $\sim 260^\circ\text{C}$ , autoignition will not occur, as shown in Figure 8B.

Essentially, CEGs are mixtures of as many as 33 components. The gas mixtures can exhibit different characteristics (Bi et al., 2015) such as  $c_{CEG, ignition}$ ,  $CO_2, ignition$ , and  $T_{ignition}$ . However, no method has been found to accurately predict the  $T_{ignition}$  of the mixture. The  $T_{ignition}$  of the mixture is generally between the average  $T_{ignition}$  and lowest  $T_{ignition}$  of the components (Bi et al., 2015) and is strongly affected by the component with the lowest  $T_{ignition}$ . Therefore, we used the lowest  $T_{flash}$  or  $T_{autoignition}$  of components of the CEG to characterize its  $T_{ignition}$ . This is a method commonly used in combustion science and includes evaluation of the  $T_{autoignition}$  of the diesel-natural gas (NG) mixture in diesel-NG dual-fuel engines by the  $T_{autoignition}$  of diesel (Rossha et al., 2018).

The  $T_{ignition}$  of the mixture is also affected by the concentration of each component, particularly those with larger contents (Bi et al., 2015). Table 1 and Figure 7 show that the concentrations of CO,  $H_2$ , and  $CH_4$  in CEGs are relatively large, with  $CH_4$  having the lowest  $T_{flash}$  among the 33 CEG components. Therefore, the analysis of forced ignition in this study is credible. Table 1 and Figure 8 show that the substances with the lowest  $T_{autoignition}$ , such

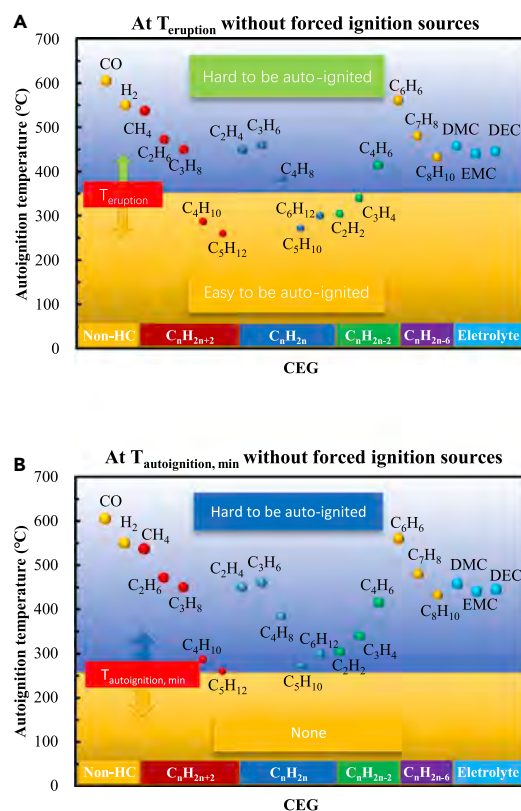


**Figure 8. Autoignition temperatures of the main CEG components**

When there is no forced ignition source, the temperature boundary is  $T_{autoignition}$ . That is, when the fuel temperature exceeds  $T_{autoignition}$ , CEG may be autoignited.

(A) When a cell erupts, the substances with  $T_{autoignition}$  lower than  $T_{eruption}$  are easy to autoignite first, and then, they ignite the substances with  $T_{autoignition}$  higher than  $T_{eruption}$ .

(B) If the CEGs are cooled below  $T_{autoignition, min}$  of  $\sim 260^\circ\text{C}$ , autoignition will not occur.

as  $\text{C}_5\text{H}_{12}$ , and  $\text{C}_5\text{H}_{10}$ , have low concentrations. However, according to the thermal ignition theory, even a relatively small amount of a substance can play a leading role in the ignition process. For example, the ignition of a premixed main charge containing gaseous fuel (more than 98% of the total fuel energy) occurs through direct injection of a small amount of diesel fuel (usually 0.5 to 2% of the total fuel energy) in a micro-pilot dual-fuel engine (Park et al., 2021). Diesel is a complex mixture of hydrocarbons containing 10–22 carbon atoms, and its  $T_{autoignition}$  is  $254^\circ\text{C}$ – $285^\circ\text{C}$ . Gases having a high  $T_{autoignition}$  include NG, which contains mainly  $\text{CH}_4$ ,  $\text{C}_2\text{H}_6$ ,  $\text{C}_3\text{H}_8$ ,  $\text{C}_4\text{H}_{10}$ ,  $\text{N}_2$ , and  $\text{CO}_2$ ; biogas, which contains mainly  $\text{CO}$ ,  $\text{CO}_2$ ,  $\text{CH}_4$ , and  $\text{H}_2$ ;  $\text{H}_2$ ; and others. This ignition process is strongly similar to that of the CET. Therefore, the analysis of autoignition in this study has certain reference value for evaluating the temperature boundary of the CEG. In particular, to leave a safe interval in the design target temperature to avoid fire, it is meaningful to use the lowest  $T_{ignition}$  among the CEG components to evaluate the  $T_{ignition}$  of the CEG.

In short, when there is a forced ignition source, CEGs are prone to ignite regardless of the temperature, and the substances with a low  $T_{flash}$  (e.g.,  $\text{CO}$ , hydrogen, small molecular alkanes, and small molecular olefins) play a leading role in the ignition process. When there are no forced ignition sources, CEGs are prone to autoignition at the  $T_{eruption}$ , and the substances with a low  $T_{autoignition}$  (e.g., macromolecular alkanes, macromolecular alkenes, and small molecular alkynes) play a leading role in the ignition process. If the CEG temperature is cooled below the  $T_{autoignition, min}$ , autoignition will not occur. Therefore, the ignition process of a cell belongs to the self-accelerating reaction mode, which is controlled by the reaction activity, as shown in Figure 9. The CEG ignition mode can be controlled by changing the CEG temperature and ignition sources, i.e., reactivity-controlled self-accelerated chemical reaction mode (Li et al., 2019a).

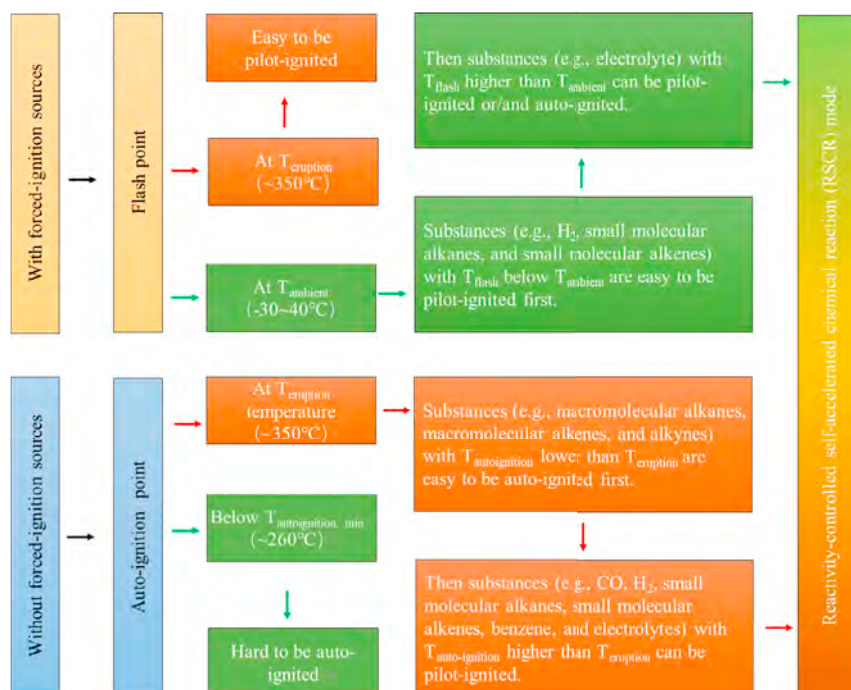


**Figure 9. CEG ignition mode**

The ignition process of a cell belongs to the self-accelerating reaction mode, which is controlled by the reaction activity.

### Significance of this research

The research results of this paper can provide guidance for cell selection, battery pack design, and safety design.

- According to  $c_{CEG, ignition}$  and/or  $CO_{2, ignition}$ , the following questions can be answered. Which cell type is safer? What is the right SOC value for cell storage? What is the CEG/ $O_2$  concentration value above which there is a possibility of fire? How much inert gases should be filled in a battery pack to ensure it does not ignite after eruption? How many cells experiencing thermal runaway can make the  $O_2$  concentration below  $CO_{2, ignition}$  by consuming the  $O_2$  inside a battery pack?
- The research results related to  $T_{ignition}$  point out the importance of controlling the sources of forced ignition. They also show that when there are no ignition sources, the CEG temperature can be lowered to the  $T_{auto-ignition}$  ( $\sim 260^\circ C$ ) to avoid fires, providing a reference for thermal management design. In addition, the relevant results of this part also indicate the ignition mode of CEGs, laying a foundation for further research on related mechanisms.

The above results are only the most important ones. In short, through the analysis of the three fire boundaries, the occurrence of fire can be avoided when any one of the boundaries is avoided. According to the research results of this paper, a variety of solutions can be designed to avoid the occurrence of fire.

### Conclusions

In this study, the three fire boundaries, which are  $c_{CEG, ignition}$ ,  $CO_{2, ignition}$ , and  $T_{ignition}$ , were theoretically analyzed based on the CEG identification results of 29 thermal runaway tests in inert atmosphere. The main conclusions were summarized as follows:

- $c_{CEG, ignition}$  decreases and then remains almost unchanged with the increase in SOC for the LFP\_1.1 Ah (2015) and the NCA\_3.35 Ah (2015) cells. For the LCO\_2.1 Ah cell, with the increase in the SOC,  $c_{CEG, ignition}$  first increases and then decreases. The respective values of  $c_{CEG, ignition}$  for the LCO, LFP, NCA, and NMC cells are 4.4%–6.2%, 7.7%–36.6%, 5.4%–12.0%, and 3.9%–3.9%, respectively, which indicates that the order of  $c_{CEG, ignition}$  from high to low is LFP > NCA > LCO > NMC.

- (2)  $c_{\text{O}_2, \text{ignition}}$  does not significantly change for the LFP\_1.1 Ah (2015) cell with the increase in the SOC. It decreases at the discharged stage but remains almost unchanged at the fully and overcharged stages for both NCA\_3.35 Ah (2015) and LCO\_2.1 Ah cells. The respective values of  $c_{\text{O}_2, \text{ignition}}$  for the LCO, LFP, NCA, and NMC cells are 12.7%–14.9%, 8.9%–10.2%, 7.6%–11.0%, and 10.0%–15.1%, respectively, which indicates that the order of  $c_{\text{O}_2, \text{ignition}}$  from high to low is LCO > NMC > LFP > NCA.
- (3) When there is a forced ignition source, CEGs are prone to ignite regardless of the CEG temperature, and the substances with low  $T_{\text{flash}}$  play a leading role in the ignition process. When there are no forced ignition sources, CEGs are prone to autoignite at  $T_{\text{eruption}}$ , and the substances with low  $T_{\text{autoignition}}$  play a leading role in the ignition process. When the CEG temperature is cooled below  $T_{\text{auto-ignition}}$  ( $\sim 260^\circ\text{C}$ ) of the CEG components, autoignition does not occur. The CEG ignition mode can be controlled by changing the CEG temperature and ignition sources.

### Limitations of the study

The release process of cell gas is a dynamic process, which is not considered in this study. In further research, the dynamic process of the cell fire boundary can be analyzed by computational fluid dynamics.

### Resource availability

#### Lead contact

Further information and requests should be directed to and will be fulfilled by the lead contact, Zhenhai Gao ([gaozh@jlu.edu.cn](mailto:gaozh@jlu.edu.cn)).

#### Materials availability

This study did not generate any new materials.

### Data and code availability

Any data utilized in this study can be found in the main manuscript and supplemental information.

## METHODS

All methods can be found in the accompanying [transparent methods supplemental file](#).

## SUPPLEMENTAL INFORMATION

Supplemental information can be found online at <https://doi.org/10.1016/j.isci.2021.102401>.

## ACKNOWLEDGMENTS

This research was supported by the Ministry of Science and Technology of the People's Republic of China under the grant no. 2019YFE0100200, the Major Science and Technology Projects in Jilin Province under the grant no. 20200501012GX, the National Natural Science Foundation of China (52003012), and the China Postdoctoral Science Foundation (2019M660401).

## AUTHOR CONTRIBUTIONS

Conceptualization, Z.G., Y.C., M.O., and W.L.; writing – original draft, W.L., S.R., and Y.X.; writing – review & editing, W.L., S.R., Y.X., Z.G., Y.C., H.W., and M.O.; supervision, Z.G., Y.C., and M.O.; All authors discussed the results and contributed to the manuscript.

## DECLARATION OF INTERESTS

The authors declare no competing interests.

Received: February 10, 2021

Revised: March 17, 2021

Accepted: April 5, 2021

Published: May 21, 2021

## REFERENCES

- Agubra, V.A., and Fergus, J.W. (2014). The formation and stability of the solid electrolyte interface on the graphite anode. *J. Power Sources* 268, 153–162, <https://doi.org/10.1016/j.jpowsour.2014.06.024>.
- Andersson, A.M., and Edström, K. (2001). Chemical composition and morphology of the elevated temperature SEI on graphite. *J. Electrochem. Soc.* 148, A1100–A1109, <https://doi.org/10.1149/1.1397771>.
- Aurbach, D., Markovsky, B., Weissman, I., Levi, E., and Ein-Eli, Y. (1999). On the correlation between surface chemistry and performance of graphite negative electrodes for Li ion batteries. *Electrochim. Acta* 45, 67–86, [https://doi.org/10.1016/S0013-4686\(99\)00194-2](https://doi.org/10.1016/S0013-4686(99)00194-2).
- Aurbach, D., Zaban, A., Ein-Eli, Y., Weissman, I., Chusid, O., Markovsky, B., Levi, M., Levi, E., Schechter, A., and Granot, E. (1997). Recent studies on the correlation between surface chemistry, morphology, three-dimensional structures and performance of Li and Li-C intercalation anodes in several important electrolyte systems. *J. Power Sources* 68, 91–98, [https://doi.org/10.1016/S0378-7753\(97\)02575-5](https://doi.org/10.1016/S0378-7753(97)02575-5).
- Baird, A.R., Archibald, E.J., Marr, K.C., and Ezekoye, O.A. (2020). Explosion hazards from lithium-ion battery eruption gas. *J. Power Sources* 446, 227257, <https://doi.org/10.1016/j.jpowsour.2019.227257>.
- Bi, M., Ren, J., and Gao, W. (2015). *Fire Safety Engineering* (Chemical Industry Press).
- Biensan, P., Simon, B., Peres, J., Guibert, A.D., Broussely, M., Bodet, J., and Perton, F. (1999). On safety of lithium-ion cells. *J. Power Sources* 81, 906–912, [https://doi.org/10.1016/S0378-7753\(99\)00135-4](https://doi.org/10.1016/S0378-7753(99)00135-4).
- Campion, C.L., Li, W., Euler, W.B., Lucht, B.L., Ravdel, B., DiCarlo, J.F., Gitzendanner, R., and Abraham, K.M. (2004). Suppression of toxic compounds produced in the decomposition of lithium-ion battery electrolytes. *Electrochem. Solid State Lett.* 7, A194–A197, <https://doi.org/10.1149/1.1738551>.
- Chen, M., Liu, J., He, Y., Yuen, R., and Wang, J. (2017). Study of the fire hazards of lithium-ion batteries at different pressures. *Appl. Therm. Eng.* 125, 1061–1074, <https://doi.org/10.1016/j.applthermaleng.2017.06.131>.
- Chen, S., Wang, Z., Wang, J., Tong, X., and Yan, W. (2020). Lower explosion limit of the vented gases from Li-ion batteries thermal runaway in high temperature condition. *J. Loss Prev. Proc.* 63, 103992, <https://doi.org/10.1016/j.jlp.2019.103992>.
- Dahn, J.R., Fuller, E.W., Obrovac, M., and Sacken, U. (1994). Thermal stability of  $\text{Li}_x\text{CoO}_2$ ,  $\text{Li}_x\text{NiO}_2$  and  $\lambda\text{-MnO}_2$  and consequences for the safety of Li-ion cells. *Solid State Ion* 69, 265–270, [https://doi.org/10.1016/0167-2738\(94\)90415-4](https://doi.org/10.1016/0167-2738(94)90415-4).
- Dong, H., Zhang, S., Li, Y., Xian, X., Yi, C., Liu, L., Yu, D., Han, G., and Sheng, Y. (2019). Thermal runaway fire characteristics of lithium-ion batteries with high specific energy NCM811. *Energy Storage Sci. Technol.* 8, 65–70, <https://doi.org/10.19799/j.cnki.2095-4239.2019.0052>.
- EIA (2020). Global EV Outlook 2020. <https://www.iea.org/reports/global-ev-outlook-2020>.
- Essl, C., Golubkov, A.W., Gasser, E., Nachtnebel, M., Zankel, A., Ewert, E., and Fuchs, A. (2020). Comprehensive hazard analysis of failing automotive lithium-ion batteries in overtemperature experiments. *Batteries* 6, 30, <https://doi.org/10.3390/batteries6020030>.
- Fairweather, M., Hargrave, G.K., Ibrahim, S.S., and Walker, D.G. (1999). Studies of premixed flame propagation in explosion tubes. *Combust. Flame* 116, 504–518, [https://doi.org/10.1016/S0010-2180\(98\)00055-8](https://doi.org/10.1016/S0010-2180(98)00055-8).
- Finegan, D.P., Scheel, M., Robinson, J.B., Tjaden, B., Hunt, I., Mason, T.J., Millichamp, J., Michiel, M.D., Offer, G.J., Hinds, G., et al. (2015). In-operando high-speed tomography of lithium-ion batteries during thermal runaway. *Nat. Commun.* 6, 6924, <https://doi.org/10.1038/ncomms7924>.
- Fleischhammer, M., and Döring, H. (2013). Chemische Sicherheit. In *Handbuch Lithium-Ionen-Batterien*, R. Korthauer, ed. (Springer Vieweg), pp. 285–298, [https://doi.org/10.1007/978-3-642-30653-2\\_23](https://doi.org/10.1007/978-3-642-30653-2_23).
- Gachot, G., Grugeon, S., Eshetu, G.G., Mathiron, D., Ribière, P., Armand, M., and Laruelle, S. (2012). Thermal behaviour of the lithiated-graphite/electrolyte interface through GC/MS analysis. *Electrochim. Acta* 83, 402–409, <https://doi.org/10.1016/j.electacta.2012.08.016>.
- Gachot, G., Ribiere, P., Mathiron, D., Grugeon, S., Armand, M., Leriche, J.B., Pilard, S., and Laruelle, S. (2010). Gas chromatography/mass spectrometry as a suitable tool for the Li-ion battery electrolyte degradation mechanisms study. *Anal. Chem.* 83, 478–485, <https://doi.org/10.1021/ac101948u>.
- Garche, J., and Brandt, K. (2018). Electrochemical power sources: fundamentals, systems, and applications. Elsevier. <https://doi.org/10.1016/C2015-0-00574-3>.
- Gnanaraj, J.S., Zinigrad, E., Asraf, L., Gottlieb, H.E., Sprecher, M., Schmidt, M., Geissler, W., and Aurbach, D. (2003). A detailed investigation of the thermal reactions of  $\text{LiPF}_6$  solution in organic carbonates using ARC and DSC. *J. Electrochem. Soc.* 150, A1533–A1537, <https://doi.org/10.1149/1.1617301>.
- Golubkov, A.W., Fuchs, D., Wagner, J., Wiltsche, H., Stangl, C., Fauler, G., Voitic, G., Thaler, A., and Hackere, V. (2014). Thermal-runaway experiments on consumer Li-ion batteries with metal-oxide and olivin-type Cathodes. *RSC Adv.* 4, 3633–3642, <https://doi.org/10.1039/C3RA45748F>.
- Golubkov, A.W., Scheikl, S., Planteu, R., Voitic, G., Wiltsche, H., Stangl, C., Fauler, G., Thaler, A., and Hacker, V. (2015). Thermal runaway of commercial 18650 Li-ion batteries with LFP and NCA cathodes - impact of state of charge and overcharge. *RSC Adv.* 5, 57171–57186, <https://doi.org/10.1039/c5ra05897j>.
- Gourley, S.W., Or, T., and Chen, Z. (2020). Breaking free from cobalt reliance in lithium-ion batteries. *iScience* 23, 101505, <https://doi.org/10.1016/j.isci.2020.101505>.
- Guo, C., and Zhang, Q. (2016). Determination on explosion limit of venting gas released by lithium-ion battery and its risk analysis. *J. Saf. Sci. Technol.* 12, 46–49, <https://doi.org/10.11731/j.issn.1673-193x.2016.09.008>.
- Han, X., Lu, L., Zheng, Y., Feng, X., Li, Z., and Li, J. (2019). Ouyang, M. A review on the key issues of the LIB degradation among the whole life cycle. *eTransportation* 1, 100005, <https://doi.org/10.1016/j.etrans.2019.100005>.
- Huang, Y., Lin, Y.C., Jenkins, D.M., Chernova, N.A., Chung, Y., Radhakrishnan, B., Chu, L., Fang, J., Wang, Q., Omenya, F., et al. (2016). Thermal stability and reactivity of cathode materials for Li-ion batteries. *ACS Appl. Mater. Interfaces* 8, 7013–7021, <https://doi.org/10.1021/acsami.5b12081>.
- Joachim, H., Kaun, T.D., Zaghib, K., and Prakash, J. (2009). Electrochemical and thermal studies of carbon-coated  $\text{LiFePO}_4$  cathode. *J. Electrochem. Soc.* 156, A401–A406, <https://doi.org/10.1149/1.3106121>.
- Kawamura, T., Okada, S., and Yamaki, J.I. (2006). Decomposition reaction of  $\text{LiPF}_6$ -based electrolytes for lithium-ion cells. *J. Power Sources* 156, 547–554, <https://doi.org/10.1016/j.jpowsour.2005.05.084>.
- Kocha, S., Fill, A., and Birke, K.P. (2018). Comprehensive gas analysis on large scale automotive lithium-ion cells in thermal runaway. *J. Power Sources* 398, 106–112, <https://doi.org/10.1016/j.jpowsour.2018.07.051>.
- Lammer, M., Königseder, A., and Hacker, V. (2017). Holistic methodology for characterization of the thermally induced failure of commercially available 18650 lithium-ion cells. *RSC Adv.* 7, 24425–24429, <https://doi.org/10.1039/C7RA02635H>.
- Li, J., Zhang, Z., Guo, X., and Yang, Y. (2006). The studies on structural and thermal properties of delithiated  $\text{Li}_x\text{Ni}_{1/3}\text{Co}_{1/3}\text{Mn}_{1/3}\text{O}_2$  ( $0 < x \leq 1$ ) as a cathode material on lithium-ion batteries. *Solid State Ion* 177, 1509–1516, <https://doi.org/10.1016/j.ssi.2006.03.055>.
- Li, W., Wang, H., Ouyang, M., Xu, C., Lu, L., and Feng, X. (2019a). Theoretical and experimental analysis of the lithium-ion battery thermal runaway process based on the internal combustion engine combustion theory. *Energ. Convers. Manage.* 185, 211–222, <https://doi.org/10.1016/j.enconman.2019.02.008>.
- Li, W., Wang, H., Zhang, Y., and Ouyang, M. (2019b). Flammability characteristics of the battery vent gas: a case of NCA and LFP lithium-ion batteries during external heating abuse. *J. Energy Storage* 24, 100775, <https://doi.org/10.1016/j.est.2019.100775>.
- Liu, B., Tan, Y., and Fu, Z. (2004). The determination of minimum oxygen density of combustible gases (Vapors). *J. Shijiazhuang Inst. Railway Eng.* 3, 35–38.
- Liu, K., Kong, B., Liu, W., Sun, Y., Song, M., Chen, J., Liu, Y., Lin, D., Pei, A., and Cui, Y. (2018). Stretchable lithium metal anode with improved mechanical and electrochemical cycling stability.

- Joule 2, 1857–1865, <https://doi.org/10.1016/j.joule.2018.06.003>.
- Long, B., Xu, R., and Liu, Y. (2014). Gas-flammability testing for Li-ion cells during abusing. *Battery 44*, 121–123.
- Maleki, H., Deng, G., Anani, A., and Howard, J. (1999). Thermal stability studies of Li-ion cells and components. *J. Electrochem. Soc.* 146 (9), 3224–3229, <https://doi.org/10.1149/1.1392458>.
- Mao, B., Chen, H., Cui, Z., Wu, T., and Wang, Q. (2018). Failure mechanism of the lithium-ion battery during nail penetration. *Int. J. Heat Mass Transf.* 122, 1103–1115, <https://doi.org/10.1016/j.ijheatmasstransfer.2018.02.036>.
- Martha, S.K., Haik, O., Zinigrad, E., Exnar, I., Drezek, T., Miners, J.H., and Aurbach, D. (2011). On the thermal stability of olivine cathode materials for lithium-ion batteries. *J. Electrochem. Soc.* 158, A1115–A1122, <https://doi.org/10.1149/1.3622849>.
- Mikolajczak, C., Kahn, M., White, K., and Long, R.T. (2011). *Lithium-ion Batteries Hazard and Use Assessment* (Springer).
- Onuki, M., Kinoshita, S., Sakata, Y., Yanagidate, M., Otake, Y., Ue, M., and Deguchi, M. (2008). Identification of the source of evolved gas in li-ion batteries using <sup>13</sup>C-labeled solvents. *J. Electrochem. Soc.* 155, A794–A797, <https://doi.org/10.1149/1.2969947>.
- Orendorff, C.J. (2012). The role of separators in lithium-ion cell safety. *Electrochem. Soc. Interfaces* 21, 61–65, <https://doi.org/10.1149/2.f07122if>.
- Park, H., Wright, Y., Seddik, O., Srna, A., Kyrtatos, P., and Boulouchos, K. (2021). Phenomenological micro-pilot ignition model for medium-speed dual-fuel engines. *Fuel* 285, 118955, <https://doi.org/10.1016/j.fuel.2020.118955>.
- Pasquier, A.D., Disma, F., Bowmer, T., Gozdz, A., Amatucci, G., and Tarascon, J.M. (1998). Differential scanning calorimetry study of the reactivity of carbon anodes in plastic li-ion batteries. *J. Electrochem. Soc.* 145, 472–477, <https://doi.org/10.1149/1.1838287>.
- Pfrang, A., Kriston, A., Rulz, V., Lebedeva, N., and Perslo, F. (2017). Safety of rechargeable energy storage systems with a focus on Li-ion technology. In *Emerging Nanotechnologies in Rechargeable Energy Storage Systems*, L.M. Rodriguez-Martinez, ed. (Elsevier), pp. 253–290, <https://doi.org/10.1016/B978-0-323-42977-1.00008-X>.
- Ravdel, B., Abraham, K.M., Gitzendanner, R., DiCarlo, J., Lucht, B., and Campion, C. (2003). Thermal stability of lithium-ion battery electrolytes. *J. Power Sources* 119–121, 805–810, [https://doi.org/10.1016/S0378-7753\(03\)00257-X](https://doi.org/10.1016/S0378-7753(03)00257-X).
- Ribiere, P., Grugeon, S., Morcrette, M., Boyanov, S., Laruelle, S., and Marlair, G. (2012). Investigation on the fire-induced hazards of Li-ion battery cells by fire calorimetry. *Energy Environ. Sci.* 5, 5271–5280, <https://doi.org/10.1039/C1EE02218K>.
- Richard, M.N., and Dahn, J.R. (1999). Accelerating rate calorimetry study on the thermal stability of lithium intercalated graphite in electrolyte I. experimental. *J. Electrochem. Soc.* 146, 2068–2077, [https://doi.org/10.1016/S0140-6701\(00\)96499-3](https://doi.org/10.1016/S0140-6701(00)96499-3).
- Rosha, P., Dhir, A., and Mohapatra, S. (2018). Influence of gaseous fuel induction on the various engine characteristics of a dual fuel compression ignition engine: a review. *Renew. Sust. Energ. Rev.* 82, 3333–3349, <https://doi.org/10.1016/j.rser.2017.10.055>.
- Roth, E., and Orendorff, C. (2012). How electrolytes influence battery safety. *Electrochem. Soc. Interfaces* 21 (2), 45–49, <https://doi.org/10.1149/2.F04122if>.
- Shin, J.S., Han, C.H., Jung, U.H., Lee, S.I., Kim, H.J., and Kim, K. (2002). Effect of Li<sub>2</sub>CO<sub>3</sub> additive on gas generation in lithium-ion batteries. *J. Power Sources* 109, 47–52, [https://doi.org/10.1016/S0378-7753\(02\)00039-3](https://doi.org/10.1016/S0378-7753(02)00039-3).
- Somandepalli, V., Marr, K., and Horn, Q. (2014). Quantification of combustion hazards of thermal runaway failures in lithium-ion batteries. *SAE Int. J. Alt. Power* 3, 98–104, <https://doi.org/10.4271/2014-01-1857>.
- Spotnitz, R., and Franklin, J. (2003). Abuse behavior of high-power lithium-ion cells. *J. Power Sources* 113 (1), 81–100, [https://doi.org/10.1016/S0378-7753\(02\)00488-3](https://doi.org/10.1016/S0378-7753(02)00488-3).
- Stephan, A., Anadon, L.D., and Hoffmann, V.H. (2021). How has external knowledge contributed to lithium-ion batteries for the energy transition? *iScience* 24, 101995, <https://doi.org/10.1016/j.isci.2020.101995>.
- Sun, P., Huang, X., Bisschop, R., and Niu, H. (2020). A review of battery fires in electric vehicles. *Fire Technol.* 56, 1361–1410, <https://doi.org/10.1007/s10694-020-00958-2>.
- Turns, S., and Haworth, D.C. (2021). *An Introduction to Combustion: Concepts and Applications* (Mc Graw Hill).
- Wang, H., Zhang, Y., Li, C., Li, W., and Ouyang, M. (2019a). Venting process of lithium-ion power battery during thermal runaway under medium state of charge. *Energy. Stor. Sci. Technol.* 8 (6), 1043–1048, <https://doi.org/10.10288/j.issn.2095-4239.2019.0057>.
- Wang, Q., Mao, B., Stolarov, S.I., and Sun, J. (2019b). A review of lithium-ion battery failure mechanisms and fire prevention strategies. *Prog. Energ. Combust.* 73, 95–131, <https://doi.org/10.1016/j.pecs.2019.03.002>.
- Wang, Q., Ping, P., Zhao, X., Chu, G., Sun, J., and Chen, C. (2012). Thermal runaway caused fire and explosion of lithium-ion battery. *J. Power Sources* 208, 210–222, <https://doi.org/10.1016/j.jpowsour.2012.02.038>.
- Wang, Q., Sun, J., and Chen, C. (2007a). Thermal stability of delithiated LiMn<sub>2</sub>O<sub>4</sub> with electrolyte for lithium-ion batteries. *J. Electrochem. Soc.* 154, A263–A267, <https://doi.org/10.1149/1.2433698>.
- Wang, Y., Jiang, J., and Dahn, J. (2007b). The reactivity of delithiated Li (Ni<sub>1/3</sub>Co<sub>1/3</sub>Mn<sub>1/3</sub>)O<sub>2</sub>, Li (Ni<sub>0.8</sub>Co<sub>0.15</sub>Al<sub>0.05</sub>)O<sub>2</sub> or LiCoO<sub>2</sub> with non-aqueous electrolyte. *Electrochem. Commun.* 9, 2534–2540, <https://doi.org/10.1016/j.elecom.2007.07.033>.
- Wang, Q., Sun, J., Yao, X., and Chen, C. (2005). Thermal stability of LiPF<sub>6</sub>/EC+DEC electrolyte with charged electrodes for lithium-ion batteries. *Thermochim. Acta* 437, 12–16, <https://doi.org/10.1016/j.tca.2005.06.010>.
- Wang, Q., Sun, J., Yao, X., and Chen, C. (2006). Thermal behavior of lithiated graphite with electrolyte in lithium-ion batteries. *J. Electrochem. Soc.* 153, A329–A333, <https://doi.org/10.1149/1.2139955>.
- Watanabe, I., and Yamaki, J. (2006). Thermal gravimetry-mass spectrometry studies on the thermal stability of graphite anodes with electrolyte in lithium-ion battery. *J. Power Sources* 153, 402–404, <https://doi.org/10.1016/j.jpowsour.2005.05.027>.
- Xie, S., Sun, J., Chen, X., and He, Y. (2020). Thermal runaway behavior of lithium-ion batteries in different charging states under low pressure. *Int. J. Energy Res.* 1–11, <https://doi.org/10.1002/er.6200>.
- Xu, T., and Hui, S. (2017). *Combustion Science* (China machine press).
- Yang, H., Bang, H., Amine, K., and Prakash, J. (2005). Investigations of the exothermic reactions of natural graphite anode for li-ion batteries during thermal runaway. *J. Electrochem. Soc.* 152, A73–A79, <https://doi.org/10.1149/1.1836126>.
- Yoshida, H., Fukunaga, T., Hazama, T., Terasaki, M., Mizutani, M., and Yamachi, M. (1997). Degradation mechanism of alkyl carbonate solvents used in lithium-ion cells during initial charging. *J. Power Sources* 68, 311–315, [https://doi.org/10.1016/S0378-7753\(97\)02635-9](https://doi.org/10.1016/S0378-7753(97)02635-9).
- Zhang, Y., Wang, H., Li, W., and Li, C. (2019). Quantitative identification of emissions from abused prismatic Ni-rich lithium-ion batteries. *eTransportation* 2, 100031, <https://doi.org/10.1016/j.etrans.2019.100031>.
- Zhang, Y., Wang, H., Li, W., Li, C., and Ouyang, M. (2019). Size distribution and elemental component of vent particles from abused prismatic Ni-rich automotive lithium-ion batteries. *J. Energy Storage* 26, 100991, <https://doi.org/10.1016/j.est.2019.100991>.
- Zhang, Y., Wang, H., Li, W., Li, C., and Ouyang, M. (2020). Quantitative analysis of eruption process of abused prismatic Ni-rich automotive batteries based on in-chamber pressure. *J. Energy Storage* 31, 101617, <https://doi.org/10.1016/j.est.2020.101617>.
- Zhang, Z., Fouchard, D., and Rea, J. (1998). Differential scanning calorimetry material studies: implications for the safety of lithium-ion cells. *J. Power Sources* 70, 16–20, [https://doi.org/10.1016/S0140-6701\(98\)93827-9](https://doi.org/10.1016/S0140-6701(98)93827-9).
- Zhou, M., Zhao, L., Okada, S., and Yamaki, J. (2012). Quantitative studies on the influence of LiPF<sub>6</sub> on the thermal stability of graphite with electrolyte. *J. Electrochem. Soc.* 159, 44, <https://doi.org/10.1149/2.066201jes>.

**iScience, Volume 24**

**Supplemental information**

**Fire boundaries of lithium-ion cell  
eruption gases caused by thermal runaway**

**Weifeng Li, Shun Rao, Yang Xiao, Zhenhai Gao, Yupeng Chen, Hewu Wang, and Minggao Ouyang**

## Transparent Methods

### Calculation model of minimum CEG concentration required for ignition

The minimum CEG concentration required for ignition refers to the LFL of CEGs. When the CEG concentration is lower than a certain value, it is too lean to ignite. The calculation of  $c_{\text{CEG,ignition}}$ , i.e., LFL, is based on Le Chatelier's mixing rule (Chatelier, 1891; Mashuga et al, 2000), as shown in Equation 1.

$$c_{\text{CEG,ignition}} = \text{LFL} = \frac{1}{\sum_{i=1}^n \frac{x_i}{\text{LFL}_i}} \times 100\% \quad (\text{Equation 1})$$

where  $\text{LFL}_i$  refers to the LFL of component  $i$  in CEG, and  $x_i$  refers to the volume percentage of component  $i$  in CEG.

During the calculation, the inert gas in CEG is considered to get a more accurate value of the flammability limit (Li, 1998; Tian et al., 2006; Wu et al., 1994)

### Calculation model of minimum oxygen concentration required for ignition

The minimum  $\text{O}_2$  concentration required for ignition refers to the oxygen concentration in the CEG-air mixture at the UFL (i.e., the CEG concentration in the mixture), as shown in Equation 2. When the oxygen concentration is lower than this value, the oxygen is too lean to support ignition. UFL has a similar calculation method to that of LFL, as shown in Equation 2.

$$c_{\text{O}_2,\text{ignition}} = (1 - \text{UFL}) * c_{\text{O}_2 \text{ in air}} = \left(1 - \frac{1}{\sum_{i=1}^n \frac{x_i}{\text{UFL}_i}} \times 100\%\right) * c_{\text{O}_2 \text{ in air}} \quad (\text{Equation 2})$$

where  $c_{\text{O}_2 \text{ in air}}$  refers to the  $\text{O}_2$  volume percentage in air,  $\text{UFL}_i$  refers to the UFL of component  $i$  in CEG, and  $x_i$  refers to the volume percentage of component  $i$  in CEG.

### Supplemental References

Chatelier, L. (1891). Estimation of Firedamp by Flammability Limits (Annals of mines).

Li, D. (1988). Calculation of explosive concentration limit of flammable gas. Chem. Des. Commun. 14, 63-65.

Mashuga, C.V., and Crowl, D.A. (2000). Derivation of Le Chatelier's mixing rule for flammable limits. Process Saf. Prog. 19, 112–117.

Tian, G., Yu, C., and Li, X. Study on calculation on method of gas explosion limits, Gas Heat 26 (2006) 29-33.

Wu, J., Kong, Q., and Wang, B. (1994). Theoretical calculation method for the explosion limit of mixed gas. Oil Gas Storage Trans.13, 10-12.



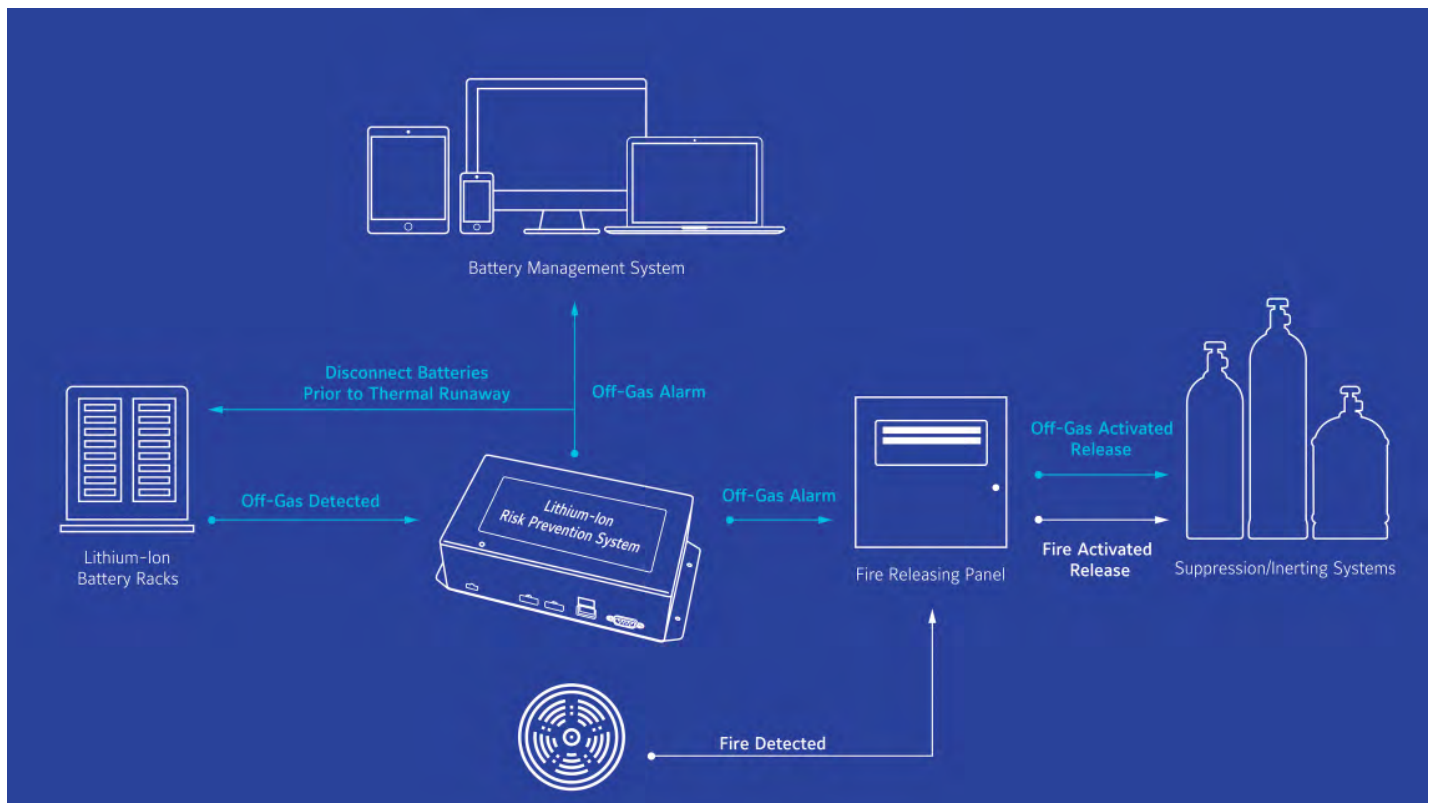
Global news, analysis and opinion on energy storage innovation and technologies



- News
- Residential
- Commercial
- Grid Scale
- Off Grid
- Market Watch
- Resources
- Events ▾
- Jobs
- More ▾



# Preventing thermal runaway in lithium-ion energy storage systems



COMMERCIAL  
GRID SCALE  
OFF GRID  
RESIDENTIAL  
TECHNOLOGY

**Published:** 10 May 2021, 09:43

**By:**



**Alan Elder**

Fellow, Industry Relations



**Derek Sandahl**

Global product manager

*Safely managing the use of lithium-ion batteries in energy storage systems (ESS) should be priority number one for the industry. In this exclusive Guest Blog, Johnson Controls' industry relations fellow Alan Elder, with over four decades of experience in*

*the field of gaseous fire suppression systems and Derek Sandahl, product manager for the company's engineered fire suppression products, talk about the best ways to prevent fire incidents stemming from thermal runaway in lithium cells.*

Countries around the world have set ambitious goals to reduce global emissions. The resulting investments made in renewable energy sources are driving rapid growth in the Energy Storage System (ESS) industry. In fact, the global energy storage market is expected to grow at 35% compound annual growth rate between 2018 and 2026.

Right now, lithium-ion batteries are the world's primary energy storage medium. Based on their current popularity, this market is expected to reach US\$23 billion by 2026. Wind farms, solar farms and data centres choose lithium-ion battery energy storage for many reasons, including their affordability. For one, lithium-ion batteries have a high energy density, with potential for even higher capacities. They also have relatively low self-discharge, with less than half that of nickel-based batteries. Their cost-effectiveness extends to maintenance, too. Lithium-ion batteries require little maintenance and no periodic discharge.

With all their benefits, lithium-ion batteries also have some limitations. Lithium-ion batteries require complex battery management systems (BMS) to ensure they operate within controlled parameters, such as voltages, temperature and charge states, which adjust as the battery cells age. If not managed properly, or the battery suffers from other forms of abuse, it could lead to the risk of battery failure, increasing the risk of thermal runaway and fire.

Industries that depend on lithium-ion batteries need a new, comprehensive solution that effectively detects battery failure and intervenes to help prevent thermal runaway and the fire dangers that follow.

## **The dangers of thermal runaway**

Thermal runaway may occur if a battery suffers abuse, resulting in the release of toxic and flammable gases. Thermal runaway occurring in a single battery cell can quickly

spread, causing a cascading of thermal runaway in adjacent battery cells. Thermal runaway could culminate in a catastrophic high heat release fire event.

Lithium-ion battery fires are notoriously challenging to fight. Gaseous suppression and water systems simply are not effective. While fire suppression systems can slow fire growth and heat release, they are not sufficient to provide complete extinguishment once thermal runaway has started. The most effective method of extinguishing these types of fires requires large amounts of water applied for many hours or even days. In many locations, especially those that are remote or where water is scarce, this is not desirable or even achievable.

Unfortunately, there have been a number of these fire events in the last few years. In November of 2017, a fire at a Belgium grid-connected lithium-ion battery energy storage site near Brussels resulted in a cloud of toxic fumes that forced thousands of residents to stay at home. In April of 2019, a lithium-ion battery system exploded at an Arizona Public Service site, severely injuring eight firefighters. Following the catastrophe, U.S. energy utilities made safety a key focus. And between 2017 and 2019, there were 28 ESS fires in Korea, resulting in the suspension of 522 ESS facilities.

## **Understanding the stages of battery failure helps reveal a solution**

In order to prevent incidents like these from happening again, it's critical to understand each stage of battery failure. Divided into prevention and containment regions, there are four stages:

### **Prevention Region**

#### **Stage 1: Battery Abuse**

During this first stage, thermal, electrical or mechanical abuse results in cell damage, causing battery cell temperatures and pressures to increase.

## **Stage 2: Off-Gas Generation**

As cell temperatures and pressures rise, flammable gases vent from the cells. This is the critical point at which action must be taken to avoid thermal runaway and a fire event.

## **Stage 3: Thermal Runaway**

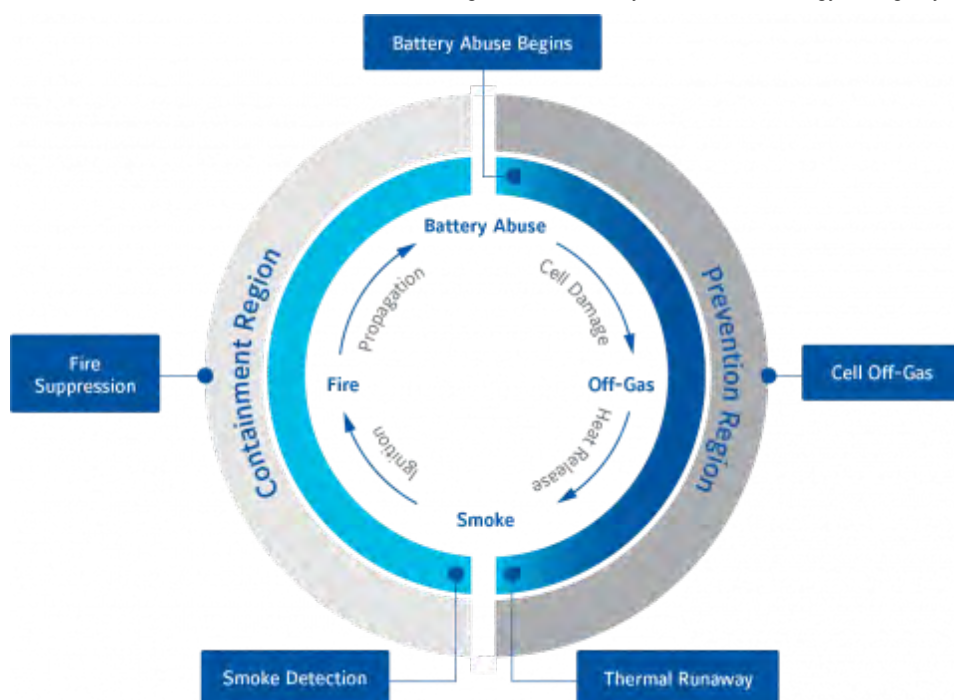
Thermal runaway marks the very end of the prevention region and the start of the containment region. Temperatures rapidly rise several hundred degrees and smoke is produced. It is at this point that catastrophic failure is imminent.

## **Containment Region**

## **Stage 4: Fire Generation**

After thermal runaway, fire ignites. While lithium-ion battery racks are structured to maximise energy storage density, this also allows for fast fire spread. Once ignited, fire can easily move to adjacent cells and construction materials and become uncontrollable.

Taking a closer look at these four stages reveals the ideal moment when early intervention can prevent thermal runaway. Reaction should ideally occur in the prevention region, but this requires a means of detection in stages one or two. If off-gases can be detected and batteries shut down before thermal runaway can begin, it is possible that fire danger can be averted.



## Early intervention prevents thermal runaway

As analysing the four stages of lithium-ion battery failure shows, one of the best early warning signs to detect is the release of off-gases. By definition, an off-gas is the by-product of a chemical process. When lithium-ion batteries begin to fail, the chemical process produces electrolyte vapour from battery cells. This off-gas is produced soon after cell damage occurs and several minutes before thermal runaway starts.

Lithium-ion battery failure eventually produces detectable smoke, too, but only after thermal runaway has already begun. Detecting smoke alone results in a response that is too late. Instead, by detecting the presence of off-gases, affected batteries can be shut down in time to prevent thermal runaway.

## An integrated solution makes early intervention possible

An effective lithium-ion risk-prevention solution features monitoring and reference sensors that continuously check battery racks for the presence of lithium-ion off-gases. Reference sensors provide surrounding ambient air data to a controller, while monitoring sensors within the battery racks capture data relating to the air close to lithium-ion batteries. These sensors can detect lithium-ion off-gases in concentrations

as small as one part per million (ppm) and are compatible with all current lithium-ion chemistries.

This risk prevention system is designed to disconnect batteries and prevent thermal runaway in less than five seconds. However, even after batteries have been shut down, flammable off-gases may still be present. Unless the area is sufficiently large or can be ventilated, these off-gases can still present a fire hazard.

This is where fire detection and suppression come in. If used at inerting concentrations, the fire suppression system can be used to inert the space after off-gases have been released. This can help prevent off-gases from reaching combustion levels in conjunction with oxygen. The point at which an inerting system is released requires careful consideration to be effective and may require integration with other systems.

At regulation design concentrations, the suppression system can be used to help protect batteries from fire sources, such as Class A materials, and other electronic component failures before they become sources of heat that could ignite batteries.

Integrating off-gas detection with fire detection and suppression provides the early intervention required to help keep thermal runaway and fire danger at bay. The system does not require electrical or mechanical contact with battery cells and is essentially an upgrade for existing systems, allowing it to perform in live, working environments.

The number of energy storage systems with lithium-ion batteries is projected to significantly increase over the next five years. Because lithium-ion cells can fail and explode — and often with little warning — it is more critical than ever to detect and prevent thermal runaway before the worst can happen. Combining early off-gas detection with fire detection and suppression or inerting systems provides a holistic solution that delivers the early warning needed to help keep the ESS industry operating safely and sustainably.

*Images: Johnson Controls.*

Stay up to date with the latest news, analysis and opinions. [Sign up here](#) to the Energy-Storage.news Newsletter.

---

UK 'energy storage infrastructure specialist' Flexion gets US\$206m investment

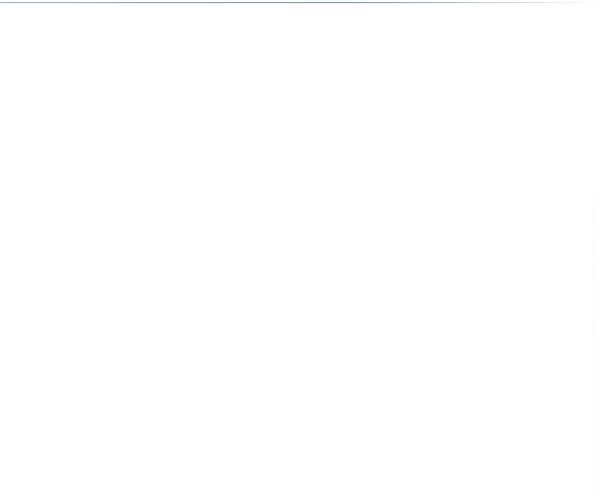
---

Koch Industries subsidiary invests US\$100m in zinc battery energy storage company Eos

---

Startup Nostromo targets commercial cooling and air conditioning's heavy burden on electricity grids

---



---

Large-scale and virtual power plant solar-plus-storage projects make progress in Oahu, Hawaii

---

'Industry should propose solutions' to break down barriers for energy storage in Southeast Asia

---

ROUNDUP: Investors acquire US developers Cypress Creek, Clēnera and Dimension Renewable Energy

---

**Want to receive the latest news straight to your inbox?**

**SIGN UP TO OUR NEWSLETTER**

South Australia: Maoneng, SAPGen seek approval for 465MW of large-scale battery storage

---

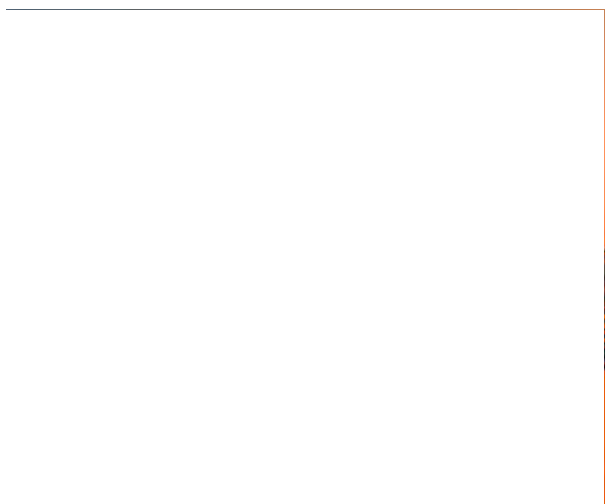
GUEST BLOG

Beyond weatherisation: Energy storage can give ERCOT the flexibility & resilience its networks need

---

DNV opening Battery Safety Lab in Netherlands

---



Australian transmission operator's commercial arm to tender for 300MW unsubsidised battery project

---

Engie Chile wins 1.5GW of hybrid wind-solar-storage development rights

---

SK Innovation forms North America battery supply partnership with ESS provider IHI Terrasun

---

Queensland commits to 'major overhaul' to refurbish state's only pumped hydro plant

---

UK ESS investor Gresham House acquires 425MW of projects, plans US\$140 million share offer

---

Vanadium flow battery player VRB gets US\$24m investment from Thai renewables company BCPG

---

Amazon invests in ESS battery analytics startup ION Energy

---

Stem Inc dispatched over 500MWh energy during North American heat waves in June

---

VIDEO: A new approach to shorten installation and simplify the logistics of energy storage projects

---

Leyline JV provides financing support for 400MW / 1,400MWh of Virginia and Texas battery projects

---

Pumped hydro plant operator applies for 600MW expansion project in Scotland

Facebook told to rewrite energy storage contracts for New Mexico data centre

Engie, Canadian Solar among bidders in Colombia's first-ever battery storage tender

Microsoft, NYPA in group urging Congress to spend US\$50 billion to modernise US electricity sector

Large-scale battery storage plant chosen by California community as alternative to gas goes online

India state-owned power producer NTPC wants to install 1GWh of energy storage at power plants

Battery installation begins at world's biggest solar-plus-storage project - so far

ROUNDUP: Africa solar-plus-storage projects from Jinko, DHYBRID, JIRAMA

California takes 'major step to carbon neutrality' with 11.5GW clean energy procurement

#### ANALYSIS

Hybrid renewables: Why 'better for the planet' doesn't have to mean 'bad for business'

#### ANALYSIS

Vanadium flow batteries for a zero-emissions energy system



### More articles in:

FIRE DETECTION

GAS DETECTION

FIRE SUPPRESSION

THERMAL RUNAWAY

ENERGY DENSITY

LITHIUM-ION

EXPLOSION

SAFETY

BANKABILITY

OFF-GAS

ELECTROLYTE

BATTERY MANAGEMENT SYSTEM

ALSO ON ENERGY STORAGE NEWS

**SolarEdge customers to get Tesla ...**

6 years ago · 1 comment

The vice-president for marketing and product strategy at one of only ...

**Lux: Lithium-ion rules for now but wise ...**

6 years ago · 1 comment

While lithium-ion is expected to hold its leading position as the battery chemistry ...

**SolarCity starts taking Powerwall orders in ...**

6 years ago · 1 comment

The go-to resource for in-depth news, analysis, blogs and more on the ...

**GTM: Aust residential**

6 years ago ·

US analysis · Research ha latest comm

0 Comments

Energy Storage News

Disqus' Privacy Policy

Login ▾

Recommend

Tweet

Share

Sort by Best ▾



Start the discussion...

LOG IN WITH

OR SIGN UP WITH DISQUS

Name

Be the first to comment.

Subscribe

Add Disqus to your siteAdd DisqusAdd

Do Not Sell My Data

## Solar Media

[Events](#)

[PV Tech](#)

[Solar Power Portal](#)

[Current News](#)

[Solar Media](#)

## **Social**

[Twitter](#)

[LinkedIn](#)

[YouTube](#)

[Google Plus](#)

[Facebook](#)

## **Energy Storage News**

[Advertising](#)

[Privacy Policy](#)

[Terms of Use](#)

[Cookies](#)

## **Support**

[Contact](#)

*Global news, analysis and opinion on energy storage innovation and technologies*

Copyright 2021 [Solar Media Ltd.](#) All rights reserved.

# Facts About Hydrogen Fluoride (Hydrofluoric Acid)

## Related Pages

Facts about Hydrogen Fluoride (Hydrofluoric Acid)

[Case Definition: Hydrofluoric Acid](#)

[Case Definition: Caustic or Corrosive Agents](#)

## FACT SHEET

### What hydrogen fluoride is

- Hydrogen fluoride is a chemical compound that contains fluorine. It can exist as a colorless gas or as a fuming liquid, or it can be dissolved in water.
- When hydrogen fluoride is dissolved in water, it may be called hydrofluoric acid.
- Hydrogen fluoride can be released when other fluoride-containing compounds such as ammonium fluoride are combined with water.

### Where hydrogen fluoride is found and how it is used

- Hydrogen fluoride is used to make refrigerants, herbicides, pharmaceuticals, high-octane gasoline, aluminum, plastics, electrical components, and fluorescent light bulbs. Sixty percent of the hydrogen fluoride used in manufacturing is for processes to make refrigerants.
- Hydrogen fluoride is also used for etching glass and metal.

### How you could be exposed to hydrogen fluoride

- In a natural disaster, you could be exposed to high levels of hydrogen fluoride when storage facilities or containers are damaged and the chemical is released. This release could occur at an industrial site or even a retail location.
- You could be exposed to hydrogen fluoride if it is used as a chemical terrorism agent.
- If you work in an occupation that uses hydrogen fluoride, you may be exposed to this chemical in the workplace.
- You may be exposed to hydrogen fluoride as part of a hobby.

### How hydrogen fluoride works

- Hydrogen fluoride goes easily and quickly through the skin and into the tissues in the body. There it damages the cells and causes them to not work properly.
- The seriousness of poisoning caused by hydrogen fluoride depends on the amount, route, and length of time of exposure, as well as the age and preexisting medical condition of the person exposed.
- Breathing hydrogen fluoride can damage lung tissue and cause swelling and fluid accumulation in the lungs (pulmonary edema).
- Skin contact with hydrogen fluoride may cause severe burns that develop after several hours and form skin ulcers.

# Immediate signs and symptoms of exposure to hydrogen fluoride

- Swallowing only a small amount of highly concentrated hydrogen fluoride will affect major internal organs and may be fatal.
- Hydrogen fluoride gas, even at low levels, can irritate the eyes, nose, and respiratory tract. Breathing in hydrogen fluoride at high levels or in combination with skin contact can cause death from an irregular heartbeat or from fluid buildup in the lungs.
- Even small splashes of high-concentration hydrogen fluoride products on the skin can be fatal. Skin contact with hydrogen fluoride may not cause immediate pain or visible skin damage (signs of exposure).
- Often, patients exposed to low concentrations of hydrogen fluoride on the skin do not show effects or experience pain immediately. And, severe pain at the exposure site may be the only symptom for several hours. Visible damage may not appear until 12 to 24 hours after the exposure.
- Depending on the concentration of the chemical and the length of time of exposure, skin contact with hydrogen fluoride may cause severe pain at the point of contact; a rash; and deep, slow-healing burns. Severe pain can occur even if no burns can be seen.
- Showing these signs and symptoms does not necessarily mean that a person has been exposed to hydrogen fluoride. Other chemicals also can cause these effects.
- Exposure to hydrogen fluoride can result in severe electrolyte problems.

# Long-term health effects of acute exposure to hydrogen fluoride

- People who survive after being severely injured by breathing in hydrogen fluoride may suffer lingering chronic lung disease.
- Skin damage caused by concentrated hydrogen fluoride may take a long time to heal and may result in severe scarring.
- Fingertip injuries from hydrogen fluoride may result in persistent pain, bone loss, and injury to the nail bed.
- Eye exposure to hydrogen fluoride may cause prolonged or permanent visual defects, blindness, or total destruction of the eye.
- Swallowing hydrogen fluoride can damage the esophagus and stomach. The damage may progress for several weeks, resulting in gradual and lingering narrowing of the esophagus.

# How you can protect yourself, and what to do if you are exposed to hydrogen fluoride

- First, if the hydrogen fluoride was released into the air, get fresh air by leaving the area where the chemical was released.
  - If the hydrogen fluoride release was outside, move away from the area where the chemical was released.
  - If the hydrogen fluoride release occurred indoors, get out of the building.
- If you are near a release of fluorine or hydrogen fluoride, emergency coordinators may tell you either to evacuate the area or “shelter in place” inside a building to avoid being exposed to the chemical. For more information on evacuation during a chemical emergency, see [“Facts About Evacuation.”](#) For more information on sheltering in place during a chemical emergency, see [“Facts About Sheltering in Place.”](#)
- If you think you may have been exposed to hydrogen fluoride, you should remove your clothing, rapidly wash your entire body with water, and get medical care as quickly as possible.
- **Removing your clothing**
  - Quickly take off clothing that may have hydrogen fluoride on it. Any clothing that has to be pulled over the head should be cut off the body.
  - If you are helping other people remove their clothing, try to avoid touching any contaminated areas, and remove the clothing as quickly as possible.
- **Washing yourself**
  - As quickly as possible, wash any hydrogen fluoride from your skin with large amounts of water.

- As quickly as possible, wash any hydrogen fluoride from your skin with large amounts of water.
- If your eyes are burning or your vision is blurred, rinse your eyes with plain water.
- If you wear contacts, remove them after washing your hands and put them with the contaminated clothing. Do not put the contacts back in your eyes (even if they are not disposable contacts). If you wear eyeglasses, wash them with soap and water. You can put your eyeglasses back on after you wash them.
- **Disposing of your clothes**
  - After you have washed yourself, place your clothing inside a plastic bag. Avoid touching contaminated areas of the clothing. If you can't avoid touching contaminated areas, or you aren't sure which areas are contaminated, put the clothing in the bag using tongs, tool handles, sticks, or similar objects. Anything that touches contaminated clothing should also be placed in the bag.
  - Seal the bag, and then seal that bag inside another plastic bag. Disposing of your clothing in this way will help protect you and other people from any chemicals that might be on your clothes.
  - When local or state health department or emergency personnel arrive, tell them what you did with your clothes. The health department or emergency personnel will arrange for further disposal. Do not handle the plastic bags yourself.
- For more information about cleaning your body and disposing of your clothes after a chemical release, see "[Chemical Agents: Facts About Personal Cleaning and Disposal of Contaminated Clothing.](#)"
- If someone has swallowed hydrogen fluoride, **do not** induce vomiting. **Do not** give the person activated charcoal.
- Seek medical attention immediately. Dial 911 and explain what has happened.
- If you are sure the person has swallowed hydrogen fluoride, do not attempt CPR unless you are able to take appropriate measures to protect yourself from exposure to hydrogen fluoride. Performing CPR on someone who has swallowed hydrogen fluoride could expose you to the chemical.

## How hydrogen fluoride poisoning is treated

Exposed people should seek medical treatment as soon as possible. Your doctor may recommend or use products to help neutralize the effects of poisoning. Calcium gluconate (a calcium sugar) containing gels, solutions, and medications are used to treat hydrogen fluoride poisoning.

## How you can get more information about hydrogen fluoride

People can contact one of the following:

- Regional poison control center: 1-800-222-1222
- Centers for Disease Control and Prevention
  - Public Response Hotline (CDC)
    - 800-CDC-INFO
    - 888-232-6348 (TTY)
  - E-mail inquiries: [cdcinfo@cdc.gov](mailto:cdcinfo@cdc.gov)
- Centers for Disease Control and Prevention (CDC), National Institute for Occupational Safety and Health (NIOSH), [Pocket Guide to Chemical Hazards](#)





---

## Tools for Practitioners

---

# Emerging Hazards of Battery Energy Storage System Fires

**Grant Number:** EMW-2016-FP-00833

**Principle Investigator:** Ofodike Ezekoye Ph.D., P.E.  
University of Texas at Austin

In April 2019, an unexpected explosion of batteries on fire in an Arizona energy storage facility injured eight firefighters. More than a year before that fire, FEMA awarded a Fire Prevention and Safety (FP&S), Research and Development (R&D) grant to the University of Texas at Austin to address firefighter concerns about safety when responding to fires in battery energy storage systems of all sizes. Professor O.A. ('DK') Ezekoye is working with other engineers, firefighters, and industry partners to develop a better understanding of the magnitude of the fire hazards.

There has been a dramatic increase in the use of battery energy storage systems (BESS) in the United States. These systems are used in residential, commercial, and utility scale applications. Most of these systems consist of multiple lithium-ion battery cells. A single battery cell (7 x 5 x 2 inches) can store 350 Whr of energy. Unfortunately, these lithium cells can experience thermal runaway which causes them to release very hot flammable, toxic gases. In large storage systems, failure of one lithium cell can cascade to include hundreds of individual cells. The hot flammable gases can result in an explosion, or a very difficult to extinguish fire.

Although the fire service routinely responds to explosive scenarios, such as those associated with natural gas leaks, standard operating procedures do not exist for scenarios like a battery energy storage system for which there is no way to cut off the gas supply. The fire service is unaware and inexperienced with the fire and explosion hazards of BESS.

The FP&S R&D study started with a laboratory test in which a single cell failed in one commercial storage module containing a total of 14 cells. In one of the early tests, when a single cell failed, smoke and gases were released that ignited and burned intensely for 12

seconds. Toxic smoke and gases filled the test space.

The research team has subsequently connected small-scale battery failure test results to large scale fire and explosion consequences associated with these systems. Through this research, one of the biggest lessons learned for the fire service is that the utilities and commercial entities that own large battery systems are equally unfamiliar with the potential fire hazards. As well, there remain many questions about the toxicity of the battery vent gas.

From 2014 to 2018, residential BESS installations have increased by 200% annually. Further research into residential BESS hazards is essential as BESS hazards could eventually become a regular part of dwelling fires.

According to Professor Ezekoye, the results of this study will lead to wider awareness of the BESS hazards, a greater understanding of the underlying fire behavior of these systems, and eventually the development of safe standard operating guidelines and procedures for firefighters.

Link: [www.UTFireResearch.com](http://www.UTFireResearch.com)

For more information on Fire Prevention & Safety Grants including how to apply, please visit <https://www.fema.gov/fire-prevention-safety-grants>.

**Tags:**

● [Assistance to Firefighters Grants](#)

Last updated October 27, 2020

[Accessibility](#) [Accountability](#) [Careers](#) [Contact Us](#) [FOIA](#) [Glossary](#) [No FEAR Act](#)

[Plug-Ins](#) [Privacy](#) [Report Disaster Fraud](#) [Website Information](#) [DHS.gov](#) [USA.gov](#)

[Inspector General](#)



**FEMA**

**FOLLOW FEMA**



HOME (/)

750+ COMPANIES WORLDWIDE APPROACH US EVERY YEAR FOR THEIR REVENUE GROWTH INITIATIVES

LITHIUM-ION BATTERY RECYCLING MARKET (MARKET REPORTS) LITHIUM-ION BATTERY RECYCLING

MARKET 153488928.HTML)  
KNOW MORE (/Knowledgestore.asp)

> PURCHASE REPORT

## Lithium-ion Battery Recycling Market by Battery Chemistry (Lithium-nickel Manganese Cobalt, Lithium-iron Phosphate, Lithium-Manganese Oxide, LTO, NCA, LCO), Industry (Automotive, Marine, Industrial, and Power), and Region - Global Forecast to 2030

Research shows that more than 40% of the times, clients do not get the specific intelligence they need in multi-client market research reports. We offer **10% customization** in our reports at no extra cost. Get the exact market intelligence you require with real value for money.

### PURCHASE REPORT

Email (Username)

Password

Re-enter Password

Name

Designation

Company

Phone





MARKETSANDMARKETS

(/)

ndmarkets.com)

f (https://www.facebook.com/sharer/sharer.php?

u=https://www.m...ar...HTML) In (REPORTS/TOP-MARKET-REPORTS.ASP) (mini.asp) 928)  
HOME (/) PRESS RELEASES (/PRESS-...  
CAREER (/CAREER.ASP) CONTACT US (/CONTACTUS.ASP) RESOURCE CENTER ABOUT MNM

🐦 (https://www.twitter.com/share?url=https://www.marketsandmarkets.com/Market-Reports/id=153488928)

in (https://www.linkedin.com/shareArticle?mini=true&url=https://www.marketsandmarkets.com/Market-Reports/id=153488928)

GET 10% FREE CUSTOMIZATION ON THIS REPORT! →

(/requestCustomizationNew.asp?id=153488928)



Speak to Analyst

(/speaktoanalystNew.asp?id=153488928)

OR FACE-TO-FACE MEETING

### PERSONALIZE THIS RESEARCH

- Triangulate with your Own Data
- Get Data as per your Format and Definition
- Gain a Deeper Dive on a Specific Application, Geography, Customer or Competitor
- Any level of Personalization

REQUEST A FREE CUSTOMIZATION (/requestCustomizationNew.asp?id=153488928)



- (/) • What are the Known and Unknown Adjacencies Impacting the Lithium-ion Battery Recycling Market

- Who will be your Top Customer; what will make them switch?
- Defend your Market Share or Win Competitors
- Get a Scorecard for Target Partners

CUSTOMIZED WORKSHOP REQUEST (/FreeWorkshop.asp?id=153488928)

### ADJACENT MARKETS

Electric Vehicle Charging Stations Market (/Market-Reports/electric-vehicle-charging-stations-market-21599205.html)

Industrial Batteries Market (/Market-Reports/industrial-batteries-market-36754108.html)

Battery Recycling Market (/Market-Reports/battery-recycling-market-147696175.html)

Lead Acid Battery Market (/Market-Reports/lead-acid-battery-market-161171997.html)

Lithium Compounds Market (/Market-Reports/lithium-compounds-market-167191191.html)

Flexible Battery Market (/Market-Reports/flexible-battery-market-190884508.html)

Automotive NVH Materials Market (/Market-Reports/automotive-nvh-material-market-227596009.html)

REQUEST BUNDLE REPORTS (/RequestBundleReport.asp?id=153488928)

- Home (/)
- Press Releases (/press-release-2.html)
- Career (/Career.asp)
- Contact us (/ContactUs.asp)

### • PRACTICES



- [knowledge Store \(/Knowledgestore.asp\)](#)
- [Reports \(/top-market-reports.asp\)](#)
- [Events \(https://events.marketsandmarkets.com/\)](https://events.marketsandmarkets.com/)
- [CUSTOMER SUMMIT \(/Customer\\_Summit\\_Listing.asp\)](#)
- [Resource Center](#)
  - [Case Studies \(/casestudies.asp\)](#)
  - [Competitive Leadership \(/competitiveLeadership.asp\)](#)
  - [Engage Forums \(/EngageForums.asp\)](#)
  - [Flyers & Brochures \(/FlyersandBrochures.asp\)](#)
  - [Infographics \(/infographics.asp\)](#)
  - [Perspectives \(/Perspective.asp\)](#)
  - [Testimonials \(/Testimonials.asp\)](#)
  - [Top Trends \(/Top\\_Trends.asp\)](#)
- [Market Research Reports](#)
  - [Information & Communications Technology \(telecom-and-IT-market-research-113.html\)](#)
  - [Semiconductor & Electronics \(semiconductorand-electronics-market-research-87.html\)](#)
  - [Medical Devices \(medical-device-market-research-11.html\)](#)
  - [Chemicals \(chemicals-market-research-10.html\)](#)
  - [Advanced Materials \(advanced-material-market-research-12.html\)](#)
  - [Energy and Power \(energy-power-supplies-market-research-4.html\)](#)
  - [Food and Beverage \(food-and-beverages-market-research-6.html\)](#)
  - [Biotechnology \(biotech-market-research-5.html\)](#)
  - [Aerospace & Defence \(aerospace-defence-148.html\)](#)
  - [Automotive & Transportation \(automotive-and-transportation-market-research-121.html\)](#)
  - [Automation & Process Control \(industrial-automation-market-research-110.html\)](#)
  - [Agriculture Industry \(agriculture-market-research-173.html\)](#)
  - [Packaging \(packaging-market-research-183.html\)](#)
  - [Pharmaceuticals \(pharmaceutical-market-research-3.html\)](#)
  - [Building & Construction \(building-construction-market-research-187.html\)](#)
  - [Mining, Minerals and Metals \(mining-minerals-and-metals-market-research-191.html\)](#)
- [About MnM](#)
  - [About Us \(/AboutUs-8.html\)](#)
  - [Board Of Directors \(/BoardOfDirectors.asp\)](#)
  - [Leadership Team \(/LeadershipTeam.asp\)](#)
  - [Research Experts \(/ResearchLeadership.asp\)](#)



MARKETSANDMARKETS (/)

+1-888-600-6441  
(Corporate office hours)

+1-888-600-6441  
(US/Can toll free)

HOME (/) PRESS RELEASES (/PRESS-RELEASE-2.HTML) **REPORTS (TOP MARKET REPORTS.ASP)** [/TOP-MARKET-REPORTS.ASP](#) [/ACTUS.ASP](#) [/CONTACT-US](#) [/CAREER](#) [/CAREER.ASP](#) [/CONTACT-US](#) [/ACTUS.ASP](#) [/RESOURCE-CENTER](#) [/ABOUT-MNM](#)

(UK office hours)

### CONNECT WITH US

[Top Market Reports \(/top-market-reports.asp\)](#) | [Conferences \(/conferences.html\)](#) | [Press Releases \(/press-release-2.html\)](#) | [SiteMap \(/sitemap.html\)](#) | [XML \(/sitemap.xml\)](#) | [Feeds \(/feeds/feeds.xml\)](#) | [Blog \(https://blog.marketsandmarkets.com/\)](#) | [Report/17016700-78834](#) | [Careers \(/Career.asp\)](#) | [New Reports \(/new-reports.asp\)](#) | [Research Insight \(/Research-Insight.html\)](#)

[Disclaimer \(/Disclaimer.asp\)](#) | [Privacy Policy \(/Privacy-12.html\)](#) | [Terms and Conditions \(/Terms-13.html\)](#) | ©2021 MarketsandMarkets Research Private Ltd. All rights reserved | [\(/www.dandb.com/verified/business/113335487/\)](#)

### ABOUT TRUST ONLINE

## **Perez-McEvoy, Paloma (LAX - X52564)**

---

**From:** Crosby, Josephine@Energy <Josephine.Crosby@Energy.ca.gov>  
**Sent:** Wednesday, June 30, 2021 12:34 PM  
**To:** Hernandez, Jennifer L (SFO - X56927); Perez-McEvoy, Paloma (LAX - X52564)  
**Cc:** Lee, Ralph@Energy  
**Subject:** Holland & Knight Records Request  
**Attachments:** SPRN\_BSO21062810260.pdf

*[External email]*

Dear Jennifer Hernandez and Paula Perez-McEvoy,

We received Holland & Knight's request seeking a copy of the following report cited by the California Energy Commission (CEC) in the Draft Environmental Impact Report (Draft EIR) for the Amendments to the Building Energy Efficiency Standards:

1. Markets and Markets report on Lithium-ion Battery Recycling Market by Battery Chemistry (Lithium-nickel Manganese Cobalt, Lithium-iron Phosphate, Lithium-Manganese Oxide, LTO, NCA, LCO), Industry (Automotive, Marine, Industrial, and Power), and Region - Global Forecast to 2030.

The CEC does not have possession of the above-requested report. CEC has no additional responsive documents other than the summary document available on the webpage cited in Chapter 4 of the Draft EIR. The Draft EIR can be found in docket 21-BSTD-02 (available at <https://efiling.energy.ca.gov/Lists/DocketLog.aspx?docketnumber=21-BSTD-02>). Additionally, the summary of the requested report is available on the Markets and Markets website (available at <https://www.marketsandmarkets.com/Market-Reports/lithium-ion-battery-recycling-market-153488928.html#:~:text=Key%20Market%20Players,lithium-ion%2Obattery%20recycling%20market>).

Please let me know if you have any questions. This concludes CEC's review of your request.

Best,  
Josey Crosby



Energy  
Storage  
Association

# ***End-of-Life Management of Lithium-ion Energy Storage Systems***

***April 22, 2020***

# Contents

- Contents..... 1
- Acronyms ..... 2
- Introduction ..... 3
- Circular Economy and Li-ion Batteries ..... 4
- Energy Storage System End of Life ..... 6
- Decommissioning..... 6
- Transport of Batteries ..... 9
- Refurbishment and Reuse: “Second Life” ..... 10
- The State of U.S. Recycling of Li-ion Batteries ..... 11
- Recycling Processes..... 13
- Economics of Recycling ..... 15
- Disposal ..... 17
- Promoting Sustainable End-of-Life Management..... 18
- Conclusion..... 19
- Additional Resources ..... 21
- Bibliography ..... 22

## Disclaimer

The U.S. Energy Storage Association assumes no responsibility or liability for the use of this document. Descriptions of legal requirements and rules governing the disposition of Li-ion battery systems are for general awareness purposes only, and parties should consult with legal advisors concerning liability and other issues associated with the end-of-life management of energy storage systems.

## Acknowledgements

This white paper was written by Marc Chupka, Vice President of Research & Programs at the U.S. Energy Storage Association (ESA). ESA wishes to thank members of the Corporate Responsibility Initiative who provided input and comments on several drafts of this paper, including Call2Recycle, Inc., Clearway Energy Group, Dimension Renewable Energy, Renewance, Inc., and Wärtsilä.

## *Acronyms*

DOE	U.S. Department of Energy
DOT	U.S. Department of Transportation
EPA	U.S. Environmental Protection Agency
EPC	Engineering, procurement, and construction
ESA	U.S. Energy Storage Association
ESS	Energy storage system
EV	Electric vehicle
GHG	Greenhouse gas
LFP	Lithium iron phosphate
Li-ion	Lithium-ion
LMO	Lithium manganese oxide
NCA	Nickel cobalt aluminum
NMC	Nickel manganese cobalt
NYSERDA	New York State Energy Research & Development Authority
OEM	Original equipment manufacturer
RBRC	Rechargeable Battery Recycling Corporation (now Call2Recycle)
RCRA	Resource Conservation and Recovery Act
SO <sub>x</sub>	Sulphur oxides

# Introduction

Energy storage is experiencing a period of rapid deployment growth, and even in the midst of an economic downturn, global analysts' projections indicate this trend is poised to continue due to increasingly attractive economics and the value storage provides from multiple grid services.<sup>1</sup> While many developers and owners are gaining experience deploying and operating grid-connected energy storage systems (ESS), few have yet to manage ESS facilities at the end of a system's life. But ESS owners, operators and developers may be able to apply some of the lessons learned from the auto industry's experience as it confronts the task of managing an increasing stock of used Lithium-ion (Li-ion) batteries from electric vehicles (EVs).

Both grid-connected ESS and EVs rely on Li-ion batteries, and the phenomenal growth in Li-ion applications creates stress along the entire value chain—from mining raw material inputs, such as lithium and rarer elements, to manufacturing and disposition of the batteries once they reach the end of their useful lives. This linear depiction of material and energy use in the economy – from extraction of natural resources to production, use, and disposal – may present significant environmental consequences as the volume of battery production increases. An alternative model has emerged that instead attempts to mimic nature in the way inputs are used in production of goods, which upon reaching the end of their useful lives are then reused and/or recycled as inputs again. Such “circular economy” concepts are prevalent in the debates surrounding how to best manage the Li-ion battery life cycle.

In April 2019, the U.S. Energy Storage Association (ESA) launched the Corporate Responsibility Initiative (CRI) with dozens of industry leaders to share advanced safety practices and develop educational materials and resources on safety, emergency preparedness, and lifecycle management. This paper focuses on the end-of-life management of Li-ion batteries, offering a review of options from the circular economy perspective. A related forthcoming CRI track will look at supply chain issues, which represents another arc along the circular economy, one which may increasingly rely on materials recovered after the end of (first or subsequent) life application.

---

<sup>1</sup> In this paper, ESS primarily refers to “Front-of-the-Meter” (FTM) battery storage systems connected to the grid at the transmission or distribution system level. However, the concepts and end-of-life pathways identified are also relevant for “Behind the Meter” (BTM) customer systems.

### Why Focus on Li-ion?

While there are many other energy storage technologies and several battery chemistries, Li-ion currently commands the bulk of the market for electric vehicle and stationary grid-connected systems. Its use in both applications is expected to grow at a rapid pace. According to Wood Mackenzie Power & Renewables, 99% of stationary energy storage deployments in 2019 used Li-ion technologies.<sup>2</sup> Moreover, the vast majority of lead acid batteries (predominantly automotive batteries) are already recycled, and other battery chemistries are not expected to gain significant market shares in EV or ESS applications in the near term.

## Circular Economy and Li-ion Batteries

The primary objective of the circular economy framework is to promote a sustainable economic system by minimizing material and energy used to provide economic goods and services. Some of these principles are expressed in shorthand slogans, such as “reduce, reuse, recycle,” and frequently are congruent with greenhouse gas (GHG) reductions objectives. However, *given current technology and markets*, not all production and waste can be brought into a circular economy with beneficial results. For some goods, more energy would be used in collecting and recycling activities than is used to produce virgin materials, or the costs of reuse or recycling are prohibitive compared with relatively benign disposal options. Life-cycle analysis (LCA) can help identify these factors and may identify challenges and opportunities that can lead to improved technologies and more effective markets. Indeed, the current constraints and limitations to beneficial reuse or recycling within the Li-ion battery value chain have already prompted recent initiatives and new programs to address these barriers as discussed later in this document.

Circular economy reasoning generally superimposes a loose hierarchy on end-of-life options, with reuse (in the original application or some other less demanding application) taking precedence over recycling, and recycling all, or at least some, of the material inputs preferred over disposal. These paths are shown for EV batteries in Figure 1, with green and blue arcs representing environmentally-sustainable flows. This hierarchy is a reasonable way to frame end-of-life management options for Li-ion batteries —

---

<sup>2</sup> Wood Mackenzie Power & Renewables and Energy Storage Association, *U.S. Energy Storage Monitor 2019 Year in Review*, March 2020.

though, again, the desirability of any specific end-of-life management pathway on costs, emissions, or other measures depends on technologies, systems and markets. Circular economy principles even apply at the start, in designing products for more economic refurbishment or recycling, or for a longer service life that reduces the need for energy and material inputs for manufacture of new products.

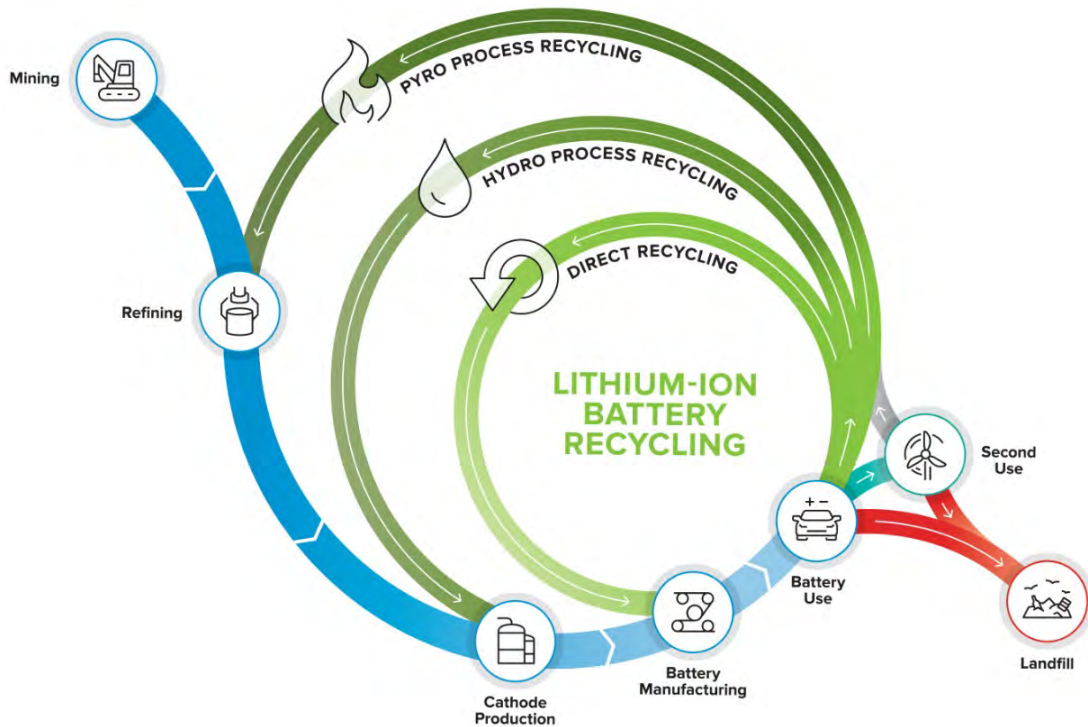


**Figure 1:**  
**Circular Economy Pathways for EV Batteries**  
 Source: ReCell; Argonne National Laboratory

While this paper addresses stationary ESS, much of the information and experience with Li-ion end-of-life management is derived from the increasing management of spent EV batteries around the world. While ESS and EV Li-ion batteries have different applications, they share many material inputs and thus have similar reuse and recycle opportunities. Some of the practices that evolve to reuse and recycle EV batteries will influence, and sometimes determine, the end-of-life requirements and management practices applicable to stationary ESS batteries. Finally, the substantial number of EV batteries that will end service during this period as stationary ESS deployments rapidly increase has sparked research and commercial interest in the reuse and refurbishment of EV batteries for “second life” applications in stationary ESS, further linking the two applications.

# Energy Storage System End of Life

For the vast majority of stationary ESS installations, the end of life represents a planning decision rather than an unexpected moment. Operating a Li-ion battery ESS under prudent safety guidelines and adhering to codes and standards helps prevent significant accidents or failures and thus extends its useful life. In the absence of catastrophic failure, owners generally have discretion on when to remove a Li-ion battery ESS from service.

The effective lifespan of the ESS can also sometimes be extended with enhanced maintenance and replacement activities. Li-ion battery-based ESS are inherently modular, being composed of individual battery cells assembled into modules (packs, trays or assemblies), arrayed in racks, connected into various control systems and enclosed in containers. Individual cells, modules and even entire racks can be replaced as needed (when, for example, one degrades unusually quickly compared to other components that maintain performance). Where economic, overall ESS performance can be maintained at acceptable levels by selectively refreshing individual components, thus extending the overall economic lifetime and deferring the retirement of the facility. Currently, the validation to ensure that a mixture of old and new battery cells or modules can work together effectively can be costly, although those costs will likely fall as operating experience accumulates. Extending the effective lifetime of a durable asset is consistent with circular economy benefits as it reduces both virgin material input requirements as well as potential waste, although at some point performance, safety and economic considerations will dictate decommissioning.

## Decommissioning

As with any other asset within the power sector, the decommissioning process involves dismantling the ESS and removing it from the site in compliance with applicable federal and local rules that govern the safe transport and disposition of used equipment or waste. A primary issue in end-of-life planning is who bears the legal and financial liability for the equipment once a facility shuts down and components are moved offsite. Even if an engineering, procurement, and construction (EPC) or an operating contract assigns decommissioning cost responsibilities to another party,<sup>3</sup> the used Li-ion batteries will be

---

<sup>3</sup> Renewance estimated costs for dismantling, shipping, and recycling the batteries for a 10 MWh facility at over \$474,000, or almost \$50/kWh. See Renewance, Inc., "Commercial Liability Considerations for End-of-Life Industrial Batteries," 5.

classified as hazardous waste and thus the owner will be considered a hazardous waste generator liable for proper disposal under the Environmental Protection Agency (EPA) rules under the Resource Conservation and Recovery Act (RCRA).<sup>4</sup>

Decommissioning obligations, processes, and costs for stationary storage were not always considered in earlier installations and remain to some extent discretionary, in part due to currently limited standards and ambiguous regulatory frameworks. Long before owners face actual decommissioning decisions, they should understand and evaluate the options and develop a decommissioning plan, considering current and future potential regulations. And because the options to consider in eventual decommissioning continue to evolve, the plan should be capable of adapting to new information to take advantages of emerging opportunities.

It is becoming more common for contract language to specify that system decommissioning responsibilities and their costs lie with the operations and maintenance provider or EPC contractor, even though the EPA deems the owner liable for proper treatment of removed equipment. Under such arrangements, the contractor identified as responsible typically provides all decommissioning services (including restoration of the site to original state if required, and removal of the equipment). However, the details of how decommissioning is to be done, or what happens to the decommissioned battery, have not commonly been specified in the contracts.

State agencies and utilities are also encouraging or requiring the development of energy storage decommissioning plans at project inception. For example, utilities such as Portland General Electric in Oregon are now making decommissioning responsibilities explicit in requests for proposals. The New York State Energy Research and Development Authority (NYSERDA) published *New York Battery Energy Storage System Guidebook for Local Governments*, which includes a model rule for localities that specifies that applicants for new energy storage projects must have a decommissioning plan and a decommissioning fund.<sup>5</sup> The NYSERDA model rule states that applicants must have a narrative description of the decommissioning process, the estimated life of the energy storage system, details

---

<sup>4</sup> The characteristics of Li-ion batteries determine their classification as hazardous waste, and a waste generator means “any person, by site, whose act or process produces hazardous waste...or whose act first causes a hazardous waste to become subject to regulation.” ([40 CFR § 260.10](#)) and “a used battery becomes waste becomes a waste on the date it is discarded (e.g., when sent for reclamation)” ([40 CFR § 273.2\(c\)\(1\)](#)).

<sup>5</sup> See New York State Energy Research and Development Authority, *New York Battery Energy Storage System Guidebook for Local Governments*, 2019.

about the estimated cost of decommissioning and plans for ensuring its funding, and contingency plans for removal of damaged batteries.

The actual scope of decommissioning depends on project-specific conditions, the type of system, and the disposition pathway chosen, such as whether some or all of the ESS will be reused or recycled.<sup>6</sup> In some cases, the battery modules are removed, while the balance of the system (controls, enclosures, etc.) remain and are re-used with new battery modules. In other cases, the full systems are replaced as integrated packages. If the site itself is being entirely decommissioned (no future energy storage or similar infrastructure will occupy it), contractual agreements govern the final state of the site (e.g. resulting in remediated land, residual foundations, gravel, etc.).

Once a used battery is removed from service and diverted toward end-of-life management, it is designated as “Universal Waste,” a special category of hazardous waste under EPA regulations.<sup>7</sup> These rules generally require recordkeeping, labeling, and storage methods that keep material out of the environment, and they outline approved recycling or disposal pathways. Damaged cells, e.g., where the cell casing has been breached, may face additional requirements than those imposed under Universal Waste rules.<sup>8</sup> A battery intended for refurbishment and reuse is not considered “waste” under RCRA, because it is not discarded.<sup>9</sup>

Although this paper addresses the end-of-life management of batteries, the balance of plant can represent a significant quantity of materials, including concrete pads, steel enclosures, cabling, and an array of electronics that are part of the entire energy storage system package. Concrete and steel are readily recyclable, and many enclosures can be reused, particularly if a site is being repowered with new batteries at the end of old equipment’s lifespan. Inverters, control systems, and other electronic equipment share many of the challenges of e-waste more broadly, but useful materials can often be recovered. Some of the dismantled equipment from an ESS can be reused with minimal processing. For

---

<sup>6</sup> Strictly speaking, the ESS decommissioning applies to the battery-related elements of an ESS. The site itself, including interconnection facilities, could be reused with a new ESS, much like generating facilities can be “repowered” and thus re-commissioned with new generating equipment. However, the existing battery components would be dismantled and removed, thus becoming available for re-use, recycling or disposal.

<sup>7</sup> See [40 CFR § 273](#).

<sup>8</sup> See U.S. Environmental Protection Agency, “May a handler of universal waste manage broken or damaged batteries as universal wastes?” for a discussion of damaged battery classification.

<sup>9</sup> For material to be classified as hazardous waste, it first must be considered solid waste, and material “used or reused as effective substitutes for commercial products” is exempt from solid waste designation ([40 CFR § 261.2\(e\)\(1\)\(ii\)](#)).

example, rack systems can be reused in new or existing ESS facilities or returned to original equipment manufacturers (OEMs) for spare parts inventory.

## Transport of Batteries

After dismantling and removal from the site, the old batteries are transported to facilities for refurbishment, recycling, or disposal. Moving Li-ion batteries can pose a fire risk if still-energized batteries short circuit or their containers are damaged. Transport of batteries, whether new or used, is governed by U.S. Department of Transportation (DOT) regulations that treat batteries as “Class 9” miscellaneous hazardous material and specify packaging and materials containment to mitigate the risk of accidental activation or reaction of the batteries during transport.<sup>10</sup> All batteries must be packed in a strong outer package which prevents short circuits or accidental activation, prevents the release of any hazardous materials, ensures no leakage, and inhibits any combustion, and damaged batteries are subject to additional packaging and labeling requirements.<sup>11</sup> However, Li-ion batteries shipped by motor vehicle to a permitted storage or disposal facility, or to a recycling facility, are exempted from certain labeling, marking, testing and record-keeping requirements.<sup>12</sup>

Both shippers who package battery waste and carriers (e.g., trucking firms and drivers) who haul the waste batteries must comply with training and certification requirements for hazardous materials transport. The packing, labeling, and training regulations are fairly detailed, and a lack of significant experience with the exact requirements that apply to transporting large-format Li-ion batteries may make carriers and/or individual drivers reluctant to accept loads where they lack regulatory experience.

Transport regulations generally apply to both individual Li-ion cells as well as battery modules; decommissioned ESS will generally yield battery modules for shipment. Batteries may be completely discharged prior to shipment to a recycling facility, while batteries destined for refurbishment and reuse will maintain some charge in transport (and while placed in temporary storage after transport). For reuse in particular, ensuring that the batteries are not damaged or further degraded is important (*e.g.*, leaving them exposed to weather or in a fully-discharged state can harm later reuse). The growing stockpiles of spent EV batteries may not become available for eventual refurbishing and reuse if not

---

<sup>10</sup> These rules are implemented and enforced by the Pipeline and Hazardous Materials Safety Administration and are found at [49 CFR § 173.185](#).

<sup>11</sup> See [49 CFR § 173.185\(f\)](#).

<sup>12</sup> See [49 CFR §173.185\(d\)](#). The exemptions relate to requirements found in UNECE, UN standard 38.3.

properly protected. The duration of time stored between transport and processing also raises liability issues for Universal Waste. Temporary storage must keep the decommissioned equipment in a safe state, shielded from fire risk, protected from risk of pollution and from safety hazards caused by trespassers.

## Refurbishment and Reuse: “Second Life”

Where economically feasible, reusing battery systems and other components is more environmentally sound than recycling constituent materials. As batteries degrade over time, they may be less useful for their originally intended purpose, but still valuable for other applications. For example, backup power systems or batteries coupled with renewables to power remote irrigation systems may not need the same performance characteristics as commercial grid systems. These “second life” applications can substitute for newly-manufactured battery energy storage systems and in some cases expand the role of stationary energy storage, such as when new systems may be prohibitively expensive, but a lower cost refurbished system can meet the desired performance requirements.

There is increasing attention placed on reusing EV batteries for less exacting stationary service, and where energy density (Wh/kg) does not pose a significant design constraint. Projections of EV deployment indicate an immense and growing number of Li-ion battery systems will soon face end of life in their vehicle applications. Reconditioning EV batteries, either by original equipment manufacturers (OEMs) or third parties, is an active area of research and emerging commercial opportunity. Once EV batteries degrade to 70-80% of their original rated capacity they are typically retired, although future EV owners may retain their vehicle or original battery longer (even with degraded range) if it continues to serve their specific needs.<sup>13</sup> And while the current level of second-life battery deployment is very small in North America (10 MWh) and Europe (100 MWh), China had re-deployed almost 1 GW of used batteries by 2018, primarily as back-up power at telecommunication facilities.<sup>14</sup>

---

<sup>13</sup> EV range increases could also lower that retirement threshold somewhat, as batteries at roughly 60% of their capacity could meet most driving needs (with charging at work). Even at 30% of their capacity, LBNL anticipates most (55%) of US driving needs could be met. See Lawrence Berkeley National Laboratory, V2G-Sim.

<sup>14</sup> See Melin, Hans Eric, “The lithium-ion battery end-of-life market – a baseline study,” Global Battery Alliance. The figures from China likely reflect the impact of government mandates to assess for second life opportunities and subsidies.

Refurbishing or reconditioning batteries for second use is a significant undertaking. First, a processor must conduct tests to determine the condition or “state of health” of used batteries. The batteries must then be assembled into modules suitable for stationary service. Coupling batteries of varying states of health can require more advanced control systems, as the control hardware and software that interacts with original batteries to ensure optimal – and safe – operation is usually proprietary and designed for the original battery application. Developing new controls and software to convert older batteries into use for new applications remains a significant challenge.

The cost savings must be significant enough, and the performance of second-life batteries high enough, to make refurbishing appealing compared to new batteries. The discounted cost of reconditioned batteries relative to new ones must offset increased integration costs and reduced performance relative to new ones for a robust market for second-use batteries to develop. Declining prices and improved performance of new batteries may limit the demand for use of reconditioned EV batteries in stationary energy storage projects. As costs for new batteries continue to fall, it may become harder to convince manufacturers and users to refurbish and use old ones. Designing for reuse at the outset could reduce refurbishment cost substantially and increase the commercial viability of this path.

Second-life battery system applications in the U.S. are currently limited to pilot demonstrations and small projects. Several companies and academic institutions are investigating the reuse of EV batteries for stationary applications, and this research likely will be useful and broadly applicable to second-life use for stationary batteries. The codes and standards that apply to refurbished batteries also continue to evolve. UL recently finalized its standard 1974 for Evaluation of Repurposing Batteries, which seeks to establish consistent processes and metrics for assessing batteries destined for second-life applications.<sup>15</sup>

## The State of U.S. Recycling of Li-ion Batteries

The primary loop for spent Li-ion batteries to reenter the economy remains some form of recycling. Ultimately this becomes the only alternative to disposal for of all batteries: even if second life

---

<sup>15</sup> “This standard covers the sorting and grading process of battery packs, modules and cells and electrochemical capacitors that were originally configured and used for other purposes, such as electric vehicle propulsion, and that are intended for a repurposed use application, such as for use in energy storage systems and other applications for battery packs, modules, cells and electrochemical capacitors.” UL, Standard 1974 for Evaluation of Repurposing Batteries, Edition 1 (2018).

applications become prevalent, at some point batteries can no longer perform useful service. Therefore, recycling is currently the only viable long-term path to manage spent Li-ion battery waste consistent with circular economy principles.

Beyond enhancing stationary energy storage market sustainability, increasing the volume of batteries that are recycled rather than disposed may also improve supply chain economics. Recycling reduces solid waste streams and allows for the recovery of valuable materials from batteries to reduce reliance on raw material mining that imposes inherent energy and environmental burdens. Many of the materials in lithium-ion batteries such as cobalt and nickel are valuable; reinjecting these domestic resources into the supply chain can reduce costs and reduce imports of raw materials.<sup>16</sup>

Recycling materials has been practiced for decades in consumer waste streams (such as paper, bottles and cans) and commercial recycling (such as scrap metal). However, recycling Li-ion batteries, particularly from large stationary applications, is a relatively new industry.<sup>17</sup> It lacks stable markets for the collection, transport, and recovered resource sales, and applicable federal and state regulations are not always consistent or clear to market participants. As economic, safety and environmental issues are intensifying interest in battery recycling options, related business practices in different stages of project development, operation and decommissioning are still evolving. Some battery recycling methods exist and are well understood. Yet significant research & development (R&D) efforts to improve recycling processes and make them applicable to Li-ion batteries are underway, which will drive new commercial opportunities, regulatory frameworks and best practices. In order to make Li-ion battery recycling commercially viable, innovations (particularly in automated processes) must reduce the cost of collecting, managing, and recycling batteries, and market demand for the recovered materials must support prices to maintain profitability.

At present, no facility in the U.S. fully recycles Li-ion batteries, *i.e.*, renders used batteries into constituent materials and sells or otherwise reintroduces all the resultant material back into commodity markets, although several U.S.-based companies will accept and treat batteries to some degree. However, market demand for recovered materials is likely to strengthen as domestic Li-ion battery

---

<sup>16</sup> Mayyas, Ahmad et. al. present a comprehensive overview of Li-ion battery recycling in “The case for recycling: Overview and challenges in the material supply chain for automotive li-ion batteries,” *Sustainable Materials and Technologies*, Volume 19 (April 2019): e00087.

<sup>17</sup> Recycling li-ion EV batteries began approximately a decade ago in the U.S.; see Taylor, Phil, “When an Electric Car Dies, What Will Happen to the Battery? Can millions of lithium ion batteries be recycled?” *Scientific American*, (September 14, 2009).

production capacity is poised to grow substantially in the next few years.<sup>18</sup> Thus, the industry has a narrowing window of time to establish best practices at the outset, encourage the development of an effective recycling market, and implement efficient recycling processes at scale.

## Recycling Processes

Sorting recovered batteries is a critical first step to ensure that same-chemistry batteries are being fed into the system. This is less of a concern for ESS and EVs than it is for collections of heterogeneous consumer electronic batteries, given the relative large size and low volumes of the former currently sent to recycling facilities.<sup>19</sup> The recycling facilities ensure that the correct type of batteries flow into a given recycling process, including separating different types of lithium-based chemistries, such as lithium iron phosphate (LFP) versus lithium nickel manganese cobalt (NMC). For this reason, labeling cells and batteries with chemistry information is critical during manufacturing to ensure accuracy, using a consistent, standard labeling approach. Japan has developed labeling requirements that use color coding and material data labeling to aid recycling efforts, in addition to a pre-existing color coding of basic battery chemistries (Ni-Cd, Ni-MH, Li-ion, Pb) for quick visual identification.<sup>20</sup>

The recycling process begins with dismantling electrically discharged batteries. The current diversity of Li-ion battery types, sizes, and chemistries makes this process difficult to automate, so it must largely be done manually. The steps consist of removing the battery casings, separating the connectors, disassembling modules from packs, separating cells from modules, and removing the electrolyte. In addition to manual separation, some recyclers employ ultrasound and/or mechanical agitation to remove cathode material. After shredding, or milling and pre-treatment, the cells undergo the recycling process.

Today, there are two primary commercial pathways for recycling batteries: the most common being pyrometallurgical processes (*i.e.*, smelting), and emerging hydrometallurgical processes that include chemical methods such as precipitation, solvent extraction, ion exchange and electrowinning.

---

<sup>18</sup> U.S. Li-ion battery manufacturing capacity is projected to surge from 47 GWh currently to almost 160 GWh by the end of 2023. See Business Council for Sustainable Energy and Bloomberg New Energy Finance, *2020 Sustainable Energy in America Factbook* (February 2020): 104.

<sup>19</sup> Conventionally-recycled materials such as plastics, copper, and steel are readily separated without specialized sorting facilities or complex labeling.

<sup>20</sup> Battery Association of Japan, "Program to Make the Portable Secondary Battery Recycle Mark an International Standard." While the Japanese system does not yet indicate Li-ion sub-chemistries, BAI has proposed augmenting the current system with cathode material information. See Battery Association of Japan, "Revised Guideline for Recycle Marking on Li-ion Batteries for the Japanese Market."

Pyrometallurgy is based on 100-year old technology; the primary advantage of pyrometallurgy is that the smelters can easily handle battery cells of mixed chemistries.<sup>21</sup> Hydrometallurgical recycling processes reduce cells to elemental products using leaching techniques, which dissolve the metallic fraction and recycled metal solutions for separation and recovery. Leaching agents include organic and inorganic acids, and ammonia-ammonium salt systems. The main advantage for hydrometallurgy is the ability to recover transition metals and lithium from the cathode.

A major new research and development effort is focused on a third process called “direct cathode recycling.” Direct cathode recycling aims to recover relatively intact cathode materials for easier reinsertion into the battery manufacturing process and may provide a method to recover significant value from lithium iron phosphate (LFP) and lithium manganese oxide (LMO) cathodes. This direct recycling is expected to have lower energy costs than other processes and produce more reclaimed and readily reusable material when scaled commercially.<sup>22</sup>

### **Lessons from Lead-Acid Battery End-of-Life Management**

Unlike Li-ion, every stage in lead-acid recycling is profitable, owing to fundamental differences between lead-acid battery and Li-ion recycling. First, it is illegal to dispose of lead-acid batteries without recycling them, creating an enforced closed-loop market. Lead-acid battery recycling is also far simpler than Li-ion, having fewer materials, less material complexity, and less system design complexity. Manufacturers of car batteries all use the same materials: lead, lead oxide, and sulfuric acid in a standard sized polypropylene case. Moreover, the designs are nearly identical so dismantling can easily be automated.

The more complex the input material and design, the more complicated and costly the recycling. Other than some cylindrical Li-ion battery cells of common sizes, there are no prevailing standards for size and design, particularly for EV batteries that are customized for a specific model chassis. The lead in lead-acid batteries is used to manufacture new batteries, but the materials in a Li-ion battery do not always have a substantial market value and the dealer may be charged a fee to dispose of such materials. Lead-acid processors also enjoy an economy of scale, given their ubiquity in most cars and trucks, as well as in other consumer applications and some stationary storage systems.

---

<sup>22</sup> Pyrometallurgical, hydrometallurgical and direct cathode recycling processes are depicted on Figure 1.

Recycling methods that reintroduce raw materials into cell production can also reduce overall environmental impacts of battery production; life cycle analysis generally finds that upstream raw material extraction and processing creates more environment and energy burdens than cell production and pack assembly.<sup>23</sup> For example, since cobalt, nickel and copper are produced from sulfide ores, their virgin production is not just energy-intensive but also results in high sulfur oxide (SO<sub>x</sub>) emissions, which are avoided by recycling.<sup>24</sup> Hence recycling or reclamation can be an efficient strategy to reduce overall environmental impacts from using Li-ion batteries.

However, overall environmental benefits depend on the recycling methods and particular battery chemistries. For example, both hydrometallurgy and direct cathode recycling would reduce greenhouse gas (GHG) emissions for NMC and nickel cobalt aluminum (NCA) batteries, whereas using pyrometallurgy to recycle NMC and NCA batteries may actually increase GHG emissions. Variation in the energy intensity of virgin metals production relative to the recycling process can produce counterintuitive results; *e.g.*, recycling LFP batteries may actually increase emissions relative to production from virgin materials, even using direct cathode recycling methods.<sup>25</sup> This underscores the importance of R&D into improving the processes used in battery recycling, both to improve environmental outcomes and economic viability.

## Economics of Recycling

Currently, high processing costs and insufficient demand (and related low market prices for some of the constituent materials such as battery-grade lithium carbonate) impede full U.S. recycling.<sup>26</sup> For recycling to be economically viable for stand-alone commercial processors, the recovered materials must have more market value than the costs of the obtaining and recycling the batteries. Economies of scale in recycling processes and automation are key to reducing recycling costs, although very few ESS batteries are being decommissioned, while larger quantities of spent EV batteries increase slowly.

---

<sup>23</sup> Dai, Qiang et. al., "Life Cycle Analysis of Lithium-Ion Batteries for Automotive Applications," *Batteries*, 5 (2019): 48.

<sup>24</sup> Gaines, Linda et. al. "Key issues for Li-ion battery recycling" *MRS Energy & Sustainability: A Review Journal*, 5 (2018).

<sup>25</sup> Ciez, Rebecca, "Lithium-Ion Battery Recycling Processes: Environmental Impacts and Economics" ESA Webinar: *Decommissioning, End of Life and Recycling* (March 13, 2019).

<sup>26</sup> Standard battery-grade lithium carbonate (99.5% pure) represents one potential market, while applications requiring less refined grades of lithium compounds could also present sales opportunities.

The primary element working in favor of recycling economics is that the concentration of metals in scrap is much higher than in virgin ores. Under favorable commodities market conditions, and affordable costs for collection and recycling processes, using recycled materials can reduce the costs of production. The cost of materials comprises more than 50% of new cell cost, of which cathode materials comprise the most significant portion, so Li-ion recycling depends heavily on cost-effectively recovering cathode material. Pyrometallurgy yields cobalt and nickel metals which are valued at their commodity prices. In some instances, the value of cathode chemical material is actually greater than that of its constituent elements, so recovering a reusable cathode yields more revenue than recovery of individual elements. For example, one process cost analysis of direct cathode recycling estimates that if NMC cathode material can be recovered for \$15/kg or less, then direct cathode recycling would be economically competitive with traditional NMC cathode manufacturing methods.<sup>27</sup> However, the promising economics of direct cathode recycling processes depend on a stable value of specific cathode formulations, which will decline as battery manufacturers move to newer chemistries and render old cathodes obsolete.

A significant barrier to investment in recycling processes is the evolution of Li-ion battery chemistry in response to market conditions. Li-ion batteries contain relatively low percentages of retrievable metals by weight, therefore recyclers get relatively low value from post-process commodities. Cobalt is one of the more valuable recoverable elements, but because of its high cost and supply chain challenges, battery manufacturers are already finding ways to use less cobalt, in turn reducing the demand for cobalt. Market volatility in cobalt and magnesium prices can significantly alter the economic viability of their recovery, and this uncertainty can impede long-term investment decisions in recycling facilities. Rapid technological advances also can challenge recyclers: a facility might invest in the equipment to recycle today's common battery chemistries and face stranded investments if chemistries change to reduce upstream input costs.

Many of the economic uncertainties surrounding investment in recycling R&D, technologies, and processes involve the time lag between initial deployment and end of life of Li-ion batteries in EV and ESS applications. For EVs, the lag between initial deployment and reclamation can be a decade or longer. ESS battery lifespans vary according to their use pattern and the number of discharge / recharge cycles, however 15 years of first use is not uncommon. As EV battery life improves and second life

---

<sup>27</sup> Ciez, ESA Webinar.

applications flourish, the quantity of EV batteries introduced into the recycling markets may decline somewhat from expected levels. Increasing the useful life of batteries can reduce environmental impacts from initial production, but conversely longer battery lives could also impede recyclers who might otherwise invest in Li-ion processing facilities, particularly in new technologies which need to scale in order to realize cost efficiencies. These impediments to expanding recycling could limit future opportunities for ESS Li-ion battery recycling.

## Disposal

Where recycling facilities are unavailable or the recovered materials are uneconomic, batteries are disposed as waste. The management of disposed Li-ion batteries is governed by EPA Universal Waste rules that require waste handlers to separate hazardous materials for disposal under federal laws but allow the disposal of the remaining non-hazardous waste to comply with state and local requirements.

Proper collection, identifying battery chemistries, and fully de-energizing batteries are as important to a disposal site as to the recycling processes discussed above. Once rendered inert from fire risk (mechanically or chemically), non-hazardous materials not recovered for reuse or recycling can be disposed of through municipal waste streams. While some lithium chemistries are considered non-hazardous, many batteries have toxic constituents that require treatment as hazardous materials. The potential toxicity of Li-ion battery materials varies widely by chemistry; for example, where nickel, cobalt, or lead are present in battery chemistries in significant quantities, precautions must be taken at disposal or incineration sites in line with the hazards of those individual materials.

Small Li-ion batteries found in consumer electronics have proliferated in recent years, leading to state efforts to deter improper disposal and encourage recycling. However, even in states such as New York that have implemented rules against disposal, consumer batteries have improperly entered municipal waste streams. Although the experience of small consumer goods batteries is not a reliable predictor of the fate of large-scale Li-ion batteries, federal requirements promulgated decades ago did not contemplate the disposal of significant quantities of large Li-ion batteries, and no clear prospects for action at the federal level to strengthen the rules governing recycling or disposal have emerged. In response, some state and regional policies are emerging, such as California legislature creating an Advisory Group to consider approaches to effectively prohibit landfilling Li-ion EV batteries and

incentivize reuse and recycling.<sup>28</sup> The ESS industry will also need to work with regulators to ensure that waste managers utilize safe disposal practices for Li-ion batteries.

## Promoting Sustainable End-of-Life Management

Numerous international and U.S. initiatives have recently launched to promote sustainable practices in managing the disposition of used Li-ion batteries. The European Union has established goals for recycling and directed its member states to establish collection programs; industry is working on strategies to meet them. The Global Battery Alliance, a public-private partnership initiated by the World Economic Forum in 2017, issued a report on sustainable battery production and use in September 2019, and announced in January 2020 that 42 organizations had agreed to abide by ten guiding principles to promote the realization of that objective.<sup>29</sup>

The U.S. manufacturing and consumer electronics industries have also been proactive in establishing standards and guidelines. The Rechargeable Battery Recycling Corporation (RBRC), now known as Call2Recycle, established a consumer ‘seal’ that is formally recognized by EPA; fees collected for licensing the seal help to fund consumer battery collection and recycling efforts. Other initiatives are led by associations of companies such as battery manufacturers, users and recyclers, including the National Alliance for Advanced Technology Batteries (NAATBatt) and the Responsible Battery Coalition.

The U.S. Department of Energy (DOE) has also recently initiated new projects to push forward recycling technology and develop a domestic recycling industry for Li-ion batteries recovered from consumer products, EVs, and stationary ESS facilities.

The ReCell Lithium Battery Recycling R&D Center,<sup>30</sup> led by Argonne National Laboratory along with other national labs and universities, is pursuing several areas of recycling innovation:

- **Designing for recycling** that would make recycling easier and cheaper by planning for disassembly and recycling in the physical layout or chemistry of batteries.

---

<sup>28</sup> See Lithium-ion Car Battery Recycling Advisory Group in Additional Resources for information and materials.

<sup>29</sup> See World Economic Forum, *A Vision for a Sustainable Battery Value Chain in 2030: Unlocking the Full Potential to Power Sustainable Development and Climate Change Mitigation* (September 2019), and Global Battery Alliance, “42 Global Organizations Agree on Guiding Principles for Batteries to Power Sustainable Energy Transition” (January 23, 2020).

<sup>30</sup> Argonne National Laboratory, “DOE launches its first lithium-ion battery recycling R&D center: ReCell” (February 15, 2019).

- **Direct cathode recycling** that would improve recovery of cathode material and enhance the value of lithium batteries in recycling.
- **Improving the recovery** of other materials to create more value from recycling.
- **Reintroduction** of recycled materials into new batteries.

In November 2019, ReCell and the Responsible Battery Coalition announced a partnership to jointly pursue advancements in Li-ion battery recycling. In addition, DOE’s Li-ion Battery Recycling Prize, administered by the National Renewable Energy Laboratory, seeks to increase Li-ion recycling rates from consumer, EV, and stationary storage to 90% with \$5.5 million in awards to improve collection, separating and sorting, safe storage and transportation, reverse logistics, and other areas.<sup>31</sup>

Other DOE-led efforts seek to reduce critical mineral dependence in Li-ion batteries, which will promote domestic recycling. Most recently, in January 2020, DOE announced the Energy Storage Grand Challenge, which includes a call to create “a secure domestic manufacturing supply chain that is independent of foreign sources of critical materials, by 2030.”<sup>32</sup> Recent DOE workshop materials highlight the importance of materials recovered from domestic recycling efforts as critical to attaining that goal.<sup>33</sup>

## Conclusion

Most U.S. grid-connected energy battery storage systems have only recently been installed and system lifetimes can span more than 15 years; therefore few storage systems in the U.S. have confronted end-of-life issues and undergone decommissioning.<sup>34</sup> Thus, end-of-life alternatives to disposal for ESS facilities have not yet developed into a consistently regulated and economically viable activity. However, the U.S. storage industry is preparing to develop responsible industry practices.

Used EV Li-ion batteries are increasingly being diverted from disposal pathways into a growing recycling industry and even reuse in stationary ESS applications. The lessons learned from used EV Li-ion batteries may help develop sustainable pathways for decommissioned ESS facilities. Not only can

---

<sup>31</sup> NREL, “Competition Spurs Transformative Lithium-Ion Battery Recycling Solutions” (February 28, 2019).

<sup>32</sup> U.S. Department of Energy, “U.S. Department of Energy Launches Energy Storage Grand Challenge” (January 8, 2020).

<sup>33</sup> Howell, David, “Lithium Battery Technology Discussion,” Presentation at NREL (March 16, 2020).

<sup>34</sup> As of March 24, 2020, U.S. Energy Information Administration Form 860m data showed only 11 ESS systems (totaling 52.5 MW) retired to date.

recycling of Li-ion batteries be environmentally beneficial, it can be economically desirable given the right combination of materials, processes, and commodity market prices. Right now, commercial recycling does not yet exist at a scale sufficient to process today's used EV batteries or the forthcoming decommissioned ESS batteries. Significant R&D efforts and increasing investments in recycling capacity are needed to ensure that recycling at scale is economic and practicable. In the meantime, states and other jurisdictions are beginning to develop rules and processes regarding decommissioning, transportation, disposal, and reuse.

The U.S. Energy Storage Association continues to lead the U.S. storage industry and engage with key stakeholders to foster innovation and advanced practice guidelines in emergency preparedness, safety, supply chain, end-of-life and recycling issues. To learn more about how ESA is working proactively on these issues, visit the ESA's [Corporate Responsibility Initiative](#) webpage to obtain previously-published and forthcoming resources.

## Additional Resources

1. Argonne Lab ReCell Center: <https://recellcenter.org/>
2. California Environmental Protection Agency Lithium-ion Car Battery Recycling Advisory Group homepage: <https://calepa.ca.gov/climate/lithium-ion-car-battery-recycling-advisory-group/>
3. Call2Recycle interactive map of recycling laws by state: <https://www.call2recycle.org/recycling-laws-by-state/>
4. NAATBatt “Laws, Regulations and Best Practices for Lithium Battery Packaging, Transport and Recycling in North America” <https://naatbatt.org/lithium-recycling-laws/>
5. NREL Lithium Ion Battery Recycling Prize: <https://www.herox.com/BatteryRecyclingPrize>
6. U.S. Department of Energy, Energy Storage Grand Challenge: <https://www.energy.gov/energy-storage-grand-challenge/energy-storage-grand-challenge>
7. U.S. Energy Information Administration Form 860m: <https://www.eia.gov/electricity/data/eia860m/>

# Bibliography

- Argonne National Laboratory. "[DOE launches its first lithium-ion battery recycling R&D center: ReCell.](#)" February 15, 2019.
- Battery Association of Japan. "[Program to Make the Portable Secondary Battery Recycle Mark an International Standard.](#)" Accessed April 20, 2020.
- Battery Association of Japan. "[Revised Guideline for Recycle Marking on Li-ion Batteries for the Japanese Market.](#)" Accessed April 20, 2020.
- Business Council for Sustainable Energy and Bloomberg New Energy Finance. [2020 Sustainable Energy in America Factbook.](#) February 2020.
- Ciez, Rebecca. "Li-ion Battery Recycling Processes: Environmental Impacts and Economics." Energy Storage Association Webinar: [Energy Storage Decommissioning, End of Life and Recycling.](#) March 13, 2019.
- Dai, Qiang Jarod C. Kelly, Linda Gaines and Michael Wang. "[Life Cycle Analysis of Lithium-Ion Batteries for Automotive Applications.](#)" *Batteries* 2019, 5, 48. June 1, 2019.
- Gaines, Linda, Kirti Richa and Jeffrey Spangenberg. "[Key issues for Li-ion battery recycling.](#)" *MRS Energy & Sustainability: A Review Journal.* 2018.
- Global Battery Alliance. "[42 Global Organizations Agree on Guiding Principles for Batteries to Power Sustainable Energy Transition](#)" [News Release.](#) January 23, 2020.
- Hanley, Steve. "[Tesla Batteries Have 90% Capacity After 160,000 Miles, May Last For 500,000 miles.](#)" *Clean Technica.* April 16, 2018. Accessed April 20, 2020.
- Howell, David. "[Lithium Battery Technology Discussion.](#)" Presentation at NREL. March 16, 2020.
- Lawrence Berkeley National Laboratory, V2G-Sim. "[Redefining the Useful Lifetime and the Start of EV Battery 2nd Life.](#)" 2019.
- Mauer, David. "Battery Reuse and Recycling: A Maturing Ecosystem." Energy Storage Association Webinar: [Energy Storage Decommissioning, End of Life and Recycling.](#) March 13, 2019.
- Mayyas, Ahmad, Darlene Steward, and Margaret Mann, "[The case for recycling: Overview and challenges in the material supply chain for automotive li-ion batteries](#)" *Sustainable Materials and Technologies* No. 17. April 2018.
- Melin, Hans Eric. "[The lithium-ion battery end-of-life market – a baseline study.](#)" Prepared for the Global Battery Alliance. 2019. Accessed April 20, 2020.
- National Renewable Energy Laboratory (NREL). "[Competition Spurs Transformative Lithium-Ion Battery Recycling Solutions.](#)" February 28, 2019.

New York State Energy Research and Development Authority. "[New York Battery Energy Storage System Guidebook for Local Governments.](#)" July 2019.

Renewance, Inc. "[Commercial Liability Considerations for End-of-Life Industrial Batteries.](#)" Accessed April 20, 2020.

Spangenberg, Jeff. "ReCell Center. Working Towards a Cost-Effective Li-ion Battery Recycling Process." Energy Storage Association Webinar: [Energy Storage Decommissioning, End of Life and Recycling.](#) March 13, 2019.

Taylor, Phil. "[When an Electric Car Dies, What Will Happen to the Battery? Can millions of lithium ion batteries be recycled?](#)" *Scientific American*. September 14, 2009. Originally published in Greenwire. Accessed April 20, 2020.

UL. [Standard 1974 for Evaluation of Repurposing Batteries.](#) 2018.

United Nations Economic Commission for Europe. [Manual of Tests and Criteria: Seventh Revised Edition.](#) 2019. Accessed April 20, 2020.

U.S. Department of Energy. "[U.S. Department of Energy Launches Energy Storage Grand Challenge.](#)" January 8, 2020. Accessed April 20, 2020.

U.S. Environmental Protection Agency. "[May a handler of universal waste manage broken or damaged batteries as universal wastes?](#)" Accessed April 20, 2020.

World Economic Forum. [A Vision for a Sustainable Battery Value Chain in 2030: Unlocking the Full Potential to Power Sustainable Development and Climate Change Mitigation.](#) September, 2019.

### WHO WE ARE

An independent organization of leading scientists and journalists researching and reporting the facts about our changing climate and its impact on the public.

### WHAT WE DO

Climate Central surveys and conducts scientific research on climate change and informs the public of key findings. Our scientists publish and our journalists report on climate science, energy, sea level rise. [Read More](#)

### ABOUT OUR EXPERTISE

Members of the Climate Central staff and board are among the most respected leaders in climate science. Staff members are authorities in communicating climate and weather links, sea level rise, climate. [Read More](#)

## Climate Central Solutions Brief: Battery Energy Storage

Published: November 13th, 2019



### Batteries are having a moment.

In early October, the Royal Swedish Academy of Sciences awarded the [2019 Nobel Prize in Chemistry](#) to three scientists for their research on lithium-ion batteries. Their work decades ago led to batteries becoming smaller, more powerful, more portable, and rechargeable, all of which have transformed our laptops, our phones, and our lives.

The same month, news headlines lauded [batteries' ability to act as backup generators during grid outages](#), as millions endured planned blackouts [during this year's fire season](#) in California.

Batteries are also being touted as the “Holy Grail” for reducing greenhouse gas emissions as we electrify our vehicles and seek to convert our energy grid to a carbon-free system. When connected to a renewable energy source, such as photovoltaic solar panels, batteries can take in the clean energy produced when the skies are clear and sunny, store it, and then send it back to the electricity grid at night, on cloudy days, or whenever needed. And batteries can potentially [reduce electricity bills](#) for customers who use them to send power back to the grid when demand is at its peak and energy prices are at their highest.

Also, rechargeable batteries are powering the rise in plug-in electric vehicles. In 2018, more than 360,000 electric vehicles were sold in the United States, an [increase of 81%](#) over 2017. With transportation [contributing 29% of U.S. carbon emissions](#), electric vehicles have the potential to significantly lower those emissions, provided the electricity grid that supports them is powered by low-carbon energy.

Just as the cost of energy derived from wind turbines and photovoltaics has dropped in recent years, the [price of battery energy storage is declining as well](#). But there are still [regulatory hurdles](#), [safety issues](#), and [other challenges](#) before battery energy storage can become a major component of the electricity grid in the United States. This Climate Central Solutions Brief provides an overview of batteries, including the science, their potential applications, and the market and policy forces shaping the current status and future of batteries.

[Download this report as a PDF.](#)

## The science behind batteries

Lithium-ion batteries [currently have the highest energy and power densities](#) among alternative battery chemistries, which is why they're in all of our cell phones and other portable devices. They can store a large amount of energy and deliver it quickly.

Lithium-ion batteries store energy in the form of chemical energy, and have three main parts: the anode (negative electrode), the cathode (positive electrode), and the electrolyte, a chemical medium separating the two electrodes. Chemical reactions at the anode release electrons that travel through an external circuit (to power your laptop or your electric vehicle or something as complex as the [Mars Curiosity rover](#)) and back to the cathode where they recombine with the positive ions that traveled through the electrolyte. The process also works in reverse when a stream of electrons (electricity) from an external source is fed to the battery circuit. This is how batteries are recharged.

Despite their advantages, lithium-ion batteries' components [are inherently volatile](#). Remember the hoverboards that caught fire a few years back? An explosion can result when the thin separator that keeps the elements of the battery apart weakens or disintegrates and the battery overheats. Even small lithium batteries can store large amounts of energy, and e-cigarettes, cell phones, and hoverboards have been known to explode. Still, for all their widespread use, instances of catching fire are [still relatively uncommon](#) and [technology advances](#) in lithium-ion batteries continue, including [efforts to make them safer](#).



**MICROGRID PILOT IN BORREGO SPRINGS, CALIF.**

The 2,800 people who reside in Borrego Springs, nearly 90 miles northeast of San Diego, are served by a 60-mile transmission line subject to wildfires, windstorms, flooding, and extreme temperatures. After a 2007 wildfire took out the transmission line, San Diego Gas & Electric piloted the nation's first renewables-plus-storage microgrid in the town, which incorporates diesel generators, solar power, batteries, and control systems.

In addition, lithium mining has potentially negative environmental effects. With more electric vehicles being produced, [lithium consumption](#) has correspondingly increased, and many researchers are studying the [environmental sustainability of lithium extraction](#). Lithium is found in the brine beneath salt flats; to extract it, holes are drilled to pump the brine to the surface. The process can divert great amounts of clean water [away from communities and agriculture](#). Further, recycling infrastructure [has not yet been developed for lithium-ion batteries](#), and they can be toxic or flammable when disposed of in landfills.

Lithium-ion batteries represent only one type of energy storage. Several other [types of batteries](#) can be developed for different applications.

### Batteries and resilience

Historically, some residents and business owners have kept their lights on during storms or blackouts with gas or diesel generators, which tend to be noisy and [polluting](#). [Distributed energy resources](#)—small-scale power generation from sources like rooftop solar panels or battery storage—can [increase resilience](#), particularly as climate change brings more extreme weather events and greater potential for loss of power. As this power is produced by a residence or business, it is referred to as “behind the meter” and is controlled by the customer producing it, and backed up by the grid.

The vast majority of homeowners or businesses that produce their own power through solar will still find themselves without power during a grid outage. To truly be [independent of the electrical grid](#), solar panels generally must be accompanied by a storage system and an inverter (which converts the electrical output of solar panels into a usable form of electricity) that enables them to become their own freestanding energy system, acting as a microgrid.

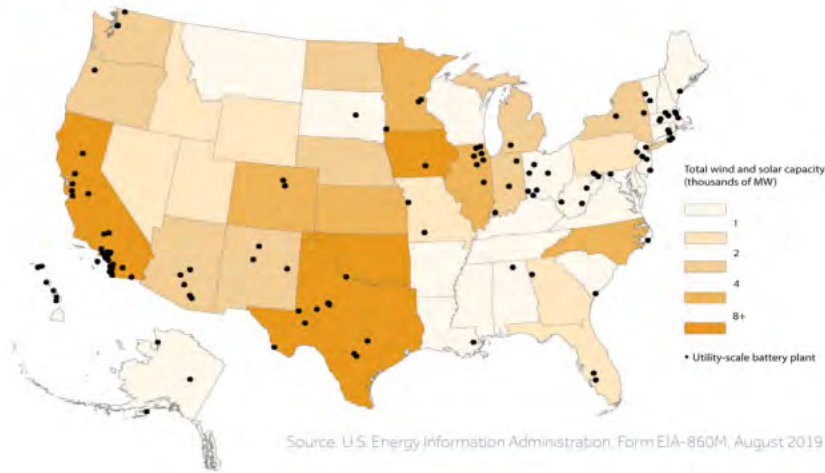
But battery storage is expensive, and many in California or other parts of the country who are vulnerable to fires or outages from storms cannot afford to simply purchase a system. Plus, traditional [utilities and regulators have long struggled](#) with the growth of distributed generation, and are still working to figure out policies and rate designs to allow for its increase. This attitude may be changing in the [wake of the fires and outages in California](#). In September, the California Public Utilities Commission announced changes to their [Self-Generation Incentive Program](#) that focuses on wildfire prevention, creating larger subsidies to assist low-income customers and critical service facilities, in addition to focusing on reducing greenhouse gas emissions.

## SECOND LIFE FOR ELECTRIC VEHICLE BATTERIES

When electric vehicle (EV) batteries are no longer able to meet the high standard performance thresholds for transportation, they can still be reconditioned to store energy for the stationary grid for another 10 years. The National Renewable Energy Laboratory is exploring this reuse to help increase EV ownership and reduce the cost of grid-connected energy storage systems.

## Figure 1. Solar, Wind and Battery Energy

Large-scale installations powering the country



Microgrids can [deliver resiliency](#) by allowing a facility to operate during an electrical grid outage. Microgrid systems are already in use by many entities that must have uninterrupted access to electricity, including military installations, industrial facilities, hospitals, wastewater treatment plants, and universities. In the past, microgrids often relied on natural gas and/or diesel generation, but [microgrids using renewables increased](#) from about 4 MW in 2008 to 164 MW in 2016, with solar accounting for 73% of this growth. In addition to providing resilience, in some instances microgrid systems reduce energy costs, as the microgrid can sell excess energy back to the grid, especially during peak demand times. [In the U.S., microgrids typically coordinate with the larger distribution grids, until a blackout occurs](#), when the microgrid is able to become its own “island.” Microgrids also can [eliminate the need to transmit power over long distances](#), taking the pressure off large power lines and making fire-prone areas safer.

### Batteries help with intermittency of solar and wind

As costs of solar and wind energy have plummeted in recent years, their installed capacity has grown dramatically. But the sun doesn't always shine and the wind doesn't always blow, and this can threaten the reliability of the electric grid.

On the nation's current electric grid, energy is typically used as soon it's generated; supply must match demand, or customers will face power surges or blackouts. California now produces so much solar energy in the middle of sunny days [that it pays Arizona and other states to take the power off its grid](#) so it doesn't overload its transmission lines. Batteries can store some of this energy making them critical to ensure grid stability and for the wider deployment of renewable energy.

In the U.S., [renewable generation has doubled since 2008](#), providing a record 18% of all electricity generation in the United States in 2018. Most of that increase in renewable energy—nearly 90%—came from wind and solar generation. And more wind and solar is expected to come online, with [renewable growth expecting to outdistance fossil fuel growth](#) by June 2022. The MAPTK shows the utility-scale solar and onshore and offshore wind capacity by state as of August of 2019, for installations larger than 1 megawatt.

This growth has been encouraged by adoption of [“renewable portfolio standards”](#) in 29 states that require a specified percentage of the state's electricity to come from renewable sources. [Eleven states currently have targets of 50% or more](#) by mid-century. For example, California aims to achieve 60% renewable energy by 2030 and 100% zero-carbon electricity by 2045.

As renewables have grown, so has [battery storage](#) at the utility-scale (one megawatt or greater). Total installed capacity of [utility-scale battery storage \(one megawatt or greater\) has more than quadrupled from](#) 214 MW installed in 2014 to 1,000 MW installed by August 2019. [Projections are for an additional 2,500 MW to come online by 2023](#), according to the U.S. Energy Information Administration. Figure 1 shows installed large-scale battery systems as of August 2019, which most commonly use [lithium-ion battery technology](#).

**BATTERY TO PROVIDE RESILIENCY FOR ANDERSON COUNTY, S.C.**

Duke Energy is installing a 5-MW lithium-ion battery storage system to support the Anderson Civic Center, which operates as an emergency shelter and command center during hurricanes and other crises. The battery capacity allows the center to run for roughly 30 hours without grid power and will also allow Duke Energy to use it for grid stability during periods of peak customer demand.

**Table 1. Utility Scale Capacity in Megawatts, Installations > 1MW as of August 2019**

Battery Storage		Wind		Solar	
California	262	Texas	26,407	California	11,203
Illinois	133	Iowa	8,922	North Carolina	4,104
Texas	114	Oklahoma	8,071	Florida	1,976
Hawaii	63	Kansas	6,150	Texas	1,965
West Virginia	50	California	6,080	Nevada	1,833

### Batteries help with demand

Battery energy storage can play a critical role during periods of high energy demand—notably, when people get home from work and turn on the lights, appliances, and plug-in electric vehicles, precisely at the time when the sun is setting. The resulting mismatch of supply and demand results in the so-called “[duck curve](#)” (Figure 2).



**NEVADA TO HAVE LARGEST SOLAR COMPLEX IN U.S.**

NV Energy, which provides more than 80% of Nevada’s electricity, recently announced another 590 megawatts of battery storage paired with three new solar projects totaling 1,200 megawatts.

For years, utilities have used natural gas “peaker plants” that come online quickly when the grid demands more energy. Peakers operate infrequently—only at times of peak demand when they get paid a higher price, relying on these peak periods to cover their costs of operation. But as they’re used only for a few hundred hours per year, and with the costs of battery storage declining, analysts [see the potential for batteries to serve peak demand](#) instead, offering a [carbon-free alternative](#).

### Batteries’ declining costs and government policy

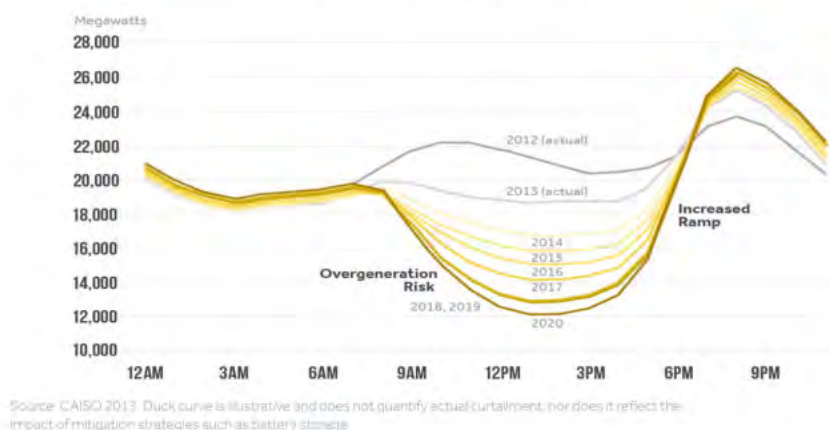
Although its price is declining, battery storage is more expensive than other energy sources, and state and federal government policies, such as [procurement goals, financial incentives, or requiring storage capacity](#) in state energy plans, will impact the future growth of battery storage.

Most utility-scale storage systems are overseen by independent, federally regulated organizations charged with controlling the power grid and electricity pricing, called [Independent System Operators \(ISOs\) and Regional Transmission Organizations \(RTOs\)](#). In February 2018, the Federal Energy Regulatory Commission approved an [order](#) requiring these state and regional overseers to lower regulatory barriers to new energy storage technologies, in order for them to compete with other energy generation.

PJM (Pennsylvania-Jersey-Maryland, the RTO for 13 eastern states) has the [largest amount of large-scale battery installations](#), with a storage capacity of [nearly 300 MW](#). California’s ISO is the second largest, overseeing batteries with a total storage capacity of [136 MW as of October 2019](#), but has the most storage expected to come online because of California’s [mandate to procure 1325 MW by 2020](#).

**Figure 2. Solar Energy “Duck Curve”**

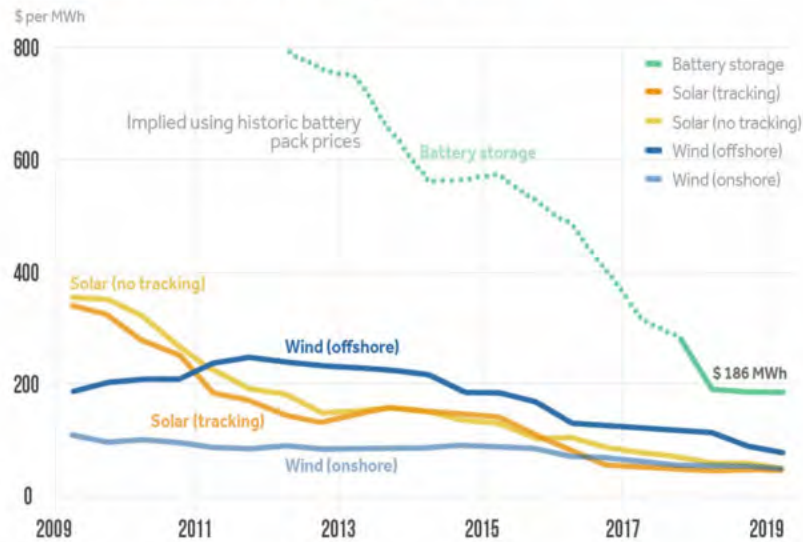
The power grid must balance daily energy supply and demand



The Figure 3 shows the recent decline in cost of both lithium storage batteries and renewable energy sources - costs that are projected to continue to fall. Battery storage projects with four-hour [duration](#) cost \$186/MWh in the second half of 2019, a 35% decrease since the beginning of 2018, and a 76% drop since 2012. Onshore and offshore wind prices have also dropped, about 57% since 2009, and utility scale PV system costs have fallen 86% over the last decade. Large scale battery-plus-solar system prices are becoming more competitive with traditional generation, especially in areas with abundant solar energy output, like the Southwest. With more extreme weather, they may be seen as economically viable—particularly [when potential financial losses from grid outages are considered](#).

### Figure 3. Solar, Wind and Battery Prices Falling

BloombergNEF Levelized Cost of Energy 2009-2019



Source: BloombergNEF Note: The global benchmark is a country weighted-average using the latest annual capacity additions. The storage LCOE is reflective of a utility-scale Li-ion battery storage system with four-hour duration running at a daily cycle and includes charging costs assumed to be 60% of wholesale average power price. Data as of October 22, 2019

#### The future of batteries

Battery storage technologies are constantly [evolving](#), as scientists and engineers work to [find energy storage solutions](#) that are cheaper, safer, denser, lighter, and more powerful. The lithium ion battery could be replaced by [any number of challenger](#) technologies, including [aluminum](#) or [iron](#) batteries. Electric vehicles are becoming increasingly prevalent, and scientists are [predicting longer driving ranges and shorter charging times](#) with innovations in batteries. Even passenger airplanes may one day be powered by batteries [powerful enough to meet the demands of liftoff](#), helping to curb carbon emissions from air travel. Who knows? In another decade or so, more Nobel prizes may be awarded for breakthroughs in battery technology.

<sup>1</sup> While energy generation sources (such as natural gas or solar) are described in terms of capacity—the maximum instantaneous amount of power they can emit in units such as megawatts (MW) or kilowatts (kW)), Batteries are restricted by how much power they can provide before they need to recharge, [known as duration](#). So a storage system is referred to by both its capacity and its duration. For example, a 50-MW battery with 4 hours of duration would be expressed as being 200 MWh in size. A megawatt hour (MWh) is the amount of electricity produced by a generator operating for one hour.

Posted in [Energy](#), [Solutions](#), [Research](#)

#### Comments

[\[+\] View our comment guidelines.](#)

Please note: Comment moderation is enabled. Your comment will not appear until reviewed by Climate Central staff. Thank you for your patience.

Post Your Comment

CLIMATE  CENTRAL

EMAIL NEWSLETTER

Copyright © 2021 Climate Central. [Contact](#) | [Terms](#) | [Content Licensing](#) | [Privacy](#) | [Site Map](#)

---